

Modeling and analysis of miniaturized magnetorheological valve for fluidic actuation

Présentée le 26 octobre 2023

Faculté des sciences et techniques de l'ingénieur
Laboratoire d'actionneurs intégrés
Programme doctoral en robotique, contrôle et systèmes intelligents

pour l'obtention du grade de Docteur ès Sciences

par

Sofia Lydia NTELLA

Acceptée sur proposition du jury

Prof. J.-P. R. Kneib, président du jury
Prof. Y. Perriard, Dr C. Köchli, directeurs de thèse
Prof. E. Lomonova, rapporteuse
Dr D. Grivon, rapporteur
Prof. C. Enz, rapporteur

"Every science begins as philosophy and ends as art."
— Will Durant

To my family...

Acknowledgements

I would like to begin by expressing my sincere gratitude to my supervisor, Prof. Yves Perriard, for providing me with the opportunity to pursue my PhD thesis at EPFL and especially at LAI. I would also like to express my deepest gratitude to my co-supervisor, Dr. Christian Koechli, for being a source of support throughout both the joyful and challenging moments of my thesis. Additionally, I extend my appreciation to all the jury members for their participation in my examination and their time spent reading and comprehending my work. I also want to acknowledge all the BRIDGE-project partners, Dr. Civet, Dr. Trung, Dr. Hemler, and Prof. Pataky for their great collaboration throughout my four years of research.

I would also like to express my deep appreciation to two individuals without whom my thesis would not have been possible. First, Paolo Germano, the heart of LAI, for his unwavering support and wealth of knowledge in electronics, fabrication, and testbenches and all other aspects of our project, for his administrative support for all aspects of our work, for organizing our courses, for purchasing everything for our project, for teaching me the virtues of patience, Swiss precision, and organization, and for always brightening our lab with his kind nature. Second, I owe a debt of gratitude to Kenny Jeanmonod, a superb engineer and collaborator, who made all the practical work of our project possible, who taught me French, and who made working together an absolute pleasure.

I would also like to extend a special thanks to Dr. Bhawnath Tiwari, whose scientific and academic guidance on conducting experiments and writing papers were invaluable in propelling me towards completing my PhD. My heartfelt appreciation also goes out to Pooneh and Marjan, with whom I have shared countless fond memories and whose presence in the lab has been invaluable. My thanks goes also to all the members of LAI, past and present, who have contributed to making my PhD a truly enriching experience.

I would like to express my gratitude to my beloved friends, Athina, Paschalia, Georgia, Giannis, Maria, Despina, Irini, Myrto, Konstantinos, and Vaios for their unwavering support throughout this journey. I would also like to thank Kostas who has always been by my side, no matter what. Finally, I want to thank my family, my parents and grandparents, for working hard to give me a great education and for always supporting and inspiring me in my pursuit of knowledge.

Lausanne, July 17, 2023

S. L. N.

Abstract

Fluidic actuation enables movement in a wide range of mechanical systems, from simple laboratory devices to more complex industrial machinery. Fluids are used to generate motion of mechanical pieces. The term "fluids" encompasses two types of technologies: hydraulics, employing fluids in a liquid state, and pneumatics, which uses gases. Fluidic systems offer significant advantages over traditional mechanical actuation systems, including a high power-to-weight ratio and high forces and torques. Valves are an integral part of fluidic control and are based on different working principles, such as solenoids and servo valves. These mechanisms are quite bulky and power-consuming.

Alternatively, valves are enabled by smart materials, such as dielectric elastomer actuators, shape memory alloys, electrorheological, or magnetorheological fluids. This thesis focuses on magnetorheological valves due to their advantages of controllable viscosity, low power consumption, fast response, and simple and compact structure. Magnetorheological fluids consist of ferromagnetic particles dispersed in a carrier medium that align parallel with the lines of an external magnetic field increasing the fluid viscosity. This property is exploited in valves for their switching. The current thesis focuses on the miniaturization of a magnetorheological valve and modeling with regard to the distribution of magnetic field in its interior and with the pressure drop that is developed between its two sides. The functionality is validated experimentally and the results are analyzed. The conventional design of the valve is enhanced by the addition of a soft magnetic material in its core, which together with a coil plays the role of an electropermanent magnet. This addition allows for zeroing of the valve steady-state power consumption, while energy consumption takes place only during state switching.

Magnetorheological valves are also used in combination with sensors as part of control systems of dampers providing damping feedback for the valve control. In this direction, multiple works studied the creation of displacement and force self-sensing valves avoiding the use of external sensors and increasing the compactness and robustness of the system. This thesis aims at investigating further the pressure self-sensing phenomenon in magnetorheological valves, which is based on electromagnetic induction. Induced signals are measured in a magnetorheological valve with two coils. Additionally, a microfluidic device attempts to imitate the structure of the valve, in order to observe the phenomenon microscopically.

Finally, the application of the developed miniaturized valve in a wearable device for diabetic patients is studied. Diabetic amputation is attributed to two reasons: high plantar pressures and peripheral neuropathy that leads to the loss of pain feeling and ulceration creation. Existing ulceration prevention methods rely on bulky mechanical systems, reducing patients'

Abstract

quality of life. This work presents a wearable device in the form of an insole, consisting of multiple modules and battery-powered electronics for control. Each module contains a MR valve and is filled with MR fluid, while it is capable of sustaining or offloading foot load. The entire footwear system is presented, including a 31-module insole, plantar pressure measurement methods, control electronics, and preliminary results that are promising for the future use of the application as a prescribed medical device.

Keywords: Fluidic actuation, magnetorheological fluids, miniaturized valve, electropermanent magnet, self-sensing, diabetic foot ulceration prevention, intelligent footwear

Résumé

L'actionnement fluide permet le mouvement dans une large gamme de systèmes mécaniques, allant des dispositifs de laboratoire simples aux machines industrielles plus complexes. Les fluides sont utilisés pour générer le mouvement de pièces mécaniques, telles que des pistons. Le terme « fluides » englobe deux types de technologies : l'hydraulique, qui utilise des fluides à l'état liquide, tels que l'huile ou l'eau, et la pneumatique, qui comprend des gaz, le plus courant étant l'air. Les systèmes fluidiques offrent des avantages significatifs par rapport aux systèmes d'actionnement mécanique traditionnels, notamment un rapport puissance-poids élevé, des forces et des couples élevés, et la capacité à fonctionner dans une large gamme de pressions et de températures.

Le flux des liquides et la pression dans les systèmes d'actionnement fluide sont surveillés et régulés par plusieurs composants, tels que des pompes, des valves et des capteurs externes, permettant une plus grande précision. Les valves font partie intégrante du contrôle fluide et sont basées sur différents principes de fonctionnement, tels que les solénoïdes et les servo-valves. Ces mécanismes sont assez encombrants et consomment beaucoup d'énergie. En revanche, des valves sont activées par des matériaux intelligents, tels que des actionneurs à diélectrique élastomère, des alliages à mémoire de forme, des fluides électrorhéologiques ou magnétorhéologiques. Cette thèse se concentre sur les valves magnétorhéologiques en raison de leurs avantages de viscosité contrôlable, de faible consommation d'énergie, de réponse rapide et de structure simple et compacte. Le fluide magnétorhéologique est un matériau intelligent qui est constitué de particules ferromagnétiques dispersées dans un milieu porteur. Les particules s'alignent parallèlement aux lignes d'un champ magnétique externe, augmentant ainsi la viscosité du fluide. Cette propriété est exploitée dans les valves pour leur commutation.

La présente thèse se concentre spécifiquement sur la miniaturisation des valves magnétorhéologiques et leur optimisation. Elle présente un modèle de la distribution du champ magnétique à l'intérieur des valves et de la chute de pression à leurs bornes. La fonctionnalité de la valve est validée expérimentalement et les résultats sont analysés, fournissant des informations utiles sur son fonctionnement. La conception conventionnelle de la valve est améliorée par l'ajout d'un aimant permanent de type AlNiCo dans le noyau de la valve. Ce type d'aimant peut être magnétisé ou démagnétisé à l'aide de la bobine au moyen d'impulsions de courant - ce qui permet de réduire la consommation d'énergie en régime permanent. La valve ne consomme alors d'énergie que lors de la commutation d'états.

Les valves magnétorhéologiques sont généralement utilisées en combinaison avec des cap-

teurs dans le cadre de systèmes de contrôle, tels que les amortisseurs. Les capteurs fournissent une rétroaction d'amortissement pour le contrôle de la valve. De multiples articles ont étudié la création de valves auto-sensibles à la force et au déplacement, évitant ainsi l'utilisation de capteurs externes et augmentant la compacité et la robustesse du système. Cette thèse, basée sur des recherches précédentes menées au LAI, vise à étudier plus avant la technique de mesure de pression dans les valves magnétorhéologiques sans capteurs externes. Cette dernière est basée sur l'induction électromagnétique. Des signaux induits sont mesurés dans la valve magnétorhéologique avec deux bobines. Les signaux diffèrent avec l'application de différentes valeurs de pression. Afin de pouvoir observer le phénomène de manière microscopique, un dispositif microfluidique imitant la structure de la valve a également été développé.

Enfin, l'application de la valve magnétorhéologique miniaturisée développée dans un dispositif portable pour les patients diabétiques est étudiée. Le diabète constitue aujourd'hui la cause prédominante d'amputation non traumatique des patients diabétiques. L'amputation est attribuée à deux raisons : des pressions plantaires élevées et une neuropathie périphérique qui entraîne la perte de sensation de douleur et la création d'ulcères. Les méthodes existantes de prévention des ulcères reposent sur des systèmes mécaniques volumineux, réduisant la qualité de vie des patients. Ce travail présente un dispositif portable sous la forme d'une semelle intérieure, composé de plusieurs modules et d'une électronique de contrôle alimentée par batterie. Chaque module contient une valve magnétorhéologique et est rempli de fluide. Il est ainsi capable de soutenir ou de décharger la charge du pied. L'ensemble du système de chaussures est présenté : il comprend une semelle intérieure avec 31 modules, diverses méthodes de mesure de la pression plantaire, une électronique de contrôle et il donne des résultats préliminaires prometteurs pour une utilisation future de l'application en tant que dispositif médical prescrit.

Mots clefs : actionnement fluide, fluides magnétorhéologiques, valve miniaturisée, aimant permanent de type AlNiCo, self-sensing, prévention des ulcérations du pied diabétique, chaussure intelligente.

Contents

Acknowledgements	i
Abstract	iii
List of Figures	xi
List of Tables	xvii
1 Introduction	1
1.1 Rheological models	2
1.2 Yield stress	3
1.3 Forces acting on the MR fluid particles	3
1.4 Magnetic properties and micromechanical modeling	4
1.5 Particle and medium influence	5
1.6 MR fluid operational modes	5
1.7 MR fluid between parallel fixed plates	7
1.8 Magnetorheological valve configurations	10
1.8.1 Annular	11
1.8.2 Radial	11
1.9 Original contributions & thesis outline	12
2 State of the Art	14
2.1 Fluidic actuation systems	14
2.2 Valves for fluidic system control	15
2.2.1 Working principles	15
2.3 Magnetorheological (MR) valves	19
2.3.1 Design optimization	20
2.3.2 Valve miniaturization	22
2.3.3 Self-Sensing	24
2.3.4 MR fluid challenges and material improvements	24
2.3.5 Applications	25
2.4 Conclusions	31
3 Magnetorheological valve design, modeling, and validation	32
3.1 Annular MR valve analytical modeling	33

3.2	MR valve design and fabrication	35
3.2.1	Design optimization with Design of Experiments (DoE) and Response Surface Methodology (RSM)	35
3.2.2	MR valve final design and fabrication	41
3.3	Finite Element Model (FEM)	43
3.4	Experimental validation	46
3.4.1	Open valve	47
3.4.2	Closed valve	49
3.4.3	State transition	53
3.5	Conclusions and main contributions	54
4	Magnetorheological Valve Based on Electropermanent Magnet	55
4.1	Electropermanent magnet principle	56
4.2	Analytical and numerical modeling	60
4.3	Experimental validation	63
4.3.1	Working principle of the experimental setup	63
4.3.2	Results	64
4.4	Conclusions and main contributions	69
5	Self-Sensing Magnetorheological Valve	71
5.1	Introduction to self-sensing MR valves	71
5.2	Pressure self-sensing miniaturized MR valve with two coils	72
5.2.1	Design and working principle	72
5.2.2	Experimental results	75
5.3	Microfluidic device for the self-sensing phenomenon	78
5.3.1	Self-sensing phenomenon in the microfluidic device	79
5.3.2	Microfluidic device fabrication	82
5.3.3	MR fluid dilution	84
5.3.4	Results	85
5.4	Impedance variation measurements	86
5.5	Conclusions and main contributions	88
6	Novel applications of miniaturized MR valve: Intelligent footwear for diabetic ulceration prevention	90
6.1	Introduction: Intelligent footwear for diabetic ulceration prevention	90
6.1.1	Existing diabetic foot ulcer (DFU) prevention methods	91
6.1.2	State of the art on plantar pressure measurements	92
6.2	Proposed intelligent footwear for DFU prevention	94
6.2.1	MR module design and validation	95
6.2.2	Plantar pressure measurement methods	101
6.3	Control electronics for multi-module insole system	103
6.3.1	Control electronics system architecture	103
6.3.2	Optimization process and final electronic platform	105

6.4 MR module integration in insole	107
6.5 Conclusions and main contributions	112
7 Conclusions	114
A PCB schematics & layout	117
B Materials	127
B.1 MR fluid	127
B.2 MR module	127
B.3 Bill of electronic components	128
Bibliography	129
Curriculum Vitae	150

List of Figures

1.1	Rheological flow curves for the Bingham plastic, Herschel-Bulkley, and Casson model in comparison with the Newtonian fluid curve.	2
1.2	(a) Valve mode (b) Shear mode (c) Squeeze mode (d) Pinch mode.	6
1.3	(a) MR fluid flow between two fixed plates. The magnetic field is applied perpendicularly to the flow. (b) Representation of the fluid velocity profile regions in between the two stationary fixed plates.	7
1.4	Annular magnetorheological (MR) valve in sectional view.	11
1.5	Radial MR valve in sectional view.	11
2.1	Different fluidic actuation systems: (a) The mGrip soft pneumatic gripper (Photo: Soft Robotics, Inc.) (b) Miniature pneumatic soft robotic manipulator (Copyright: 2377-3766 © 2016 IEEE) (c) Soft robotic glove enabling hand impairment rehabilitation (Copyright: 2377-3766 © 2017 IEEE).	15
2.2	(a) Working principle of solenoid valve and (b) application on a pneumatic regulator of soft robot control (Copyright: 978-1-5386-4516-1/18/\$31.00 © 2018 IEEE). (c) Schematics of a conventional servo valve. (d) Servo valve presented in (Copyright: 2377-3766 © 2020 IEEE). (e) Valve fabricated with DEA in (Copyright: 2377-3766 © 2022 IEEE) and (f) photo of fluidic actuator controlled by the DEA valve.	16
2.3	Pictures of (a) ER fluid valve, (b) ER valve schematics, (c) octopus-inspired soft robot actuated with ER fluid and ER valve, (d) soft robot schematics are extracted from (Mary Ann Liebert, Inc. Copyright License No: 5537670197977). MR valve (e) bistable (Copyright: 2377-3766 © 2021 IEEE) or with (f) meandering path (IOP Copyright Licence No: 1349852-1).	17
2.4	Comparison of different valves depending on their physical driving principle, maximum sustained pressure, and size. (Copyright: 2377-3766 © 2023 IEEE) . .	19
2.5	Examples of miniaturized devices with MR fluid: (a) on-chip microfluidic valve (Copyright: 1057-7157 © 2016 IEEE), and (b) haptic device with valve (Elsevier Copyright Licence No: 5537671094344). Valves based on EPM (c) (IOP Copyright Licence No: 1349873-1), and (d) (Copyright: 2377-3766 © 2022 IEEE).	22
2.6	Schematics and prototype photos of MR dampers in different configurations: (1) (IOP Copyright Licence: CC BY 4.0), (2) (IOP Copyright Licence No: 1349838-1), (3) (Copyright: 0018-9464/\$31.00 © 2013 IEEE).	26

List of Figures

2.7	Pictures of (1) knee orthosis with MR damper (Copyright © 2022 Alvarado-Rivera, Niño-Suárez and Corona-Ramírez), (2) one-degree-of-freedom ankle rehabilitation robot with MR damper (Copyright: 978-1-7281-6479-3/20/\$31.00 © 2020 IEEE), (3) smart ankle-foot orthosis with MR damper (Copyright: 1083-4435 © 2019 IEEE), (4) finger rehabilitation robotic system (Elsevier Copyright Licence No: 5537720809140), and (5) catheterization testing system with MR fluid (Copyright: 1552-3098 © 2019 IEEE).	28
2.8	Pictures of (1) soft shock absorber (Copyright: 978-1-7281-9680-0/22/\$31.00 © 2022 IEEE), (2) Pneu-Net-like gripper with MR fluid (Copyright: 2377-3766 © 2021 IEEE), (3) pouch-like gripper filled with MR fluid (Copyright: 2377-3766 © 2021 IEEE), (4) MR fluid gripper controlled with EPM MR valve (Copyright: 2377-3766 © 2022 IEEE).	29
2.9	Pictures of (1) MR fluid suction gripper (Elsevier Copyright Licence: CC BY 4.0), (2) soft crawling robots filled with MR fluid and placed in between Helmholtz coils (Copyright: 1083-4435 © 2020 IEEE), (3) universal MR fluid gripper (IOP Copyright Licence No: 1349885-1).	30
3.1	Annular MR valve in sectional view. The different dimensions are represented. The MR phenomenon is taking place at the active regions of the valve.	33
3.2	MRF-132DG (a) B-H and (b) τ_y -H characteristic curves.	34
3.3	The standardized effects of the various factors and interactions of factors on (a) pressure drop, and (b) flow rate.	37
3.4	Main effects of experiment factors on the different responses.	39
3.5	Magnetic flux density distribution in the length of the gap, with maximum value in the active regions.	41
3.6	Schematics of the MR valve after introducing fabrication imperfections.	42
3.7	Top view and side view disassembly of the prototype of MR valve with 0.2 mm gap width.	42
3.8	Axis-symmetric magnetostatic simulations of the MR valve (A) with MR fluid only in the gap (B) with MR fluid in the gap and around the valve (C) with MR fluid as in case B and with the addition of fabrication differences. The coil is supplied with 0.77 A in all the cases.	44
3.9	The flux density B in the middle of the gap is plotted for the three different simulation cases of Fig. 3.8.	45
3.10	Schematic of the experimental setup with sectional view to highlight the position of the valve and hydraulic circuit diagram of the system.	46
3.11	Piston displacement (Δx) over time for multiple pressure difference ΔP values measured between the two sides of the valve.	48
3.12	Flow rate Q over pressure difference ΔP and experimental estimation of the MR valve flow resistance.	48
3.13	Valve closed with different currents.	49

3.14	Piston displacement over time for different excitation currents and applied pressure values in the dynamic condition.	50
3.15	Maximum sustained pressure by a closed MR valve with regard to the excitation current.	51
3.16	Flux density in the length of the gap for different current values.	52
3.17	Switching of the valve from the closed to the open state.	53
3.18	Repetitive switching of the valve between the ON and OFF state (closed-open).	53
4.1	EPM made from hard (NdFeB) and soft (AlNiCo) magnetic material. (a) Unmagnetized AlNiCo magnet. (b) AlNiCo magnet magnetized at the same direction to NdFeB magnetization. Seen externally as magnetized. (c) AlNiCo magnet magnetized at the opposite direction to NdFeB magnetization. Seen externally as demagnetized.	56
4.2	Annular MR valve in sectional view. The different dimensions are represented. The inner rod of the valve is made from AlNico-5 material that generates the magnetic field. (Copyright: 2377-3766 © 2023 IEEE)	57
4.3	Differences between the conventional and an EPM MR valve. The white arrow represents the magnetization orientation in the rod. (Copyright: 2377-3766 © 2023 IEEE)	58
4.4	The EPM MR valve can function in two states, open and closed. Each stated is depicted accordingly on an ideal M-H characteristic of an AlNiCo-5 device. Demagnetizing the rod can happen with a decaying oscillating external field. (Copyright: 2377-3766 © 2023 IEEE)	58
4.5	Demagnetizing the rod can also happen with a negative pulsed external field reaching the remanence coercivity of the material. (Copyright: 2377-3766 © 2023 IEEE)	59
4.6	A 2-D axisymmetric magnetic simulation of the EPM MR fluid valve. The lines and colorbar represent the magnetic flux density B . (Copyright: 2377-3766 © 2023 IEEE)	62
4.7	Distribution of B in the length of the gap.	63
4.8	(a) Prototype of the EPM MR valve and valve disassembled with the AlNiCo-5 rod in the inner part. (b) Setup to simulate fluidic flow and validate experimentally the functionality of the EPM MR valve. (Copyright: 2377-3766 © 2023 IEEE)	64
4.9	Schematics of control electronics for the EPM MR valve.	65
4.10	The magnetization and demagnetization characteristics (M-H and B-H), and the B_{rod} and H_{rod} for each current value obtained analytically and numerically. (Copyright: 2377-3766 © 2023 IEEE)	65
4.11	Voltage and current pulse over the valve's coil. The positive current corresponds to the magnetization of the AlNiCo-5 rod and the negative to the demagnetization. (Copyright: 2377-3766 © 2023 IEEE)	66

List of Figures

4.12	Piston displacement over the pressure difference between the two chambers of the setup. The valve's state is either open or closed but with different magnetization currents. (Copyright: 2377-3766 © 2023 IEEE)	68
4.13	Maximum sustained pressure over magnetization current.	69
4.14	Pressure difference ΔP and piston displacement Δx over time in an EPM MR valve. The valve is initially closed. At $t = 3\text{ s}$ the demagnetization is taking place and the valve opens, allowing fluid flow and piston displacement. (Copyright: 2377-3766 © 2023 IEEE)	69
5.1	Structure of magnetorheological valve with two coils in a 2D cross-section plane. (Copyright: 978-1-6654-4139-1/21/\$31.00 © 2021 IEEE)	72
5.2	(a) The magnetic path in a 2-D axis-symmetric cross-section of MR valve, observing the elongation of chains with applied pressure (b) Magnetic circuit equivalent. (Copyright: 978-1-6654-4139-1/21/\$31.00 © 2021 IEEE)	73
5.3	Prototype of the MR valve with two coils. The 3D-printed holder facilitates the alignment of the inner and outer ferromagnetic parts of the valve. (Copyright: 978-1-6654-4139-1/21/\$31.00 © 2021 IEEE)	75
5.4	Experimental results of measurements using the MR valve and a piston pressure application of 0.1 s duration to elongate the chains: Voltage measurements for 0.1 A, 0.2 A, and 0.3 A exciting current. (Copyright: 978-1-6654-4139-1/21/\$31.00 © 2021 IEEE)	77
5.5	Minimum voltage peaks achieved when the pneumatic piston is activated at $t = 0.1\text{ s}$. (Copyright: 978-1-6654-4139-1/21/\$31.00 © 2021 IEEE)	78
5.6	(a) Schematics of the microfluidic device; (b) Equivalent of the magnetic circuit of the microfluidic device.	79
5.7	Electrical lumped element model of the microfluidic device with exciting and sensing coil. The red part on the left represents the exciting coil, and the blue part on the right represents the sensing coil. (Copyright: 978-1-6654-1308-4/22/\$31.00 © 2022 IEEE)	80
5.8	Cut view of the microfluidic device with the different fabrication layers. (Copyright: 978-1-6654-1308-4/22/\$31.00 © 2022 IEEE)	82
5.9	Device with one exciting coil, one sensing coil, and a microchannel for MR fluid flow. Each coil is wound around the sheet in three parts, starting from the left and continuing to the bottom and right. The two coils are layered one on top of the other as in the side view. (Copyright: 978-1-6654-1308-4/22/\$31.00 © 2022 IEEE)	83
5.10	MRF-132DG with particles concentration in the carrier medium (a) 33% (b) 15% (c) 2% (d) 1% volume-on-volume ratio. Photos captured with Dino-Lite optical microscope by Timothy Loayza.	84

5.11 Top: four video frames separated by 67ms. (1) Existence of magnetic field and particle chains (2) Chains breakage (3) Chains begin to reform (4) Chains completely recreated. Bottom: filtered and amplified induced voltage on the sensing coil with red dots representing the video frames. (Copyright: 978-1-6654-1308-4/22/\$31.00 © 2022 IEEE)	85
5.12 Impedance magnitude and phase for different frequencies.	87
6.1 Diabetic ulceration prevention methods: (a) Total Contact Cast, (b) Removable cast walkers, (c) Rocker shoes.	91
6.2 Schematics of the proposed footwear with offloading modules based on MR fluids.	94
6.3 Different sectional views of the MR module.	96
6.4 Setup for experimental validation of the MR module and picture of the MR module prototype. (Copyright: 978-1-6654-9302-4/22/\$31.00 © 2022 IEEE)	97
6.5 MR module under the pull tester setup for measuring force vs. displacement.	98
6.6 MR module validation results with the use of the pull tester.	98
6.7 Pisont displacement and force over time for (a) open (b) closed MR module. (Copyright: 978-1-6654-9302-4/22/\$31.00 © 2022 IEEE)	99
6.8 Pisont displacement and force over time showing the transition from the closed to the open state of the MR module. (Copyright: 978-1-6654-9302-4/22/\$31.00 © 2022 IEEE)	100
6.9 MR module in the closed state with iterative applications of force. (Copyright: 978-1-6654-9302-4/22/\$31.00 © 2022 IEEE)	101
6.10 Different plantar pressure/force measurement methods: (A) & (B) Nanopaint insoles with different textiles (C) Flexible PCB insole with piezoresistive sheet (D) Piezoresistive sheet with electrodes made with silver evaporation (E) Tekscan A301 FSR sensor (F) Senstech force sensor (G) Piezoresistive sensor with 3 cells.	102
6.11 Block-diagram and prototype of the first PCB.	104
6.12 Block-diagram of control electronics. (Copyright: 978-1-6654-9302-4/22/\$31.00 © 2022 IEEE)	105
6.13 Fabricated PCB.	106
6.14 Picture of the insole prototype with 9 MR modules, and their numbering principle. The rest of the places in the insole are filled with fake modules.	108
6.15 Measurements from Pedar-X right insole (only front part) before and after opening the MR modules (A) M1 (B) M1, M2 (C) M3 (D) M4 (E) M5, M6, M7, M9 (F) M6 (G) M7 (H) M9, M8, M6, M5. The bottom part is not shown because the plantar pressure distribution does not change after turning off the MR modules.	109
6.16 Average pressure on the whole plantar surface of the right foot before and after turning off different modules at $t = 4$ s (left), pressure over time on pressure sensor where peak pressures have been created with the addition of the object (middle), peak pressure on the total insole surface (all 99 sensors) over time (right).	110

List of Figures

6.17 (a) Prototype of the full shoe, with MR modules in the front part and faked modules at the heel. The control electronics are placed in the middle of the insole and on top of all of these, the plantar force measurement insole is placed. The green insole is a soft insole placed on top of our system to increase comfortability for the patients. (b) The bottom view of the insole, with flexible PCB connectors that link the modules with the control electronics. (c) Flexible force measurement insole. (d) Control electronics and battery integration. 112

A.1 Top and bottom layers 125

A.2 Middle layers 126

List of Tables

2.1	Sorting of various MR valve/damper design optimization works according to the optimization method and the algorithm used.	21
3.1	Definition of the different factors of the fractional factorial design and their upper and lower levels.	36
3.2	Characteristics of the optimal MR valve design resulting from the DoE optimization.	40
3.3	Dimensions of the optimal design of the MR valve and of the fabricated MR valve derived from the optimal design.	41
4.1	Curve fitting coefficients.	61
5.1	MR valve dimensions and coil characteristics.	75
5.2	Appearance of induced voltage for different combinations of current and pressure.	76
5.3	Geometrical, electrical, and magnetic characteristics of the components of the microfluidic device.	84
B.1	Bill of materials for the PCB	128

1 Introduction

Magnetorheological (MR) fluids constitute a type of smart material with rheological properties that can be altered rapidly with the application of an external magnetic field. The fluid consists of micro-meter-sized iron particles, suspended in a carrier medium, such as silicon oil or water. Additives, such as surfactants and detergents are sometimes added to enhance the properties of the fluid. The application of an external magnetic field leads to the alignment of the particles in parallel with the lines of the magnetic field. A direct consequence of this event is the increase in the fluid viscosity.

MR fluids have been proposed for the first time in 1948 by J. Rabinow, who obtained their first patent [1]. However, they still intrigue the interest of researchers and their use in different types of applications has extensively spread during the last three decades. MR fluids present important technical and commercial advantages, such as fast response, high controllability, low power consumption, as well as the simple interfaces needed between the electrical power input and the mechanical power output [2]. They constitute an attractive working fluid for numerous applications, such as MR valves [3], MR dampers or shock absorbers [4], clutches or breaks [5]. Their application is prevalent but not limited to industrial or automotive systems [6], medical devices, such as orthoses [7], gripping and handling systems [8, 9], and haptic devices [10].

This chapter is an introduction to the MR fluid properties, as well as to the methods and models applied in their study. The fluid is, initially, approached from the macroscopic view as a continuum, and is modeled as a homogeneous fluid with an effective viscosity that varies with the strength and direction of the applied magnetic field. Besides, information is provided for the microscopic structure of the MR fluid, which is considered in this case as a collection of individual ferromagnetic particles that are dispersed in a carrier medium and interact with each other and with an external magnetic field. Furthermore, the MR fluid operational modes are presented, focusing on the flow mode, while the modeling of the developed pressure drop and the fluid velocity profile are presented in this case. Finally, the outline of this thesis and the original contributions deriving from it are described.

1.1 Rheological models

MR fluids classify as Newtonian fluids in the absence of an external magnetic field. This means that the shear stresses arising from their flow are linearly correlated to the local strain rate. When a magnetic field is applied, the particles form chain structures, and the viscosity of the fluid increases. This means an alteration to the rheological properties of the fluid, which also depends on the strength of the applied magnetic field. As a result, the MR fluids classify among the non-Newtonian fluids when an external magnetic field exists.

The MR fluid behavior has been explained with different rheological models. Some examples are the Bingham plastic [11, 12], the Herschel-Bulkley [12], the Casson [13], the Papanastasiou [14], or the Biviscous model [15, 16]. Fig. 1.1 shows the curve of shear stress over shear rate for Newtonian fluids, as well as for Non-Newtonian fluids modeled with the Bingham plastic, the Herschel-Bulkley, and the Casson model. Among them, the Bingham plastic model is simpler and provides a linear relationship between the fluid shear rate and yield stress, and, thus, it is the most commonly used in MR fluids studies and it is also the model that will be used in the formulations in the rest of this thesis. According to the Bingham model, the shear stress τ on the MR fluid when an external magnetic field H is applied can be defined as:

$$\begin{cases} \tau = \tau_y(H) + \eta\dot{\gamma}, & |\tau| > \tau_y \\ \dot{\gamma} = 0, & |\tau| \leq \tau_y \end{cases} \quad (1.1)$$

where τ_y is the yielding shear stress of the MR fluid controlled by the magnetic field, η is the viscosity of the MR fluid that does not depend on the magnetic field and $\dot{\gamma}$ is the shear strain rate. In this model, the flow behavior of the MR fluid consists of two regions, the pre-yield ($|\tau| \leq \tau_y$), where no shear strain rate exists, and the post-yield ($|\tau| > \tau_y$).

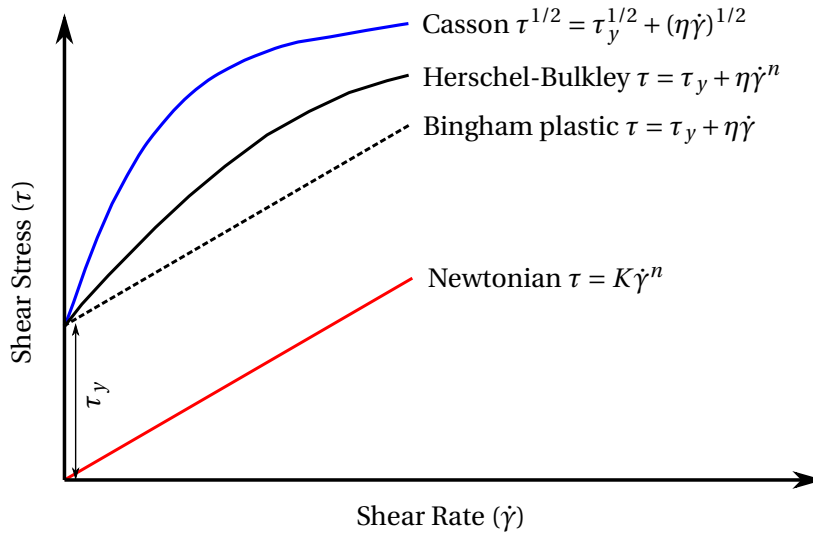


Figure 1.1: Rheological flow curves for the Bingham plastic, Herschel-Bulkley, and Casson model in comparison with the Newtonian fluid curve.

1.2 Yield stress

One of the most important parameters of MR fluid behavior is the yield stress τ_y , which constitutes the critical value of shear stress. Beyond this point, the chain-like structures of the particles break and the fluid flow begins. However, since the magnetic field is still present, there exist attractive forces between the particles that increase the overall fluid viscosity compared to the no-field condition. The yield stress is a measure of efficiency for the MR fluids and can be affected by several factors, like the applied magnetic field H , the particles volume fraction and size, or the viscosity of the carrier medium. Besides the efforts of research to explicitly formulate the relationship between τ_y and these factors, there are no complete and exclusive analytical models. A simple analytical equation that correlates τ_y and H is provided by [12]:

$$\tau_y(H) = \kappa \cdot H^\nu \quad (1.2)$$

The coefficients κ and ν are intrinsic parameters of the MR fluid and represent the effect of the previously described factors on the MR fluid behavior. Experimental measurement of the MR fluid yield stress with rheometers after applying different values of magnetic field can provide the relationship between τ_y and H and facilitate the definition of κ and ν .

1.3 Forces acting on the MR fluid particles

In the previous sections, the MR fluid has been approached from the prism of a continuum. However, if the behavior of each individual particle is considered independently, it can be described using equations of the fundamental physics laws. The forces applied to the i^{th} MR fluid particle of mass m_i and velocity v_i include:

- the contact forces F^c between particles;
- the non-contact F^{non-c} forces between particles;
- the fluid-particle interactions F^f , with the most important among them the drag force or hydrodynamic force, i.e. the force exerted by the fluid on the particle moving through it, which opposes the motion of the particle. The drag force is a result of the shear stress between the fluid and the surface of the particle;
- the external forces F^e acting on the particles. Those include the gravitational, magnetic field, and Brownian forces.

The particles' motion equation according to the second Newton's law can be written as follows:

$$m_i \cdot \frac{dv_i}{dt} = \sum_j F_{ij}^c + \sum_k F_{ik}^{non-c} + F_i^f + F_i^e \quad (1.3)$$

1.4 Magnetic properties and micromechanical modeling

The particle magnetization model is a commonly used model in MR fluid research that describes the behavior of the magnetic particles suspended in the fluid. This model assumes that each particle has a magnetic moment that can be influenced by an external magnetic field. The magnetic moment \vec{m} is typically modeled as a vector quantity that represents the strength and direction of the particle's magnetization. When a magnetic field is applied, the magnetic moments of the particles align with the field, creating a structure within the fluid that alters its rheological properties. The strength and direction of the alignment depend on factors such as the strength and direction of the magnetic field, the size and shape of the particles, and the interactions between the particles. The particle magnetization model is typically combined with a fluid mechanics model to describe the behavior of MR fluids. Three dimensionless numbers have been defined to formulate the rheological behavior of the MR fluid, the λ number, the Mason number M_n , and the Peclet number Pe [17]. These parameters show the ratios between the various forces exerted on the MR fluid particles as described in the previous section.

λ number shows the ratio of magnetic interaction energy to kT , where k is the Boltzmann constant and T is the fluid temperature in Kelvin. It can be expressed as:

$$\lambda = \frac{1}{2\pi\mu_0\mu_f} \cdot \frac{m^2}{\alpha^3} \cdot \frac{1}{kT} = 4\pi\mu_0\mu_f\beta^2\alpha^3H^2 \cdot \frac{1}{kT} \quad (1.4)$$

where $m = 4\pi\mu_0\mu_f\beta\alpha^3H$ is the magnetic moment of an isolated single particle surrounded by the carrier fluid, with a magnetic field H acting on it, μ_0, μ_f, μ_p are the magnetic permeabilities of the free space, the carrier fluid, and the particle respectively, α is the radius of the particle, $\beta = (\mu_p - \mu_f)/(\mu_p + 2\mu_f)$.

Mason number M_n is the ratio of drag to magnetic forces and is defined as:

$$M_n = \frac{8\eta_f\dot{\gamma}}{\mu_0\mu_f\beta^2H^2} \quad (1.5)$$

In this equation, η_f is the viscosity of the carrier fluid. The definition of M_n is important since the magneto-static polarization forces and the hydrodynamic forces are the most significant on the MR fluids particles.

Peclet number Pe is the ratio of hydrodynamic to Brownian forces and represents the significance of Brownian forces compared to the shear forces. It is defined as:

$$Pe = \frac{6\pi\eta_f\dot{\gamma}\alpha^3}{kT} \quad (1.6)$$

The three parameters can be related to each other with the following equation:

$$M_n \cdot \lambda = \frac{2Pe}{3} \quad (1.7)$$

1.5 Particle and medium influence

Since MR fluids are a suspension of micro-meter-sized particles in a carrier medium, parameters such as particle size and volume fraction as well as the medium's physical properties can affect their behavior.

Particles

The MR fluid particles are made of different ferromagnetic materials, such as iron, cobalt, or nickel, and are usually coated with a surfactant material to prevent agglomeration and sedimentation. Studies have shown that in MR fluids with small ferromagnetic particles ($\lambda > 1$) the increase in particle size leads to increased yield stress [18, 19]. On the contrary, for very high values of λ the particle size does not affect the yield stress. The influence of particle size on the MR fluids' behavior can be attributed to the Brownian motions, which are the random, uncontrolled movements of particles in the carrier medium while they repetitively collide with other particles, and are significant in dispersions of small particles. Besides, there is an extensive list of studies that investigate and model the relationship between the MR fluid yield stress and the volume fraction of particles in the carrier medium [20, 21, 22]. These studies have uncovered a linear relationship between the two quantities.

Carrier medium

The carrier medium in MR fluids can be a variety of liquids, such as oils, water, or glycols, depending on the application specifications. It is chosen taking into account parameters, such as the desired rheological properties of the MR fluid, the temperature range of the targeted application, as well as the compatibility with other materials used. An illustrative example is shock absorbers for automotive systems, where silicon oil is used as the carrier medium due to its good thermal stability and compatibility with rubber seals [23, 24]. Although the effect of the medium's viscosity on the overall behavior of the fluid exists, it is considerably less important than the effects of particle size and volume fraction.

1.6 MR fluid operational modes

MR fluids can be used in different modes depending on the application. There are mainly three operational modes, as depicted in Fig. 1.2: (a) the valve mode (or flow mode), (b) the shear mode, (c) the squeeze mode, and (d) the pinch mode.

- In the **valve mode**, a fluid flow is created between two fixed parallel plates, due to a pressure gradient. The external magnetic field is applied perpendicularly to the fluid

flow.

- In the **shear mode**, the fluid is again constrained between two parallel plates, and the external magnetic field is applied in the same way. However, the two plates are not fixed and there exists a relative movement to one another in the horizontal plane.
- In the **squeeze mode**, the fluid is between parallel plates that move relative to one another in the vertical plane.
- Finally, in the **pinch mode**, the fluid flow happens between two parallel walls that include a non-magnetic spacer. The magnetic field is applied to the direction of the walls, as in Fig. 1.2(d). When it reaches the non-magnetic spacer it is forced to deviate and pass through the MR fluid flow, increasing the viscosity of the fluid in this region and creating an orifice. The dimensions of the orifice can be controlled with the magnetic field intensity.

The most common modes are the valve and the shear mode. The first one is present in devices, such as servo valves, dampers, or shock absorbers [25, 26, 27]. The second one is employed in clutches, brakes, chucking, and locking devices [28, 29, 30]. The squeeze mode and pinch mode are the least frequently encountered in literature, for example in slow motion or high force applications [31].

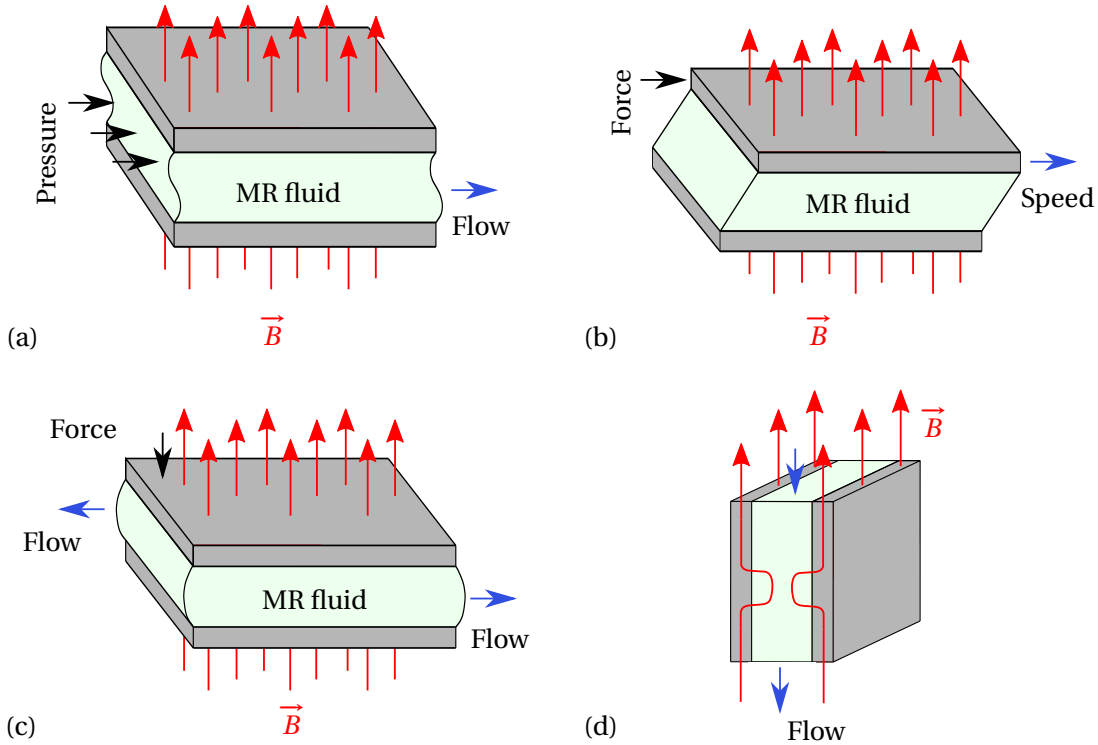


Figure 1.2: (a) Valve mode (b) Shear mode (c) Squeeze mode (d) Pinch mode.

1.7 MR fluid between parallel fixed plates

The next chapters of this thesis focus on the valve mode, among the different MR fluid operational modes. For this reason, it is important to provide information and mathematical formulations of the fluid flow velocity in this mode, as well as of the developed pressure drop. In MR fluid flow mode, the flow is taking place between two stationary plates or in a duct, due to the pressure difference between two different points of the described structure. Fig. 1.3(a) depicts this flow between two parallel fixed plates. The magnetic field direction is perpendicular to the fluid flow, inducing the activation of the MR fluid and the flow control. More specifically, activation means an increase in the yield stress of the MR fluid, and, consequently, of the MR fluid viscosity. The shear stress τ distribution between the two parallel plates can be assumed as linear and uniform. The fluid velocity profile presents a different shape. Fig. 1.3(b) represents the typical velocity profile of the MR fluid in the flow mode, according to the Bingham-plastic model [32] (see Fig. 1.1). According to this model, the MR fluid behavior below the yield shear stress ($\tau \leq |\tau_y|$) is similar to a rigid body. In this state, a plug flow region with constant velocity is formed between the plates, which is called *pre-yield* region. On the contrary, in the regions close to the two plates, the local shear stress exceeds the yield shear stress ($\tau > |\tau_y|$). In this state, the MR fluid behaves as a viscous fluid, while the region is called *post-yield* region.

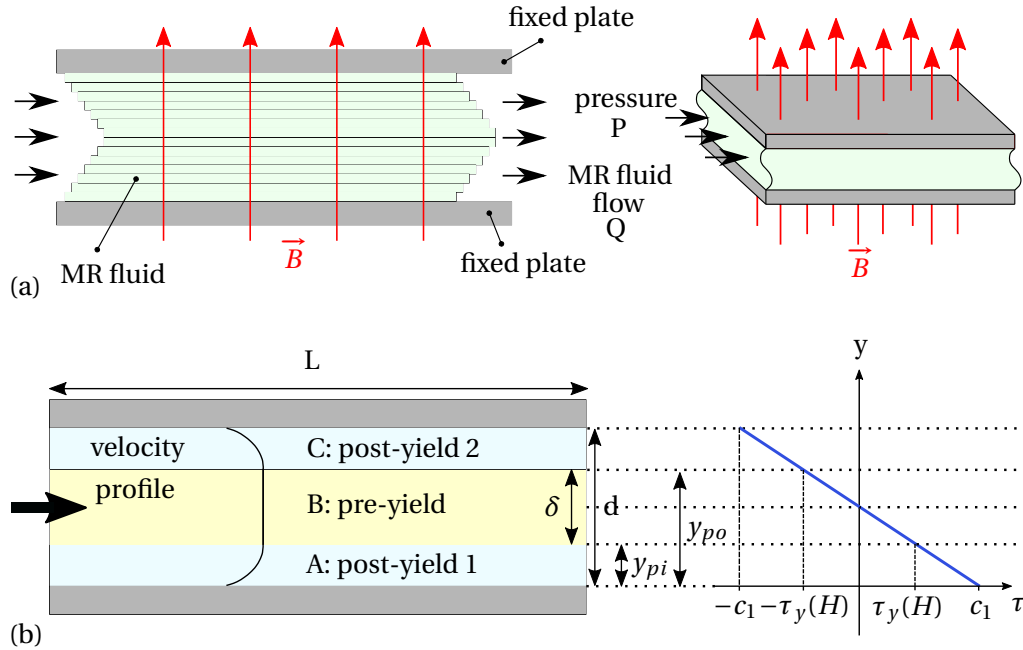


Figure 1.3: (a) MR fluid flow between two fixed plates. The magnetic field is applied perpendicularly to the flow. (b) Representation of the fluid velocity profile regions in between the two stationary fixed plates.

The parallel plate geometry can be approximated by a 1D axis-symmetric geometry. Thus, assuming linear pressure variation across the length of the plates, the following equation can

be derived from the force equilibrium [32]:

$$\frac{d\tau}{dy} = \frac{\Delta P}{L} \quad (1.8)$$

where ΔP is the pressure drop developed between the two sides of the flow.

The velocity $u(y)$ and the shear stress $\tau(y)$ profiles of the fluid in the approximate parallel plate analysis, where y is the coordinate perpendicular to the plates and referenced to the bottom fixed plate (Fig. 1.3 (b)), are as follows for Newtonian flow [32]:

$$u(y) = \frac{\Delta P}{2\eta L}(y^2 - d \cdot y) \quad (1.9)$$

$$\tau(y) = \frac{\Delta P}{2L}(2y - d) \quad (1.10)$$

The Newtonian velocity profile is the upper bound of the Bingham plastic velocity profile. For Bingham plastic flow, using Eq. 1.1 and 1.8, and solving the differential equation that is created, the velocity profile can be written as:

$$u(y) = \frac{\Delta P}{2\eta L}y^2 + C_1 y + C_2 \quad (1.11)$$

where C_1 and C_2 are two constants calculated in the following steps using the boundary conditions of our system. According to Fig. 1.3(b), the area between the two parallel plates is split into three regions. We consider u_A , u_B , and u_C the velocity in the post-yield region 1, pre-yield, and post-yield region 2 respectively. In order to determine u_A , we take into account the boundary conditions $u_A(0) = 0$, and $u'_A(y_{pi}) = 0$. Thus, the corresponding velocity profile becomes:

$$u_A(y) = \frac{\Delta P}{2\eta L}(y^2 - 2y_{pi}y) \quad (1.12)$$

In the pre-yield region, the shear stress is:

$$\tau = \frac{\Delta P}{L}y + C_3 \quad (1.13)$$

where C_3 is a constant and the boundary conditions are $\tau(y_{pi}) = \tau_y$, $\tau(y_{po}) = -\tau_y$. Using the boundary conditions in Eq. 1.13 results to the following relationships:

$$\tau_y = \frac{\Delta P}{L}y_{pi} + C_3 \quad (1.14)$$

$$-\tau_y = \frac{\Delta P}{L}y_{po} + C_3 \quad (1.15)$$

The plug thickness δ can be obtained by the subtractions of Eq. 1.14 and 1.15:

$$y_{po} - y_{pi} = \frac{2L\tau_y}{|\Delta P|} = \delta \quad (1.16)$$

Using the boundary conditions for the post-yield region 2, $u_C(d) = 0$ and $u'_C(y_{po}) = 0$, we can formulate the velocity profile in the second post-yield region as:

$$u_C(y) = \frac{\Delta P}{2\eta L} [y^2 - d^2 + 2y_{po}(d - y)] \quad (1.17)$$

Using Eq. 1.16 and the fact that the velocity is constant across the plug, as already explained, which means that $u_A(y_{pi}) = u_C(y_{po})$ we have:

$$y_{po} - y_{pi} = \delta \quad (1.18)$$

$$y_{po} + y_{pi} = d \quad (1.19)$$

The above system of equations can be solved for the location in the plug as follows:

$$y_{pi} = \frac{d}{2}(1 - \bar{\delta}) \quad (1.20)$$

$$y_{po} = \frac{d}{2}(1 + \bar{\delta}) \quad (1.21)$$

where $\bar{\delta}$ is the normalized plug thickness $\bar{\delta} = \delta/d$.

Using the above analysis, the velocity profile can be written as:

$$u_A(y) = \frac{\Delta P}{2\eta L} [y^2 - (d - \delta)y] \quad (1.22)$$

$$u_B(y) = \frac{\Delta P}{8\eta L} (d - \delta)^2 \quad (1.23)$$

$$u_C(y) = \frac{\Delta P}{2\eta L} [y^2 - (d + \delta)y + d\delta] \quad (1.24)$$

Accordingly, we can obtain the shear stress profile in the gap as follows:

$$\tau_A(y) = \tau_y + \frac{\Delta P}{2L} [2y - (d - \delta)] \quad (1.25)$$

$$\tau_B(y) = \frac{\Delta P}{2L} (2y - d) \quad (1.26)$$

$$\tau_C(y) = -\tau_y + \frac{\Delta P}{2L} [2y - (d + \delta)] \quad (1.27)$$

Regarding the developed pressure drop ΔP driven by the MR fluid flow, the combination of the two conditions, with and without magnetic field excitation, can be used to define it. Thus, it can be calculated as the sum of the yield-stress dependent pressure drop ΔP_τ and viscosity dependent pressure drop ΔP_η [11]:

$$\Delta P = \Delta P_\tau + \Delta P_\eta \quad (1.28)$$

The developed yield-stress dependent pressure drop can be approximated as follows [11, 32]:

$$\Delta P_\tau = \frac{c\tau_y(H)L}{d} \quad (1.29)$$

c is a fluid parameter whose range depends on the dynamic ratio D that is defined as follows:

$$D = \frac{\Delta P_\tau}{\Delta P_\eta} \quad (1.30)$$

c lies between 2 (when $D \approx 1$) and 3 ($D > 100$) [33, 34]. Thus, c can be approximated after calculating the ratio D between the yield-stress and viscosity component of pressure difference.

In case no magnetic field is applied, which means that the MR fluid yield stress is zero, the plug thickness decreases to zero ($\delta = 0$) and the velocity profile of the fluid between the plates can be considered as the one of Newtonian fluids. In this case, the fluid flow rate between the two plates of Fig. 1.3(b), for w being the width of the planar geometry and using Eq. 1.9, can be written as:

$$Q = w \int_0^d u(y) dy = \frac{wd^3 \Delta P}{12\eta L} \quad (1.31)$$

and ΔP_η can be calculated as:

$$\Delta P_\eta = \frac{12\eta QL}{d^3 w} \quad (1.32)$$

Thus, Eq. 1.28 becomes:

$$\Delta P = \Delta P_\tau + \Delta P_\eta = \frac{2\tau_y(H)L}{d} + \frac{12\eta QL}{d^3 w} \quad (1.33)$$

1.8 Magnetorheological valve configurations

This section describes the two basic geometrical configurations of MR valves, the annular and the radial. The difference lies in the geometric path the MR fluid follows. The different configurations have been used independently as well as in combination in several works.

1.8.1 Annular

The annular MR valve is depicted in Fig. 1.4. In this configuration, the MR fluid flows in a cylindrical path without any changes in the flow direction. This geometry is characterized by its simplicity in manufacturing compared to the radial valve.

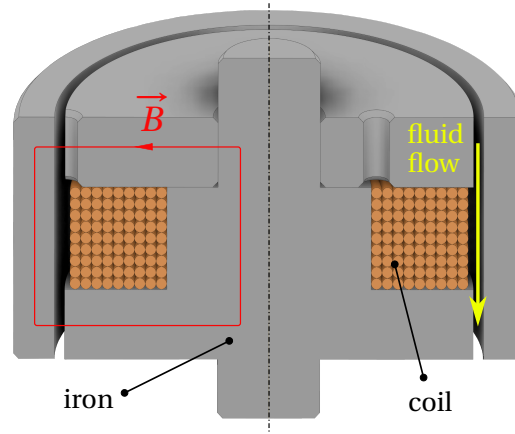


Figure 1.4: Annular MR valve in sectional view.

1.8.2 Radial

The radial MR valve is depicted in Fig. 1.5. In this configuration, the MR fluid flows with changes in its direction. As a result, the MR effect takes place in different regions. Radial MR valves can achieve high flow rates due to their unique geometry, allowing for a larger flow area compared to other types of MR valves.

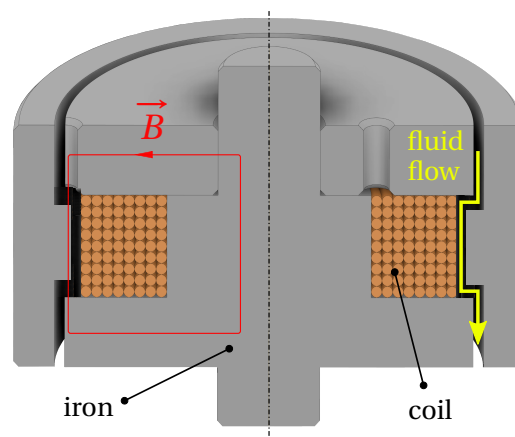


Figure 1.5: Radial MR valve in sectional view.

1.9 Original contributions & thesis outline

This thesis proposes original and novel contributions on:

- MR valve miniaturization;
- MR valve power consumption minimization;
- Self-sensing MR valves with regard to pressure and their microscopical study;
- A wearable device based on miniaturized MR valves that can drastically improve the lives of diabetic patients by actively preventing diabetic foot ulcerations.

The outline of the thesis, following *Chapter 1 - Introduction*, together with the main contributions of each chapter are presented below:

Chapter 2 - State of the Art provides an overview of the valves used for the control of fluidic actuation systems. This includes the different working principles in valves as well as their comparison with respect to the maximum pressure they can sustain, their volume, and the consumed energy. The chapter then focuses on valves based on MR fluids. Furthermore, the state-of-the-art on MR valves is presented with respect to the main innovation areas, which are the design optimization, the miniaturization, the development of self-sensing valves, as well as the challenges and improvements of MR fluid materials, and the MR valve applications in different domains.

Chapter 3 - Magnetorheological valve design, modeling, and validation focuses on optimizing a miniaturized MR valve with the use of the Design of Experiments and Response Surface Methodology techniques. The goal of the optimization is the miniaturization of the valve with simultaneous maximization of the sustained pressure, and flow rate, as well as minimization of the power consumption. The optimal design is modeled analytically with regard to the sustained pressure and numerically, taking into account the existence of MR fluid close to the inlet and outlet of the valve that enhances the flux fringing phenomenon. The analytical model is formulated according to the numerical results to consider the fringes. The valve is further experimentally validated in terms of the maximum sustained pressure drop as well as in terms of its functionality in two states (open and closed) with a specially designed testbench. Finally, the analytical, numerical, and experimental results are compared.

Chapter 4 - Magnetorheological valve based on electropermanent magnet includes the analytical and numerical modeling, as well as the experimental validation of a miniaturized MR valve with the same design as the optimal valve design of Chapter 3, but with the addition of a soft magnet in its core. The latter is magnetized and demagnetized with sub-millisecond current pluses decreasing the steady-state power consumption of the valve to zero. The valve has been validated in terms of its functionality in open and closed condition as well as in terms of the maximum pressure it can sustain.

Chapter 5 - Self-Sensing magnetorheological valve reports the pressure self-sensing phenomenon in miniaturized MR valves, which is based on the electromagnetic induction. The phenomenon is studied in a 2-coil valve and the correlation between the applied pressure and the measured induced voltage on the valve's coil is demonstrated. Besides, a microfluidic device is presented, which allows the study of the self-sensing phenomenon under the microscope, to better understand the electromagnetic induction mechanism in the MR valve. Finally, the feasibility of measuring the coil's impedance variation for the same self-sensing purpose is investigated.

Chapter 6 - Novel applications of miniaturized MR valve: Intelligent footwear for diabetic ulceration prevention describes a novel application of the proposed miniaturized MR valve in the form of a shoe for the prevention of diabetic foot ulcerations. The chapter includes a description of the working principle of the shoe, the system's architecture, and the validation tests. The system includes multiple novel MR devices that act as shock absorbers and can sustain or offload the applied foot pressure, as well as the MR devices' control electronics and a plantar pressure measurement insole. Separate tests of the system's modules and in-the-lab tests of the shoe on human feet validate the functionality of the shoe.

Finally, *Chapter 7-Conclusions* provides a summary of the work and the leading scientific contributions accomplished during this thesis. Additionally, the chapter proposes future perspectives in different applications.

The work presented in this thesis has also been presented in different conference or journal articles, which were published during the four years of my research at LAI. As a result, part of the text and some figures in the following chapters are extracted from the published articles. They are either completely the same or partly modified. All the material comes from articles published in IEEE conferences and journals and IEEE does not require individuals working on a thesis to obtain a formal reuse license. However, at the end of each chapter and below the figures, the related publications are listed and the copyright is added if needed. In the state-of-the-art chapter, figures from several works in journals other than IEEE ones are presented together with the reuse license. None of the figures coming from other people's work is modified. In some cases, according to the topic of the chapter only part of the figure is shown since this part is relevant to the chapter's contents.

2 State of the Art

This chapter presents the importance of fluidic actuation and one of the main controlling elements in fluidic systems, the valves. The different working principles of valves are explained while the main focus of the chapter is the magnetorheological valves. For the latter, the main state-of-the-art topics are explored.

2.1 Fluidic actuation systems

Power transmission is omnipresent in engineering applications, involving the conversion of energy into different forms. The conversion is followed by distribution of the energy to different systems for further exploitation. Electrical, mechanical, or fluid technologies are deployed for the energy conversion and distribution process.

Fluid power is a term referring to hydraulics and pneumatics technologies. In fact, hydraulics makes use of fluids in the liquid state, such as water and oil, while pneumatics makes use of fluids in the gas state, such as air. Fluid power transmission systems present the advantages of high power-to-weight ratio [35], ability to handle high-magnitude forces and torques compared to mechanical transmissions [36], and increased heat transfer capability [37]. In addition, fluid systems are able to easily produce linear motion with the use of hydraulic and pneumatic cylinders, unlike electrical and mechanical methods that need an additional device that converts the rotational motion to linear. Besides, they facilitate miniaturization, compared to the electrical systems, without compromising on the produced force and torque. Finally, they provide simplicity in terms of control of direction, speed, force, and torque, with the use of controlling valves with a relatively simple structure.

Due to the aforementioned advantages, fluidic-system-based power transmission is exploited in a wide range of applications. A common application of hydraulics is off-highway equipment used in different domains. Some examples include construction machinery [38], agricultural activities like cropping [39], and mining [40]. In addition, hydraulic applications are widely involved as heavy industrial equipment for activities like bending, pressing, and cutting, as

well as for the automation of several industrial applications [41]. For instance, there exist cutting machines for underwater operation [42] or for rescuing during natural disasters [43]. As regards pneumatics technology, factory automation appears to be the most important sector. Pneumatics is used for manipulating products, or for packaging operations [44]. While primarily controlling large-scale motion, pneumatic and hydraulic soft actuators are getting miniaturized. A great showcase is minimally invasive surgery [45] and rehabilitation systems [46], enabled by fluidic technologies that use miniaturized valves. Finally, another important field where fluidic systems are used is automotive systems. Automotive devices, such as clutches [47] or vehicle suspensions [48] are actualized by fluidic actuators. Fig. 2.1 depicts some of the applications where fluidic systems are deployed for power transmission.



Figure 2.1: Different fluidic actuation systems: (a) The mGrip soft pneumatic gripper (Photo: Soft Robotics, Inc.) (b) Miniature pneumatic soft robotic manipulator [45] (Copyright: 2377-3766 © 2016 IEEE) (c) Soft robotic glove enabling hand impairment rehabilitation [46] (Copyright: 2377-3766 © 2017 IEEE).

In this chapter, one of the main regulation devices of fluidic systems will be presented - the valve. Firstly, different working principles of valves will be demonstrated as well as their comparison with regard to volume, maximum sustained pressure, and energy consumption. Then, the chapter will focus on MR valves exploring the main state-of-the-art works and their important applications.

2.2 Valves for fluidic system control

In fluid systems, the motion of fluid mass must be controlled by regulation devices. The static characteristics of the system, which are related to the control accuracy of positioning forces, as well as the dynamic characteristics, which are related to the pressure and fluid flow regulation, are closely associated with the regulation device. Valves constitute an example of regulation devices that act as integral parts of fluid power transmission systems.

2.2.1 Working principles

Numerous attempts have been made in the last decades to further enhance valves capabilities through different working principles. For example, solenoid valves are the most frequently used regulation devices employed in actions, such as stopping or releasing fluid flow, dosing,

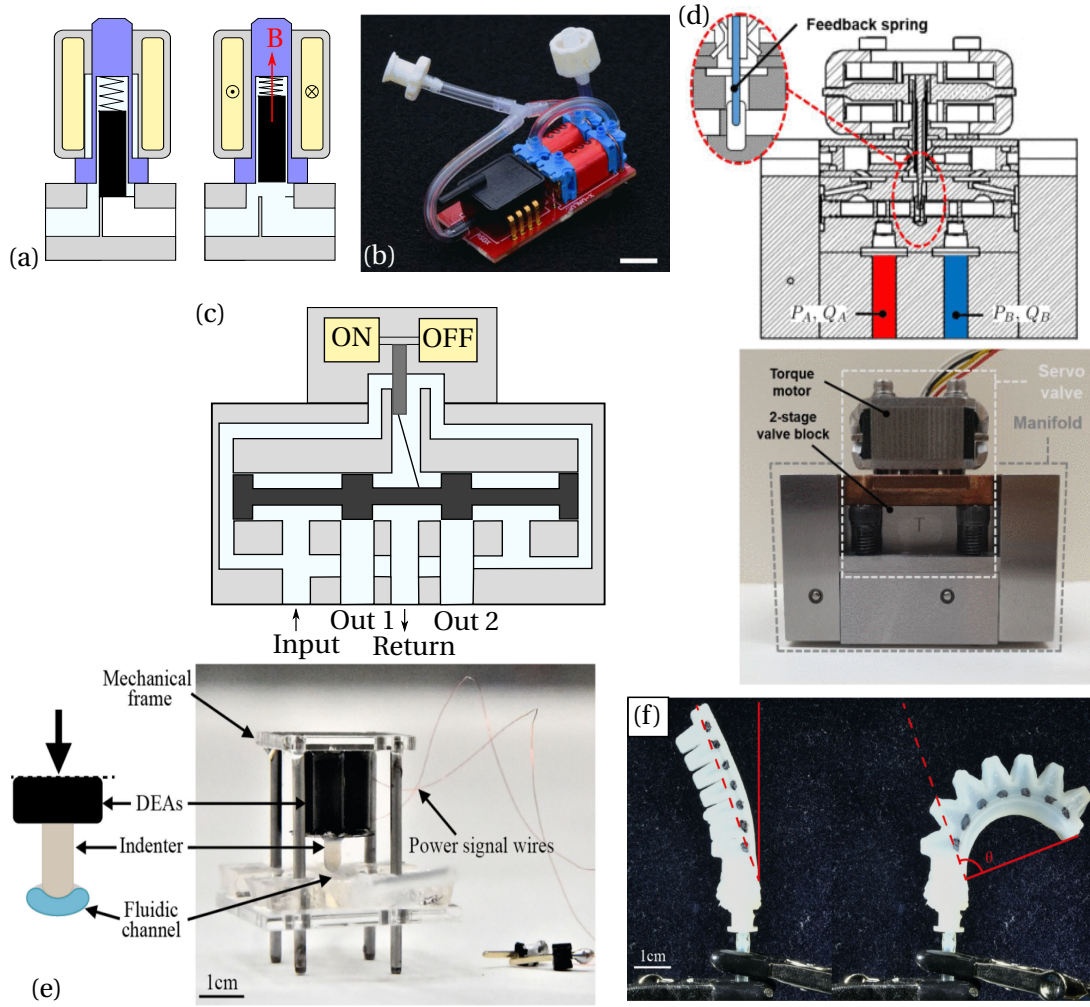


Figure 2.2: (a) Working principle of solenoid valve and (b) application on a pneumatic regulator of soft robot control [50] (Copyright: 978-1-5386-4516-1/18/\$31.00 © 2018 IEEE). (c) Schematics of a conventional servo valve (d) Servo valve presented in [54] (Copyright: 2377-3766 © 2020 IEEE). (e) Valve fabricated with DEA in [55] (Copyright: 2377-3766 © 2022 IEEE) and (f) photo of fluidic actuator controlled by the DEA valve.

distributing, or mixing fluids. The solenoid valves are electromechanically activated by electromagnets. When supplied with current, a magnetic field is created, pulling an armature against the action of a spring, and opening the valve, as in Fig. 2.2(a). When the current supply stops the armature returns back to its original position in the spring and the valve closes. Solenoid valves have been a popular solution due to the low price, simple functionality, and accuracy in several fluidic applications [49, 50, 51, 52, 53]. Fig. 2.2(b) depicts the use of such a valve in a pneumatic regulator for soft robot control.

Furthermore, servo valves are electrically operated valves that control the fluid flow and direction of powerful fluidic systems with the use of small electric signals [54, 56] (Fig. 2.2(c),

Fig. 2.2(d)). The working principle of servo valves is based on the use of a servomotor, which moves a piston inside the valve body. The movement controls the fluid flow through the valve and determines the position of the actuator that is being controlled. The servo valves function with high accuracy, repeatability, and frequency response. Besides, there are active mechanical valves based either on thermal principle [57, 58] with the use of Shape Memory Alloys (SMA), or on elastomeric principle [59, 60]. Valves based on Dielectric Elastomer Actuators (DEA) have been developed recently to achieve lightweight and compact fluidic regulation systems, as in Fig. 2.2(e) and Fig. 2.2(f) [55].

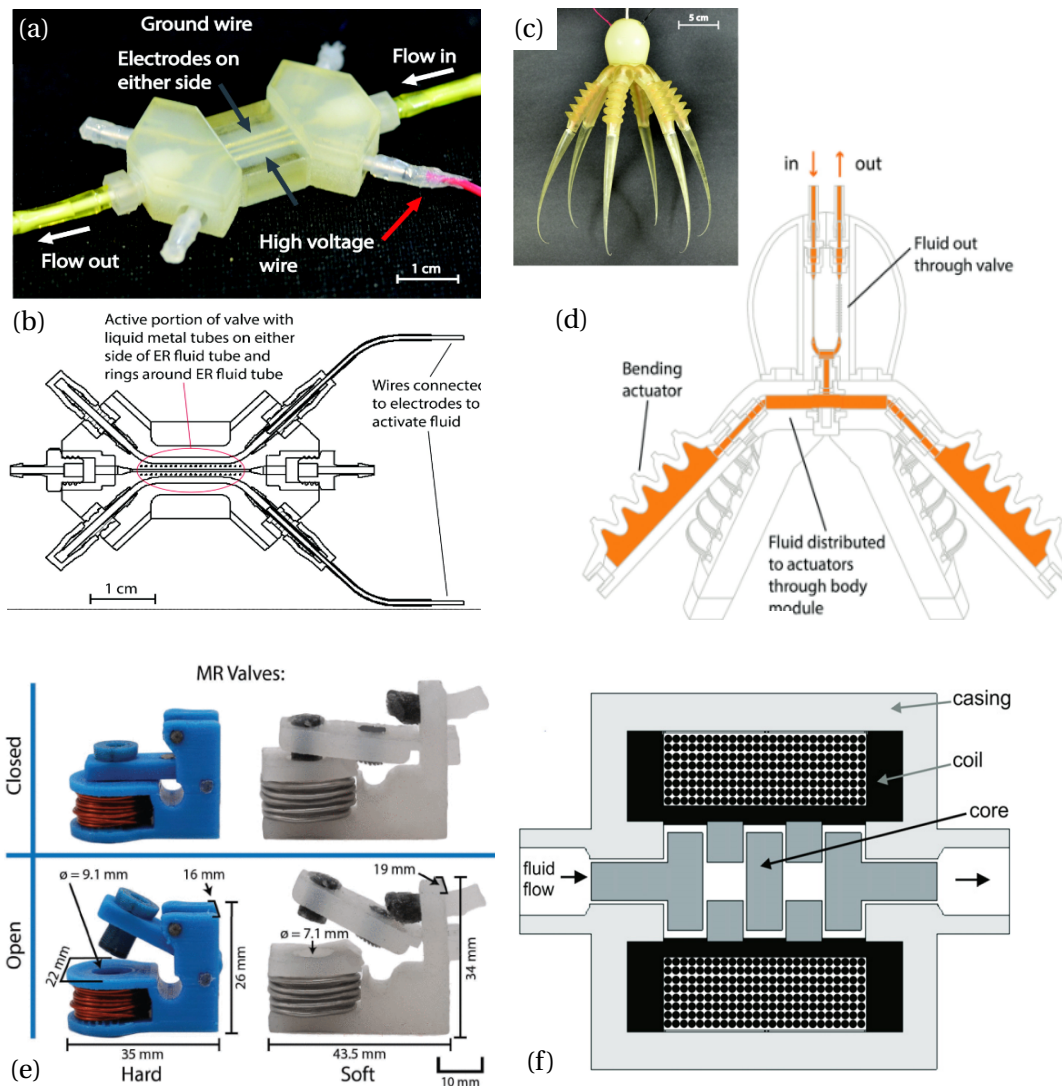


Figure 2.3: Pictures of (a) ER fluid valve, (b) ER valve schematics, (c) octopus-inspired soft robot actuated with ER fluid and ER valve, (d) soft robot schematics are extracted from [61] (Mary Ann Liebert. Inc. Copyright License No: 5537670197977). MR valve (e) bistable [9] (Copyright: 2377-3766 © 2021 IEEE) or with (f) meandering path [62] (IOP Copyright Licence No: 1349852-1).

Besides, valves utilize other smart materials for fluid control. More specifically, electrorheological (ER) fluids [61, 63, 64, 65, 66] and magnetorheological (MR) fluids, two types of smart materials, have been used as pressurized liquids controlled by fluidic valves in actuation applications such as automotive or medical [33, 62, 67, 68, 69]. ER and MR fluids are characterized by the controllable, reversible change of viscosity with the application of an external electric or magnetic field respectively. As a result, they allow the creation of valves with simple structure and fast response when supplied constantly with DC current and voltage. Fig. 2.3 depicts an ER valve used in a soft robot inspired by an octopus [61] and two types of MR valves, one bistable [67] and one with meandering path [62]. Lastly, another smart material that has been studied in valve applications is the magnetic shape memory alloys [70]. The valve's principle is based on the property of the material to deform in response to the application of an external magnetic field.

In addition to smart materials, both permanent magnet (PM) and electropermanent magnet (EPM) have been employed in valves for pneumatic systems due to the advantages of low power consumption, compactness, and minimal weight [71, 72]. The advantages of EPMs have also been exploited in actuation applications different from valves, such as latching mechanisms in self-assembled robots [73, 74]. The addition of EPM technology in MR fluid valves has paved the way for miniaturized MR fluid valves that overcome the constraint of steady-state power supply and allow low energy functionality [75, 76].

Fig. 2.4 depicts a comparative plot of the various principles mentioned previously, on a logarithmic scale for clarity. It shows the maximum reported pressure sustained by the valves with regard to their volume. Besides, the representation of several works with circles and triangles differentiates them according to the activation principle and, thus, their power consumption. Working principles requiring continuous current for valve activation consume significant amounts of power and energy. On the contrary, valves activated with a single pulse of current, which is necessary only for switching from one state to the other, tend to consume negligible power in the steady state. As depicted in Fig. 2.4, the size of the valve affects the maximum sustained pressure. The highest pressure is achieved in very high volumes. At the same time, valves that sustain more than 1100 kPa consume considerably higher power, due to the continuous activation current. On the other hand, the smallest-in-volume solutions, with negligible power consumption in the steady state, present very low sustained pressure. This work is related to a miniaturized MR valve with a volume of 353 mm^3 . Two versions of the valve are presented in this thesis, one powered by an electromagnet with a continuous current, sustaining more than 1000 kPa statically, and one optimized version powered by an electropermanent magnet with zero steady-state power consumption that can sustain 1010 kPa as depicted in Fig. 2.4. Both versions of the MR valve presented in this thesis have the same volume, with the only difference being the addition of the electropermanent magnet in the second case, after removing a piece of iron from the initial conventional version of the valve.

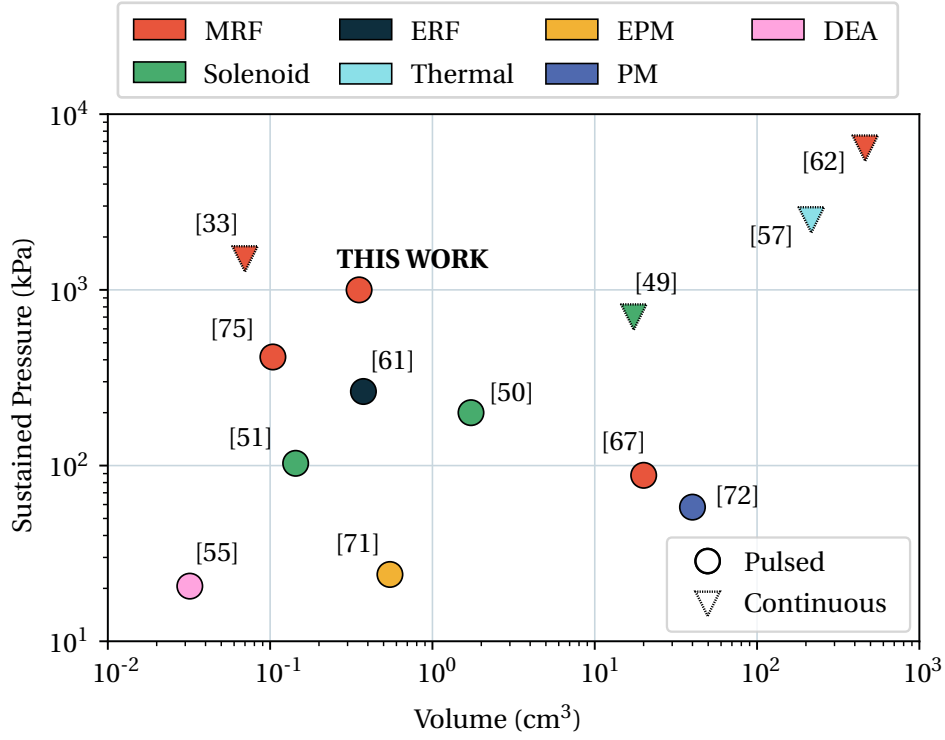


Figure 2.4: Comparison of different valves depending on their physical driving principle, maximum sustained pressure, and size. (Copyright: 2377-3766 © 2023 IEEE)

2.3 Magnetorheological (MR) valves

Magnetorheological (MR) valves are devices that use MR fluid as working fluid and an external magnetic field controls the fluid's rheological properties. The application of the magnetic field results in the increase of viscosity of the fluid inside the valve. This reversible phenomenon is used in MR devices for fluid control. MR valves have various applications in fields such as automotive, aerospace, civil engineering, and medicine. Using them in hydraulic actuation systems includes many advantages. The most important among them is the lack of moving parts in the valves, compared with their mechanical counterparts, as well as the flow control, which is performed electronically with the use of an electromagnet. These facts lead to decreased weight and complexity. MR valves have attracted significant interest in various industrial and research applications also due to their high response time, high controllability, and low power consumption.

The state of the Art in MR valves is focused on improving their performance, reliability, and applicability. For these reasons, some recent advances in MR valves involve developing new materials, designs, and control strategies. This section focuses on the following state-of-the-art topics on MR valve research that can be used as the background knowledge for the rest of this thesis:

1. **Design optimization:** Researchers are using analytical methods and computational tools such as finite element analysis (FEA) to optimize the design of MR valves, leading to improved performance and efficiency in terms of pressure, force, energy, and time response.
2. **Miniaturization:** Many studies are focusing on developing smaller MR valves that can be integrated into smaller devices, enabling new applications in fields such as microfluidics or soft robotics.
3. **Self-Sensing:** A number of studies lately focus on the development of self-sensing MR valves with displacement, velocity, acceleration, and force self-sensing capabilities that are injected as feedback to the MR damper control system.
4. **MR fluid challenges and material improvements:** New magnetorheological fluids with improved properties such as higher yield stress, faster response time, and improved stability are being developed to address the existing material challenges.

The following subsections include a detailed presentation of state-of-the-art works related to each of the above topics.

2.3.1 Design optimization

Due to their aforementioned advantages, MR valves hold great potential for commercial applications. MR valve is the most commonly used operational mode of MR fluids and is mainly employed in MR dampers, while their design is affected by many parameters, sometimes with a contradictory effect on improving their performance. As a result, a considerable amount of studies have been carried out toward the optimization of MR valve and MR damper design. Especially when the number of parameters is large, the use of optimization techniques is crucial to obtain the optimal design. The optimization process consists of the following important steps: the choice of the design parameters and constraints, the choice of the objective function, which can be one or multiple (multi-objective optimization), and, finally, the choice of the right optimization technique.

Table 2.1 classifies a number of MR valve and MR damper optimization works according to the optimization method they use. The earliest attempts of optimization of valves independently or inside damper structures are based on the magnetostatic Finite Element Analysis (FEA) in the valve circuit to obtain the magnetic flux density in the gap as a function of different geometrical parameters [77, 78, 79, 80, 81, 82, 83]. In the majority of these cases, the optimization objective is the maximization of the flux density in the gap, which allows higher pressure drop and maximum damping force in the damper case [82]. Another objective is the valves dynamic ratio maximization [83]. The dynamic ratio D is defined in Eq. 1.30. The valve's volume minimization is an additional objective in [77, 78], while in [79] the optimization is performed for a constrained volume.

Method		Work
Parametric FEA		[77, 78, 79, 80, 81, 82, 83]
FEA	Golden Section and Local Quadratic Fitting	[84, 85, 86, 87]
	Particle Swarm Optimization (PSO)	[88, 89]
	First-order Method of ANSYS	[90, 91, 92, 93]
	Sequential Quadratic Programming (SQP)	[94]
	DoE and RSM or Taguchi	[94, 95, 96, 97, 98, 99] [100, 101, 102, 103, 104, 105]
	Genetic Algorithm (GA)	[98, 106, 107]
Feedforward Neural Network		[108]
Analytical		[109, 110, 111]
Analytical	Non-Dominated Sorting GA (NSGA-II)	[112]
	GA and SQP	[113]
	PSO	[89]

Table 2.1: Sorting of various MR valve/damper design optimization works according to the optimization method and the algorithm used.

The use of magnetostatic FEA for MR valve design optimization has been improved with the use of specific algorithms, which are frequently incorporated in the FEA software. Some examples include the use of Golden Section and Local Quadratic Fitting [84, 85, 86, 87]. These works perform either single-objective optimization targeting at minimizing the consumed energy [85], or multi-objective with a combination of objectives, such as dynamic ratio minimization and pressure drop maximization [84], or damping force, dynamic range, and inductive time constant optimization [86, 87]. Besides, the Particle Swarm Optimization (PSO) [88, 89], the first-order method integrated into the FEA software (i.e. in ANSYS) [88, 89], or the Sequential Quadratic Programming (SQP) [94] are used for the same purpose. Another popular optimization method includes DoE and FEA analysis to create a table of experimental runs. The variable parameters are the geometric dimensions of the valve or other parameters like the coil current or wire size and the outputs are the FEA results. This step is followed by RSM or Taguchi method for the acquisition of the optimal design [94, 95, 96, 97, 98, 99, 100, 101, 102, 103, 104, 105]. The Genetic Algorithm (GA) is also used with FEA in some cases [98, 106, 107].

Apart from the more traditional algorithms for optimization, Feedforward Neural Networks have also been applied in MR valve optimization [108]. Finally, valve optimization has been conducted with the use of the analytical model [109, 110, 111], sometimes enhanced by algorithms such as the Non-Dominated Sorting GA (NSGA-II) [112], the GA and SQP combination [113], or the PSO [89].

In the vast majority of the reported works the typical design parameters are the geometric dimensions. There are, however, some cases where apart from the geometry, factors like the coil current and the wire cross-section [80, 85], or the coil turns and the fluid volume fraction [82] are included as design parameters. Regarding the optimization objectives, they include

the magnetic flux density in the gap of the MR valve, the pressure drop, the consumed energy, the dynamic ratio, the inductive time constant, the weight of the valve, or the number of coil turns. Especially in the case of MR valve integration into the damper, the damping force is the most important objective.

In conclusion, using magnetostatic FEA in combination with an optimization algorithm appears to be an effective method that provides an optimized design with good performance. Especially, in the cases where the optimization tool is included in the FEA software, the optimization process is even more simplified leading to optimal designs that can be obtained quickly and accurately.

2.3.2 Valve miniaturization

Currently, the majority of conventional MR valve structures are powered by bulky electromagnets and require currents in the order of one amp to be switched on and stop the fluid flow. In automation applications, especially when dealing with soft robotic systems, or medical

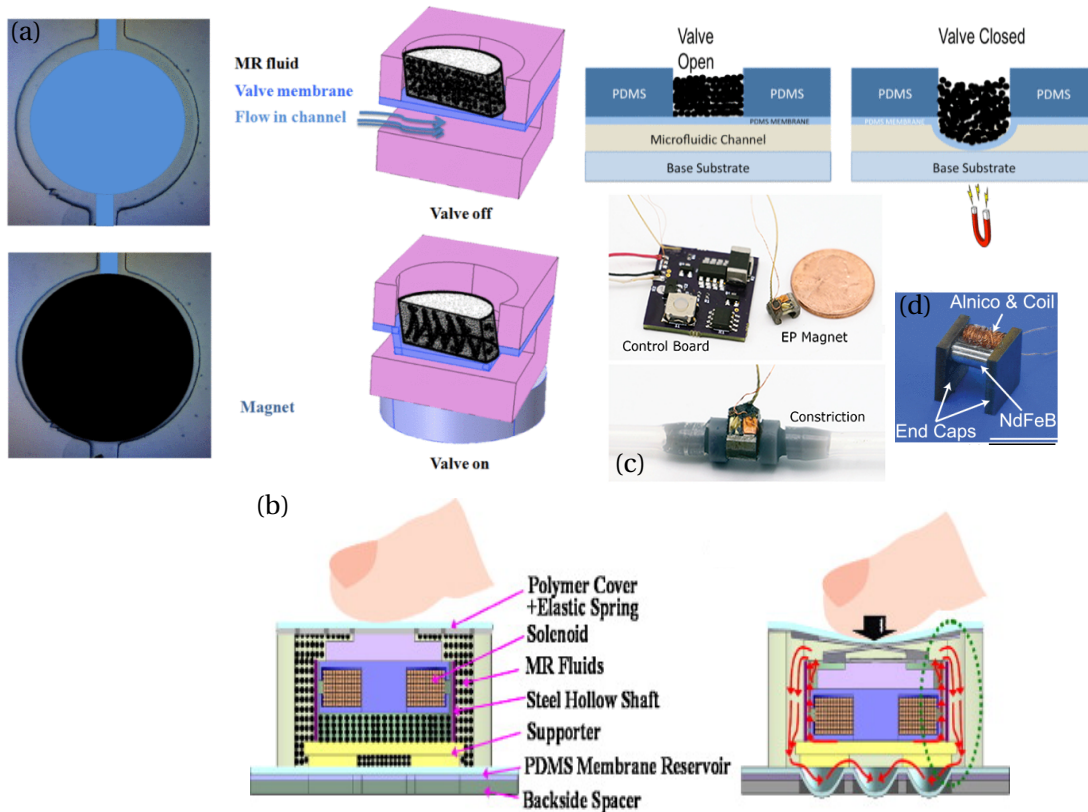


Figure 2.5: Examples of miniaturized devices with MR fluid: (a) on-chip microfluidic valve [114] (Copyright: 1057-7157 © 2016 IEEE), and (b) haptic device with valve [115] (Elsevier Copyright Licence No: 5537671094344). Valves based on EPM (c) [75] (IOP Copyright Licence No: 1349873-1), and (d) [8] (Copyright: 2377-3766 © 2022 IEEE).

devices, miniaturized valves facilitate integration. Especially valves sustaining hundreds of kPa of pressure enable a wide range of motion and forces. However, conventional MR valves, due to their size, are unsuitable for such miniaturized and portable applications.

Up to the present times, the miniaturization of MR valves has attracted the interest of some researchers. [77] is one of the first optimization works that aim at volume minimization of a meso-scale MR valve integrated into a damper, with an outer diameter (OD) of less than 25 mm and a gap (g) of less than 1 mm. MR valve optimization has also been performed minimizing the weight of the valve without achieving, however, sub-millimeter gap size and with an outer diameter of 40 mm [78]. The valve has also been designed with a combination of fluid paths that allow increased efficiency but without improvement in terms of volume compared to the previous studies [116, 62, 117, 118, 119]. In the same direction and size ranges, [120] reports a MR valve integrated into a micro-damper, while [121] achieves the damper's miniaturization but with the volume minimization of the piston and not the valve. A great improvement in volume with OD=10 mm and g=0.1 mm has been conducted by [27, 122] that propose the design and testing of a MR valve integrated into a shock absorber with potential medical use.

Furthermore, miniaturized valves different from the conventional MR valve, where the flow duct is created between two cylindrical iron parts and the magnetic field is induced by an electromagnet, have been reported in literature. For example, a magnetically controlled, on-chip microfluidic valve uses MR fluid micropatterned on an elastomeric membrane, as in Fig. 2.5(a), to control microfluidic circuits [114]. Miniaturized jamming MR valves [75] or traditional flow MR valves [8] are developed for soft robotic applications where the working fluid is MR fluid, as in Fig. 2.5(c),(d). The magnetic field is created with electropermanent magnets and, as a result, the studies exploit the capabilities of these magnets for simultaneous power consumption decrease.

The MR fluid in flow mode has been used similarly to the principle of the conventional MR valve for the control of various miniaturized devices. These include haptic applications, such as a haptic display with tunable stiffness enabled by MR fluids in flow mode (Fig. 2.5(b)) [115], or a tactile screen for navigation tasks [123]. Additionally, another miniaturized device is an MR fluid mount, which combines the flow and the squeeze mode to increase its performance [124], while the design of a miniaturized micro-brake that takes into account the heat dissipation effect on a small structure is suggested in [125]. Finally, [126] presents a miniaturized MR fluid damper for soft robotic actuators, that uses MR fluid in flow mode and external permanent magnets to block the fluid flow.

Overall, there is a number of studies that investigate the miniaturization of conventional MR valves. However, the size of the electromagnets or the permanent magnets, as well as the size of the ferromagnetic parts that allow a high enough magnetic field are important challenges toward this goal.

2.3.3 Self-Sensing

In MR valves incorporated into MR dampers the real-time measurement of the damping force produced by the devices, as well as the measurement of quantities such as displacement, velocity, acceleration, and flow rate, is crucial for accurate control of the damper. Research on the design of MR valves and dampers has been accompanied by studies on self-sensing techniques. Self-sensing refers to the use of a transducer for dual functionality, as an actuator and a sensor. In comparison with traditional dampers where damping feedback is accomplished with sensors, self-sensing offers significant advantages, including a reduction in system complexity, bulkiness, cost, and power consumption. Furthermore, a self-sensing damper can ensure robustness, as it avoids failure attributed to sensor hardware, external magnetic fields, temperature variations, and noise.

The technology surrounding self-sensing MR valves and dampers is continuously evolving, with ongoing research aimed at attaining multiple functions and improving their performance, reliability, and applicability in various industries. The first attempt to our knowledge to design self-sensing MR dampers used an excitation coil for the creation of the MR effect, as the conventional MR dampers, and a second coil, the induction coil [127, 128]. On the latter, the electromagnetic induction phenomenon is sensed, which is provoked by the movement of the damper and the subsequent flux variation. The functionality of this self-sensing MR damper was then validated experimentally [129]. This work was, finally, enhanced with energy harvesting properties that allowed self-powering of the MR damper [130, 131], as well as techniques for handling the trade-off between the damping force and sensing performance [132].

Other works based on the same electromagnetic induction principle and the use of additional induction coils have been reported in literature [133, 134, 135, 136, 137, 138, 139, 140, 141]. Among them, some achieve to be self-powered [133, 135, 140]. AC currents are normally used for electromagnetic induction, however, [141] used DC current in an independent MR valve and observed the correlation of the electromagnetic induction phenomenon with variations in pressure drop, flow rate, fluid displacement, and velocity. Other studies are performing self-sensing but with the addition of sensors, such as piezoelectric [142], or optical [143] in the damper structure. Finally, there have been studies that are based on triboelectric nanogeneration to achieve self-sensing [144].

All in all, a number of works are dedicated to self-sensing in MR valves, but there is space for further investigation of this technique, especially, when it comes to pressure self-sensing.

2.3.4 MR fluid challenges and material improvements

Apart from studies on the MR valves and the devices where the valves are used, research has been conducted on the improvement of the properties of MR fluids that will subsequently lead to MR devices of higher performance. Some of the leading problems appearing in MR

fluids and deteriorating their functionality are [145]:

- **Sedimentation:** Occurs due to the density differences between the ferromagnetic particles and the carrier medium, destroying the homogeneity of the MR fluid and its functionality in MR devices.
- **Hard cake formation:** It is created by the agglomeration of particles with the application of magnetic field. The agglomerations remain even after removing the field, due to factors such as the remnant magnetization, causing disruption of the homogeneity of the MR fluid and improper function of the MR device. Especially in MR valves with small gaps ($g < 1$ mm), the gap can be completely blocked.
- **Clamping effect:** The application of a high external magnetic field for a long duration leads to a permanent formation of particle chains, while the carrier fluid flows freely. As a result, the chains are not blocked anymore by the lines of the magnetic field and they flow along with the fluid forming agglomerations.
- **Particle oxidation:** A chemical process that can take place due to the existence of air, moisture, and very high temperatures. In this case, rust appears on the particle surface, destabilizing the MR fluid behavior.
- **Temperature effects:** Besides oxidation, rise/decrease of temperature above/below the proposed limit for the MR fluids (it ranges between -20 and 150 °C depending on the fluid) can prevent effective control of the fluid viscosity.

In order to overcome the above problems, a number of studies have focused on the research of material advancements. A common technique for MR fluid stabilization and sedimentation prevention includes particle coating with organic polymers [146]. In this way, the density mismatch between the particles and the carrier medium is reduced. Another example involves using nanoparticles in the place of microparticles with a low volume-to-volume concentration (6.2%), achieving fluid homogeneity and no agglomeration, without validating though the MR fluid functionality in multiple operation cycles and for a long duration [147]. Coating the particles also helps with oxidation problems, when using silica shells with the sol-gel technique [148]. Better resistance to oxidation was seen among other observations in this study, albeit weakening of the MR effect. Finally, studies have been conducted on the effect of temperature on MR fluid stability [23], demonstrating a direct relationship between temperature and fluid yield stress.

2.3.5 Applications

MR valves are used in a variety of applications across different industries, where precise and adjustable fluid flow control is necessary. From the automotive and aerospace industry to medical devices and civil engineering, MR valves have been proven to be a versatile and reliable solution for controlling fluid flow. In this context, this technology has gained increasing

attention in recent years due to its potential for improving performance, safety, and efficiency in different applications. In this section, we will explore some of the most common applications of MR valves and their advantages over traditional valve technologies in the fields of automation, medicine, and soft robotics.

Automotive applications

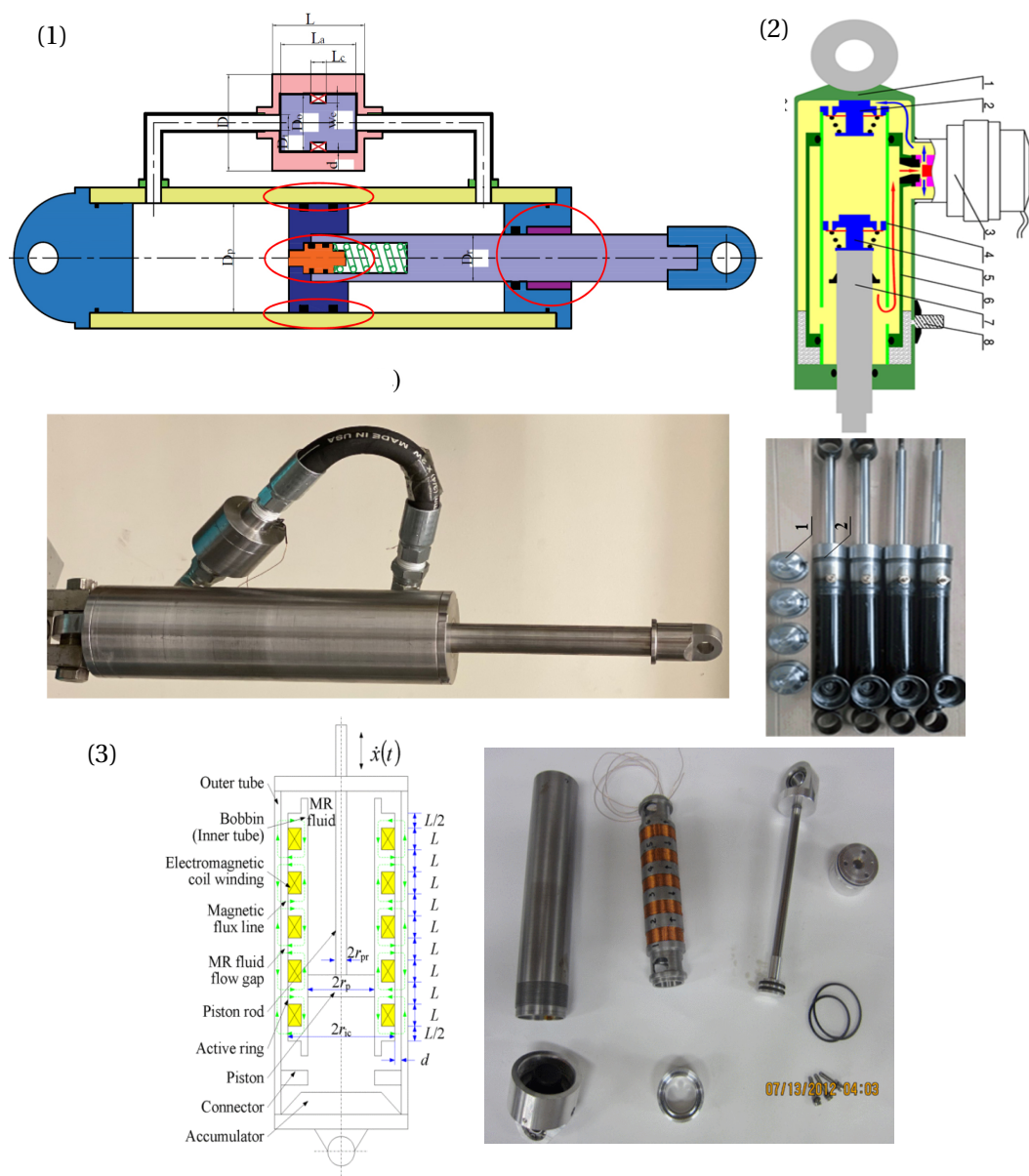


Figure 2.6: Schematics and prototype photos of MR dampers in different configurations: (1) [119] (IOP Copyright Licence: CC BY 4.0), (2) [149] (IOP Copyright Licence No: 1349838-1), (3) [150] (Copyright: 0018-9464/\$31.00 © 2013 IEEE).

One of the most important and well-known contributions of magnetorheological valves is within the automotive field for suspension systems. Dampers are used together with springs in vehicles to improve riding quality and vehicle control. They usually involve valving of fluids, such as oil or gasses to absorb the excess of energy from the springs. MR dampers that make use of the MR valve principle have been used in many automotive applications instead of conventional suspension technologies.

There are studies that focus on the design and testing of such dampers considering a low-cost device [151], or higher performance in terms of dynamic ratio and damping force [119, 152, 150, 153, 154]. [149] proposes a MR damper with high performance combining it with reduced weight, energy consumption, and cost. A MR damper for passenger vans has also been designed and tested for a wide range of forces [155], while works that emphasize on control algorithms of the damping system have been presented [156]. Fig. 2.6 depicts some of the previously mentioned MR damper prototypes and their schematics.

Medical applications

Exploiting the MR fluid advantage of controlling its viscosity with the application of an external magnetic field, multiple medical applications are based on MR fluids. A domain where MR technology is inserted into medicine is robot surgeries, which allow the doctor to operate outside the operation room avoiding dangerous radiation and achieving higher precision at the same time. The robot surgery systems comprise a master and a slave robot, while a haptic interface is provided to the doctor [157], giving information to the master robot from the slave one. Catheterization systems allow doctor's force feedback with the use of MR fluids [158, 159, 160]. The MR fluid is enclosed in a cylinder, in the axis of which the catheter is placed. The use of permanent magnets controls the MR fluid viscosity and the feedback resistance force by the fluid to the catheter. This feedback is received by the end user, which is the doctor.

Another example of MR valve use in medicine is exoskeletons, which are wearable devices designed to enhance the physical abilities of the person wearing them. They typically consist of a frame, sensors, and actuators that work together to provide mechanical assistance, strength, endurance, or mobility to the user. MR dampers have been integrated into exoskeletons for purposes, such as rehabilitation of stroke patients that suffer from finger movement difficulties [161], back support exoskeletons that can be used by caregivers [162], or hand exoskeletons for tremor suppression [163].

Except for exoskeletons, lower limb prostheses based on MR dampers are used to assist individuals with amputated limbs in movement. The MR dampers are used to enhance prostheses with shock absorbing [166], knee prostheses [88, 167], above-knee prostheses [168, 169], or leg prostheses [170]. Similarly to prostheses, orthoses can assist with movement for individuals with pathological conditions or injuries affecting the lower limbs. The shock-absorbing capabilities offered by MR dampers during patients walking are exploited in orthotic systems, too [164, 7].

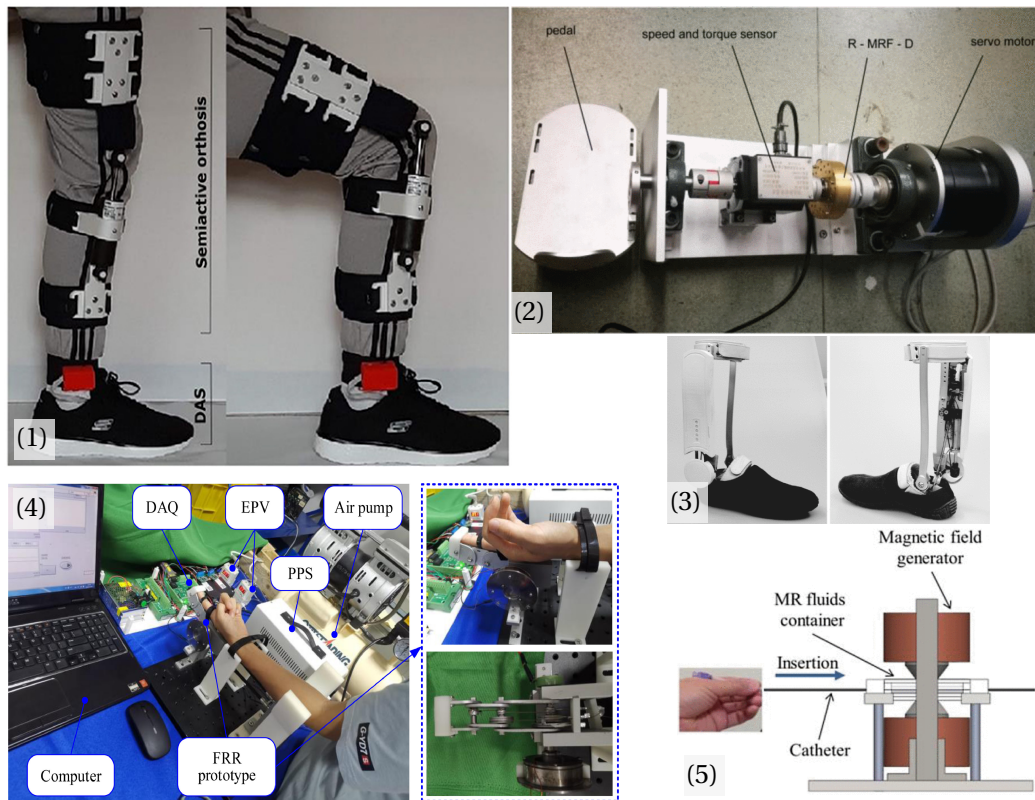


Figure 2.7: Pictures of (1) knee orthosis with MR damper [164] (Copyright © 2022 Alvarado-Rivera, Niño-Suárez and Corona-Ramírez), (2) one-degree-of-freedom ankle rehabilitation robot with MR damper [165] (Copyright: 978-1-7281-6479-3/20/\$31.00 © 2020 IEEE), (3) smart ankle-foot orthosis with MR damper [7] (Copyright: 1083-4435 © 2019 IEEE), (4) finger rehabilitation robotic system [161] (Elsevier Copyright Licence No: 5537720809140), and (5) catheterization testing system with MR fluid [158] (Copyright: 1552-3098 © 2019 IEEE).

Rehabilitation devices aim at strengthening and training specific body muscles. A rotating MR fluid damper has been designed and tested for an ankle rehabilitation robot [165]. Additionally, haptic interfaces enabled by MR fluids have not only been employed in robot surgery but also for rehabilitation purposes. MR dampers in haptic interfaces provide different levels of resistance force and allow different rehabilitation tasks [171, 172]. Low-cost, small devices based on MR dampers are also used for muscle-strengthening rehabilitation, showing the advantages of programmable applied resistance, tailored to each patient's rehabilitation needs [173]. Fig. 2.7 depicts images of some of the aforementioned devices.

Finally, a first attempt to design a single MR shock absorber that can be used in footwear for diabetic foot ulcer prevention has been presented [174]. This is the only case to our knowledge where MR fluid valves have been employed for this purpose. However, the full device has not been implemented and has not been integrated into a shoe for testing in human subjects.

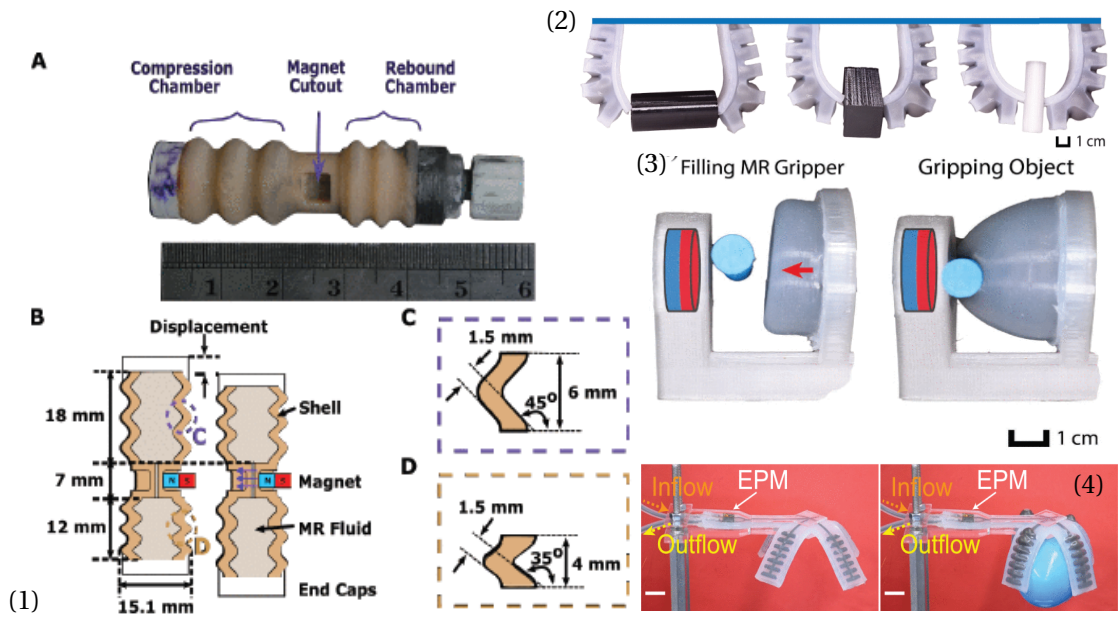


Figure 2.8: Pictures of (1) soft shock absorber [126] (Copyright: 978-1-7281-9680-0/22/\$31.00 © 2022 IEEE), (2) Pneu-Net-like gripper with MR fluid [9] (Copyright: 2377-3766 © 2021 IEEE), (3) pouch-like gripper filled with MR fluid [9] (Copyright: 2377-3766 © 2021 IEEE), (4) MR fluid gripper controlled with EPM MR valve [8] (Copyright: 2377-3766 © 2022 IEEE).

Soft robotic applications

Soft robotics is a rapidly emerging field where the hard materials that constitute the traditional rigid robots are replaced by soft materials. The use of compliant materials is promising for a vast variety of domains. For example, soft robots can facilitate human-robot interaction and the completion of minimally invasive surgical procedures. Additionally, soft grippers can manipulate delicate objects, such as vegetables and fruit, or allow navigation into tight spaces. Besides, soft robotics presents exciting opportunities in fields such as prosthetics, wearable devices, and assistive technologies for people with disabilities. They can provide lightweight and comfortable solutions that are more closely aligned with the natural movement and flexibility of the human body, improving the quality of life for individuals with physical limitations. Lastly, the choice of eco-friendly materials for soft robot construction allows for sustainable solutions by reducing the environmental impact of traditional robots.

Soft robotics have also been implemented with the use of magnetorheological fluids. A soft shock absorber made of urethane rubber utilizes MR fluid in flow mode and magnets to induce the magnetic field and control the damping [126] (Fig. 2.8(1)). The device is aimed at biomimetic robots, mimicking the behavior of biological muscles in terms of shock absorption, posture maintenance, and limb positioning. Bistable MR valves have been investigated and tested in soft gripping structures [9]. In Fig. 2.8(2) the valve is controlling a Pneu-Net actuator used for gripping. The same study presents a membrane pouch filled with MR fluid that functions again as a gripper and is activated with a permanent magnet, as in Fig. 2.8(3). MR

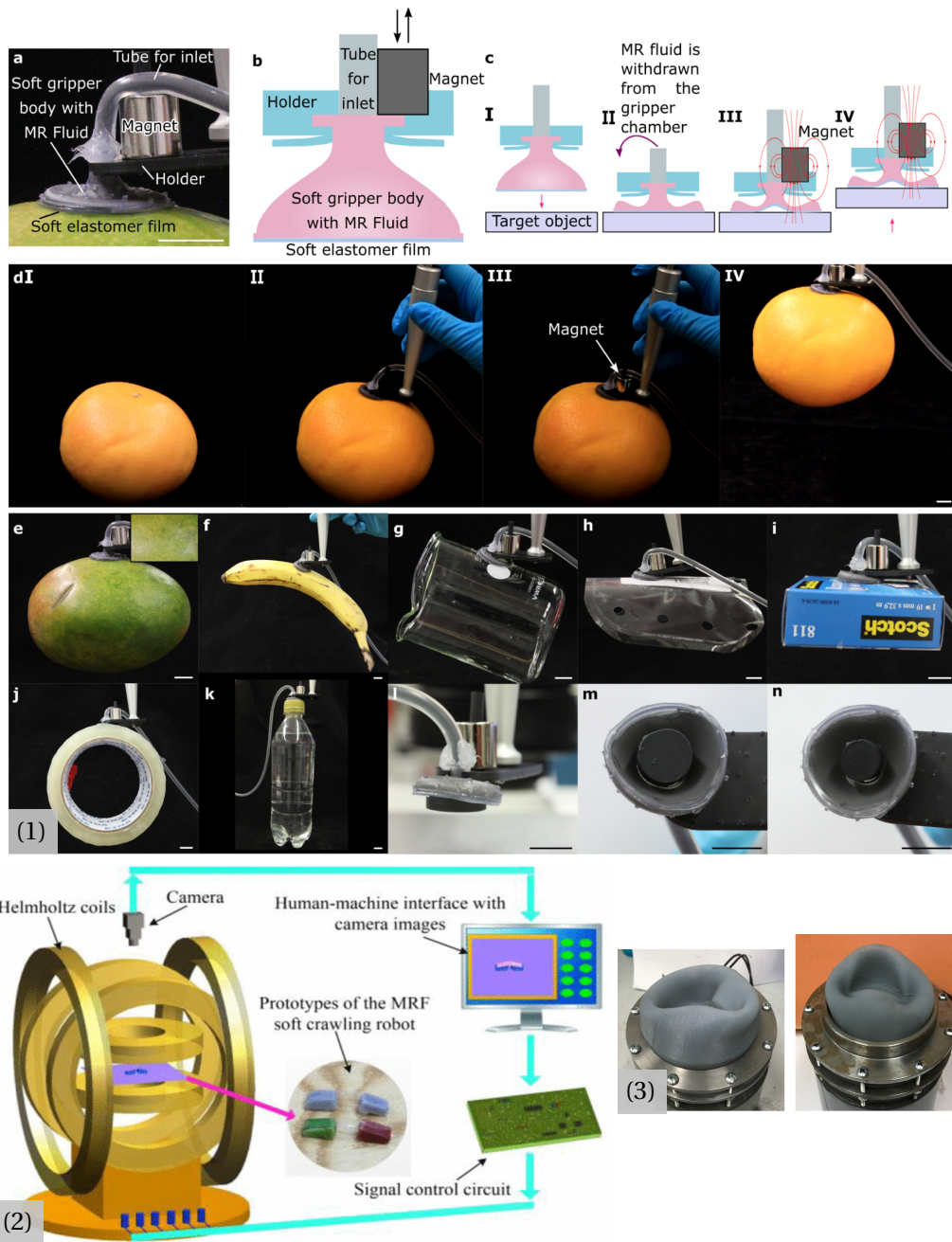


Figure 2.9: Pictures of (1) MR fluid suction gripper [175] (Elsevier Copyright Licence: CC BY 4.0), (2) soft crawling robots filled with MR fluid and placed in between Helmholtz coils [176] (Copyright: 1083-4435 © 2020 IEEE), (3) universal MR fluid gripper [177] (IOP Copyright Licence No: 1349885-1).

valves with electropermanent magnets have been proposed as a simple, low-power solution for the control of MR fluid flow in soft robotics [8, 178, 75]. An example of their use is depicted in Fig. 2.8(4) where a soft gripper is actuated with MR fluid and controlled by the aforementioned

EPM valve. A similar MR gripper as [9] is presented targeting the handling of delicate food products [179].

Other soft robotic structures have been proposed in literature, without the use of valves though. For example, a soft gripper is created with MR fluid filling a soft membrane and using the suction technique, which is controlled with the application of a magnetic field [175]. Fig. 2.9(1) shows the working principle and the gripper managing to grasp different objects. MR fluid is also added inside the walls of a soft gripper, and in this way, the actuator's stiffness can be controlled with the stiffness of the fluid [180]. In another work, MR fluid is filling a compliant structure, which is placed between Helmholtz coils that control the MR fluid stiffness, allowing the movement of a soft crawling robot [176], as in Fig. 2.9(2). Universal MR fluid grippers are actuated with the application of a magnetic field [181], preventing the use of vacuum for suction and reinflation [177], as in Fig. 2.9(3).

2.4 Conclusions

In this chapter, the importance of fluidic actuation control is presented with one of its main elements, the valve. Different valving working principles are also demonstrated and compared with each other in terms of the maximum pressure they can sustain, their volume, and their power consumption. Among them, MR valves are thoroughly investigated due to their advantages of low complexity, low cost, high pressure, and high force, as well as low power consumption. Furthermore, the most important innovation fields with regard to MR valves are discussed: (1) the design optimization, (2) the miniaturization, (3) the self-sensing MR valves, and (4) the challenges around MR fluid fabrication and use and the methods to overcome these challenges. Finally, the use of MR fluids in flow mode (mostly in damper devices) is examined in different applications in the fields of automation where the first traditional MR dampers appeared, medical devices, where our laboratory has already contributed with the invention of a miniaturized MR shock absorber with potential use in diabetic foot ulceration prevention footwear, and the emerging field of soft robotics, where MR fluids have not been extensively studied. In other fields, such as in civil engineering MR dampers are used for seismic damping. Also, different devices where the MR fluid appears in shear or squeeze mode, such as MR clutches and breaks, exist. However, these devices are not of interest to this thesis. Thus, they are only briefly mentioned. The investigation of the state-of-the-art works in this section reveals that there is space for improvement in terms of MR valve miniaturization, power consumption minimization, and self-sensing in miniaturized valves. In parallel, new low-power miniaturized valves can pave the way for novel applications.

3 Magnetorheological valve design, modeling, and validation

MR valves classify among the most commonly used devices enabled by MR fluids. They are characterized by fast and precise response, relatively low power consumption, robustness, and reliability. As a result, they find applications in a wide range of industries, from automotive and aerospace to robotics and civil engineering, where precise fluid control is crucial for optimal system performance. At the Integrated Actuators Laboratory (LAI), research has been conducted on the development of miniaturized MR valves with potential application in wearable devices for diabetic patients [122]. This chapter, as a continuation of previous research conducted at LAI, is aiming at:

- (a) the analytical modeling of the MR valve with regard to magnetostatics and pressure drop developed over the two sides of the valve;
- (b) the design optimization and the fabrication of a miniaturized magnetorheological valve;
- (c) the numerical modeling of the valve used for the calculation of the maximum pressure that it can sustain;
- (d) the experimental validation of the functionality of the valve in the open and closed condition and the validation of the maximum pressure it can sustain.

The analytical model has been derived from already known models for annular MR valves with regard to flux density distribution and sustained pressure and the valve design optimization has been performed with the use of DoE and RSM. The optimal design obtained is modeled numerically. According to this finite element model, the phenomenon of flux fringing is observed as well as its consequences on the maximum sustained pressure by the valve. Finally, the functionality of the fabricated optimal valve design is validated experimentally in terms of maximum sustained pressure with the use of a specially designed testbench.

3.1 Annular MR valve analytical modeling

This section consists of the mathematical modeling of the annular MR fluid valve with regard to the distribution of the magnetic field as well as the pressure difference developed between the two sides of the valve. Among different types of MR valves, single-coil ones in annular configuration are used in different applications such as throttle valves [182], and dampers [183] due to their simple structure and easy fabrication compared to other types, such as radial valves. Our research focuses on the design of miniaturized single-coil MR valves in annular configuration, due to the advantages of simplicity in modeling and fabrication. The analytical model will further be used in the next sections for the design optimization of the MR valve, as well as for the estimation of the maximum sustained pressure by the valve.

In the MR valve, the MR fluid operates in flow mode. The structure of the valve is cylindrical as in Fig. 3.1. Thus, in this case, the fixed parallel plates (see section 1.7) are replaced by two cylindrical structures made of ferromagnetic material. The fluid flow is taking place through the gap that is formed between the two structures. A coil is wound around the inner structure for the excitation of the magnetic field. The MR phenomenon occurs in the active regions of the valve, where the magnetic field is perpendicular to the fluid flow. The field excitation leads to the increase of viscosity of the MR fluid in the active regions, blocking the fluid flow.

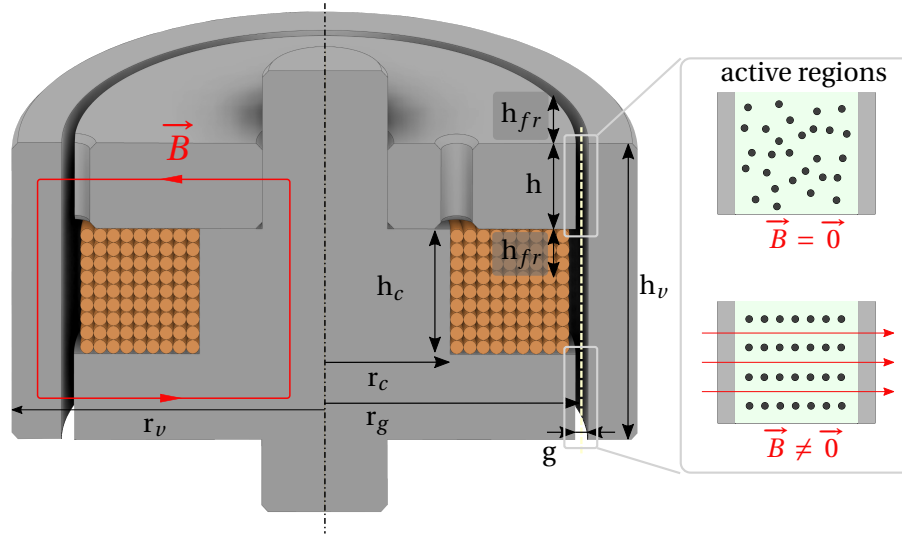


Figure 3.1: Annular MR valve in sectional view. The different dimensions are represented. The MR phenomenon is taking place at the active regions of the valve.

The mathematical modeling of pressure drop between the two parallel plates was introduced earlier. In this chapter, the mathematical model of pressure drop for the annular shape of the MR valve is defined. Thus, Eq. 1.28 is adapted for the cylindrical structure of the MR valve. In order to use this equation the assumption that $g \ll r_v$ needs to be made (see the dimensions in Fig. 3.1). The flux fringes are also not considered. Thus, the total pressure drop can be written for this geometry as a sum of the magnetic field-dependent component ΔP_τ , and the

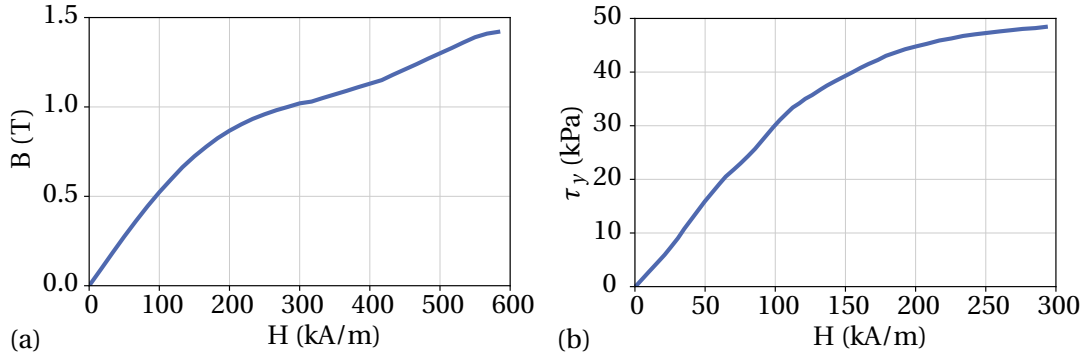


Figure 3.2: MRF-132DG (a) B-H and (b) τ_y -H characteristic curves.

viscous component ΔP_η , which is purely rheological [2, 11]:

$$\Delta P = \Delta P_\tau + \Delta P_\eta = \frac{c\tau_y(H) \cdot 2h}{g} + \frac{6\eta Q \cdot 2h}{\pi(r_g - \frac{g}{2})g^3} \quad (3.1)$$

where c is the coefficient ranging between 2 and 3, $\tau_y(H)$ is the yield stress of the MR fluid in the active regions that depends on the applied magnetic field H , η is the viscosity of the MR fluid without magnetic field excitation, Q is the flow rate of the MR fluid, and h , g , and r_g are geometrical parameters of the valve defined in Fig. 3.1.

As shown in Eq. 3.1, the yield-stress-dependent pressure drop ΔP_τ and, thus, the total pressure drop ΔP , depend on the MR fluid yield stress $\tau_y(H)$. However, $\tau_y(H)$ is defined by the applied magnetic field. As a result, the magnetostatic modeling of the valve is also important in the direction of modeling the maximum sustained pressure by the MR valve. The calculation of ΔP is possible after solving the magnetic circuit equations in the geometry of the valve. The yield stress in the active regions can be calculated using the τ_y - H curve of the MR fluid. This curve is normally provided by the fluid manufacturers. An example of such a curve for the MRF-132DG (by Lord Corp.) can be seen in Fig. 3.2(b). The maximum sustained pressure by the MR valve occurs in the case where $Q = 0$ (no-flow condition). In this case, $\Delta P = \Delta P_\tau$.

The magnetic circuit can be analyzed using Ampere's law as:

$$\int \vec{H}_i d\vec{l}_i + 2H_g g = NI \quad (3.2)$$

where H_i is the magnetic field in the ferromagnetic part, l_i is the path in the length of the ferromagnetic part, H_g is the magnetic field in the gap, g is the width of the gap, N is the number of turns of the coil and I is the current applied to the coil.

In this case, we assume that the magnetic field is the same everywhere in a radial cross-section of the gap. The magnetic flux conservation leads to the calculation of magnetic flux Φ as:

$$\Phi = B_g S_g = B_i S_i \quad (3.3)$$

where B_g , B_i are the magnetic flux density in the gap and in the ferromagnetic part, and S_g , S_i are the active region and respective ferromagnetic part surfaces.

3.2 MR valve design and fabrication

3.2.1 Design optimization with DoE and RSM

As a continuation of the previous work accomplished at LAI, a study is conducted in this section on the design optimization of miniaturized MR valves using DoE and RSM techniques. This work has been oriented toward the use of miniaturized MR valves for the same medical application for diabetic patients. As a result, the valve design is optimized with the following objectives:

- The minimization of the total volume V and power consumption P of the MR valve, to facilitate its integration in a wearable device;
- The maximization of the flow rate Q when the valve is open and the sustained pressure ΔP when the valve is closed.

The total volume, the power consumption, the flow rate, and the pressure drop of the MR valve are considered the responses of our system. Some limitations regarding the response ΔP are listed below. The minimum limit for ΔP is 700 kPa and is obtained considering plantar pressure distribution studies on diabetic [184] and healthy feet [185] and fabrication tolerances. In fact, these studies have proven that for healthy people, the maximum plantar pressure ranges between 350 and 400 kPa in the forefoot and heel areas, while for diabetic patients, it may range from 700 kPa up to 1 MPa. Therefore, it is crucial for the MR valve to be able to sustain 350 kPa. Considering, also, the safety range for the design and fabrication of the valve, the margin of applied load that can be sustained is increased from 400 kPa to 700 kPa, to achieve higher fabrication tolerance.

The optimization process consists of the three following rounds:

- A screening fractional factorial design to pinpoint the factors that affect the design the most;
- A full factorial design after the elimination of some factors according to the previous fractional design. In this case, the response surface methodology is used for the acquisition of the optimal model;
- Another full factorial design based on the RSM and conducted in the lab to eliminate the problems introduced after the fabrication of the previous design. This is the final optimization process, based on which the miniaturized MR valve used in this thesis is fabricated.

Screening fractional factorial design

DoE is used in this case for the design optimization of the MR valve since it is a powerful statistical approach that can achieve fast optimization of the system's response. In this first optimization round, volume and power consumption minimization are not taken into account. The responses of our system are the valve's pressure drop and the flow rate, both of which must be maximized.

Full factorial designs are commonly used as the first step in planning an experimental trial. They include the experiment runs that correspond to each of the different combinations of factors. However, a large number of factors increases the number of experiments, introducing difficulties when resources are limited. Creating fractional factorial designs from the full factorial design sacrifices information about some of the interactions between the factors in favor of reducing the total number of experimental runs. The fractional factorial design is a widely known and commonly used method for the identification of critical effects and factors on the response of a system.

The first step of our DoE process is the screening experimental design that includes all the 2-level input factors that can affect the response. In the case of the MR valve, the factors affecting the response optimization are shown in Table 3.1. These factors include the dimensions of the MR valve, some ratios of dimensions, and the current density of the coil. Table 3.1 also includes the range of each factor that is chosen for the current factorial design. The total number of different factors is 7 ($2^7=128$ experiment runs for the 2-level factors), consequently, the choice of a fractional and not full factorial design appears to be the most efficient approach.

	Factor	Low	High
1	J (A/mm ²)	9.0	15.0
2	r_v (mm)	4.0	6.0
3	h_v (mm)	4.0	7.0
4	g (mm)	0.15	0.3
5	h_c/h_v	0.4	0.6
6	$r_1=(r_g-\frac{g}{2})/r_v$	0.6	0.8
7	$r_2=(r_g-r_c-\frac{g}{2})/(r_g-\frac{g}{2})$	0.5	0.7

Table 3.1: Definition of the different factors of the fractional factorial design and their upper and lower levels.

In Table 3.1, J is the current density in the coil. The range of dimensions of the MR valve is chosen so that the total volume, diameter, and height of the valve satisfy the requirements for miniaturization and use of the valve in the previously mentioned medical application. The DoE optimization process has been performed using the software Minitab 19. Using the software and choosing a $1/4$ fractional factorial design, the table of experiments has been constructed, comprising of 32 different combinations of factors. A magnetic simulation has been conducted, for each of these combinations of factors and levels.

The MR fluid used in the rest of this document is MRF-132DG by Lord Corporation. The manufacturer provides the $B - H$ and $\tau - H$ characteristic curves of the specific MR fluid, as well as its viscosity, which is 0.112 Pa·s for no magnetic field excitation. The curves are depicted in Fig. 3.2. A polynomial curve fitting led to the extraction of the following equations for the two curves:

$$B_{MRF}(H) = 1.37 \cdot 10^{-8} H^3 - 1.54 \cdot 10^{-5} H^2 + 6.89 \cdot 10^{-3} H - 0.0189 \quad (3.4)$$

$$\tau_y(H) = 1.39 \cdot 10^{-8} H^4 - 7.41 \cdot 10^{-6} H^3 + 5.06 \cdot 10^{-4} H^2 + 0.31 H - 0.4 \quad (3.5)$$

For low values of H ($H < 100$ kA/m) the $B - H$ and $\tau_y - H$ curves of Fig. 3.2 present linear characteristics. A linear interpolation can describe the curves in this range as lines of slope $a = 0.0047$ ($B = a \cdot H$) and $b = 0.2588$ ($\tau_y = b \cdot H$).

The magnetic flux density in the gap modeled in each simulation is used in combination with the curve of Fig. 3.2(a) and Eq. 3.4 to obtain the magnetic field in the gap H_g . The next step is to use H_g in Eq. 3.5 to calculate the yield stress τ_y in the gap for each of the 32 experiments. Finally, τ_y and the geometrical parameters of the valve in each case, can be used in Eq. 3.1 to calculate the maximum sustained pressure by the valve, considering the ratio $\Delta P_\tau / \Delta P_\eta = 5$. $c = 2.3$ is the choice for the approximated coefficient in all the experimental cases.

Minitab 19 has been used to perform a factorial regression analysis that studies the effects of the different factors on the various responses. The model used up to 3-way interactions between factors. Standardized effects are a way of estimating the relationship between two variables in statistical analysis, one factor and one response in our case. The standardized effect of the various factors on pressure drop ΔP and flow rate Q are depicted in Fig. 3.3. Factor D, which is the width of the gap, shows the highest effect both on ΔP and on Q . According

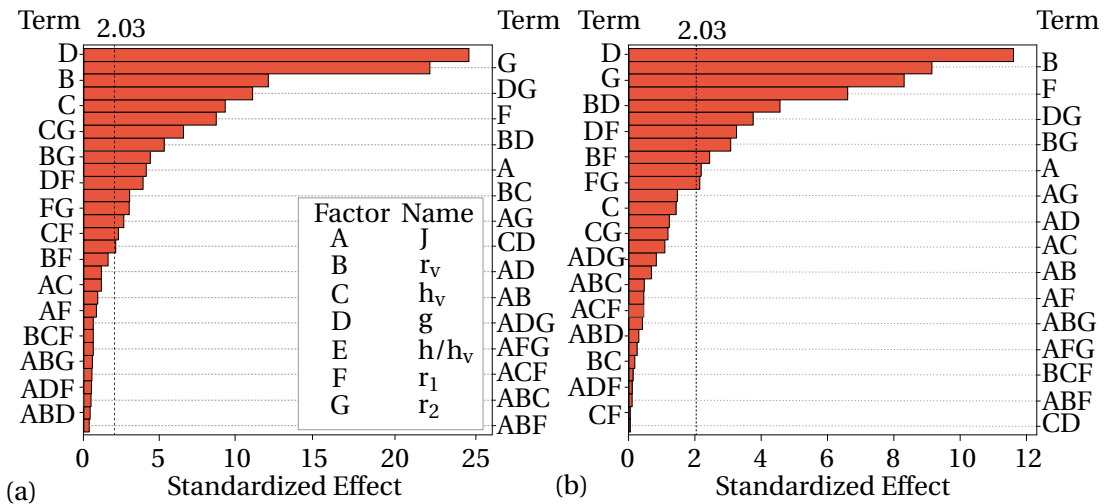


Figure 3.3: The standardized effects of the various factors and interactions of factors on (a) pressure drop, and (b) flow rate.

to the same figure, factor $E=h/h_v$ does not exist in the pareto chart because its standardized effect is very low, showing that it is the least important of all factors. Thus, it can be eliminated from the optimization design, simplifying the next steps of the process. The dotted line at 2.03 represents the reference line for statistical significance for the different factors. As a result, factors that cross this line are statistically significant at the 0.05 significance level (95% confidence level) [186], chosen for this model.

Full factorial design with Response Surface Methodology (RSM)

The fractional factorial design implemented the screening of the significant factors from the less important ones. The second step in the optimization process is the use of the RSM, based on DoE, with the aim to obtain the optimized level of factors for the MR valve. RSM is a sequential process, where initially an approximation of the relationship between the factors and the response is defined. At the end of the process, the response surface and the optimized factor levels and response are obtained [187].

In this case, initially, the number of factors is reduced from seven to six, setting the factor $E=h/h_v$ to 0.5, since it has no important effect on the responses. The value 0.5 is randomly chosen from the initially defined range. Additionally, a further decrease to five factors is accomplished, by defining the valve's outer core radius to the constant value $r_v = 5$ mm. This value satisfies the requirements of our wearable system for sufficient pressure-sensing resolution and system complexity. More specifically, the reference value for the surface of each plantar pressure measurement region is fixed to 1.5 cm^2 in previous studies [122], which means a radius of 6.9 mm for each measurement region. The reduction of the total number of factors leads to the possibility to run a full factorial design in this case with the same amount ($2^5=32$) of experimental runs as in the previous fractional factorial design. The same levels of factors are maintained for the remaining 5 factors.

The goal of this optimization round is the definition of the optimal model of the MR valve, so as to achieve minimum volume and power consumption, as well as maximum pressure drop and flow rate. The total volume V and the power consumption W of the MR valve are calculated as:

$$V = \pi r_v^2 h_v \quad (3.6)$$

$$W = I^2 R \quad (3.7)$$

where I is the current and R is the resistance of the coil. The selected coil wire is of type AWG28 with diameter $D_w = 0.321$ mm, while the coil fill factor is 50%.

The experiments table is formed as in the previous optimization round, using simulation results again. The responses pressure drop ΔP , flow rate Q , volume V , and power consumption W are then written as functions of the 5 different factors using a second-order polynomial fitting as below:

$$\begin{aligned}
 \Delta P = & -3002 + 139.7J + 620h_v - 14726g + 2474r_1 + 6735r_2 \\
 & - 2.07J^2 - 21.5h_v^2 + 25074g^2 - 639r_1^2 - 3822r_2^2 \\
 & - 0.68Jh_v - 84.6Jg + 32.9Jr_1 - 119.3Jr_2 - 372h_vg \\
 & + 167h_vr_1 - 575h_vr_2 - 4924gr_1 + 10674gr_2 - 1953r_1r_2
 \end{aligned} \tag{3.8}$$

$$\begin{aligned}
 Q = & -36.93 + 0.768J + 4.03h_v - 44.9g - 12.5r_1 + 98.5r_2 \\
 & - 0.01646J^2 - 0.1884h_v^2 + 27.5g^2 + 12.41r_1^2 \\
 & - 36.99r_2^2 - 0.0206Jh_v + 1.533Jg + 0.656Jr_1 \\
 & - 1.337Jr_2 + 2.27h_vg + 0.554h_vr_1 - 4.387h_vr_2 \\
 & + 82.8gr_1 - 34.2gr_2 - 28.88r_1r_2
 \end{aligned} \tag{3.9}$$

$$V = 78.54h_v \tag{3.10}$$

$$\begin{aligned}
 W = & 370.9 - 27.95J - 24.11h_v + 44.7g - 657.7r_1 - 140.5r_2 \\
 & + 0.3568J^2 - 1.135h_v^2 - 104.0g^2 + 116.0r_1^2 - 112.5r_2^2 \\
 & + 1.846Jh_v + 0.00Jg + 26.49Jr_1 + 6.04Jr_2 + 0.00h_vg \\
 & + 33.77h_vr_1 + 7.70h_vr_2 + 345.0r_1r_2
 \end{aligned} \tag{3.11}$$

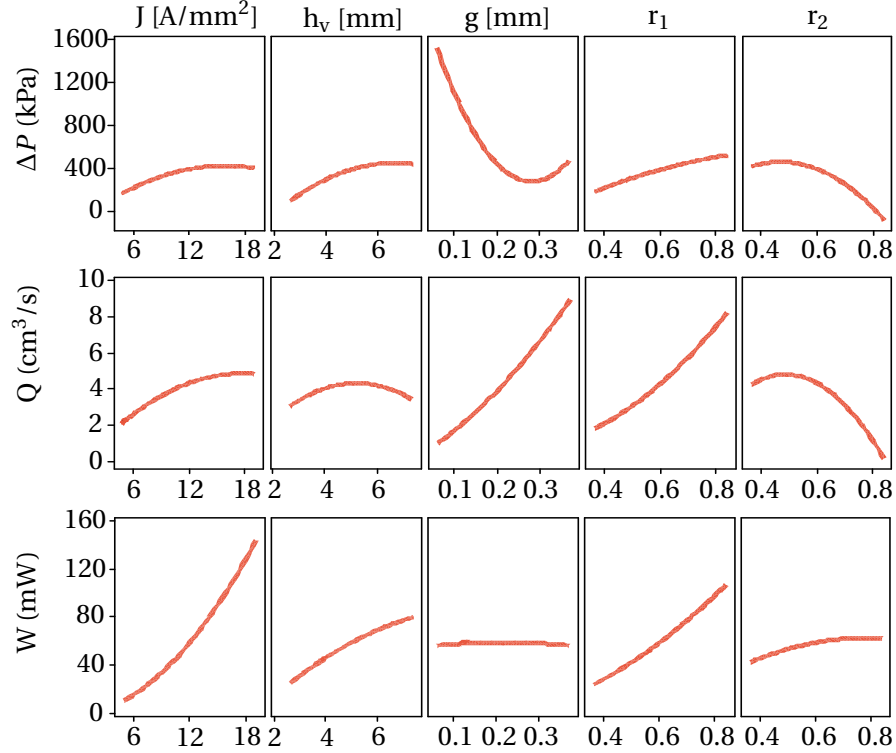


Figure 3.4: Main effects of experiment factors on the different responses.

Chapter 3. Magnetorheological valve design, modeling, and validation

Second-order polynomial fitting is used since it represents precisely the given data, without the need for polynomials of higher degrees or other more complex functions. Fig. 3.4 presents the effects of the five factors on ΔP , Q , and W . The curves derive from the analytical formulations of the responses with regard to the factors. They provide a qualitative overview of the importance of the effect of each factor on the different responses of the design. The volume V of the valve is only impacted by the total height of the valve and, as a result, it is not included in the figure. The air gap g length impacts significantly both the pressure drop and the flow rate, compared to the rest of the factors. Furthermore, the ratio $r_1 = (r_g - g/2)/r_v$ appears to have a strong effect on the flow rate, too. The same ratio impacts the power consumption, together with the current density, which, as logically expected, has the greatest effect on this response.

The maximum and minimum responses are known as the stationary points of the system. The optimized values of different factors - if they exist - give the minimum and maximum targeted responses. The partial derivatives for these points are equal to zero leading to calculation of the final optimal point by Minitab 19 optimizer function. The final optimized MR valve model is calculated together with the optimized volume, pressure drop, flow rate, and power consumption (see Table 3.2). These characteristics are inserted in a new finite element model, where the distribution of the flux density is simulated, and the flux density in the gap is calculated and presented in Fig. 3.5. Table 3.2 demonstrates the values for the optimized model.

Final optimization process

This first design has been fabricated and tested experimentally. However, the width of the gap ($g=0.1$ mm) was proved to be too small, creating problems of clogging when reusing the MR valve after some days. A new design optimization process, using again the DoE and RSM with

Item	Optimal Model
r_v (mm)	5.0
h_v (mm)	2.68
g (mm)	0.108
h (mm)	0.67
D_w (mm)	0.321
Fill factor (%)	50.0
J (A/mm ²)	13.14
V (mm ³)	210.6
B_g (T)	0.341
ΔP (kPa)	658.32
Q (cm ³ /s)	2.44
W (mW)	54.04

Table 3.2: Characteristics of the optimal MR valve design resulting from the DoE optimization.

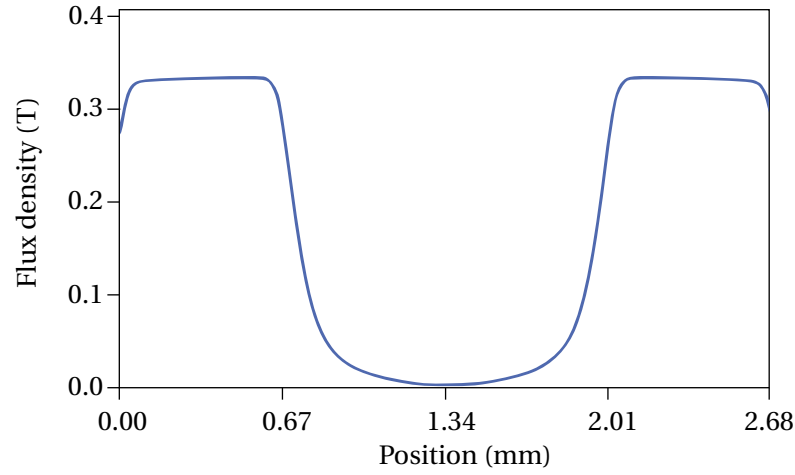


Figure 3.5: Magnetic flux density distribution in the length of the gap, with maximum value in the active regions ([69] Copyright: 78-1-7281-6794-7/20/\$31.00 © 2020 IEEE).

a full factorial design, but with a larger gap of 0.2 mm has been performed at LAI [188]. This process led to the finalized optimal design of the MR valve.

The obtained optimal design parameters that are used for the fabrication of the valve in the next steps are presented in Table 3.3. This valve can be powered with a current of 0.77 A on its coil (55 turns, 0.88 Ω) to achieve a maximum sustained pressure of 815 kPa with a flux density 0.395 T in the gap. This miniaturized design is used in the next sections of this chapter for numerical modeling and experimental validation.

Parameter	Dimension in mm	
	Optimal	Fabricated
h_v	4.5	4.62
h	1.3	1.32
h_{fr}	0.95	0.95
r_g	4.1	4.14
r_v	5	5
r_c	2	2
h_c	1.9	1.97
g	0.2	0.18

Table 3.3: Dimensions of the optimal design of the MR valve and of the fabricated MR valve derived from the optimal design.

3.2.2 MR valve final design and fabrication

The optimal valve design was fabricated according to the dimensions of the "Optimal" column of Table 3.3. However, tolerances were introduced during fabrication leading to new measured

dimensions (column "Fabricated" of Table 3.3). The deviation from the specification dimensions led to the introduction of an air gap between the two ferromagnetic parts that compose the valve and should be in perfect contact with each other (see Fig. 3.6). The air gap has a width of $w_a = 1$ mm and a height of $h_a = 0.14$ mm.

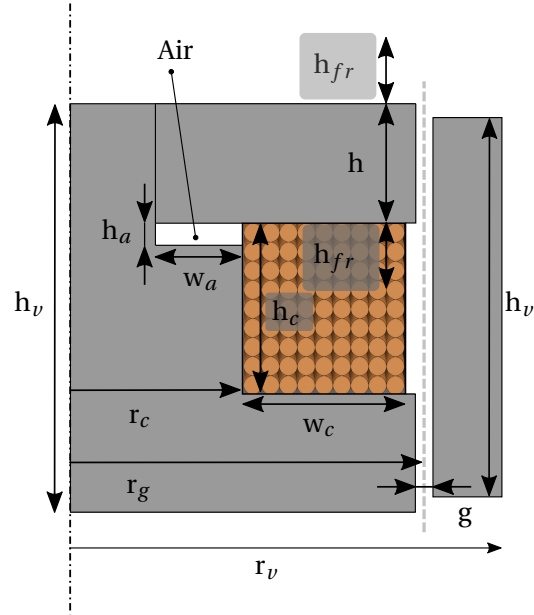


Figure 3.6: Schematics of the MR valve after introducing fabrication imperfections.

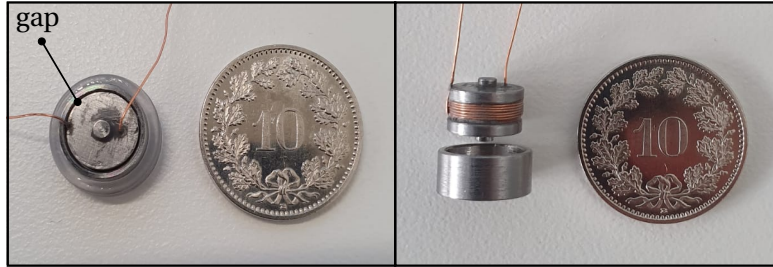


Figure 3.7: Top view and side view disassembly of the prototype of MR valve with 0.2 mm gap width.

Fig. 3.7 depicts the fabricated valve's top and side view. In the top view, the valve is placed in a plastic holder that facilitates the alignment of the two parts of the valve, the inner core and the outer ferromagnetic cylinder. In this way the gap is visible. The ferromagnetic part is made from ARMCO Telar 57, a soft magnetic iron, and the coil is fabricated with wire of 0.224 mm diameter.

3.3 Finite Element Model (FEM)

The analytical model of the MR valve is a very useful tool to understand the magnetic phenomena happening in the MR valve and how they affect the sustained pressure and to optimize its design. However, due to the complexity of the magnetostatic phenomena, a Finite Element Model can represent more accurately the distribution of the magnetic field in the valve. Thus, it allows more accurate modeling of the maximum sustained pressure by the valve. In this section, Finite Element Modeling is used to model numerically the distribution of magnetic field in the magnetic circuit of the MR valve. The magnetic field in the active regions of the gap is used to calculate the maximum pressure difference developed between the two sides of the optimal MR valve design.

The cylindrical shape of the MR valve increases the complexity of the magnetostatic analysis of the valve. Additionally, the small size of the gap ($g = 0.18\text{mm}$) and the position of the valve in working setups do not allow the measurement of magnetic field with the available measurement tools. Thus, magnetostatic analysis is enabled with the use of FEM. The symmetrical structure of the MR valve allows the finite element analysis in a 2D axis-symmetric model. The FEM model of the device is developed using FEMM 4.2 software. Table 3.3 is used to define the specifications of the magnetic simulation. Pure iron from the FEMM library is used for the ferromagnetic part of the valve that completes the magnetic circuit. The MR fluid is defined manually as a new material according to MRF-132DG $B - H$ curve (see Fig. 3.2(a)). The electromagnet consists of 55 turns.

In order to study the magnetostatic behavior of the valve, three different cases are investigated, as depicted in Fig. 3.8. In simulations A and B, the MR valve with the dimensions of Table 3.3 is modeled numerically. However, in simulation A, MR fluid is included only inside the gap of the valve, while in simulation B MR fluid exists in the gap and on the two sides of the valve as well. The addition of the MR fluid on both sides of the valve leads to a more realistic simulation since the valve is later tested experimentally in a setup where there is a large amount of MR fluid close to both sides of the valve. In simulation C, MR fluid is used on both sides, while the dimensions of the valve are the ones where the fabrication differences are introduced (Table 3.3). The flux density B in the middle of the gap, across the red line, is plotted as a function of the length of the gap for all three simulations A, B, and C in Fig. 3.9. Simulations B and C show that the existence of MR fluid around the valve leads to the increase of the magnetic field around it due to flux fringes. Thus, the length of the red line is increased so that it includes the areas where the flux fringes expand. As expected, the fabrication tolerance that leads to the introduction of a small air gap in the core of the valve results in a different distribution of magnetic field in the circuit, compared with simulations A and B which present similarities. Additionally, a drastic decrease of the flux density B in the gap happens in simulation C. In fact, B drops from 0.5 T and 0.45 T in simulations A and B close to 0.2 T in simulation C.

The existence of fabrication tolerances results in the reduction of the magnetic field in the gap. Nevertheless, the existence of MR fluid on both sides of the valve leads to flux fringes and

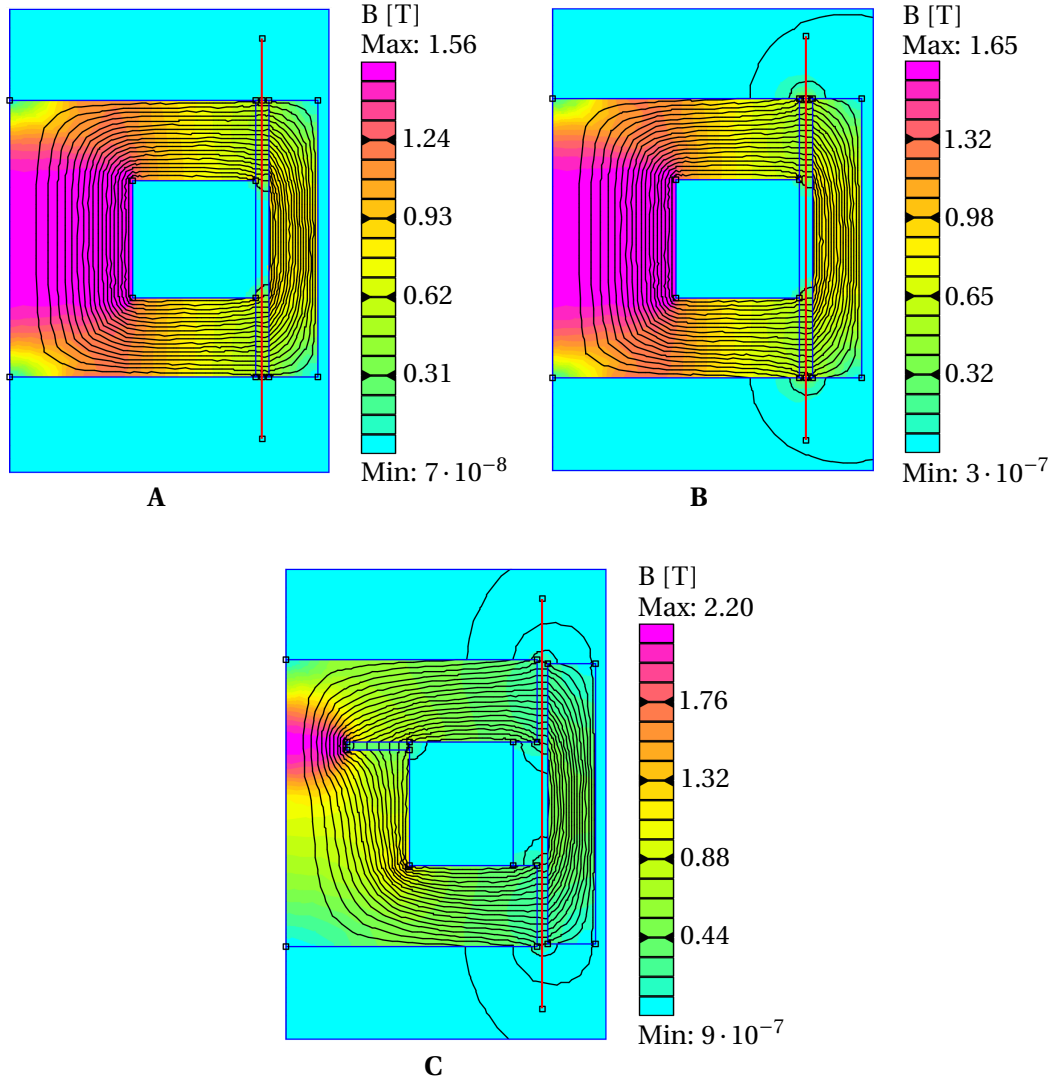


Figure 3.8: Axis-symmetric magnetostatic simulations of the MR valve (A) with MR fluid only in the gap (B) with MR fluid in the gap and around the valve (C) with MR fluid as in case B and with the addition of fabrication differences. The coil is supplied with 0.77 A in all the cases.

increase in the length of the active regions. The pressure difference developed over the two sides of the valve can be written according to Eq. 3.1, if the flux fringes are ignored (simulation A). Nevertheless, the existence of flux fringes in simulations B and C leads to a modification of Eq. 3.1 so that flux fringes are included as follows:

$$\Delta P_{\max} = \frac{c}{g} \cdot \frac{b}{a} \cdot 2 \cdot \int_{l=0}^{l=h+2 \cdot h_{fr}} B_{\text{MRF}}(l) dl. \quad (3.12)$$

where a and b are the coefficients deriving from Eq. 3.4 and Eq. 3.5 according to the linear part of the MRF-132DG characteristic curves. ΔP_{\max} calculated with Eq. 3.12 depends on the

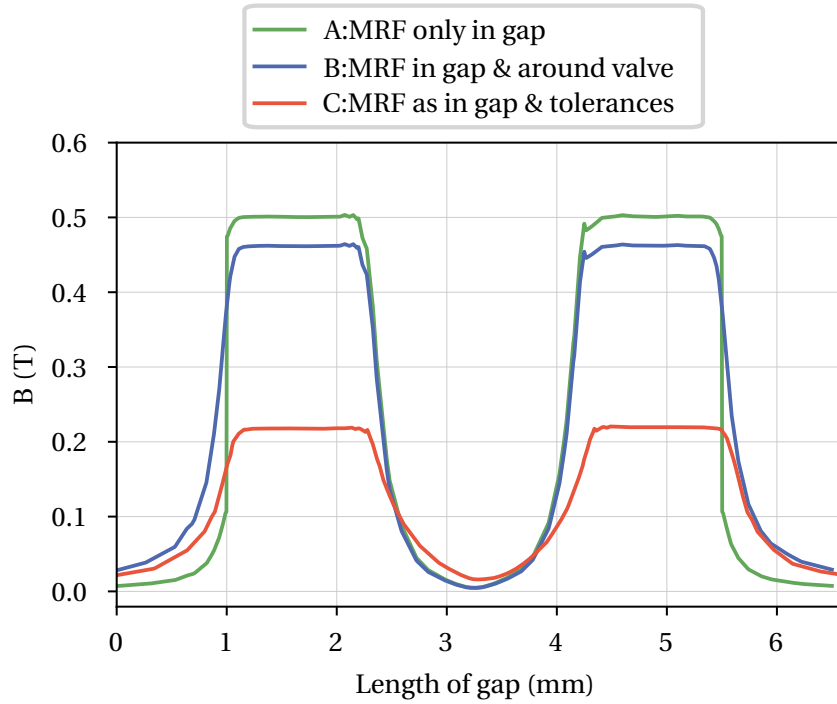


Figure 3.9: The flux density B in the middle of the gap is plotted for the three different simulation cases of Fig. 3.8.

amount of fringes taken into account, and the amount of fringes is defined from the simulation results. So, if we define h_{fr} to be the maximum length above or below the valve where fringes appear, a constant parameter k_f , $0 < k_f < 1$ can be added to Eq. 3.12, to select up to which length above and below the valve the fringes are significant. Then Eq. 3.12 can be rewritten as:

$$\Delta P_{\max} = \frac{c}{g} \cdot \frac{b}{a} \cdot 2 \cdot \int_{l=0}^{l=h+2k_fh_{fr}} B_{\text{MRF}}(l) dl. \quad (3.13)$$

To calculate the maximum sustained pressure by the valve for the three different cases A, B, and C of Fig. 3.8, Eq. 3.13 is used with $k_f = 1$. The integral in this equation is calculated using the simulated value of B in the gap for each of the three cases as depicted in Fig. 3.9. The maximum sustained pressure drop ΔP_{\max} assuming no flow rate is calculated as 1157 kPa, 1125 kPa, 696 kPa for the cases A, B, and C, respectively. The optimal valve is designed in the previous section to sustain a maximum of 815 kPa. The simulation results indicate a decrease in this pressure. The fabrication imperfections are, thus, expected to change the maximum pressure that can be sustained by the valve in the experimental trials.

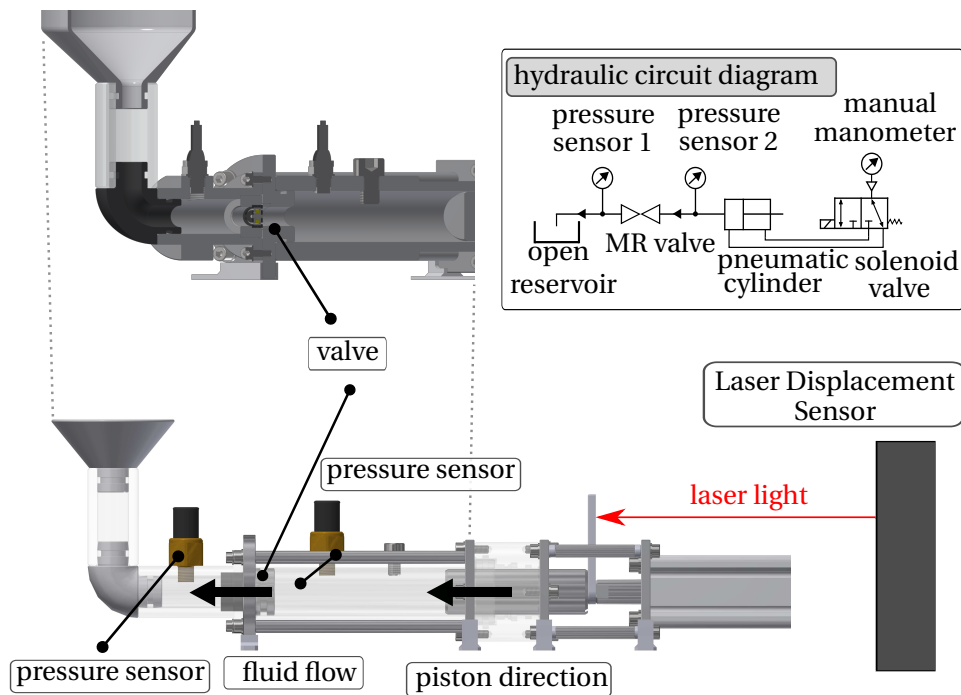


Figure 3.10: Schematic of the experimental setup with sectional view to highlight the position of the valve and hydraulic circuit diagram of the system.

3.4 Experimental validation

The design and simulation of the MR valve is followed by its experimental validation. The validation includes two parts: the functionality of the valve in two states, open and closed, as well as the maximum sustained pressure by the MR valve. A new testbench based on [122] has been designed and assembled for the validation of the valve, as in Fig. 3.10. The goal of the testbench construction is the simulation of flow conditions through tubes, where the flow control is accomplished with the proposed MR valve. The testbench consists of the following parts:

- Two chambers, one closed and one open, that are separated by the MR valve, and that are filled with MR fluid. The open chamber is constantly in atmospheric pressure;
- Two pressure sensors (Futek PFT510 Flush Mount Diaphragm Miniature Pressure Sensor) that are compatible with MR fluids and can measure the pressure in each of the two chambers. The choice of pressure sensor is important since other commercially available sensors get destroyed when in contact with MR fluid;
- A pneumatic piston that can perform a two-direction linear movement;
- A laser displacement sensor that can measure the piston displacement Δx .

Fig. 3.10 includes a hydraulic circuit diagram of the presented testbench for clarification of the testbench functionality. The control of the pneumatic piston movement is performed with the use of the solenoid valve, while the level of pressurized air is controlled with a manual manometer. The compressed air supply is limited to 1000 kPa. The piston stroke limit is 50 mm.

The state of the valve affects the pressure difference ΔP between the two testbench chambers. As explained, the magnetic field excitation leads to the increase of MR fluid viscosity in the gap of the valve. Thus, the valve functions in two states: the open state (the valve is OFF, no current supplied to the coil) and the closed state (the valve is ON, there is current flowing through the coil). In the open state, there is no limitation for the fluid flow apart from the valve geometry. In the closed state, the excitation current leads to blocking of the fluid flow due to the increase of MR fluid viscosity and development of pressure difference ΔP between the two chambers. ΔP depends on the magnitude of the current according to Eq. 3.1. It has to be clarified at this point that the valve remains closed for a certain level of current depending on the pressure difference developed between the two chambers. An increase of ΔP above a certain limit for a specific current value, leads fluid flow through the valve. Thus, the level of magnetization current can define the maximum ΔP , at which the valve remains closed and there is no fluid flow.

Three specific cases are tested to validate the functionality of the valve. In the first case, there is no current in the coil and the valve is open. In the second case, the valve closes with different levels of current. Finally, in the third case, the transition from the closed to the open state and vice-versa is tested. In all the cases, the piston is activated and it starts moving toward the valve, as the arrow indicates in Fig. 3.10. The piston displacement Δx as well as its effect on the pressure difference ΔP (pressure sensor measurements) are recorded simultaneously.

3.4.1 Open valve

The valve is initially tested without applying any current to the coil. This means no magnetic field and, consequently, a fully open valve that allows the MR fluid flow through the gap. The piston air supply is regulated at different levels. The Piston Displacement Δx is plotted over time for the different pressure values developed between the two sides of the valve, which range between 62 kPa and 756 kPa. During the experimental process, the first step is to manually set the pressure of the air supply with the manometer. Then, the piston movement starts toward the valve at $t = 1$ s and continues until the stroke limit (50 mm).

The start of movement at $t = 1$ s is depicted in Fig. 3.11, where at this timestamp Δx starts increasing. For all the different ΔP values, there is an initial increase of Δx close to 10 mm. It can be justified by the compressible nature of the air that is trapped in the closed chamber during the MR fluid-filling process. Although efforts are made to minimize the air in the closed chamber, the complete absence of air is impossible. For larger pressure values, the air compression is larger, leading to a larger initial displacement, as in Fig. 3.11. The increase of

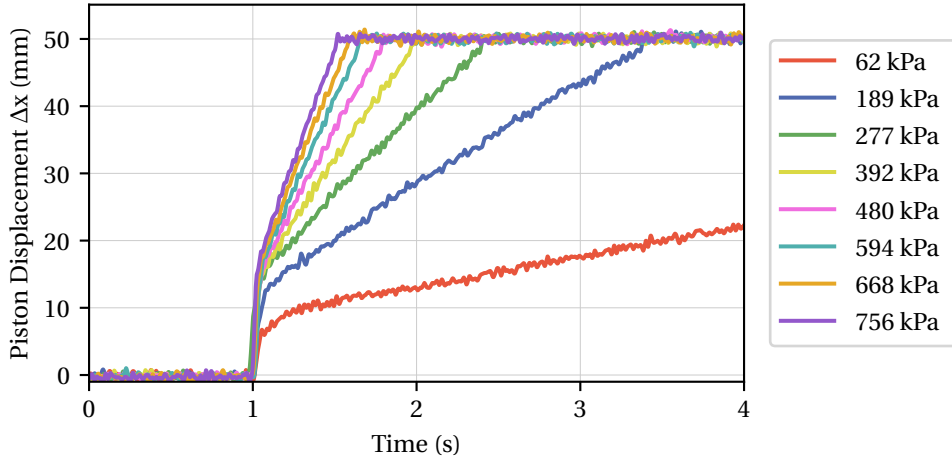


Figure 3.11: Piston displacement (Δx) over time for multiple pressure difference ΔP values measured between the two sides of the valve.

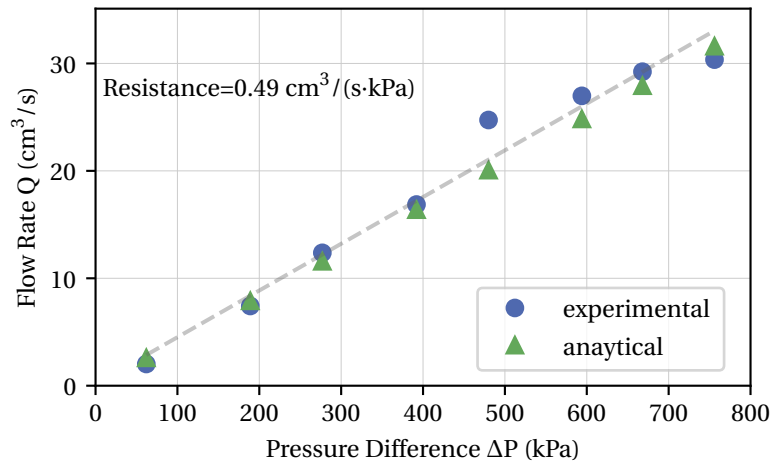


Figure 3.12: Flow rate Q over pressure difference ΔP and experimental estimation of the MR valve flow resistance.

Δx proves that the valve is in the open state.

Additionally, the increase in pressure creates faster movement of the piston according to the same figure. The flow rate through the valve is calculated indirectly using the displacement Δx of Fig. 3.11 for each pressure value. The piston velocity is calculated using Δx over time, and the flow rate Q is calculated as the product of velocity with the piston surface $A_p = 0.49 \text{ cm}^2$. The different flow rate values are plotted in Fig. 3.12 (blue circles) and derive from the experimental results. In parallel, the flow rate calculated from Eq. 1.31 is plotted in the same figure (green triangles). In this case, $\Delta P_\tau = 0$ since there is no excitation current and only ΔP_η exists.

The fluid resistance in the case of the current setup is the force opposing the movement of the MR fluid in the tubular structure of the testbench. It is caused by the friction and deflection forces generated as the MR fluid flows through the chambers and the MR valve, and results in the pressure difference ΔP development. The relationship between Q and ΔP presents a linear behavior for both analytical and experimental results. The estimated regression line for the experimental results is plotted as well in the same Fig. 3.12. From the slope of this line, we can extract the flow resistance of the valve, which is experimentally estimated to be $0.49 \text{ cm}^3/(\text{s} \cdot \text{kPa})$.

3.4.2 Closed valve

In the second experiment, the closed state of the valve is validated. The term "closed" depends on the different excitation currents and pressure values. For lower excitation currents, the closed valve (no-flow condition) is guaranteed for a certain range of ΔP . Above this range the viscosity-dependent parameter of pressure difference ΔP (see Eq. 3.1) becomes non-zero, and the MR fluid flow in the gap begins. The experiment is split into two parts, one with static and one with dynamic increase of pressure.

In the static case, the first step is the setting of the current I flowing through the coil. This current is set to six different discrete values from 0.0 A to 0.5 A with a step of 0.1 A. For each current value, the piston starts moving in the closed chamber very slowly, toward the MR valve, while the manometer value is increasing gradually and slowly as well. The latter leads to an increase of ΔP over the valve. The Piston Displacement Δx is plotted over ΔP in Fig. 3.13.

In this experimental session, an initially abrupt increase of Δx close to 10 mm is again observed and it exists due to the air compression. The piston movement is activated with a minimum air supply of 70 kPa according to its specifications. Fig. 3.13 confirms it, since below the value of

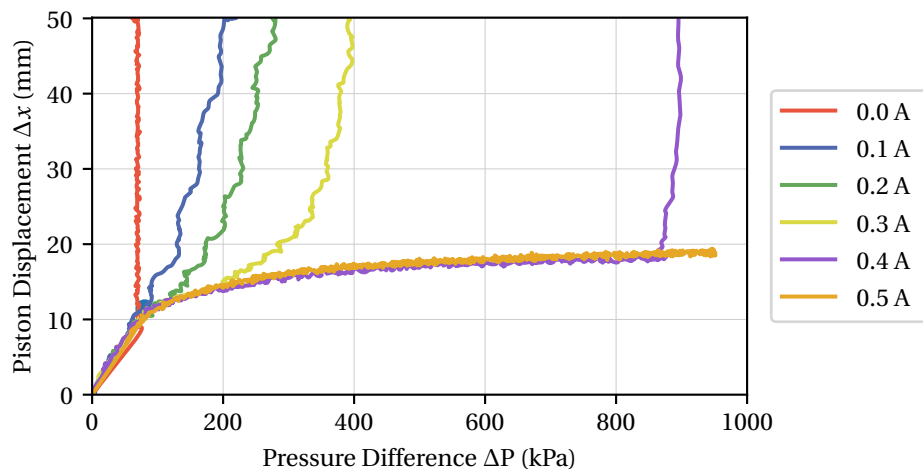


Figure 3.13: Valve closed with different currents.

70 kPa, no important displacement takes place. For $I = 0.0\text{ A}$, there is no resistance to the fluid flow and the MR fluid flows in the gap until the piston reaches the stroke limit. As soon as $I \neq 0$, some resistance appears to the fluid flow. For $I = 0.4\text{ A}$, the ΔP limit until which there is no flow increases to 870 kPa, while for $I = 0.5\text{ A}$ there exists no flow until $\Delta P = 950\text{ kPa}$ (the limit of our testing system). The maximum ΔP with no flow (maximum sustained ΔP) is plotted in Fig. 3.15 over the excitation current. Above $I = 0.3\text{ A}$, the maximum sustained ΔP increases drastically. Further increase of current has not been tested since with 0.5 A , the pressure limit

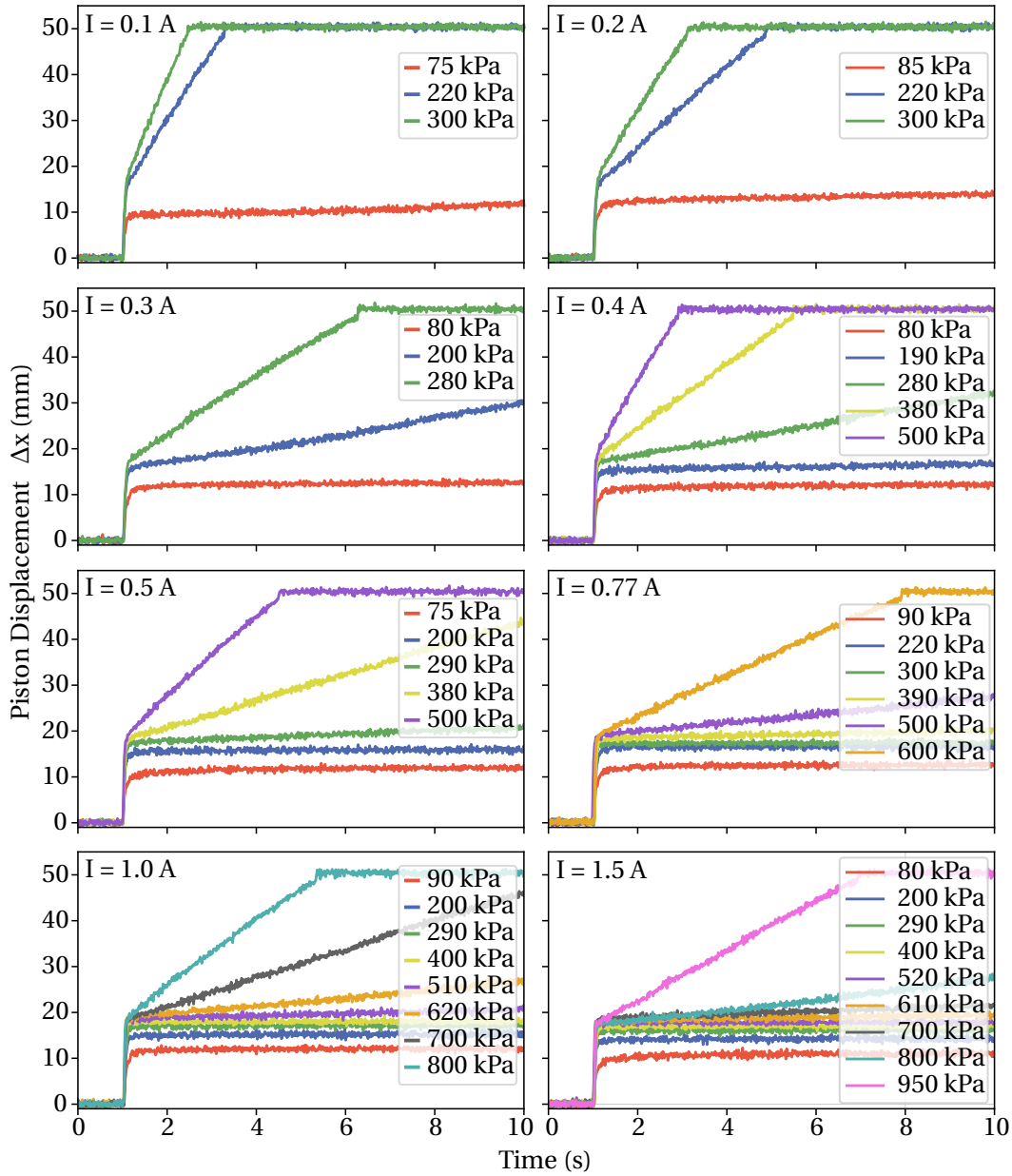


Figure 3.14: Piston displacement over time for different excitation currents and applied pressure values in the dynamic condition.

of the testing system is already reached.

In the dynamic condition, the current is set again in different values ([0.1 A, 0.2 A, 0.3 A, 0.4 A, 0.5 A, 0.77 A, 1.0 A, 1.5 A]). However, the increase of pressure is applied as a step function. Firstly, the manometer value is set and then the piston starts moving abruptly toward the valve. This movement is depicted in Fig. 3.14 where Δx is plotted over time. The piston movement starts at $t = 1$ s. The trapped air compression leads to the initial $\Delta x = 10$ mm. After that, depending on the applied current, the valve remains closed (constant Δx) for a different range of pressure values.

Fig. 3.15 depicts the maximum sustained pressure by the closed MR valve obtained experimentally for the static and dynamic conditions, as well as calculated in the following different ways:

- With the use of the numerical model of the MR valve as in simulation C (Fig. 3.8), without considering the flux fringes. H_g is obtained from the simulation in the middle of the active region. Eq. 3.1 and 3.5 are used for the calculation of ΔP_{max} .
- With the use of the numerical model of the MR valve as in simulation C (Fig. 3.8), taking into account the flux fringes. The simulation results are used for the calculation of

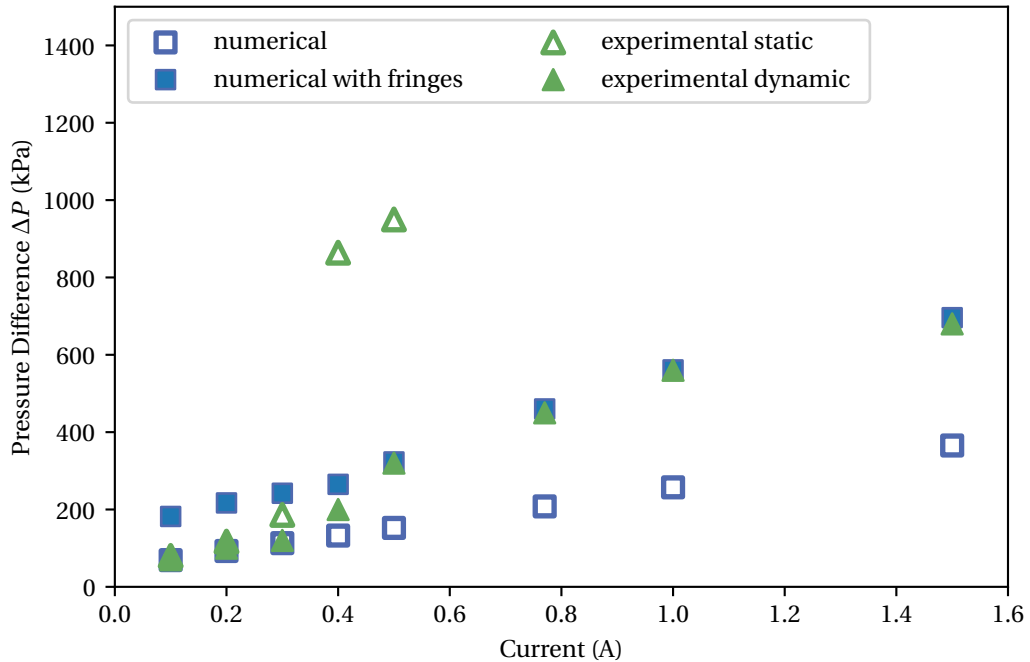


Figure 3.15: Maximum sustained pressure by a closed MR valve with regard to the excitation current.

ΔP_{max} with Eq. 3.13. $k_f = 0$ for $I = \{0.1 \text{ A}, 0.2 \text{ A}, 0.3 \text{ A}, 0.4 \text{ A}\}$, $k_f = 0.2$ for $I = 0.5 \text{ A}$, $k_f = 0.65$ for $I = 0.6 \text{ A}$, and $k_f = 0.9$ for $I = \{0.8 \text{ A}, 0.9 \text{ A}\}$.

The dimensions of the MR valve used for the calculation of ΔP_{max} are those of Table 3.3, including the fabrication tolerances. The experimental results of the dynamic condition are closer to the values estimated with the numerical model without fringes for lower current values. For higher current ($I > 0.4 \text{ A}$), the estimation is better with the numerical model that takes into account the flux fringes. This behavior is justifiable by the fact that fringes have a higher impact with higher excitation currents. This is also evident in Fig. 3.16, where the flux density in the gap is plotted over the length of the gap.

Finally, the experimental results of the static condition do not match well with any of the proposed models. In fact, ΔP_{max} is much higher compared to the dynamic condition, especially for currents higher than 0.3 A. The geometry of the testing setup in combination with the flux fringes in the MR fluid affects the experimental result. MR fluid accumulates close to the valve, while the slow movement of the piston leads to an increase in the density of the MR fluid. As a result, the flux fringes magnetize larger quantities of ferromagnetic material close to the valve, and ΔP_{max} increases compared to the static condition. Thus, it can be concluded that the proposed MR valve can sustain different maximum pressure depending on the application used that involves static or dynamic pressure application.

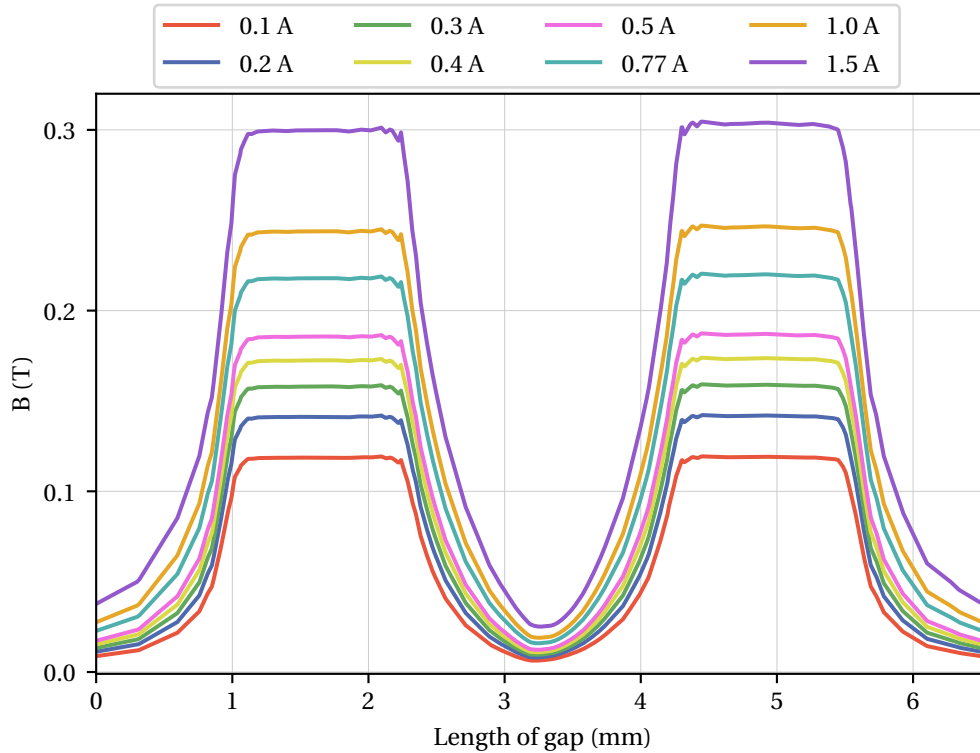


Figure 3.16: Flux density in the length of the gap for different current values.

3.4.3 State transition

The final experiments study the transition of the valve between the two different states, open and closed. Initially, the valve is in the closed state, with a current supply of $I = 0.77\text{ A}$ and the manual manometer sets the air supply close to 200 kPa. At $t = 5\text{ s}$, as shown in Fig. 3.17, the piston starts moving toward the valve. This leads to the increase of Δx close to 10 mm due to the air compression without a further increase since the valve is closed. At the same time, an increase of pressure to almost 220 kPa happens. At $t = 14.5\text{ s}$, the current supply to the coil stops.

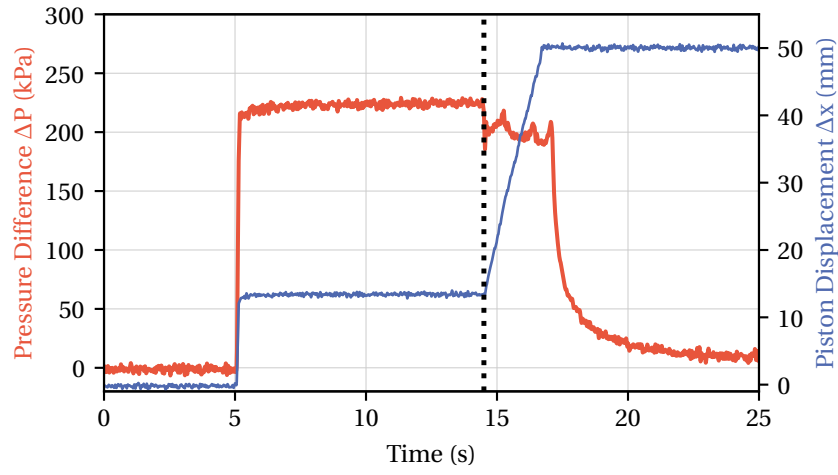


Figure 3.17: Switching of the valve from the closed to the open state.

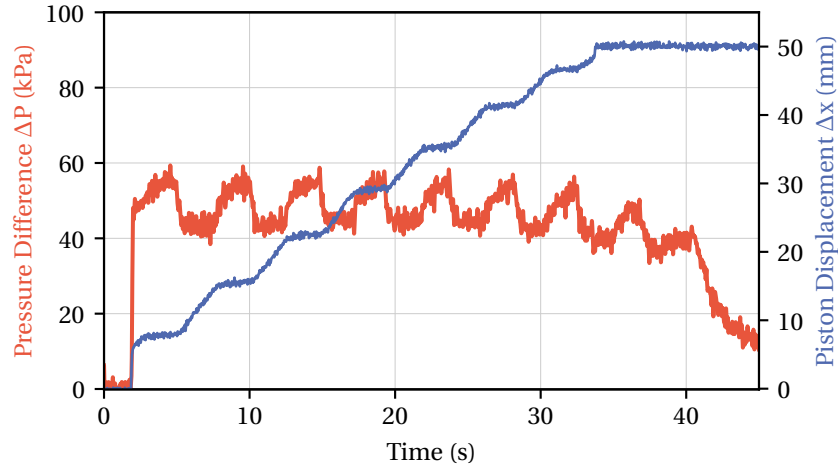


Figure 3.18: Repetitive switching of the valve between the ON and OFF state (closed-open).

The piston state does not change and it keeps applying pressure to the closed chamber. Δx starts increasing until the stroke limit, confirming the valve opening and the MR fluid flow in the gap. ΔP also starts decreasing. The moment the piston reaches the maximum stroke

($t = 16.9$ s) the pressure in the closed chamber drops close to the atmospheric pressure. This means that the pressure in both chambers is the same. In the second experiment, depicted in Fig. 3.18, the same piston movement is taking place. The pressure is set to less than 60 kPa. Every two seconds the valve is turned ON and OFF consecutively, while the initial state of the valve, before the piston starts moving is ON. The current supplied to the valve is again 0.77 A. This leads to a step increase of Δx in Fig. 3.18, confirming the opening and closing of the valve. The process is repeated 7 times until Δx reaches the stroke limit. The pressure decreases by almost 20 kPa at every repetition when the valve opens and it increases again the moment the valve closes.

3.5 Conclusions and main contributions

MR valves have been used as controlling devices in fluidic actuation systems in various domains, mainly in industrial automation. Up to now, they could achieve high sustained pressures, but with a compromise in terms of volume. In this chapter, we propose a new miniaturized MR valve with a total volume of 353 mm^3 . The main contributions are:

- The design optimization of the miniaturized MR valve with the use of DoE and RSM, aiming at pressure drop and flow rate maximization as well as at volume and power consumption minimization;
- The use of numerical modeling to introduce a new way of modeling the maximum sustained by the valve pressure, changing the traditional analytical models for the annular MR valve;
- The experimental validation of the sustained pressure and flow rate of the valve, and the comparison with the analytical/numerical model.

Publications related to this chapter:

- S. L. Ntella, et al., "Design optimization of miniature magnetorheological valves with self-sensing capabilities used for a wearable medical application," in 2020 IEEE/ASME International Conference on Advanced Intelligent Mechatronics (AIM), pp. 409-414, 978-1-7281-6794-7/20/\$31.00 ©2020 IEEE.
- S. L. Ntella, et al., "Optimization of Radial Magnetorheological Valves with Constraints of Volume, Pressure Drop and Power Consumption," in 2020 23rd International Conference on Electrical Machines and Systems (ICEMS), pp. 1578-1582, IEEE, 2020.
- M. T. Duong, S. L. Ntella, et al., "Optimal design of magnetorheological valve integrated in an intelligent footwear for diabetic patients with foot insensitivity," in 2021 24th International Conference on Electrical Machines and Systems (ICEMS), pp. 111-115, IEEE, 2021.

4 Magnetorheological Valve Based on Electropermanent Magnet

Magnetorheological fluid valves actuate with the use of electromagnets that are supplied with currents in the order of one amp, as the valve presented in the previous chapter. As a result, conventional MR valves controlled by electromagnets require power in the range of 1 W to 100 W. The continuous current supply, and, thus, the continuous power consumption of such valves leads to increased requirements with regard to energy storage. This fact limits the use of conventional MR valves powered by electromagnets in mobile applications.

On the other hand, the use of PM and EPM is extensive due to their main advantages of low power consumption, compactness, and minimal weight. They have been especially useful in controlling pneumatic systems employed for soft robotic actuators [71] and soft mobile robots [72]. Actuation applications that do not involve valves have also employed the advantages of EPMs. Such applications include miniature robotic building blocks ('pebbles') [73], or latching mechanisms in self-assembled robots [189]. The specific case of fluidic actuation systems, where the working fluid is MR fluid has also been studied, targeting again at soft robotic applications. In these studies, the addition of the EPM technology in the conventional MR valve structure has opened up interesting perspectives. It allowed valve miniaturization, combined with low energy consumption since the steady-state power supply limitation is overcome [75], [8].

In the previous chapter, the analytical and numerical modeling of the conventional structure of the MR valve in a miniaturized version was presented. The valve was powered continuously by DC current when in the closed state. This chapter presents an alternative version of this valve, which can alter state from open to closed and vice versa with a single current pulse of sub-millisecond-duration. This is achieved by adding a soft magnet in the core of the valve, which can be easily magnetized and demagnetized by the pulse. The total volume of the valve as well as the rest of its dimensions are maintained as they were in the conventional version. The change from continuous to pulsed current leads to a decisive decrease in energy consumption, maintaining at the same time the high sustained pressure and low voltage capabilities of the previously presented MR valve.

4.1 Electropermanent magnet principle

Up to the present time, a great number of studies have presented electropermanent magnets [73, 189, 190, 191, 192] built with two different ferromagnetic materials. The two pieces are usually placed next to each other, as in Fig. 4.1. One of the two materials is a hard magnet, typically NdFeB, while the other piece is made of a soft magnet, such as AlNiCo-5. A coil is wound around the soft magnet. In Fig. 4.1(a), the AlNiCo-5 material is not energized, i.e. no current pulse has passed through the coil leading to no magnetic field induction. The flow of current in Fig. 4.1(b) leads to the magnetization of the soft material in the same direction as the hard material. As a result, the EPM is seen externally as magnetized. In Fig. 4.1(c), when the current pulse that circulates the coil is of the opposite direction compared to the one in Fig. 4.1(b), the soft material is magnetized in the opposite direction with regard to the NdFeB magnet. Thus, the EPM is seen externally as demagnetized. The combination of two magnet types is usually very important to avoid self-demagnetization phenomena in the soft material.

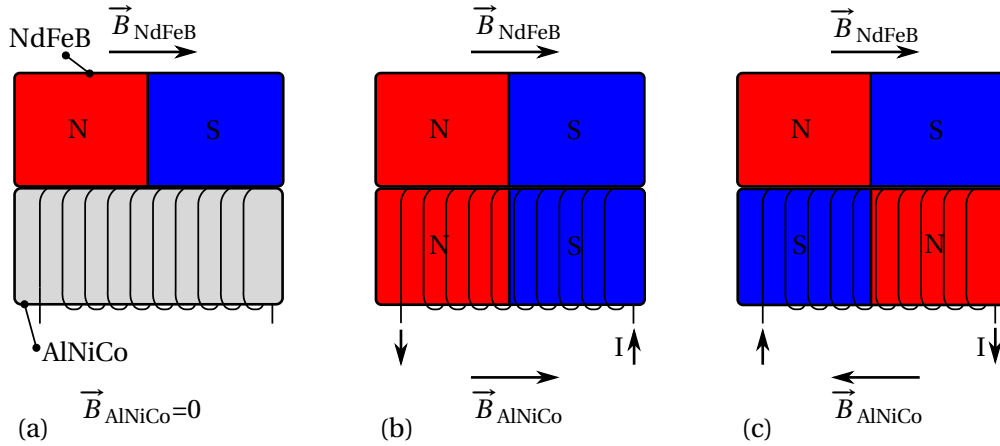


Figure 4.1: EPM made from hard (NdFeB) and soft (AlNiCo) magnetic material. (a) Unmagnetized AlNiCo magnet. (b) AlNiCo magnet magnetized at the same direction to NdFeB magnetization. Seen externally as magnetized. (c) AlNiCo magnet magnetized at the opposite direction to NdFeB magnetization. Seen externally as demagnetized.

In this chapter, the addition of an electropermanent magnet (EPM) [190] is introduced, to apply the magnetic flux density in the active regions of the MR valve. A conventional MR valve is composed of ferromagnetic material and an electromagnet for the excitation of the magnetic field and the activation of the MR fluid in the active regions. In the EPM MR valve the inner ferromagnetic rod is replaced by a soft magnetic material, as in Fig. 4.2. Soft magnetic materials can be easily magnetized and demagnetized, having typically an intrinsic coercivity of less than 1 kA/m. A careful choice of magnetic material is necessary to construct an EPM. In this application, it must be made of a ferromagnetic material with a large remanent magnetization and a low magnetizing field. AlNiCo-5 material is chosen for this purpose in our device since it meets the previously described specifications. In our case, where only one soft material is used (AlNiCo-5), the self-demagnetization is avoided, thanks to the small air gap of the valve (only 0.2 mm), and the negligible variation of magnetic permeability coming from the MR

fluid in the gap. As a consequence, the use of a hard material is redundant in our device. Only the soft AlNiCo-5 is enough for the magnetization (closing) and demagnetization (opening) of the valve. To our knowledge, there is a limited number of works, such as [193], that use a single AlNiCo-5 magnet inside an electropermanent magnet structure. There, despite taking advantage of the full magnetization curve, the large air gap and varying magnetic environment will result in its self-demagnetization, imperiling a reliable operation. The strategy proposed in this chapter is robust and highlights a great application of single-rod electropermanent magnets.

Fig. 4.2 depicts the sectional view of the structure of an annular MR valve. The coil is used in this case, not for the excitation of the magnetic field with continuous current, but for the magnetization and demagnetization of the soft magnetic rod. This is achieved by sub-millisecond current pulses of opposite directions for magnetization and demagnetization. The control of the pulse amplitude allows the magnetization of the magnet at different levels, achieving stronger or weaker magnetization. This attributes to the EPM MR valve the characteristic of tunability and programmability.

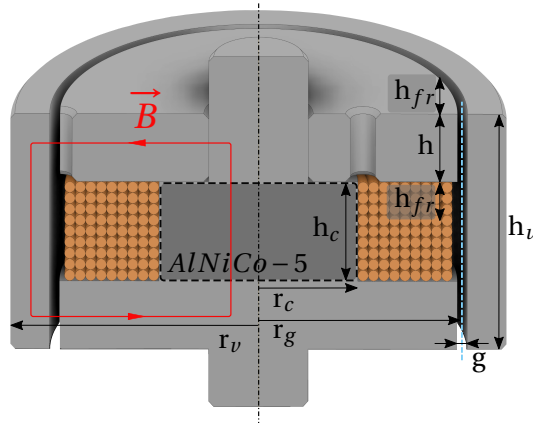


Figure 4.2: Annular MR valve in sectional view. The different dimensions are represented. The inner rod of the valve is made from AlNiCo-5 material that generates the magnetic field. (Copyright: 2377-3766 © 2023 IEEE)

Fig. 4.3 represents the differences between the conventional and the EPM MR valve in a cut-view section. The inner rod of the conventional and the proposed valve are made of different materials in the two cases, iron and AlNiCo-5 respectively. Fig. 4.4 depicts the closed and open states of the EPM MR valve, in accordance with the magnetization and demagnetization process. Each state of the valve is placed at the respective position of the magnetization curve (M-H characteristic) of the AlNiCo-5 material. The magnetizing field H , external to the material, is the one generated by the coil and is proportional to the ampere-turn product (magnetomotive force (MMF)). The resulting magnetization of the material M is defined as follows:

$$M = \frac{B}{\mu_0} - H = (\mu_r(H) - 1) \cdot H \quad (4.1)$$

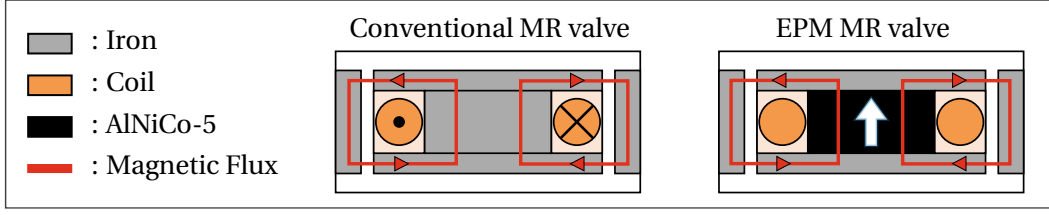


Figure 4.3: Differences between the conventional and an EPM MR valve. The white arrow represents the magnetization orientation in the rod. (Copyright: 2377-3766 © 2023 IEEE)

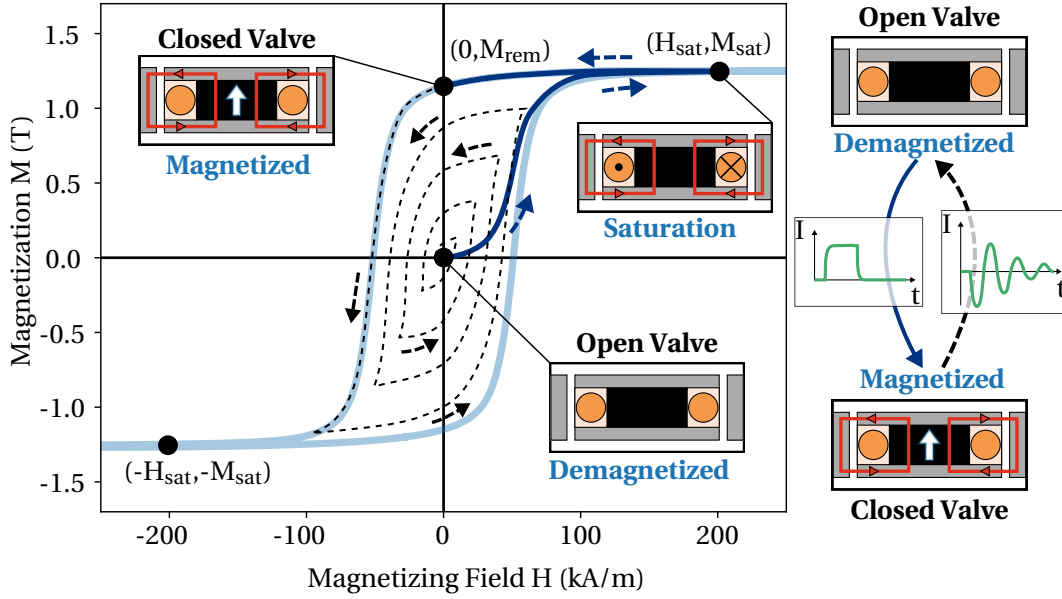


Figure 4.4: The EPM MR valve can function in two states, open and closed. Each stated is depicted accordingly on an ideal M-H characteristic of an AlNiCo-5 device. Demagnetizing the rod can happen with a decaying oscillating external field. (Copyright: 2377-3766 © 2023 IEEE)

with μ_0 the magnetic constant, and μ_r the relative magnetic permeability of the material. The non-linear relationship of the permeability with the magnetizing field: $\mu_r(H)$, results in different magnetization for the same magnetizing field. Thus, such material shows hysteresis, which means that magnetization depends on its history. This non-linear behavior is usually undesired in magnet applications. However, in our case, it is used to operate the electropermanent magnet.

The inner rod made from AlNiCo-5 is initially demagnetized ($H = 0, M = 0$). In this case, the absence of magnetic field means no activation of the MR fluid and, thus, the valve is in the open state. When the coil is supplied by an electric current of positive direction, high enough to reach the saturation of the magnet, the external magnetic field, in which the AlNiCo-5 is placed, increases. This increase continues until the saturation point ($H = H_{sat}, M = M_{sat}$). When the current is turned off, the magnetizing field disappears, and the material reaches

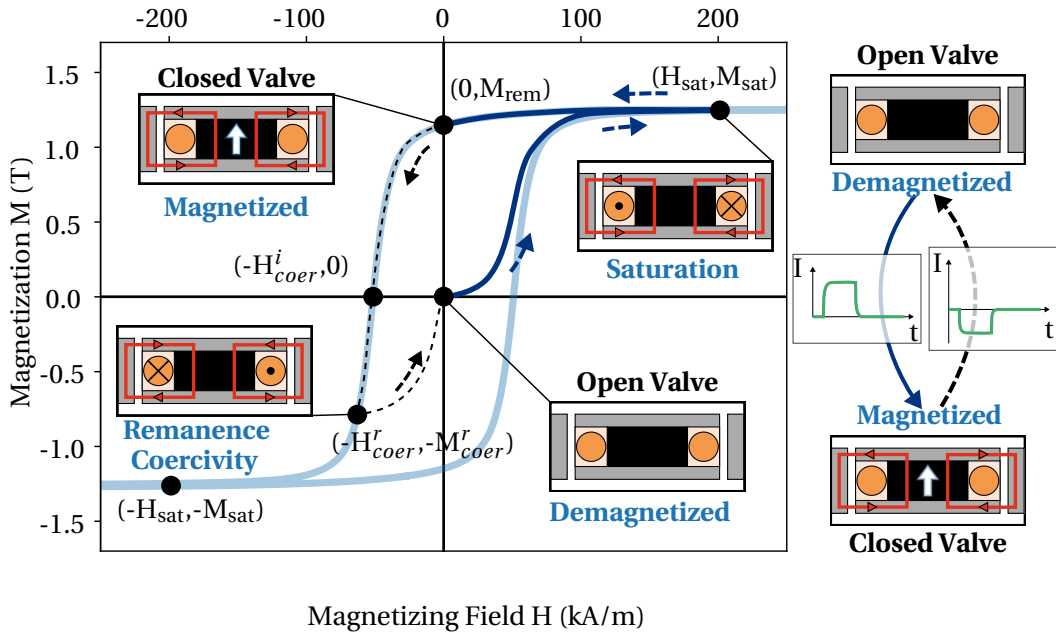


Figure 4.5: Demagnetizing the rod can also happen with a negative pulsed external field reaching the remanence coercivity of the material. (Copyright: 2377-3766 © 2023 IEEE)

its remanence ($H = 0, M = M_{rem}$). The remanent magnetization in the material means that it acts as a permanent magnet. The valve is closed in this state. The aforementioned process describes the complete magnetization of the magnet so that the valve switches to the closed state. In reality, when the material reaches its remanence, the load curve is not exactly vertical as it is assumed in Fig. 4.4 and the flux density in the material is slightly lower than B_{rem} and M_{rem} . However, the difference is negligible in the current MR valve structure and we assume that the load curve is almost vertical.

In order to open the valve, the AlNiCo-5 magnet must be demagnetized so that no magnetizing field exists. There are two ways of demagnetizing a magnetic material. The first one includes the use of a decaying oscillating external magnetic field [194]. This enables reaching the origin of the M-H curve despite the hysteresis of the material and for any initial state of the material. This process is shown in the M-H curve of Fig. 4.4.

A clarification must be made at this point regarding the difference between the *remanence coercivity* and *intrinsic coercivity*. These two terms are different and should not be confused. The *intrinsic coercivity* is the point corresponding to a null magnetization of the material under a specific external magnetic field ($H = -H_{coer}^i, M = 0$). Indeed, the hysteretic behavior of the material would result in a non-null remaining magnetization when the external magnetic field is removed. The *remanence coercivity* is a theoretical state arduously reached precisely in practice, preventing a perfect demagnetization. Nevertheless, the remaining magnetization can be considered small enough in many applications, such as this one.

The second demagnetization method (see Fig. 4.5) involves the application of a negative exter-

nal magnetic field so as to reach the *remanence coercivity* [195] ($H = -H_{\text{coer}}^r, M = -M_{\text{coer}}^r$) of the material, leading to a demagnetized state when the external field is removed. This method is preferred in this work because it requires a single demagnetization pulse implemented with a simple electronic design. If partial magnetization of the valve is desired (tunability of the sustained pressure as later explained), the first option should be considered as it is more robust and independent of the magnetization state.

4.2 Analytical and numerical modeling

In this section, the EPM MR valve is modeled analytically and numerically. The goal of this analysis is to determine analytically the amplitude of the current pulse that is applied on the coil for the actions of magnetization and demagnetization. Moreover, the analytical model estimates the maximum pressure that the valve can sustain when it is closed, which means no flow rate through the gap. The different non-linearity phenomena taking place in the valve lead to the following assumptions before continuing with the rest of the modeling process:

1. The iron core is considered as a perfect magnetic conductor;
2. The leakage fluxes are ignored;
3. The flux lines are considered normal to the surfaces when exiting a material;
4. The MR fluid flow is laminar and the distribution of particles in the carrier medium is considered homogeneous.

The simplified version of Ampere's law is deduced considering the previously mentioned assumptions:

$$H_{\text{rod}} \cdot h_c + 2H_g \cdot g = N \cdot I \quad (4.2)$$

with N the number of turns of the coil, I the electric current flowing through it, H_{rod} , H_g the magnetic field in the inner rod, and in the gap (i.e. MR fluid channel) respectively, h_c and g the height of the inner rod, and the width of the gap respectively. The iron is considered saturated in this case.

The conservation of magnetic flux gives the relationship between the two magnetic flux densities B_{rod} , and B_g in the inner rod and the channel respectively, taking into account the flux fringes:

$$B_{\text{rod}} \cdot \pi r_c^2 = B_g \cdot 2\pi r_g \cdot (h + 2 \cdot k_f h_{fr}) \quad (4.3)$$

with r_c , the radius of the inner rod and r_g the mean radius of the MR fluid channel (see Fig. 4.2). $h + 2 \cdot k_f h_{fr}$ is the length of the active region. It includes the length of the gap h and the flux fringes h_{fr} (see Fig. 4.2). This model takes into account the flux fringes, which are normally neglected, with $k_f = 1$. This is due to the magnetic simulation of the conventional MR valve presented in the previous chapter.

The relationship between the flux density B and the magnetic field H in the materials (AlNiCo-5 and MR fluid) is non-linear due to saturation effects. This relationship is extracted with polynomial interpolation of the positive B-H curve of the MR fluid in Eq. 3.4. Thus, the relationships between the magnetic field and magnetic flux density in the gap are:

$$B_g = B_{\text{MRF}}(H_g) \quad (4.4)$$

$$H_g = B_{\text{MRF}}^{-1}(B_g) \quad (4.5)$$

The magnetization and demagnetization parts of the B-H curve of the AlNiCo-5 rod, which were obtained experimentally by the German company *Magnet-Physik* (shown in Fig. 4.4 and Fig. 4.5), have different exponential fitting curves. The latter are shown bellow, using the coefficients of Table 4.1:

$$B_{\text{rod_mag}} = \alpha_1 \cdot e^{\beta_1 \cdot H_{\text{rod}}} + \gamma_1 \cdot e^{\delta_1 \cdot H_{\text{rod}}} \quad (4.6)$$

$$B_{\text{rod_demag}} = \alpha_2 \cdot e^{\beta_2 \cdot H_{\text{rod}}} + \gamma_2 \cdot e^{\delta_2 \cdot H_{\text{rod}}} \quad (4.7)$$

α_1	1.498	α_2	1.30
β_1	$1.475 \cdot 10^{-7}$	β_2	$7.71 \cdot 10^{-7}$
γ_1	-44.56	γ_2	$-5.71 \cdot 10^{-2}$
δ_1	$-9.01 \cdot 10^{-4}$	δ_2	$-6.20 \cdot 10^{-5}$

Table 4.1: Curve fitting coefficients.

The combination of Eq. 4.2, 4.3, and 3.4 leads to the expression of the current flowing through the coil as a function of the magnetic field and magnetic flux density in the magnetic rod $I = I(H_{\text{rod}}, B_{\text{rod}})$:

$$I = \frac{H_{\text{rod}} h_c}{N} + \frac{2g}{N} \cdot B_{\text{MRF}}^{-1} \left(\frac{r_c^2 \cdot B_{\text{rod}}}{2 \cdot r_g \cdot (h + 2 \cdot h_{fr})} \right) \quad (4.8)$$

$I_{\text{mag}} = I(H_{\text{sat}}, B_{\text{sat}})$ is the current that fully magnetizes the AlNiCo-5 rod creating a magnetic field that reaches the saturation point ($B_{\text{sat}} = M_{\text{sat}} + \mu_0 H_{\text{sat}}$) and can be derived analytically by the previous equations. As mentioned above, the current that corresponds to the remanence coercivity of the material cannot be derived analytically. However, the analytical equation of the current used to reach the intrinsic coercivity $I_{\text{coer}}^i = I(-H_{\text{coer}}^i, -\mu_0 H_{\text{coer}}^i)$ can be provided. The calculation of this current can be used as an upper bound for the demagnetization current with the demagnetization method of Fig 4.5 (demagnetization with a single pulse). In the following section, the estimation of the demagnetization current will be done experimentally.

The pressure difference developed between the two sides of the EPM MR valve consists of the yield-stress dependent pressure difference component and the viscosity dependent component as follows (see Eq. 3.1):

$$\Delta P = \Delta P_\tau + \Delta P_\eta = \frac{c \cdot \tau(H_{\text{MRF}})2h}{g} + \frac{6Q\eta 2h_c}{\pi(r_g - \frac{g}{2})g^3} \quad (4.9)$$

In this case the flux fringes are not taken into account.

When the valve is closed, $\Delta P_\tau \gg \Delta P_\eta$ and $Q = 0$ (no flow rate condition). Thus, the maximum pressure difference sustained by the valve is approximated by $\Delta P_{\text{max}} \approx \Delta P_\tau$, and c lies close to the value 3.

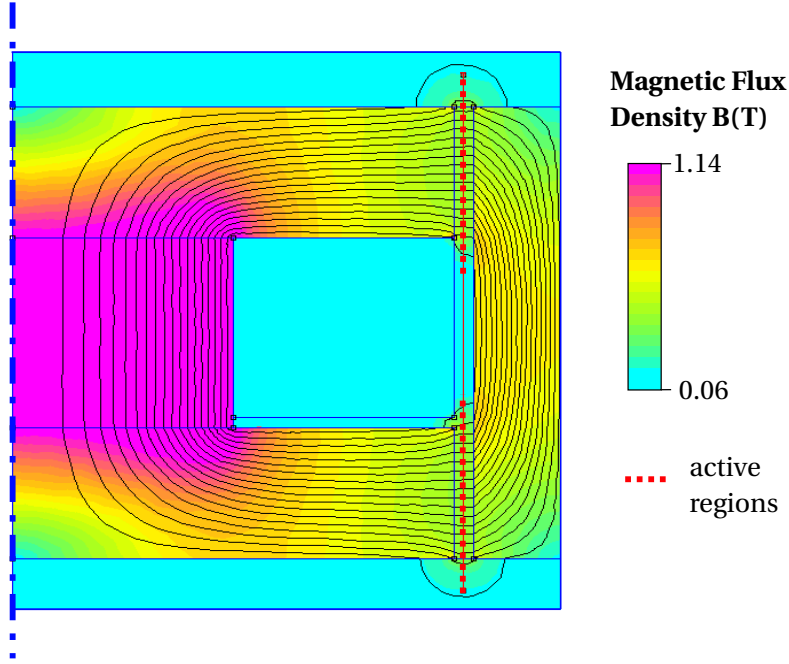


Figure 4.6: A 2-D axisymmetric magnetic simulation of the EPM MR fluid valve. The lines and colorbar represent the magnetic flux density B . (Copyright: 2377-3766 © 2023 IEEE)

The testing condition of the EPM MR device, which will be explained in the next section, includes the use of large quantities of MR fluid at the two sides of the valve. As a result, the magnetic flux fringes in this part of the fluid are not negligible and must be taken into account in the modeling process. The fringing phenomenon affects the flux density in the gap, thus its simulation is necessary.

Fig. 4.6 depicts a 2-D axis-symmetric magneto-static simulation of the EPM MR valve, which was performed using Software FEMM 4.2. The simulation was performed for the case when the AlNiCo-5 rod is fully magnetized and there is no current flowing through the coil. The dimensions of the valve are shown in column 'Optimal' of Table 3.3. The B-H characteristic curve of the AlNiCo-5 was imported into the software. Fig. 4.7 shows the distribution of magnetic field B magnitude along the length of the gap, in the axis of symmetry of the gap. Using the simulation results, which take into account the flux fringes, and Eq. 3.13 with $k_f = 1$, ΔP_{max} is estimated. From the above, we can conclude that the magnetic flux fringing

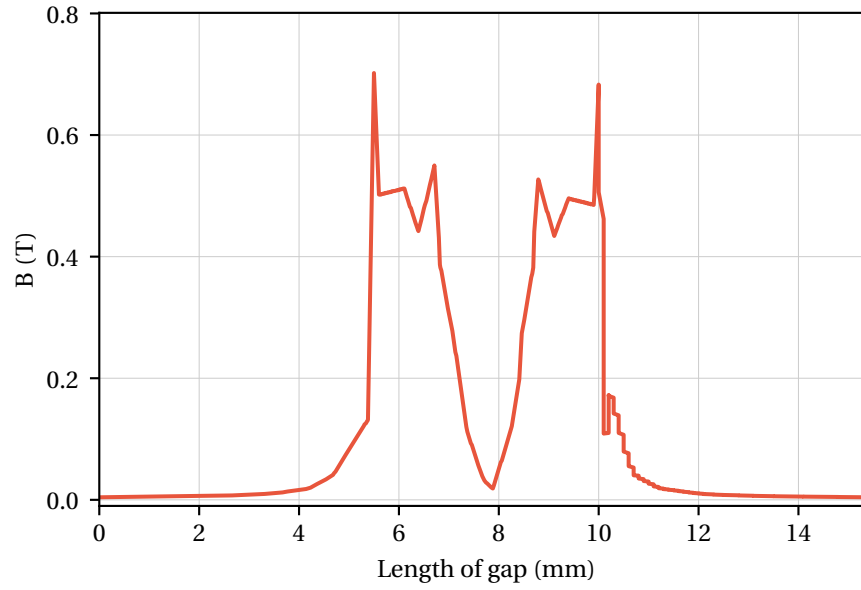


Figure 4.7: Distribution of B in the length of the gap.

phenomenon, which is usually undesirable in magnetic devices, is leading to the increase of the sustained pressure in the EPM MR valve, as in the conventional MR valve, improving the capabilities of the device.

4.3 Experimental validation

The goal of this section is to prove that the EPM MR valve has the same functionality as the conventional MR valve but with a drastic reduction of power consumption from hundreds of mW to 0 mW in the steady state. As a result, the experimental steps followed during the validation process of the EPM MR valve are firstly presented; secondly, the experimental setup used for this purpose is shown and its working principle is described; and, finally, the experimental results are demonstrated and discussed.

4.3.1 Working principle of the experimental setup

Fig. 4.8(a) depicts the prototype of the EPM MR valve with the different parts, i.e. the ferromagnetic inner and outer part, the coil placed around the magnet, as well as the valve disassembled, where the AlNiCo-5 magnet is visible. Fig. 4.8(b) is a picture of the setup used for the experiments. The same setup as the one used for testing the conventional MR valve is used for the validation of the EPM MR valve as well. In this case, too, both chambers are filled with MR fluid (MRF-132DG by Lord Corp.), while one of the two remains open in atmospheric pressure. The pneumatic piston is reducing the volume of the second, closed chamber. The

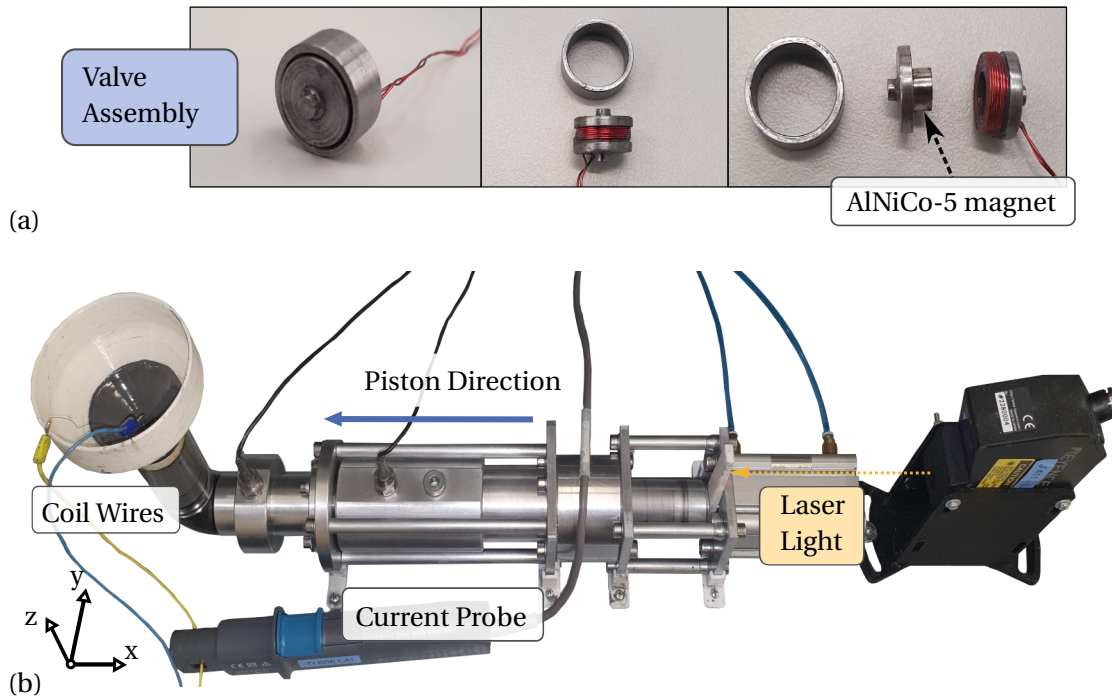


Figure 4.8: (a) Prototype of the EPM MR valve and valve disassembled with the AlNiCo-5 rod in the inner part. (b) Setup to simulate fluidic flow and validate experimentally the functionality of the EPM MR valve. (Copyright: 2377-3766 © 2023 IEEE)

volume reduction leads again to the increase of pressure in the closed chamber when the valve is closed. The pressure in both chambers as well as the movement of the piston are recorded with suitable pressure and laser displacement sensors.

A current pulse applied to the coil of the valve is responsible for both closing and opening the valve, with magnetization and demagnetization of the MR fluid respectively. The two actions are conducted with a positive and a negative current pulse of lower amplitude respectively. A dedicated electronic system is used to create these current pulses. It includes a full-bridge arrangement of MOSFETs, in order to enable the current supply in two directions (Fig. 4.9). The MOSFETs allow faster switching (N-channel type), with maximum voltage and current ratings of 80V and 80A respectively. The two gate drivers are used to drive the gates of the transistors, accelerating the switching speed. A microcontroller is driving the gate drivers. Fig. 4.9 shows the schematics of the control electronics described above.

4.3.2 Results

The first step in the validation process of our model is to compare the analytical and numerical results. To this purpose, we use the values of current at which we achieve experimentally magnetization of the valve. Fig. 4.10 shows the M-H and B-H characteristic curves. The company *Magnet-Physik* obtained these curves using the magnetic rod of our prototype in

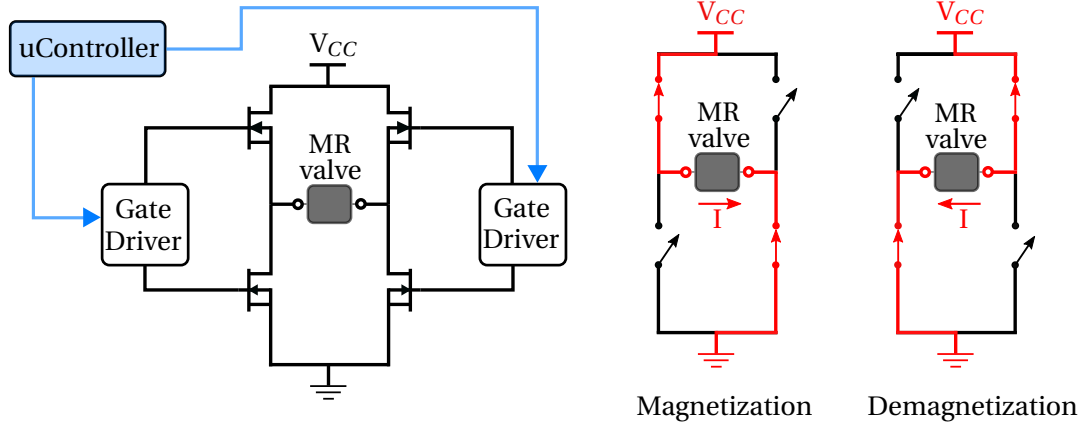


Figure 4.9: Schematics of control electronics for the EPM MR valve.

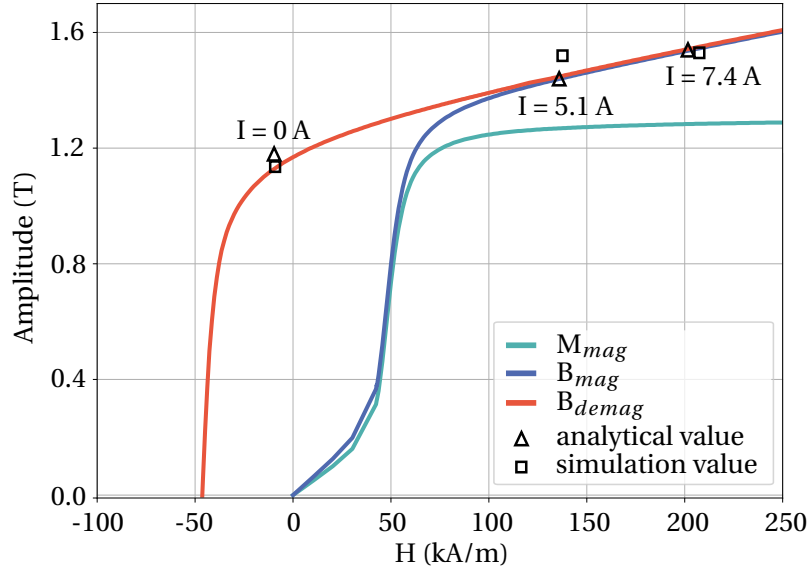


Figure 4.10: The magnetization and demagnetization characteristics (M - H and B - H), and the B_{rod} and H_{rod} for each current value obtained analytically and numerically. (Copyright: 2377-3766 © 2023 IEEE)

multiple cycles of magnetization and demagnetization. More specifically, the magnetization M over H is represented with the light blue curve, the magnetic flux density B over H during the magnetization with the dark blue curve, and finally, the curve obtained during demagnetization with the red-color line. The first two curves plotted together represent the AlNiCo-5 rod in the process of magnetization, from a condition where it is fully demagnetized to its saturation. Magnetization is taking place with the use of an external magnetic field. The third curve represents the demagnetization of the AlNiCo-5 rod. There the initial condition of the rod is a fully magnetized state, and the final condition is a fully demagnetized magnet ($B = 0$). Eq. 4.8 is used to estimate the current needed to reach the saturation point. This current is estimated as $I_{mag} = 7.4$ A. From Fig. 4.10 it is evident that even a lower magnetization current,

close to 5.1 A, will lead to a point close to saturation B_{sat} in the B-H curve. As a result, we use the minimum value for the magnetization current that reaches very close to saturation and is 5.1 A. Fig. 4.10 also shows the marked points that correspond to the current values obtained analytically and numerically from the FEA simulation (Fig. 4.6). The simulation is performed for the different fixed magnetization current values (0 A, 5.1 A, 7.4 A).

The next step includes the experimental estimation of the magnetization and demagnetization current. Fig. 4.11 depicts the voltage across the coil and its measured current during magnetization and demagnetization of the rod. A separate pulse of current is used both for the magnetization and the demagnetization. More specifically, the current for magnetizing the EPM and closing the valve is 5.1 A and is reached within $t_{\text{mag}} = 0.5$ ms. This current value is used experimentally instead of 7.4. With 5.1 A, as explained previously, a point very close to saturation is reached.

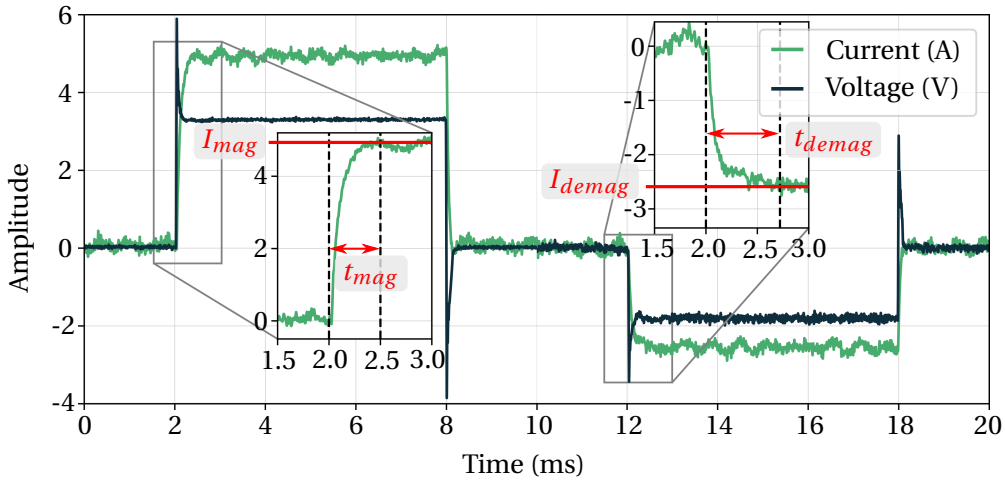


Figure 4.11: Voltage and current pulse over the valve's coil. The positive current corresponds to the magnetization of the AlNiCo-5 rod and the negative to the demagnetization. (Copyright: 2377-3766 © 2023 IEEE)

As explained in the previous section, the demagnetization current leading to the remanence coercivity point cannot be defined analytically with the previous model. Its experimental definition leads to the value of $I_{\text{demag}} = -2.5$ A. The upper bound of this current determined analytically is -1.8 A, which satisfies our experimental result. The demagnetization current is chosen during the experimental process, with respect to the state of the valve. More specifically, the valve got fully demagnetized with the current pulse, and pressure was applied with the pneumatic piston to the closed MR valve, observing no displacement when the valve is closed. Then the demagnetization pulse was applied. For the value of -2.5 A the valve opens and cannot sustain anymore the applied load. Perfect demagnetization cannot be guaranteed with this method since a small magnetization can still exist in the rod. However, it is not strong enough to block the MR fluid flow through the valve. In this application, it is not critical to achieve complete demagnetization of the valve. Fig. 4.11 shows that the demagnetizing current is obtained within $t_{\text{demag}} = 0.72$ ms, after the current starts flowing in the coil. The

magnetization and demagnetization time acquired experimentally can be used to define the switching frequency of the valve, which is 0.85 kHz for 50% and 1.25 kHz for 90% duty cycle. These values are high considering different types of fast-switching valves, where switching frequencies are lower than 1 kHz [196, 197]. According to these values, the energy consumption of the valve is 15.3 mJ for activation and 6 mJ for deactivation.

Obtaining the magnetization and demagnetization time is followed by the experimental validation of the functionality of the EPM MR valve. This is achieved with two experimental scenarios. In the first scenario, the comparison between the two states of the valve, the open and the closed, is studied. In the closed state of the valve, an attempt to magnetize the AlNiCo-5 rod with different current values of 1.8 A, 3.5 A, and 5.1 A is taking place. For each current value, pressure is applied in the closed chamber, inducing the movement of the pneumatic piston. The gradual increase of pressure is achieved with the use of the manual manometer. The maximum limit of the air supply system is close to 1000 kPa, and, consequently, values of pressure higher than this limit cannot be reached. The displacement of the piston, as well as the pressure difference between the two sides of the valve (i.e. between chambers 1 and 2), are measured while the piston is moving towards the valve.

In Fig. 4.12, the blue plot represents the displacement over pressure difference when the AlNiCo-5 material is magnetized with 5.1 A. An initial abrupt increase of displacement of maximum $\Delta x = 10$ mm is visible. This displacement remains constant with the increase of pressure difference. This abrupt increase of displacement at the beginning of the experiment can be justified as follows: during the filling of the chambers, some air is trapped in them. Since the air is compressible, the application of pressure results, firstly, in its compression. After that, the valve's closed state is confirmed by the absence of displacement. In this experiment, the maximum pressure difference measured is 1010 kPa. Thus, it can be claimed that the valve can sustain at least this pressure value. Larger pressures could not be tested since the compressed air supply for our setup has a limit of 1000 kPa. The value derived from the analytical and simulation results is 949 kPa.

The current EPM MR valve offers the possibility of tuning the pressure it can sustain, as well as of regulating the flow rate if the valve is not fully closed or fully open. The valve rod is partially magnetized in this experiment with current values lower than 5.1 A, reaching a magnetization point lower than M_{rem} when the current supply stops. As a result, the magnetic field in the active regions of the valve is lower and subsequently, the sustained pressure is also lower. Fig. 4.12 depicts the experimental results of pressure difference over piston displacement for the magnetizing currents of 1.8 A and 3.5 A. In the first case, we set the manometer manually to a pressure value of 100 kPa. The figure shows that at 75 kPa the displacement starts already increasing until the moment when it reaches the stroke limit of 50 mm. In the second case, at first, there exists abrupt displacement due to the trapped air, and once the air is fully compressed, there happens again an increase in piston displacement. This happens, though, at a higher pressure of 180 kPa. The above results show the ability of the valve to be tuned with regard to the pressure it can sustain as well as to the flow rate.

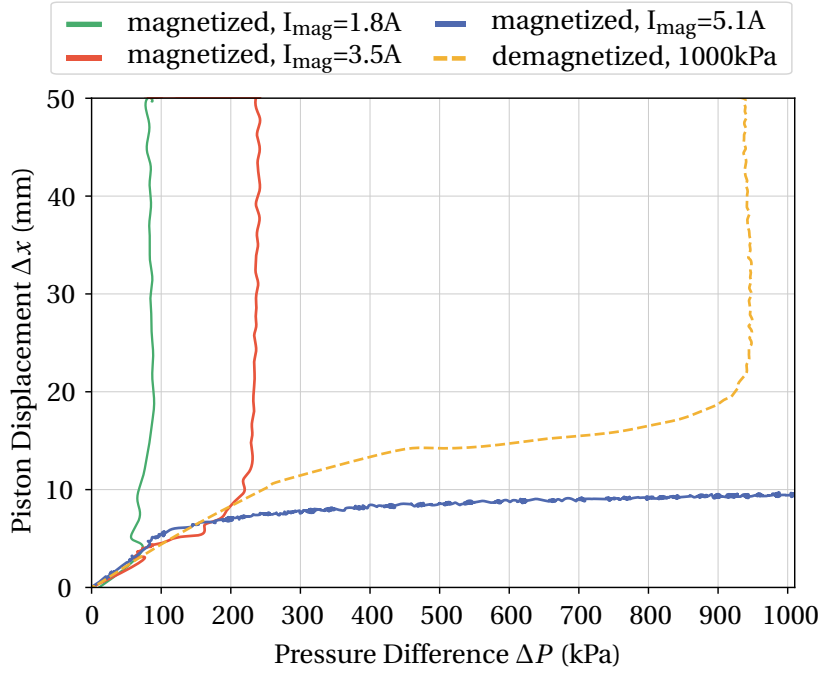


Figure 4.12: Piston displacement over the pressure difference between the two chambers of the setup. The valve's state is either open or closed but with different magnetization currents. (Copyright: 2377-3766 © 2023 IEEE)

When the valve is open, the air pressure in the pneumatic piston is again set manually to 1000 kPa. The piston displacement increases until $\Delta x = 15$ mm and the pressure in chamber 2 reaches 993 kPa. After that, the MR fluid starts flowing with a constant flow rate in the valve's gap. This leads to an increase in the piston displacement while the pressure difference remains constant. The piston's stroke is the one defining the range of the piston displacement axis in Fig. 4.12. Fig. 4.13 shows the maximum sustained pressure difference ΔP for the different magnetization current values, which increases non-linearly.

Finally, the transition of the valve from the closed to the open state is studied in the second experimental scenario. In this case, the valve is initially fully magnetized with a current pulse of 5.1 A amplitude. The experimental results are presented in Fig. 4.14, which is a common plot of the piston displacement Δx and the pressure difference ΔP over time for 1000 kPa of pressure. The piston's movement starts at $t = 2$ s, pressing the fluid in the closed chamber. The application of pressure continues for the rest of the experimental trial. The valve remains closed until $t = 3$ s, when the coil of the valve is supplied with the demagnetization pulse and the valve opens. From Fig. 4.14, it is clear that, besides the initial abrupt displacement related to the air compression, there is no further piston displacement. It can, thus, be deduced that the valve is closed. At $t = 3$ s, when the valve is open again, the displacement Δx presents a linear increase, confirming the valve opening. The piston stroke limit of 50 mm is reached within one second, considering a constant pressure difference of 1000 kPa.

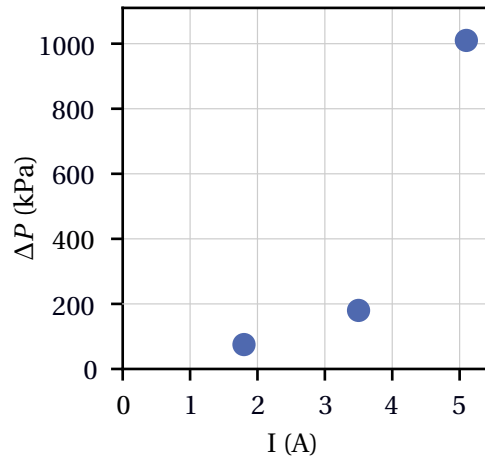


Figure 4.13: Maximum sustained pressure over magnetization current.

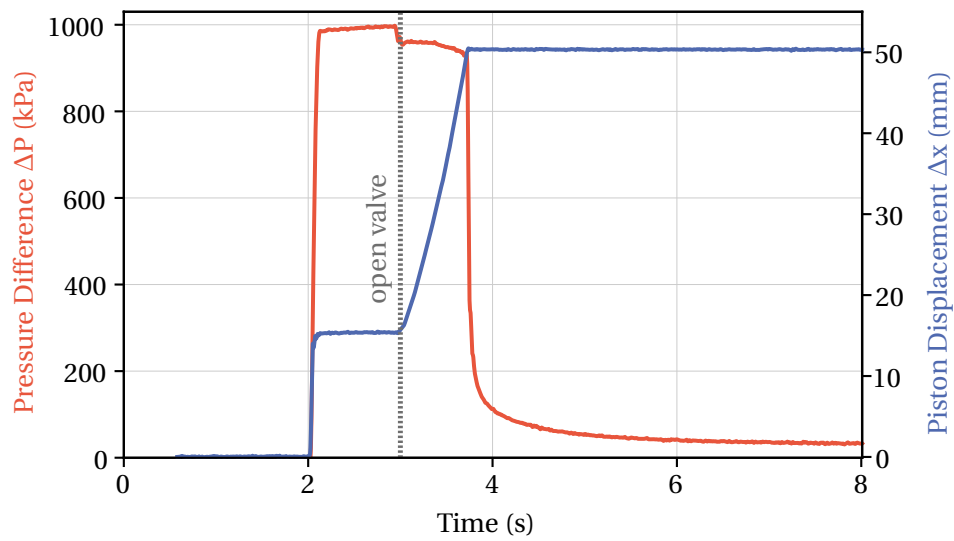


Figure 4.14: Pressure difference ΔP and piston displacement Δx over time in an EPM MR valve. The valve is initially closed. At $t = 3s$ the demagnetization is taking place and the valve opens, allowing fluid flow and piston displacement. (Copyright: 2377-3766 © 2023 IEEE)

4.4 Conclusions and main contributions

Conventional MR valves are attractive solutions for several applications, such as automotive or medical. However, their activation with continuous current leads to high power consumption compared to other types of valves. This limits the range of potential applications, hindering their use in mobile or wearable applications. This chapter summarizes the research on the

design, modeling, and experimental validation of a miniaturized MR valve that uses an EPM in its core. The main contributions are:

- Presenting the design of a miniaturized MR valve employing an EPM;
- Performing the analytical and numerical modeling of this EPM-based MR valve to estimate the magnetization and demagnetization current, as well as, the maximum sustained pressure when in the closed state;
- Validating the functionality of the valve in a fluidic flow environment.

This technology paves the way for facilitating the use of MR fluids in a wide range of applications, where low volume, high pressure, and low power consumption are critical parameters.

Publications related to this chapter:

- S. L. Ntella, A. Thabuis, B. Tiwari, K. Jeanmonod, C. Koechli, Y. Perriard, "Highly Efficient Miniaturized Magnetorheological Valves Using Electropermanent Magnets," in *IEEE Robotics and Automation Letters*, 2023. Copyright: 2377-3766 © 2023 IEEE
- S. L. Ntella, A. Thabuis, B. Tiwari, C. Koechli, K. Jeanmonod, Y. Perriard, Z. Pataky, "Miniaturized magnetorheological valve using electropermanent magnets," patent submitted in December 2022, EP Patent Application Nr 22212573.4.

5 Self-Sensing Magnetorheological Valve

In this chapter, we present the pressure self-sensing phenomenon in miniaturized MR valves. The design and working principle of the valve that can achieve self-sensing are presented, together with the analytical formulations that explain the phenomenon, as well as the experimental results that validate it. In addition, the self-sensing phenomenon is observed microscopically with the use of a specially designed and fabricated microfluidic device.

5.1 Introduction to self-sensing MR valves

MR valves in annular configuration powered by one coil have been studied with regard to their design and two-state functionality (open and closed valve). MR valves are being integrated with sensors and control systems to provide real-time feedback and better control. This includes using sensors to monitor fluid flow and pressure, and control algorithms to adjust the valve settings in response to changing conditions. In order to reduce the complexity created by the addition of external sensors, researchers have attempted the study of self-sensing MR valves.

The research interest of the existing studies centers mainly around the study of displacement and velocity self-sensing capabilities of MR valves in damper devices. The dampers are part of vibration systems where the displacement and velocity feedback is important for their control [136, 128, 133]. In these cases, the self-sensing is achieved with the addition of a second coil to the valve's conventional structure. The current applied to one of the two coils, the *exciting coil*, consists of a DC and an AC component. The second coil, the so-called *sensing coil*, facilitates the sensing functionality. The DC current on the exciting coil creates the MR effect and the blocking of the valve, while the AC current component is responsible for the alternating, self-induced voltages on the sensing coil. The induced voltages are related to the displacement and velocity of the piston of the structure. Although these devices present self-sensing capabilities concerning displacement and velocity, they have not been studied concerning pressure self-sensing. At the same time, the additional coils, as well as the need for an alternating current for the voltage induction increase the complexity, the size, and the

power consumption of the MR devices.

5.2 Pressure self-sensing miniaturized MR valve with two coils

In this section, we present the preliminary study of a miniaturized MR valve in an annular configuration based on [122] that can potentially act as a pressure sensor and fluid controller. The valve consists of two coils, and contrary to the existing self-sensing MR technologies, it is powered only by a DC current that creates both the magnetization of particles of the MR fluid and the voltage induction. The next sections present the design and working principle of this valve as well as the experimental results that demonstrate the correlation between the measured induced voltage and the pressure application.

5.2.1 Design and working principle

Fig. 5.1 depicts the structure of a miniaturized pressure self-sensing MR valve. The structure is identical to the annular valves presented in the previous chapters, except for the coil part, which consists of two coils instead of one in this case. The combination of the outer and inner ferromagnetic piece, around which the coils are wound, creates a gap and allows the MR fluid flow through it. The exciting coil, supplied by a DC current, facilitates the magnetic field excitation that leads to the particles' alignment across the magnetic poles, forming chain-like structures. The chain formation, which is reversible, leads to the increase of the viscosity of the fluid and the blocking of the valve and controlling the MR fluid flow.

The exciting coil plays the same role as in the conventional MR valves for the excitation of the

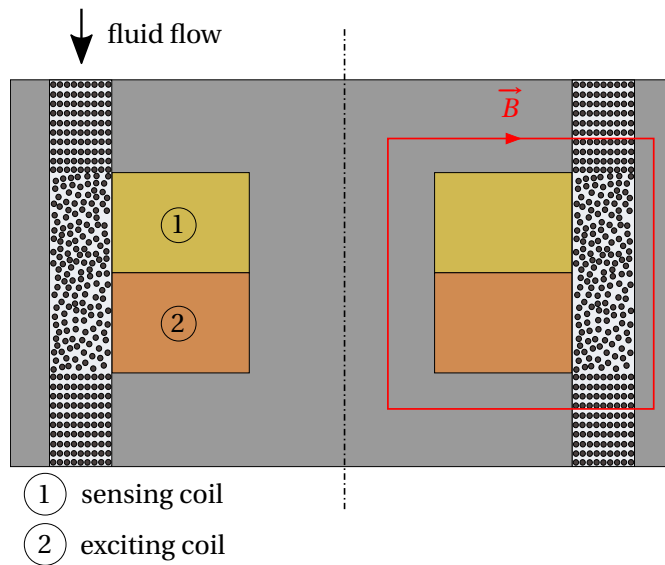


Figure 5.1: Structure of magnetorheological valve with two coils in a 2D cross-section plane. (Copyright: 978-1-6654-4139-1/21/\$31.00 © 2021 IEEE)

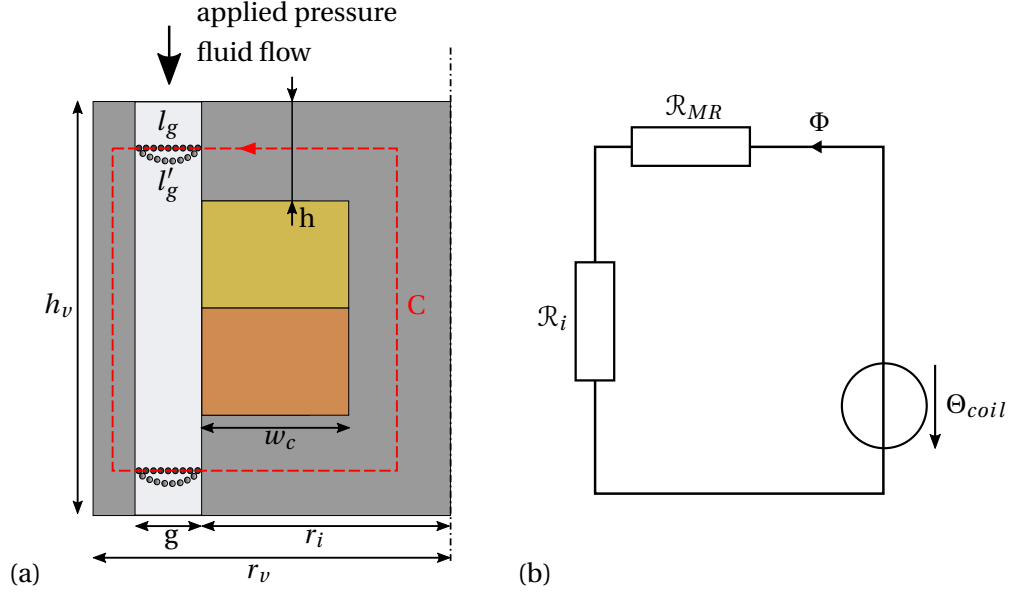


Figure 5.2: (a) The magnetic path in a 2-D axis-symmetric cross-section of MR valve, observing the elongation of chains with applied pressure (b) Magnetic circuit equivalent. (Copyright: 978-1-6654-4139-1/21/\$31.00 © 2021 IEEE)

magnetic field. The sensing coil facilitates the pressure self-sensing capabilities of the MR valve as follows. At low magnetic field values, the magnetic flux density B in the magnetic circuit of the valve is written as a function of the magnetic field H :

$$B = \mu_0 \mu_r H \quad (5.1)$$

where μ_0 and μ_r are the magnetic permeability of the free space and a specific material (MR fluid or iron) respectively. The variation of the magnetic field in the active regions of the valve leads to the variation of the fluid's yield stress τ_y , which controls the fluid resistance to flow. Between the points, where the fluid enters and exits the gap, if we assume a one-direction flow from the top to the bottom, the pressure drop explained in the previous chapters appears (Eq. 3.1).

An excitation current that is relatively low does not completely block the valve because the particles form loose bonds with each other. As a result of the loose bonding, the formed particle chains are weak and their shape can be modified in the presence of externally applied pressure. When the pressure is applied to the top part of the valve, as in Fig. 5.2(a), the chains of the MR fluid in the gap of initial length l_g tend to elongate to a larger length l'_g . The equivalent magnetic circuit of Fig. 5.2(a) is depicted in Fig. 5.2(b). \mathcal{R}_i represents the reluctance of the ferromagnetic part of the valve, while \mathcal{R}_{MR} represents the reluctance of the MR fluid in the active regions of the gap. Θ_{coil} is the Magnetomotive Force (MMF) of the coil and Φ is the flux created by the coil and flowing in the magnetic circuit, along the C loop (Fig. 5.2(a)). As a result,

Chapter 5. Self-Sensing Magnetorheological Valve

the length l_g is part of the magnetic circuit and when it is elongated due to the application of external pressure, changes in the magnetic circuit occur as well.

To study the way the applied pressure affects the chain-like structures, for the closed magnetic path C (5.2(a)) we have:

$$\Theta_{coil} = N_e \cdot I \quad (5.2)$$

where N_e is the number of turns of the exciting coil, and I is the current applied to the coil. If l_i is the total length of the iron, μ_0 the magnetic permeability of free space, μ_i the magnetic permeability of iron and S_i the cross-section of the iron, the reluctance \mathcal{R}_i of the iron is expressed as follows:

$$\mathcal{R}_i = \frac{1}{\mu_0 \mu_i 2\pi} \left(\int_0^{r_i} \left(\frac{2}{h} + \frac{1}{h_v - 2h} \right) \frac{1}{r} dr + \int_{r_i+g}^{r_v} \left(\frac{2}{h} + \frac{1}{h_v - 2h} \right) \frac{1}{r} dr \right) \quad (5.3)$$

The magnetic flux Φ_g in the gap is correlated to the length of the particle chains. Thus, the application of pressure on the chain-like structures can lead to the elongation of the chain and, as a result, to variation of the magnetic path of the circuit and the magnetic flux in the gap. Φ_g can also be expressed in correlation with the magnetic reluctance of the MR fluid \mathcal{R}_{MR} [141]:

$$\Phi_g = \frac{N_e \cdot I}{\mathcal{R}_{MR}} \quad (5.4)$$

$$\mathcal{R}_{MR} = \frac{\ln(1 + \frac{l_g}{r_i})}{\pi h \mu_0 \mu_{MR}} \quad (5.5)$$

where l_g is the chains length and μ_{MR} is the relative permeability of the MR fluid in the gap. Considering that $r_g \gg l_g$, the above equation is simplified as follows:

$$\mathcal{R}_{MR} = \frac{l_g}{\pi r_i h \mu_0 \mu_{MR}} \quad (5.6)$$

where l_g is the only variable-over-time parameter in the Eq. 5.6. The variation of magnetic flux in the gap leads to the appearance of an induced voltage:

$$\mathcal{E} = -N_s \cdot \frac{d\Phi}{dt} \quad (5.7)$$

The theoretical analysis can prove the existence of induced voltage on the sensing coil of the MR valve. If we transform Eq.(5.7), with P being the applied pressure on the MR fluid, we can

5.2 Pressure self-sensing miniaturized MR valve with two coils

Quantity	Value
h_v	10 mm
h	2.5 mm
g	0.5 mm
r_i	4.415 mm
r_v	5 mm
R_s	2.75 Ω
R_e	3.53 Ω
N_s	135.5
N_e	174.5
D_w	0.224 mm

Table 5.1: MR valve dimensions and coil characteristics.

involve the applied pressure in the analytical solution:

$$\mathcal{E} = -N_s \cdot \frac{d\Phi}{dP} \cdot \frac{dP}{dt} \quad (5.8)$$

The dimensions of the self-sensing MR valve are displayed in Table 5.1 and Fig. 5.2(a). Both the sensing and the exciting coil are wound around the inner magnetic core. The characteristics of the coils are also displayed in Table 5.1, where R_s and R_e , and N_s and N_e are the resistance and the number of turns of the sensing and exciting coil accordingly. D_w is the wire diameter, which is identical for both coils.

5.2.2 Experimental results

The goal of the experimental part is to validate the self-sensing properties of the MR valve with regard to pressure and correlate the applied pressure with the induced signal on the sensing coil. In order to achieve it, the real condition of pressure applied to the MR fluid and the

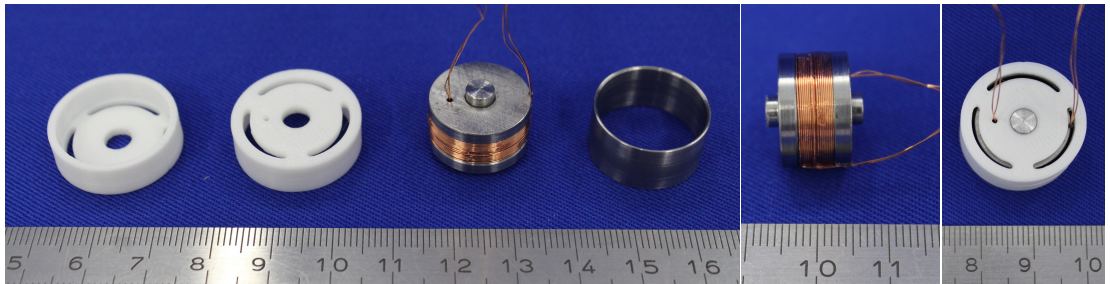


Figure 5.3: Prototype of the MR valve with two coils. The 3D-printed holder facilitates the alignment of the inner and outer ferromagnetic parts of the valve. (Copyright: 978-1-6654-4139-1/21/\$31.00 © 2021 IEEE)

creation of flow through the gap of the valve must be simulated. For this reason, the testbench of Fig. 3.10 of the previous chapter is used. The MR valve is placed between the two fluid chambers and the pneumatic piston applies pressure on the fluid that is placed in the closed chamber and creates a flow from the closed to the open chamber. A DC current is provided to the exciting coil, while the sensing coil is connected to an instrumentation amplifier with a gain of 500. Fig. 5.3 depicts the prototype of the fabricated valve, split in two pieces. The two coils are wound around the inner core one on top of the other. A 3D-printed holder facilitates the alignment of the ferromagnetic parts and the formation of the gap for the fluid flow.

As explained, the MR valve can function in two states: closed and open. In the closed state high pressures can be sustained since the particles of the fluid chains are linked with strong bonds. In this case, it is hard to create an elongation of the chains with the application of pressure. Nevertheless, the existence of a current is mandatory for voltage induction. Thus, the current value must be such that leads to the formation of chains that are not strong enough to avoid elongation and not weak enough to break. This current is defined through a series of measurements. Initially, the existence of induced voltage on the sensing coil is measured for the different combinations of current and pressure presented in Table 5.2. More specifically, the current ranges from 0.1 A to 0.7 A with a step of 0.1 A, and the pressure ranges from 100 kPa to 700 kPa with a step of 100 kPa.

For 0.7 A, the induced voltage appears only for very high pressures (≥ 600 kPa). The increase in current leads to the creation of stronger particle chains, which are difficult to be elongated with lower pressure. On the contrary, for a current of 0.1 A, an induced voltage appears on the sensing coil for all the different pressure values. Thus, $I=0.1$ A can be considered the "golden standard" for this valve geometry, to create weak particle chains and allow voltage induction. Also, taking into account that for currents higher than 0.3 A the measured pressure decreases drastically, additional measurements of the induced voltage are performed for the three first values of current (0.1 A, 0.2 A, and 0.3 A). The goal of these measurements is the study of the induced voltage and its correlation with the applied pressure.

The experimental session includes three measurements per combination of current and pressure and the average measurement per combination is calculated. In each measurement,

	0.1 A	0.2 A	0.3 A	0.4 A	0.5 A	0.6 A	0.7 A
100kPa	✓	-	-	-	-	-	-
200kPa	✓	✓	✓	-	-	-	-
300kPa	✓	✓	✓	✓	-	-	-
400kPa	✓	✓	✓	✓	-	-	-
500kPa	✓	✓	✓	✓	✓	✓	-
600kPa	✓	✓	✓	✓	✓	✓	✓
700kPa	✓	✓	✓	✓	✓	✓	✓

Table 5.2: Appearance of induced voltage for different combinations of current and pressure.

the same procedure is followed. Initially, the piston is activated and starts pressing the fluid in the closed chamber at $t = 0.1$ s and for $\Delta t = 0.1$ s, forcing the MR fluid to flow through the gap. At $t = 0.2$ s the piston stops pushing but its movement does not stop immediately. On the contrary, a small piston retraction is observed, due to a small amount of air that is trapped in the closed chamber of the testbench. The air is compressible and the forward movement of the piston leads to its compression. When the piston stops moving, the air decompresses and forces the piston back creating a tiny displacement.

Fig. 5.4 shows the induced voltage measurements over time on the sensing coil when following the above procedure. For each measurement, when the piston starts the forward movement, two voltage spikes appear, one positive and one negative. The piston movement causes the chain elongation and, thus, the increase of the magnetic reluctance of the MR fluid in the gap. This is the reason behind the first spike. However, right after this phenomenon, the chain-like structures are reorganized in the gap space, to achieve a steady state. This leads to the subsequent decrease in reluctance and the second successive spike in the graph. Finally, when the piston is blocked at $t = 0.2$ s, the very small but abrupt backward movement of the piston caused by the compressed air increases again the chain length and creates a third voltage spike. In our case, this spike is disregarded, since the exact pressure applied due to the decompression of the air is not known, and the first part of the induced voltage signal is studied.

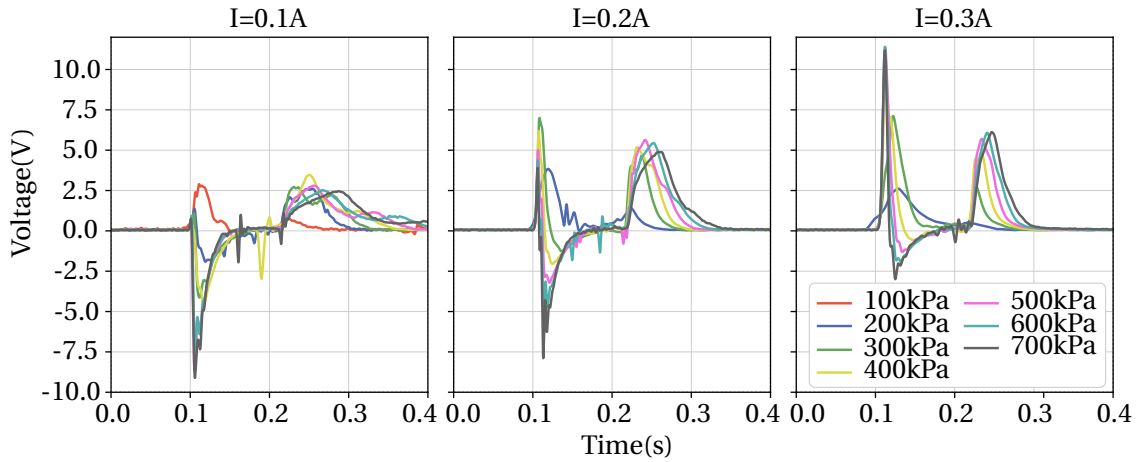


Figure 5.4: Experimental results of measurements using the MR valve and a piston pressure application of 0.1 s duration to elongate the chains: Voltage measurements for 0.1 A, 0.2 A, and 0.3 A exciting current. (Copyright: 978-1-6654-4139-1/21/\$31.00 © 2021 IEEE)

The interpretation of the experimental results is based on the second, negative peak, where a clear increase of the absolute value of voltage appears with the increase of pressure (Fig. 5.4). The positive voltage peaks are not proportional to the increase in pressure. On the one side, for lower currents, there is higher flow, weaker chain formation, and, consequently, lower positive voltage peaks since fewer chains break and elongate. On the other side, it is easier for the particles to return quickly in the steady state, so the negative peaks reach higher absolute

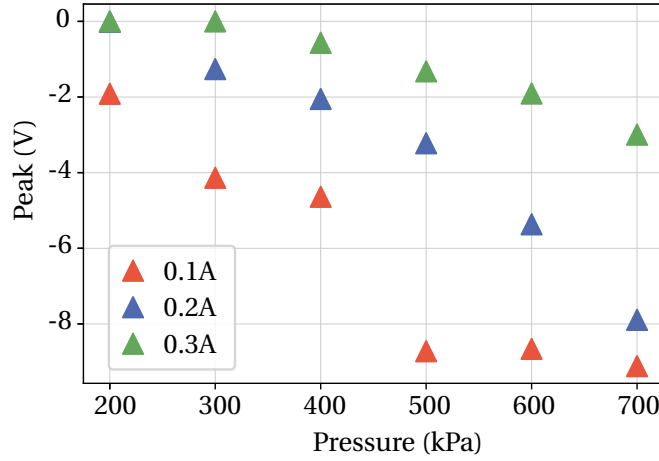


Figure 5.5: Minimum voltage peaks achieved when the pneumatic piston is activated at $t = 0.1$ s. (Copyright: 978-1-6654-4139-1/21/\$31.00 © 2021 IEEE)

values. Finally, the voltage minima of the second peak are depicted for each current value in Fig. 5.5. It is crucial to observe that the behavior of the voltage peaks is decreasing, especially in the case of 0.3 A. Consequently, depending on the system where the valve is intended to be used, the appropriate geometry and current must be chosen to achieve robust voltage and pressure measurements.

5.3 Microfluidic device for the self-sensing phenomenon

The previous section was dedicated to the study of the result that is brought about by the variation of the MR fluid properties in the magnetic circuit. This result is the induced voltage in this case (back Electromotive Force (EMF)). Nevertheless, there have been no studies on the microscopical behavior of the MR fluid while this variation is taking place. So far, researchers have investigated the association between the mechanical and rheological characteristics of MR fluids and the distribution in space of the ferromagnetic particles that compose them [198]. The method they used is the measurement of the MR fluid yield stress and the observations of the agglomerations formed by the MR fluid particles in correlation with the applied magnetic field. These studies concluded that the particle clusters have been formed due to the presence of an external magnetic field, leading to the increase of the MR fluid viscosity.

The most common technique used for the study of the MR fluid microscopical behavior is the bright field microscopy [199, 200]. Its use enabled the observation of the ferromagnetic particle clusters in the MR fluid, as well as the variation in their distribution with the change of the applied external magnetic field [201]. However, to use microscopy for the MR fluid observation, special devices had to be constructed that allow both the MR fluid flow and its study under the microscope lens. Different setups have been developed and used in this direction, with the majority of them using a Polydimethylsiloxane (PDMS) microchannel with a magnetic circuit surrounding it, to apply the magnetic field to the MR fluid [199, 200].

In this section, the design, working principle, and fabrication of a microfluidic device are presented. The device aims at simulating as accurately as possible the conditions in a slice of the gap of a self-sensing MR valve, as the one presented in the previous section. More specifically, the setup is able to reproduce the magnetic field creation and the electromagnetic induction phenomenon with the use of two coils, as well as the fluid flow in a micro-meter-sized channel and the pressure measurement. The device is fabricated with specifications of size and materials that allow, in parallel, the observation of the MR fluid under an optical microscope, while the magnetic and rheological phenomena are taking place. The use of a transparent microchannel and dark-field microscopy allows the study of the MR fluid [202]. Opting for this microscopy technique is confirmed by its advantage to enhance the spatial high-frequency details detection [203]. This is very important for the distinction of the particles. With the use of the microfluidic device, the links between the rheological, the magnetic properties of the MR fluid, and the geometrical distribution of the particles are demonstrated for the first time. This allows a deeper understanding of the electromagnetic induction phenomena appearing in the MR fluid that is placed in the self-sensing MR valve, enabling the future development of fully bi-functional MR devices as valves or as pressure sensors.

5.3.1 Self-sensing phenomenon in the microfluidic device

The study of the properties of the MR fluid microscopically is not possible in the closed environment of the cylindrical MR valve, where the gap is covered and no access to the microscope is allowed. To achieve access to the gap and to the MR fluid, a setup has been created that simulates the conditions of the MR fluid in a slice of the gap. This includes the flow

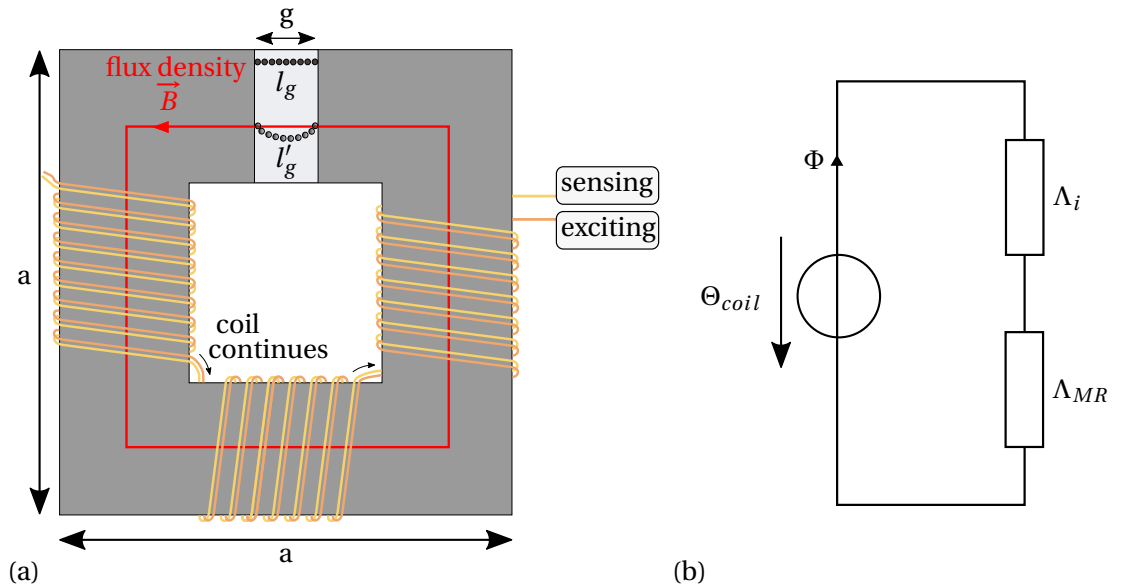


Figure 5.6: (a) Schematics of the microfluidic device; (b) Equivalent of the magnetic circuit of the microfluidic device.

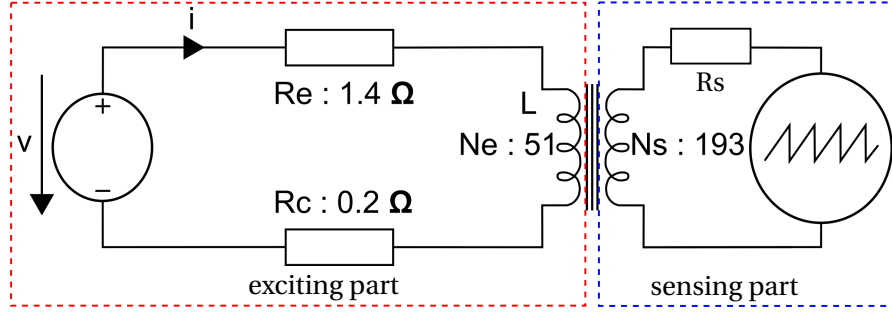


Figure 5.7: Electrical lumped element model of the microfluidic device with exciting and sensing coil. The red part on the left represents the exciting coil, and the blue part on the right represents the sensing coil. (Copyright: 978-1-6654-1308-4/22/\$31.00 © 2022 IEEE)

conditions of the MR fluid, as well as the influence of the external magnetic field on the fluid, and the measurement of pressure drop in the channel. The schematics of this setup are shown in Fig. 5.6(a). The setup is in the form of a square loop in order to create a magnetic circuit. It consists of two main parts. The gap where the MR fluid is inserted and the ferromagnetic material that closes the magnetic path around the gap. The microscope's viewpoint is above the MR fluid channel. The externally applied magnetic field is created with the use of the exciting coil, and the induced voltage is measured on the second coil, the sensing coil.

The equivalent magnetic circuit of the setup's schematics is depicted in Fig. 5.6(b). In these schematics, instead of reluctances, the permeances of the different parts of the magnetic circuit are used. This choice facilitates the development of equations in the next paragraphs. The exciting coil is supplied with a DC current, creating the MMF Θ_{coil} . The latter leads to the creation of magnetic flux Φ flowing in the magnetic circuit formed by the gap and the ferromagnetic material. The magnetic field excitation results in the formation of chain-like structures in the gap, consisting of MR fluid particles arranged in parallel with the lines of the field. This arrangement is reversible and is fully removed when the magnetic field is removed. The application of pressure perpendicularly to the arrangement of particles results in a variation of the properties of the magnetic circuit and creates the self-sensing phenomenon. More specifically, for a constant Θ_{coil} created by the current in the exciting coil, the application of pressure leads to the elongation of the particle chains from a length l_g to l'_g . Consequently, the MR fluid reluctance Λ_{MR} varies as well and changes the circuit flux Φ , inducing a voltage on the sensing coil.

Fig. 5.7 depicts the electrical lumped element model of the microfluidic device. The left part of the circuit consists of the DC power source (V , I) connected to the exciting coil. R_c and R_e are the resistance of the circuit and the exciting coil respectively. If Λ is the permeance of the magnetic circuit, then the corresponding inductance L can be written as $L = N_e^2 \Lambda$. The right side of the circuit is the sensing part and is only represented by the sensing coil and the measurement device connected to it. In our case, an oscilloscope is used to measure the induced voltage after amplifying the initial mV-range signal with an amplifier of gain of 10'000.

5.3 Microfluidic device for the self-sensing phenomenon

If Ψ_e and Ψ_s are the linkage fluxes in the exciting and the sensing coil respectively, the electrical equations for the exciting and sensing circuits are given below:

$$V = (R_c + R_e) \cdot I + \frac{d\Psi_e}{dt} = (R_c + R_e) \cdot I + \frac{d(L \cdot I)}{dt} \quad (5.9)$$

$$V_i = \frac{d\Psi_s}{dt} = N_s \frac{d\Phi}{dt} \quad (5.10)$$

As explained, Λ_{MR} is not constant, as the magnetic properties of the MR fluid are not constant when external pressure is applied or when the flow rate changes. This leads to the calculation of a non-constant relative permeability of the MR fluid μ_{MR} according to the following equations:

$$\Lambda_i = \mu_0 \mu_i \frac{S_i}{l_i} \quad (5.11)$$

$$\Lambda_{MR} = \mu_0 \mu_{MR} \frac{S_i}{g} \quad (5.12)$$

$$\Lambda = \left(\frac{1}{\Lambda_i} + \frac{1}{\Lambda_{MR}} \right)^{-1} = \frac{\Lambda_i \Lambda_{MR}}{\Lambda_i + \Lambda_{MR}} \quad (5.13)$$

$$\Phi = \Theta_{coil} \cdot \Lambda = N_e \cdot I \cdot \Lambda \quad (5.14)$$

where Λ_i is the magnetic permeance of the ferromagnetic part, S_i is the cross-section of the ferromagnetic core and is equal to $w \cdot h$ (h is the thickness of the ferromagnetic core and w is the width of the magnetic path), and l_i is the length of the magnetic field path in the ferromagnetic core and is equal to $4(a - w) - g$. The ferromagnetic material is considered saturated. Therefore, the induced voltage V_i on the sensing coil is calculated using the equations 5.10, 5.13, and 5.14 and for a constant current I , as follows:

$$\frac{d\Lambda}{dt} = \frac{\Lambda_i^2}{(\Lambda_i + \Lambda_{MR})^2} \cdot \frac{d\Lambda_{MR}}{dt} \quad (5.15)$$

$$V_i = N_s \frac{d\Phi}{dt} = N_s N_e I \cdot \frac{\Lambda_i^2}{(\Lambda_i + \Lambda_{MR})^2} \cdot \frac{d\Lambda_{MR}}{dt} \quad (5.16)$$

$$V_i = N_s N_e I \cdot \frac{\Lambda_i^2}{(\Lambda_i + \Lambda_{MR})^2} \cdot \mu_0 \frac{S_i}{g} \cdot \frac{d\mu_{MR}}{dt} \quad (5.17)$$

Moreover, the induced voltage can be used for the calculation of the variation of the magnetic permeability of the MR fluid in the gap $\Delta\mu_{MR}$ when it is provoked by external phenomena, such as the application of pressure. Integrating V_i from the time t_0 to t_1 gives $\Delta\mu_{MR}$ as follows:

$$\int_{t_0}^{t_1} V_i dt = N_s N_e I \cdot \frac{\Lambda_i^2}{(\Lambda_i + \Lambda_{MR})^2} \cdot \mu_0 \frac{S_i}{g} \cdot \Delta\mu_{MR} \quad (5.18)$$

In order to approximate the relative permeability μ_{MR} of the diluted MR fluid used in the measurements, the Maxwell-Garnett rule [204] is used:

$$\mu_{MR} = \mu_m \frac{\mu_p(1 + 2v_p) - \mu_m(2v_p - 2)}{\mu_m(2 + v_p) + \mu_p(1 - v_p)} \quad (5.19)$$

where μ_m is the relative permeability of the medium, which is silicon oil in the case of MRF-132DG and is equal to 1, μ_p is the relative permeability of the ferromagnetic particles ($\mu_p = \mu_i$), and v_p is the volume on volume ratio of the particles, which is 2% in this case. The particles must be adequately dispersed in the carrier medium in order for the Maxwell-Garnett rule to be used. However, this is not valid in the case where an external magnetic field is applied and the particles form chain-like clusters. It is valid, though, in the case when the particle chains created by the magnetic field break due to high applied pressure.

5.3.2 Microfluidic device fabrication

Microfluidics is a rapidly growing field, in which tiny volumes of fluids are manipulated and analyzed in micro-scale devices. Microfluidic devices are historically used in biological assays to study the behavior of cells, proteins, and other biomolecules [205]. In our case, the proposed microfluidic device facilitates the reconstruction of a micro-meter-sized channel as a slice of the gap of a miniaturized MR valve. This channel allows primarily the MR fluid observations under the microscope. The device fabrication consists of the following parts, shown in Fig. 5.8

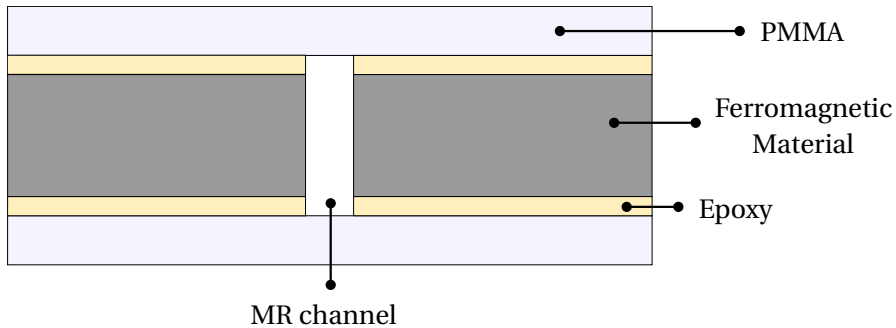


Figure 5.8: Cut view of the microfluidic device with the different fabrication layers. (Copyright: 978-1-6654-1308-4/22/\$31.00 © 2022 IEEE)

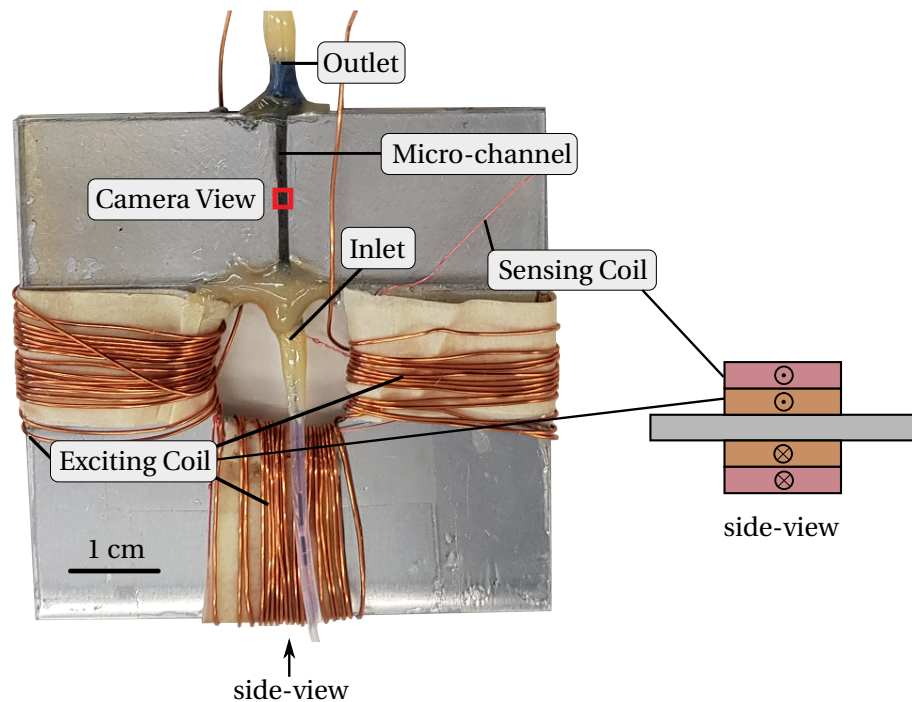


Figure 5.9: Device with one exciting coil, one sensing coil, and a microchannel for MR fluid flow. Each coil is wound around the sheet in three parts, starting from the left and continuing to the bottom and right. The two coils are layered one on top of the other as in the side view. (Copyright: 978-1-6654-1308-4/22/\$31.00 © 2022 IEEE)

as well:

- A ferromagnetic sheet is cut with the electrical discharge machining (EDM) technique to obtain the desired shape without destroying the borders of the ferromagnetic material;
- Two Polymethyl Methacrylate (PMMA) plates are glued on the top and bottom of the ferromagnetic material with epoxy glue. PMMA is used because it is a transparent material and leaves the gap visible under the microscope lens;
- The microchannel formed by the ferromagnetic material and the PMMA is connected to a fluidic circuit with the use of Mini Luer pipette adapters, which are glued onto microfluidic pipes. The pipes are placed at the inlet and outlet of the gap and facilitate the MR fluid flow in it;
- A 250 μl syringe is used to pressurize the fluid and create fluid flow;
- A pressure sensor MS583730BA01-50 is positioned after the syringe to measure the applied pressure.

Fig. 5.9 depicts the prototype of the microfluidic device. The fluid inlet and outlet are facilitated by the microfluidic tubes while a sensing and an exciting coil are wound around the

ferromagnetic material. The device can be placed in this form under the microscope, and the camera can record the MR fluid in the middle of the gap.

The different dimensions of the device are included in Table 5.3. The relative permeability of the MR fluid is $\mu_{MR} = 1.061$, the ferromagnetic material cross-section is $S_i = 30 \text{ mm}^2$, the iron path length is $l_i = 159 \text{ mm}$, the permeances Λ_i and Λ_{MR} are $2.37 \cdot 10^{-7} \text{ T}\cdot\text{m}^2/\text{A}$ and $4.00 \cdot 10^{-8} \text{ T}\cdot\text{m}^2/\text{A}$ respectively. w is the width of the ferromagnetic sheet.

Quantity	Value
g	1 mm
w	20 mm
h	1.5 mm
a	60 mm
N_e	51 turns
N_s	193 turns
μ_i	1000

Table 5.3: Geometrical, electrical, and magnetic characteristics of the components of the microfluidic device.

5.3.3 MR fluid dilution

MRF-132DG is used in the current setup as the working fluid and presents a particle concentration of 33%. Fig. 5.10 depicts the particles' distribution captured with a Dino-Lite microscope for different particle concentrations. The MR fluid concentrations for the different photos are (a) 33%, (b) 15%, (c) 2%, and (d) 1%. In Fig. 5.10(a), the high particle density leads to microscope images where the particle distribution is invisible. Thus, the fluid cannot be used in this form under the microscope and a dilution to lower densities is imperative. An initial decrease of concentration to less than half (15%) does not improve enough the observation of the particles. As a result, another two dilutions are performed for concentrations of 2% and 1%. In the last two cases, the particle distribution is more clear. The MR fluid used in the experimental section is a dilution of the MRF-132DG down to a 2% volume-on-volume ratio.

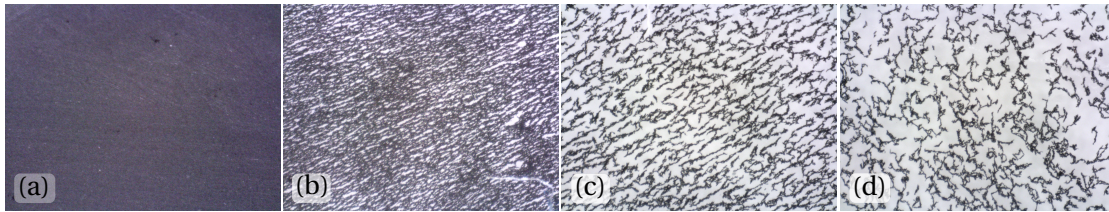


Figure 5.10: MRF-132DG with particles concentration in the carrier medium (a) 33% (b) 15% (c) 2% (d) 1% volume-on-volume ratio. Photos captured with Dino-Lite optical microscope by Timothy Loayza.

5.3.4 Results

The next step is to observe the particle distribution and the induced voltage on the sensing coil after placing the microfluidic device under the microscopic lens. To this purpose, the exciting coil is supplied with $I = 350$ mA and the microscope camera starts recording at 15 FPS, while no pressure is applied to the inlet of the microchannel. Since the outlet is open, the whole fluidic circuit remains in atmospheric pressure. The current supply on the exciting coil creates particle chains that optimize the path of the magnetic field in the gap, which is filled with MR fluid. In this scenario, the pressure is applied as a peak with the use of a syringe for a duration of 150 ms. The pressure reaches 1 MPa and breaks the chains, creating fluid flow. During this time, the pressure is measured. The induced voltage created on the sensing coil by the variation of the magnetic properties of the MR fluid is measured with the oscilloscope. Additionally, a section of the microchannel is filmed with the microscope simultaneously, using the dark field microscopy technique. The collected data show the relationship between

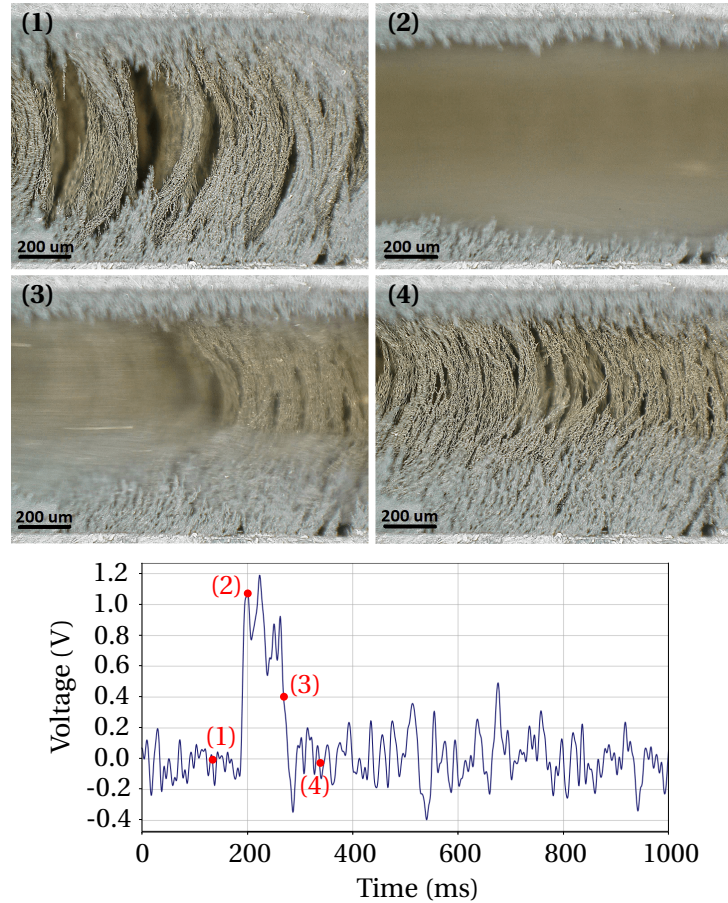


Figure 5.11: **Top:** four video frames separated by 67ms. (1) Existence of magnetic field and particle chains (2) Chains breakage (3) Chains begin to reform (4) Chains completely recreated. **Bottom:** filtered and amplified induced voltage on the sensing coil with red dots representing the video frames. (Copyright: 978-1-6654-1308-4/22/\$31.00 © 2022 IEEE)

the distribution of particles in the MR fluid and its magnetic properties. The measurements are filtered with a 50Hz cut-off frequency Gaussian filter, because the noise ratio is high during the measurement, due to the electromagnetic perturbation of the environment and the double-stage amplification.

In Fig. 5.11, four consecutive frames are presented, which depict the rupture of the chains of particles when the pressure is applied, followed by their reformation when the pressure is back to the atmospheric level. The frames are obtained with 67 ms time deference. Below the frames, the filtered and amplified induced voltage signal is presented. The particle chains are formed at frame (1) due to the magnetic field created by the exciting coil, while the application of pressure breaks them completely and lets the MR fluid flow at frame (2). The reformation of particles starts at frame (3) and is completed at frame (4).

From frame (1) to (2) and from frame (3) to (4) there exists a variation of the geometrical distribution of the ferromagnetic particles that results in a change in the magnetic properties of the MR fluid. This change creates the induced voltage on the sensing coil, according to Eq. 5.16. The measured voltage is at the same reference as the voltage source. As a consequence, the positive induced voltage corresponds to a decrease of the MR fluid permeance Λ_{MR} . This result is justified by the role of ferromagnetic particles in the magnetic circuit as a guide of the magnetic path. When the chains break, the magnetic field passes through the oil of the MR fluid (frame (2)). The relative permeability of oil, though, is lower compared to the relative permeability of the ferromagnetic particles. Thus, a proportional decrease in flux occurs in it.

The measured induced voltage shown in Fig. 5.11 is integrated from $t_0 = 160$ ms to $t_1 = 320$ ms to calculate the variation of the relative permeability of the MR fluid using Eq. 5.18. The integration result is $V_i = 6.603 \cdot 10^{-6}$ V·s and the variation of the relative permeability of the MR fluid is $\Delta\mu_{MR} = -0.050841$. At frame (1) of Fig. 5.11, where the particles form chain-like structures, μ_{MR} is higher compared to the one calculated with the Maxwell-Garnett rule. At frame (2), the chains break and particles are randomly distributed in the carrier medium. Thus, the Maxwell-Garnett rule criteria of particles' dispersion are met and the μ_{MR} can be approximated to 1.061. Using equation 5.18 results in a change of μ_{MR} from 1.112 to 1.061. Lastly, as shown in Fig. 5.11 (bottom part), the induced voltage contains frequency components in a period of around 20 ms, which corresponds to a frequency of 50 Hz, the noise that derives from the power supply of the measuring instruments.

5.4 Impedance variation measurements

In the previous sections, the applied pressure to the gap filled with MR fluid leads to the change of Λ_{MR} . This change results, finally, in the induced voltage on the sensing coil. In this section, the change of Λ_{MR} used in self-sensing valves is studied with a different approach. First of all, the conventional MR valve with one coil of N turns is used. The coil inductance L is written as:

$$L = N^2 \cdot \Lambda \quad (5.20)$$

Λ is the total permeance of the magnetic circuit, as in Eq. 5.13. The impedance \underline{Z} of the coil depends on the coil resistance R and inductance L as follows:

$$\underline{Z} = R + j\omega L \quad (5.21)$$

So, besides the induced voltage measurement in a 2-coil valve, the change of the magnetic properties induced by the applied pressure to the MR fluid can potentially be measured by measuring the change of impedance of the MR valve coil.

The measurement of the variation of the coil impedance when pressure is applied has been performed in the same testbench as in Fig. 3.10. The conventional 1-coil MR valve (see dimensions in Table 3.3) is placed again between two MR fluid chambers to allow or block the flow. The coil is connected to an impedance analyzer that measures the impedance and returns its value as a function of the frequency ω . Regarding the bias current for impedance measurement, the specific impedance analyzer can provide a current in the range 200 μA - 20 mA.

Before every measurement, the system is calibrated and the oscillation voltage is set to 500 mV.

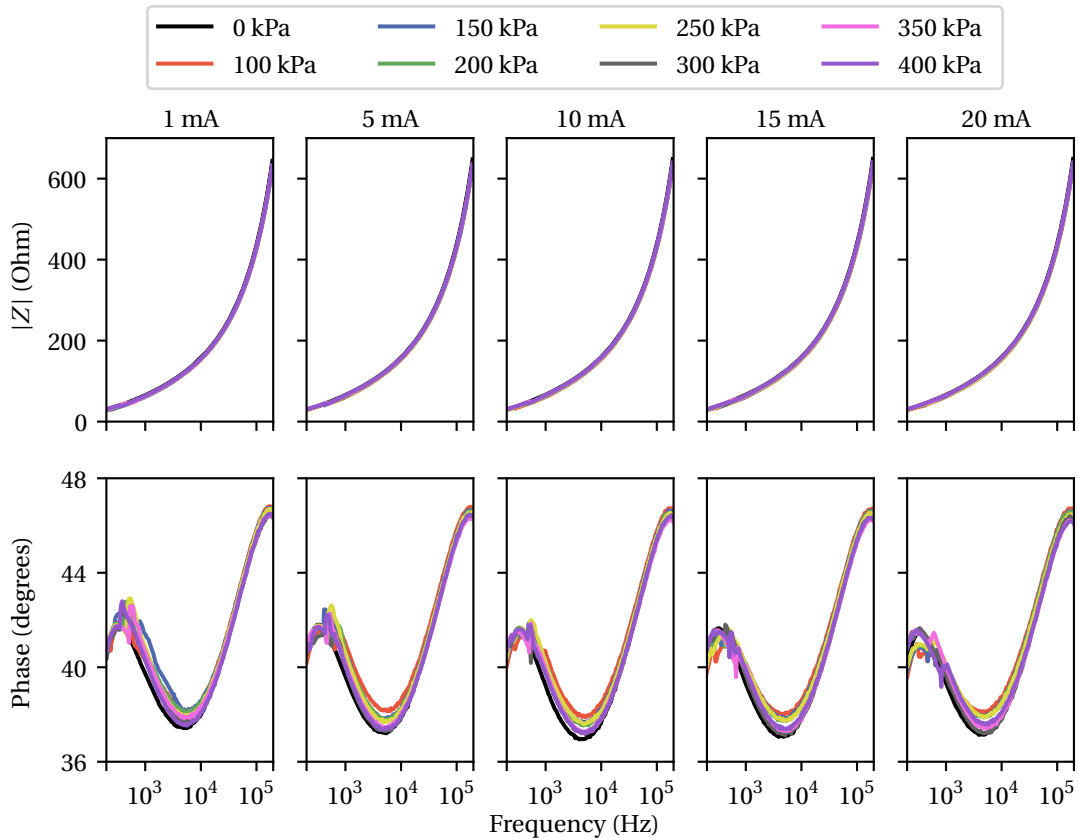


Figure 5.12: Impedance magnitude and phase for different frequencies.

The applied bias current is set from 1 mA to 20 mA with a step of 5 mA. The applied pressure is set with the manual manometer in the range of 100 kPa to 400 kPa with a step of 50 kPa. The measurement of each combination of current and pressure values is repeated four times. The mean of the measured impedance magnitude $|\underline{Z}|$ and phase are plotted in Fig. 5.12. The frequency sweep in the impedance analyzer ranges between 200 Hz and 200 kHz and is taking place while the pressure is applied.

In Fig. 5.12, the impedance magnitude remains constant with the application of pressure compared to the case where no pressure is applied. On the contrary, the impedance phase increases with the application of pressure, especially for frequencies ranging between 1 kHz and 10 kHz. The magnitude of \underline{Z} is $|\underline{Z}| = \sqrt{R^2 + (\omega L)^2}$ and the phase is $\phi = \arctan(\frac{j\omega L}{R})$. Further, $R = 0.77 \Omega$ and $L = 60 \mu\text{H}$. Since L is in the range of micro-Henry ($R \gg L$), the effect of L on the magnitude is not important and only R affects it. However, the coil resistance is constant, and as a result, $|\underline{Z}|$ remains constant as well. Additionally, the phase variation is relatively small, close to one degree. Therefore, the impedance measurement method for self-sensing can be achieved with specially designed electronics that can provide high accuracy in the measurements. Lastly, an impedance-analyzing circuit that can provide higher bias currents shall also be tested.

5.5 Conclusions and main contributions

The technology surrounding self-sensing MR valves is continuously evolving, with ongoing research and development aimed at improving their performance, reliability, and applicability in various industries. Miniaturized self-sensing MR valves are being developed for use in small-scale applications such as microfluidics, biomedical devices, and sensors. Research is investigating how to enhance the sensing capabilities of self-sensing MR valves, with the use of external sensors, such as hall sensors that sense the change of the magnetic field, or optical fiber sensors and pressure sensors in order to offer more accurate and reliable feedback on flow rates and pressure changes. The addition of external sensors increases the complexity and the price of the systems. This chapter proposes a MR valve based on previous studies [141, 122] that can function both as a valve for fluidic control and as a pressure sensor. The main contributions are:

- A preliminary study on the correlation of applied pressure with the induced voltage appearing on the sensing coil of a 2-coil MR valve according to the design of [141];
- A microfluidic device to study microscopically the magnetic and rheological properties of the MR fluid and their link with induction phenomena that facilitate the self-sensing;
- Images obtained with the electron microscope and the use of the microfluidic device, in parallel with induced voltage measurements on the sensing coil;
- A feasibility study of an alternative method that uses impedance variation to create

pressure self-sensing magnetorheological valves without the addition of a second coil, but with the use of an AC current.

All in all, this chapter provides preliminary results of how pressure self-sensing can be incorporated into a miniaturized magnetorheological valve. It also provides the explanation of the phenomenon after placing the microfluidic circuit under the microscope. However, further steps must be taken to create a fully working miniaturized MR valve that is pressure self-sensing. The repeatability and the robustness of the device must be validated as well as the use of the device alternating its functions as valve and as pressure sensor. As tested, the valve can work either in one or at the other state. This is a simplified first test of the valve. Nevertheless, further studies can explore the range of current levels and applied pressures where the valve can close and pressure can be sensed. Design optimization of the MR valve, including geometrical or coil parameters, to obtain the desired current and pressure ranges can follow this study. Another aspect is the use of one coil where the excitation and the induced voltage appear or for the impedance analyzing technique.

Publications related to this chapter:

- S. L. Ntella, K. Jeanmonod, M. T. Duong, Y. Civet, C. Koechli, and Y. Perriard. "Preliminary Study of Pressure Self-Sensing Miniature Magnetorheological Valves," in 2021 IEEE/ASME International Conference on Advanced Intelligent Mechatronics (AIM), pp. 606-611. IEEE, 2021. Copyright: 978-1-6654-4139-1/21/\$31.00 © 2021 IEEE
- T. Loayza*, S. L. Ntella*, P. Mohaghegh, C. Koechli, and Y. Perriard. "Microfluidic device for analysis of magnetorheological fluids' properties," in 2022 IEEE/ASME International Conference on Advanced Intelligent Mechatronics (AIM), pp. 563-568, IEEE, 2022. Copyright: 978-1-6654-1308-4/22/\$31.00 © 2022 IEEE *These authors contributed equally to this work.

6 Novel applications of miniaturized MR valve: Intelligent footwear for diabetic ulceration prevention

The target applications of MR valves include mostly dampers that are involved, among others, in automotive systems for increase of safety. Besides, they are also used in medical systems, such as joint orthoses, to improve biomechanical function, encourage proper joint alignment, or protect a limb. This chapter consists of the presentation of a novel application of the miniaturized MR valve shown in the previous chapters. The application is a wearable device for diabetic patients that prevents ulcerations and, consequently, amputations [122]. The chapter consists of an introduction to the etiologies of diabetic foot ulcerations and amputations, as well as to the existing prevention methods that rely on mechanical setups. Considering the importance of plantar pressure for ulceration creation, the state-of-the-art on plantar pressure measurements is presented as well. Further, the concept of a wearable device is presented where ulceration prevention is achieved with the use of MR valves, based on [122]. The different parts of the device are presented, explained, and validated experimentally. Finally, an insole with 9 modules confirms the offloading capabilities that enable ulceration prevention in static conditions.

6.1 Introduction: Intelligent footwear for diabetic ulceration prevention

Diabetes is a metabolic condition characterized by high blood glucose levels. The number of people suffering from diabetes worldwide increases steadily, while it is predicted that the disease will affect 693 million adults by 2045 [206]. Diabetic patients develop several major complications leading to high morbidity and mortality rates, including peripheral neuropathy [207]. The latter is responsible for peripheral nerve dysfunction, causing sensorimotor abnormalities that affect the biomechanics of diabetic foot [208]. This results in plantar pressure distributions that differ between diabetic and healthy persons. High load areas on the foot



Figure 6.1: Diabetic ulceration prevention methods: (a) Total Contact Cast, (b) Removable cast walkers, (c) Rocker shoes.

surface, in combination with the loss of pain sensation due to neuropathy, lead to DFU [209]. DFUs deteriorate easily in diabetic patients, due to peripheral neuropathy, leading to gangrene and establishing diabetes as the leading cause of lower limb amputation [210].

Surveys show that one amputation happens every 30 seconds somewhere in the world because of diabetes [211]. This leads to a total number of more than one million diabetic patients that lose their leg due to the disease every year, with 90'000 and 250'000 amputations to be performed yearly in the USA and in Europe respectively [212]. An important fact for the investigation of the amputation causes is that 85% of non-traumatic lower limb amputations are preceded by plantar ulceration [213]. This fact reveals the need for DFU prevention that will facilitate amputation prevention.

6.1.1 Existing DFU prevention methods

Amputation prevention for diabetic patients has long intrigued the interest of both medical specialists and engineers. It appears crucial to reduce the plantar pressure on diabetic feet to achieve it. Nevertheless, it must be accomplished in a way that does not immobilize or bring the patients to the hospital repetitively and, in general, that does not impair, additionally to diabetes itself, their quality of life. Searching for solutions to the aforementioned issues has triggered various studies up to the present times and several solutions have been presented.

A prevalent approach, widely considered the "golden standard" for ulcer prevention and healing, is the total contact cast (Fig.6.1(a)) that is a rigid plaster cast that covers the whole foot and leg area up to the knee's height. It reduces the plantar pressure up to 87% [214], while a percentage between 65% and 82% of ulcers are healed with this method within 5 to 7 weeks [215, 216, 217]. However, due to the fact that it is cumbersome and creates impairments for the patients' everyday life, it is not very often prescribed by specialists [218]. Another

Chapter 6. Novel applications of miniaturized MR valve: Intelligent footwear for diabetic ulceration prevention

less invasive solution is the removable cast walker (Fig.6.1(b)), which successfully reduces the plantar pressure, nevertheless, it presents the same drawbacks as the total contact cast [219, 220, 221, 222]. Rocker shoes, as the ones presented in Fig. 6.1(c), are an effective method, too [223, 224], but they reduce the balance control and provoke instability in patients [225, 226, 227]. Lastly, orthopedic shoes and custom-made insoles are also prescribed by doctors as a solution to ulceration. Nevertheless, they are as well passive methods of pressure offloading, and very frequently they only achieve the displacement of high pressure in a different plantar region instead of offloading [228]. All the aforementioned solutions rely on a mechanical setup and the offloading of the plantar region is performed passively. In parallel, they appear to be non-compatible with everyday life, socially impairing, and unsafe. This induces a low adherence in the patients to the footwear and, consequently, a recurrence of the ulceration.

Besides the passive methods, there exist plantar pressure measurement systems in the form of commercial products with the main target to prevent DFUs [229, 230, 231, 232]. These systems are in the form of an insole or sock for the whole plantar surface that is covered by pressure sensors. They successfully manage to measure plantar pressure in real-time in parallel with other parameters, such as temperature or motion direction. Nevertheless, they all lack pressure redistribution capabilities, which would prevent ulcerations in a flexible and automatic way. On the contrary, these systems are connected to another device like a computer or a mobile phone, to which they send their measurements. The device then generates notifications for the user in case of ulceration risk. The ulceration prevention is accomplished with the alteration of the walking style of the patient after receiving the notification.

6.1.2 State of the art on plantar pressure measurements

As explained, high plantar pressure developed on the diabetic foot is a major cause of DFU and amputation. Thus, the plantar pressure measurement can be used in the DFU prevention battle. Plantar pressure measurement systems piqued the interest of the scientific community, from both a medical and engineering point of view. Some studies surpassed the limit of research and were further investigated in industry, becoming available in the market as commercial products. There exist commercial products that perform plantar pressure measurements with the main target to prevent diabetic foot ulcers, to facilitate the rehabilitation of patients with stroke, or even to help athletes prevent injury-prone running styles [232, 231, 230, 229].

Besides the already developed and commercially available products, there exists a large number of research articles offering footwear-based plantar pressure measurement systems. The fundamental requirements for such systems' design are:

- the number of sensors, their size, and their placement on the plantar area, targeting to achieve adequate spatial resolution;
- the embedded electronics, integrating sensor elements, measurements processing, and

6.1 Introduction: Intelligent footwear for diabetic ulceration prevention

power management without blocking the free movement of users and without impairing their everyday life;

- low power consumption for portability of the system and for use as a wearable device;
- low cost, in order to achieve an affordable and high-adherence wearable solution for the patients.

The plantar measurement systems exploit different types of sensing technologies such as resistive and capacitive [233, 234, 235, 236], or piezoresistive and piezoelectric sensors [237, 238, 239, 240, 241, 242, 243]. These systems aim at different targets, such as diabetes ulceration prevention, patients rehabilitation after stroke or accidents, injury prevention in sports, or clinical gait analysis. They manage to perform successfully plantar pressure distribution measurements. However, they still remain far from the goal of a wearable, comfortable, and reliable device. In some cases, the number of sensors is too small - less than 10 - and it does not cover the high-risk foot area, hindering high spatial resolution. In other cases (more than 30 and up to 256 sensors) the data resolution is accomplished. Nevertheless, there exist problems of non-linearity of the custom-made sensing elements, which increases the complexity of data processing, or they present disadvantages concerning durability, due to the wearing of the material from which they are fabricated.

Some different approaches utilize optoelectronic-sensor-based systems [244, 245, 246, 247], with polymer optical fibers to be a common example. In such cases a comfortable wearable is achieved, however, the non-linearity of the sensors is persistent, as well as a number of photodetectors and light sources are needed, resulting in an increase in cost and a decrease in compactness and portability. Other researchers focus on the use of textile sensors [244, 248, 249], where they integrate one of the above-described sensing techniques, e.g. piezoresistive, optoelectronic, etc., in textile, so that the user can comfortably wear the device. These materials facilitate the creation of wearable devices and increase design flexibility, however, they frequently present non-linear characteristics and are subject to wear after constant and long-term use.

In summary, the current methodologies still suffer from bulkiness and lack of consideration for the placement of the embedded electronics, although they achieve effective plantar pressure measurement. But most importantly, they lack of active redistribution of plantar pressure in case high pressures are detected since they only perform plantar pressure measurements. On the contrary, up to nowadays, all the articles propose a cable or Bluetooth connection of the device with a computer or a mobile phone, so that all the data are processed and visualized there.

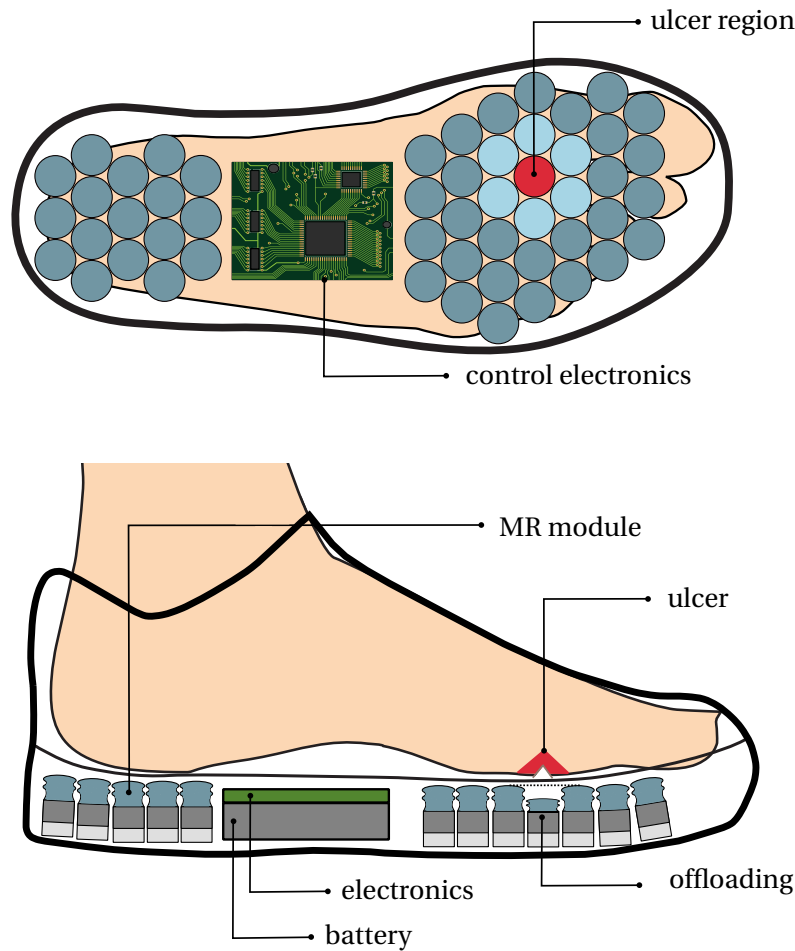


Figure 6.2: Schematics of the proposed footwear with offloading modules based on MR fluids.

6.2 Proposed intelligent footwear for DFU prevention

The disadvantages of the previous DFU prevention methods uncover the need for the development of a type of smart footwear that will measure plantar pressure and will perform high-pressure offloading actively, depending on the sensed pressure value. More specifically, the system must constantly measure the plantar pressure distribution on the high-risk areas of the diabetic foot. These areas are the forefoot and especially the metatarsal areas and the hallux, as well as the rear foot. These regions are where most of the ulcerations occur. The mid-foot area is not risky due to the limited contact of the foot skin with the ground and the shoe surface. If the sensed plantar pressure on a specific region is higher than a threshold value, the shoe must automatically offload this region. This threshold has been established in previous studies on diabetic and healthy subjects to a value close to 350 kPa [209, 210, 250].

The main engineering challenge for the creation of such a system is the availability of compact, lightweight, powerful devices, such as actuators or shock absorbers that can sustain up to 350 kPa of pressure and offload higher pressure values. In addition, such devices must be

characterized by low power consumption so that they can be integrated into a shoe. Therefore, it is vital to develop a novel system that can be incorporated into a shoe, measure plantar pressure and perform controllable offloading in the over-stressed region. Up to the present time, no such system has been fully developed. At LAI, shock absorbers have been studied for this purpose [122, 27]. These shock absorbers are based on MR fluid devices in the valve operation mode. MR valves constitute an efficient option for this application due to their fast response, high controllability, and low power consumption properties.

Thus, the basic pressure control element in the intelligent shoe presented in this chapter is the module (called MR module in the rest of the text) with variable stiffness that uses an MR valve. The MR valve used is in the miniaturized version presented in the previous chapters. The module must have the ability either to sustain the applied foot load or to offload it in case it is higher than the threshold of 350 kPa. In fact, to construct the intelligent shoe, the plantar surface must be divided into smaller control areas, as in Fig. 6.2. The reference value for the surface of each control area is fixed to 1.5 cm^2 according to [122] and is a compromise between spatial resolution and system complexity. One MR module must be placed in each control area. The modules cover only the forefoot and the heel regions. Sensing a high-pressure value means that the module must become softer and offload the high pressure. The pressure will then be redistributed in the neighboring areas, to achieve a new non-risky pressure distribution and to prevent the formation of new over-stressed areas. A printed circuit board (PCB) placed in the middle of the shoe must perform the plantar pressure measurements in real time and decide about the state of each module. The whole system must be battery-powered, with the battery placed in the same area as the PCB.

6.2.1 MR module design and validation

The core element of the proposed intelligent footwear is the MR module that can be controlled to be either stiff or softer depending on the applied foot load. In this section, the design and working principle of one MR module are presented, as well as its experimental validation. Fig. 6.3 depicts the MR module in full and sectional views. The module consists of the following elements:

- The MR valve, which is the controlling element of the module, in the middle of the structure;
- A metallic bellow that forms the upper part of the module and can be deformed with force application;
- An elastic membrane that is placed at the bottom part of the module.

The metallic bellow is hollow and is filled with MR fluid, as well as the gap of the valve and the space at the bottom of the module created by the elastic membrane. The MR valve controls the flow of the MR fluid with the coil that can be supplied with current. The valve can function

Chapter 6. Novel applications of miniaturized MR valve: Intelligent footwear for diabetic ulceration prevention

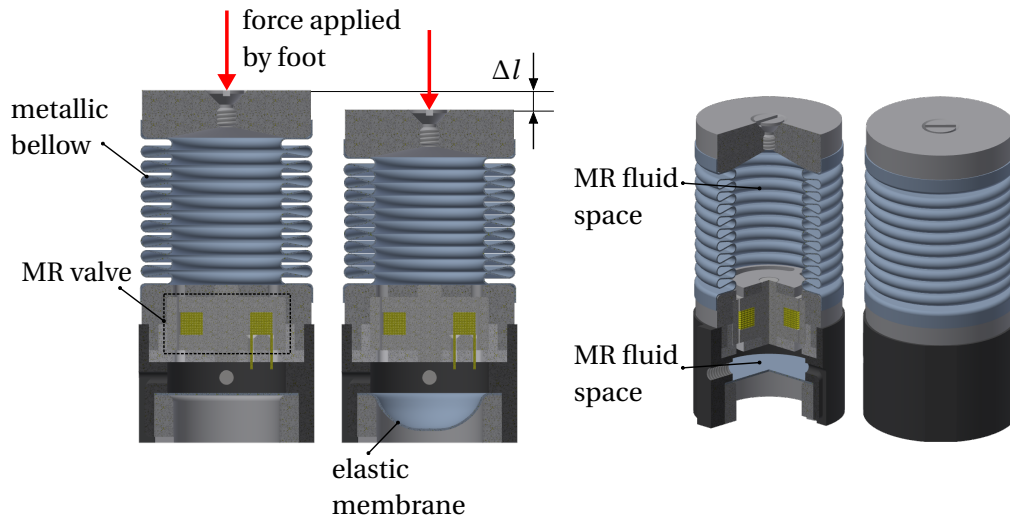


Figure 6.3: Different sectional views of the MR module.

in two states in this application: the closed state when there is current in the coil (the device is ON), and the open state when there is no current (the device is OFF). The metallic bellow can be compressed with an applied force. When the valve is closed, there is ideally no flow, and, since the MR fluid is incompressible, the bellow cannot be compressed even when an external force is exerted on it. In case the valve is open, an external vertical force will cause the compression of the bellow and the fluid flow from the bellow to the bottom space. The elastic membrane will expand in this case (see Fig. 6.3) due to the increase in the fluid volume. The bellow is made of metal to avoid radial deformations that were introduced with other types of compliant materials. Radial deformations of the upper structure of the module led to vertical displacement although the valve was closed when compliant materials were used for the bellow fabrication.

The two states of the MR module are described previously. The device can be controlled only by supplying or not the coil with a DC current. The addition of a force sensor on top of the metallic bellow is necessary to detect the level of the applied force. If the device is integrated into a shoe and the sensed force corresponds to a plantar pressure value higher than 350 kPa, then the current supply must stop and the valve must open. In this case, the bellow will be compressed leading to a decrease of the height of the module by Δl and a regional offloading of the plantar pressure. In case the applied plantar force is not high enough, the valve can remain closed and the device can sustain the load, ideally without any compression of the bellow.

The validation of the MR module is performed experimentally with the use of a modified version of the setup of the previous sections, as in Fig. 6.4. The validation steps include the application of vertical force on the top of the module, the same way force can be applied by the human foot on the MR module. To this objective, the setup consists of:

- A metallic support piece where the MR module is mounted, preventing any movement;

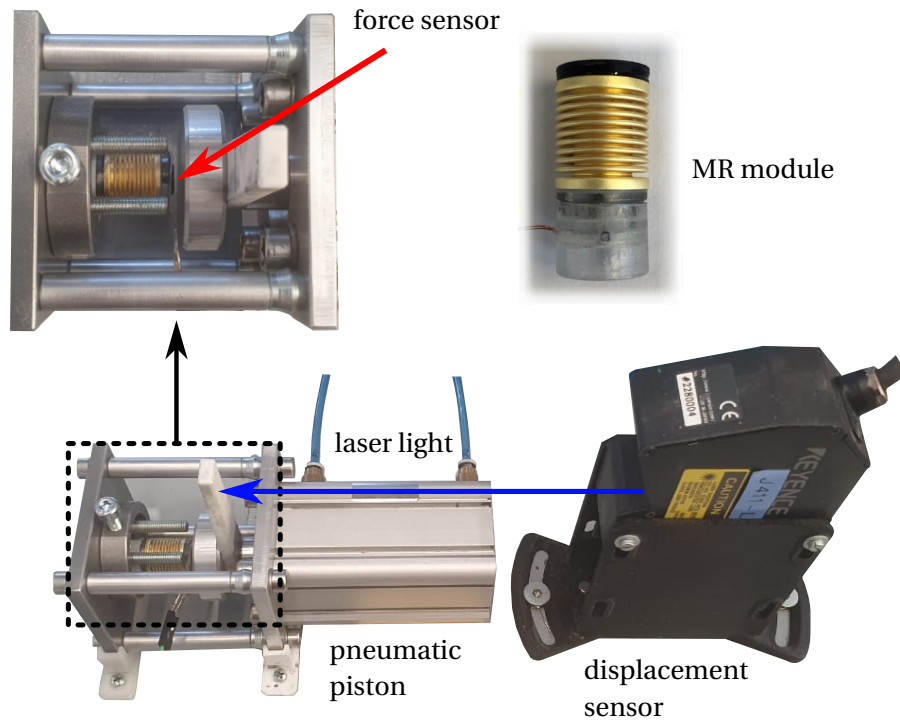


Figure 6.4: Setup for experimental validation of the MR module and picture of the MR module prototype. (Copyright: 978-1-6654-9302-4/22/\$31.00 © 2022 IEEE)

- The pneumatic piston that is again applying the force to the module;
- A force resistive sensor on top of the metallic bellow that is measuring the applied force;
- The displacement sensor that is measuring the displacement of the pneumatic piston and, consequently, the metallic bellow compression.

Initially, preliminary tests have been performed using the pull tester of Fig. 6.5. In this way, it is possible to repeat multiple cycles with low speed and represent the force applied on the module over the applied displacement in repetition for a MR module that is turned on and off. In these experiments, the force is applied vertically with the use of the pull tester, which functions in this case in the inverse way. The maximum displacement is set to 2.5 mm. The speed of the pull tester is set to 10 mm/s. The current supplied to the module is 0.77 A. The pull tester performs cycles of loading and unloading, which means that it moves vertically toward the MR module until it reaches a displacement of 2.5 mm and then it returns back to its origin. This is repeated for 20 cycles.

The results of this test are depicted in Fig. 6.6. For the OFF state of the MR module, the obtained force reaches a maximum of 40 N for a maximum vertical displacement of the cushion of 2.5 mm. Moreover, there exists a hysteretic behavior that is linked to the elasticity of the metallic bellow. The metallic bellows are elastic vessels that can be compressed when force is applied to their surface, or extended under vacuum. When the force or vacuum is released,



Figure 6.5: MR module under the pull tester setup for measuring force vs. displacement.

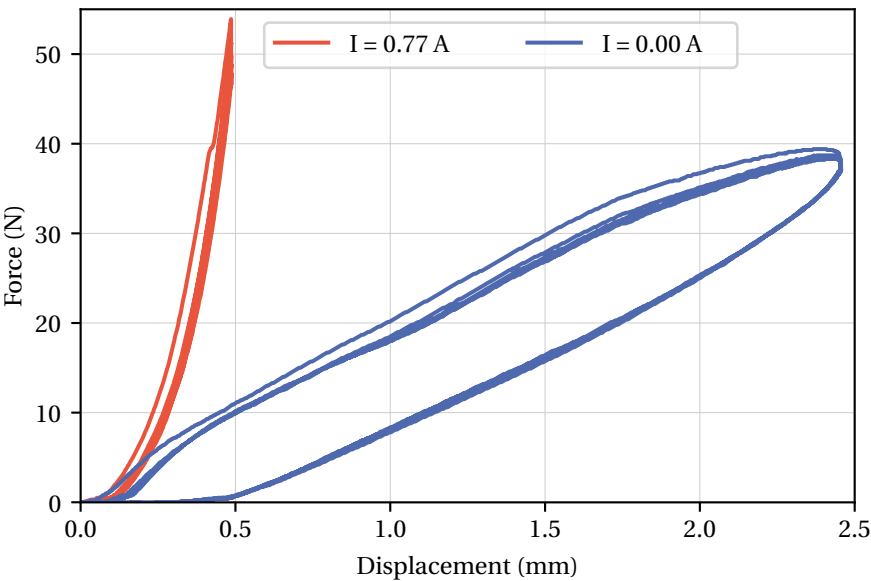


Figure 6.6: MR module validation results with the use of the pull tester.

the bellows return to their original shape, provided the material has not been stressed past its yield strength. Elastic hysteresis is the difference between the strain energy required to generate a given stress in a material and the material's elastic energy at that stress. This energy is dissipated as internal friction in the material during one cycle of loading and unloading.

This phenomenon justifies the difference between the loading and unloading phases of the metallic bellow in the force-displacement curve. Fig. 6.6 also depicts the case when the MR module is turned on with 0.77 A. In this case, the measured force reaches higher values faster. For a displacement of 0.5 mm, the force reaches already 50 N, which corresponds to 325 kPa of pressure. Thus, it can be concluded that the threshold of 350 kPa (defined by the medical application to which this module is targeted) can be reached with this module and with a small vertical displacement close to 0.5 mm.

The first preliminary test has been followed by four different experiments conducted with the setup of Fig. 6.4. This setup allows faster application of force on the module that imitates more accurately the real condition of application of force by the foot. In the first and second

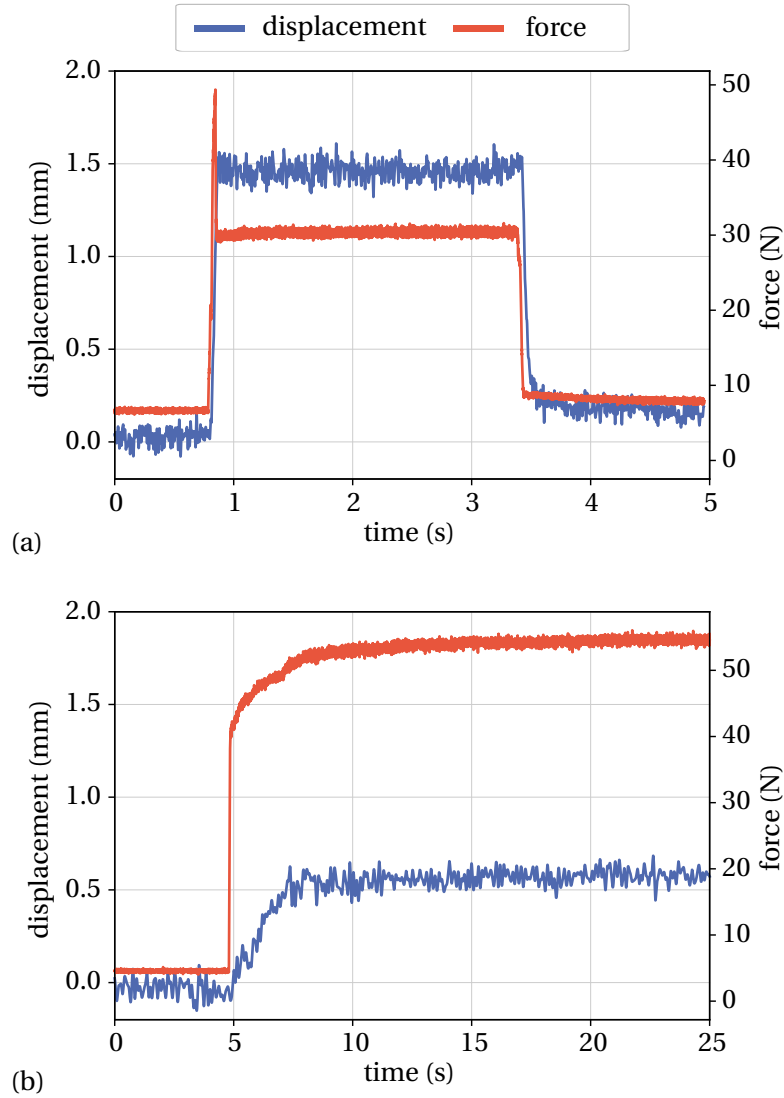


Figure 6.7: Pisont displacement and force over time for (a) open (b) closed MR module. (Copyright: 978-1-6654-9302-4/22/\$31.00 © 2022 IEEE)

Chapter 6. Novel applications of miniaturized MR valve: Intelligent footwear for diabetic ulceration prevention

experiments, the open and closed state of the MR module have been tested. In the first test, the current supply is turned off. The piston starts applying force, and since the valve is open, the displacement reaches immediately 1.5 mm, which is the limit of the piston stroke, as in Fig. 6.7(a). Since the valve is open, the fluid is not facing resistance to move through the valve and flows freely from the metallic bellow space to the bottom part of the module. In parallel, the measured force reaches only 30 N, almost half of the force measured when the valve is closed. At $t=3.5$ s the piston movement is disabled and the piston moves backward, toward its origin.

In the second test, the device is switched on with 0.77 A. The experimental results are presented in Fig. 6.7(b) and depict the displacement of the piston and the measured force applied to the device over time. The piston displacement reaches a maximum of 0.5 mm, and then it remains constant until the end of the experiment. This proves that the valve is in the closed state. The small displacement of 0.5 mm can be attributed to air trapped in the module as well as to the compression of the metallic material. However, it can be considered negligible compared to the open state. Further tests, with multiple modules in the same shoe, must be conducted to confirm this assumption. At the same time, the applied force reaches the value of 55 N, which corresponds to 357 kPa, considering the top surface of the module. This means that the device can sustain at least 357 kPa. Higher values are not of interest in our case, since for values higher than 350 kPa the device must be switched off and the pressure must be offloaded.

The MR module has been tested for both cases, closed and open, separately. The next step of the validation process is to test the transition of the module from the closed to the open state. Fig. 6.8 shows the force applied to the module by the piston and the displacement of the piston in the same plot. The module is initially closed. The piston starts moving at $t = 1$ s, achieving only a small displacement of 0.6 mm and a force of 60 N. Then the module opens at $t = 3.5$ s

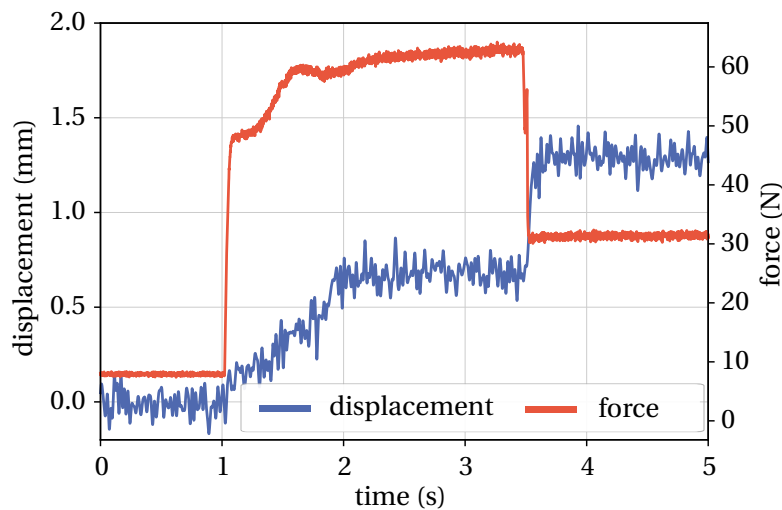


Figure 6.8: Piston displacement and force over time showing the transition from the closed to the open state of the MR module. (Copyright: 978-1-6654-9302-4/22/\$31.00 © 2022 IEEE)

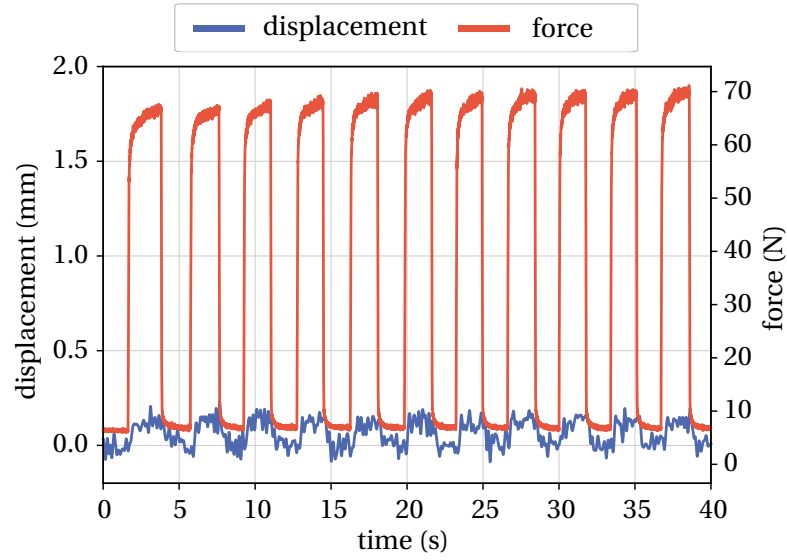


Figure 6.9: MR module in the closed state with iterative applications of force. (Copyright: 978-1-6654-9302-4/22/\$31.00 © 2022 IEEE)

when the current is removed from the coil. At this moment, when the valve is switched off, the displacement increases abruptly close to 1.5 mm and the force decreases to 30 N. This result shows the transition of the MR module from one state to the other.

In the final test, the MR valve is kept closed and the piston moves repetitively toward the MR module. 11 cycles are performed in total. The displacement is 0.2 mm in every repetition, which proves that the valve is closed and the behavior is repetitive (see Fig. 6.9). The measured force reaches 70 N. In this experiment, the piston displacement is smaller compared to Fig. 6.7(b), while the measured force is higher. This is justified by the initial position of the piston. The piston is activated towards the device and then deactivated without retraction. After that, the measurement begins. This means that without retracting the piston, the metallic bellows does not return back to its original state at 0.0 mm of piston displacement. As a consequence, the piston displacement reaches only 0.2 mm instead of 0.5 mm and encounters higher vertical resistance by the device. The latter leads to an increase in measured force. All in all, the four previous experimental scenarios prove the functionality of the module in both states. This module is, thus, capable of offloading the foot pressures in case they surpass the limit of 350 kPa.

6.2.2 Plantar pressure measurement methods

In the previous sections, the design of the MR module, controlled by MR valves and MR fluids was presented. However, as previously explained, in the offloading system there exists the need for a plantar pressure measurement system that can be connected to custom electronics to obtain the pressure measurements and then control the different modules. In the ideal case,

Chapter 6. Novel applications of miniaturized MR valve: Intelligent footwear for diabetic ulceration prevention

one pressure sensor should correspond to one MR module. Pedar-X system is a very powerful and accurate tool for plantar pressure measurements, however, it cannot be connected to custom electronics and it is linked with long wires to a bulky control system. In parallel, it consists of 99 sensors, and as a result, the mapping between sensors and MR modules in the intelligent footwear we are aiming at that will include a maximum of 48 modules is more difficult. As a consequence, this option is excluded from the plantar pressure methods for the final wearable system. Several other plantar pressure measurement options have been investigated for the final insole prototype, as presented in Fig. 6.10.

Nanopaint insole: a custom-made insole was ordered and fabricated by Nanopaint company. The design of the insole includes 31 sensing points for the 31 MR modules that exist in the wearable insole. Each sensor is made with piezoresistive ink and is in the form of a circle (Fig. 6.10(A)). Conductive ink has been used to create the conductive tracks for each sensor. Each sensor needs two electrodes, one for the ground and one for the power supply. The conductive electrodes end at a 1mm-pitch connection point that can be easily integrated with flex connectors. The sensors and electrodes are printed on textile material. After testing the insole, two main issues have been pointed out that prevent its use for the wearable device: the deposition of conductive ink on the textile led is not completely successful and the conductive trucks are easily destroyed; the resistance of the conductive tracks is in the order of MOhm while the resistance of the sensor itself is in the order of kOhm. This makes the force measurement impossible. Deposition of conductive ink with inkjet printing and the use of a mask has been used to improve the tracks, without great success. A second version of this insole is depicted in Fig. 6.10(B) where the textile material used is thinner and less elastic. The printing of conductive tracks on this material is better, however, the resistance of the track is still elevated.

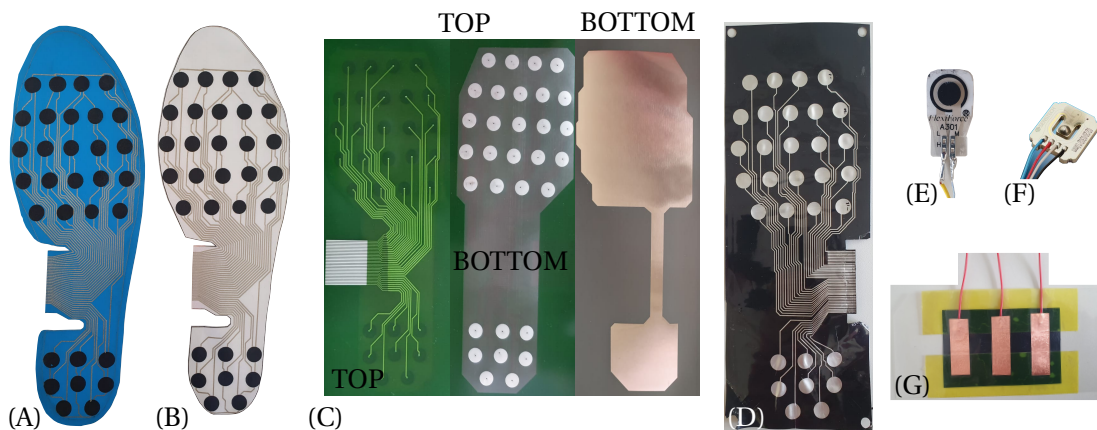


Figure 6.10: Different plantar pressure/force measurement methods: (A) & (B) Nanopaint insoles with different textiles (C) Flexible PCB insole with piezoresistive sheet (D) Piezoresistive sheet with electrodes made with silver evaporation (E) Tekscan A301 FSR sensor (F) Senstech force sensor (G) Piezoresistive sensor with 3 cells.

Flexible PCB and piezoresistive sheet: another option for plantar force measurements is the use of a piezoresistive sheet, sandwiched between two layers of flexible PCB (Fig. 6.10(C)). The bottom layer is a surface where copper is poured and is connected to the ground (the first electrode of the sensor), while it is in direct contact with the piezoresistive sheet. The top layer is used as the second electrode of the sensor. It is a custom-made flexible PCB with bare copper electrodes, again in contact with the sheet. Before testing the complete insole, a prototype consisting of three sensors, as in Fig. 6.10(G) has been used to validate the functionality of the force sensors. Copper material is placed on the top and bottom of the piezoresistive sheet in three different sections, creating three different sensors.

Piezoresistive sheet with silver electrodes: another insole (Fig. 6.10(D)) is using the same piezoresistive sheet but the electrodes are printed with silver using the evaporation technique. The silver evaporation has been conducted in the facilities of PV-LAB EPFL by Armando Walter. The silver tracks are very delicate in this case and are easily destroyed after the first use.

Separate sensors: Besides the complete insoles consisting of several sensors, two different types of individual sensors per module have been also examined. The first type is Tekscan A301 Force Resistive Sensor (FSR) with 0-110 N range (Fig. 6.10(E)). The sensor's functionality is acceptable, however, the size is too large for our application, especially due to the big connections for the electrodes. A custom-made solution from the same company is too costly. Similarly, the use of KZ-011-0400 centered force sensors by Senstech has been investigated (Fig. 6.10(F)). In this compact force sensor, the force is applied to a roundhead rivet in the center of the sensor. The electrode size and the cost of the sensors is again important limitation for our application.

Among all the above solutions, the insole made of a piezoresistive sheet and flexible PCB electrodes is chosen for the first prototype of the intelligent shoe, due to the quality of the measured force and its durability.

6.3 Control electronics for multi-module insole system

The creation of a complete insole prototype requires the MR modules, the plantar pressure measurement system, the insole that is housing them, as well as an electronic platform that coordinates the plantar pressure measurements and the MR module control. The development of the MR modules, the pressure sensing system and the electronic platform were running in parallel. As a result, the final PCB has been created through a progression of circuit versions that aim at improvement.

6.3.1 Control electronics system architecture

The circuit has been implemented considering the following features:

Chapter 6. Novel applications of miniaturized MR valve: Intelligent footwear for diabetic ulceration prevention

- Multiple force or pressure sensors (28-48 depending on the size of the shoe) must be connected to the electronic board;
- The force or pressure measurements are analog and must be collected with a microcontroller;
- Depending on the force or pressure measurements the platform must control the MR modules' state;
- The number of modules is the same as the number of sensors;
- The modules must be controlled simultaneously;
- The acquired measurements and module status must be sent wirelessly to a PC for data post-processing during pre-clinical trials with diabetes experts;
- The platform must be powered by a battery;
- The electronic platform's size must be small enough to fit in the insole;
- Each module must be supplied with a continuous DC current of a minimum of 0.5 A according to previous tests of the MR valve;
- Each module must be controlled independently.

In order to satisfy the above requirements the circuit with the schematics of Fig. 6.11 has been introduced. This design is considered a feasibility study. It only implements the force measurements and the MR module control. The sensors intended to be used in this design are the ones from Senstech that include two wires for sensing, and two for power supply. One of the power supply probes is constantly connected to the ground. The rest of the sensors' wires are multiplexed with three different multiplexers to read consecutively all the sensors. The MR modules are controlled with the implementation of one switch per module. The switch is realized with the use of nMOSFETs with minimal footprint.

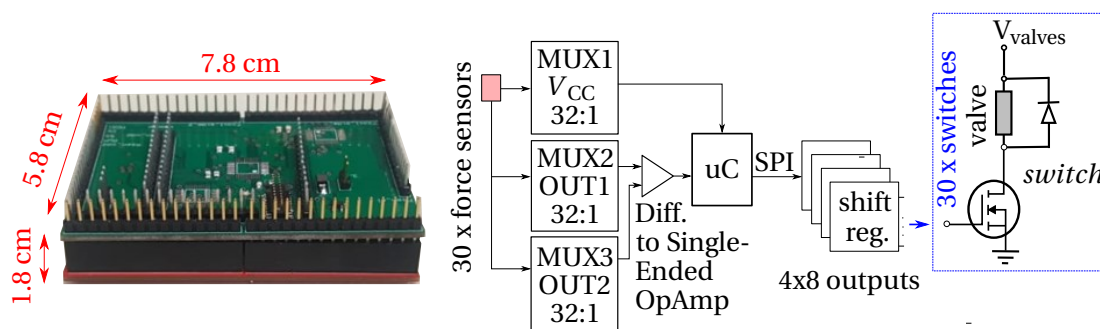


Figure 6.11: Block-diagram and prototype of the first PCB.

6.3.2 Optimization process and final electronic platform

The first prototype consists of two different PCBs that are inter-connected one on top of the other. The dimensions of the whole system are $1.8 \times 5.8 \times 7.8$ cm, as in Fig. 6.11. In this design 30 sensors and 30 modules are connected. The programming ability of the custom-made PCB, including the multiplexers' functionality, the ADC functionality, and the functionality of the MOSFET switches have been validated before continuing to a more complete electronic system.

The new optimized electronic platform is based on the one of the previous section and is completed with several improvements, as follows:

- The replacement of the 4-wire Senstech sensors with an insole of multiple sensors, where each sensor needs two wires, led to the decrease of multiplexers needed from three to one.
- A Bluetooth module has been added to send the pressure measurements and the module state to the PC.

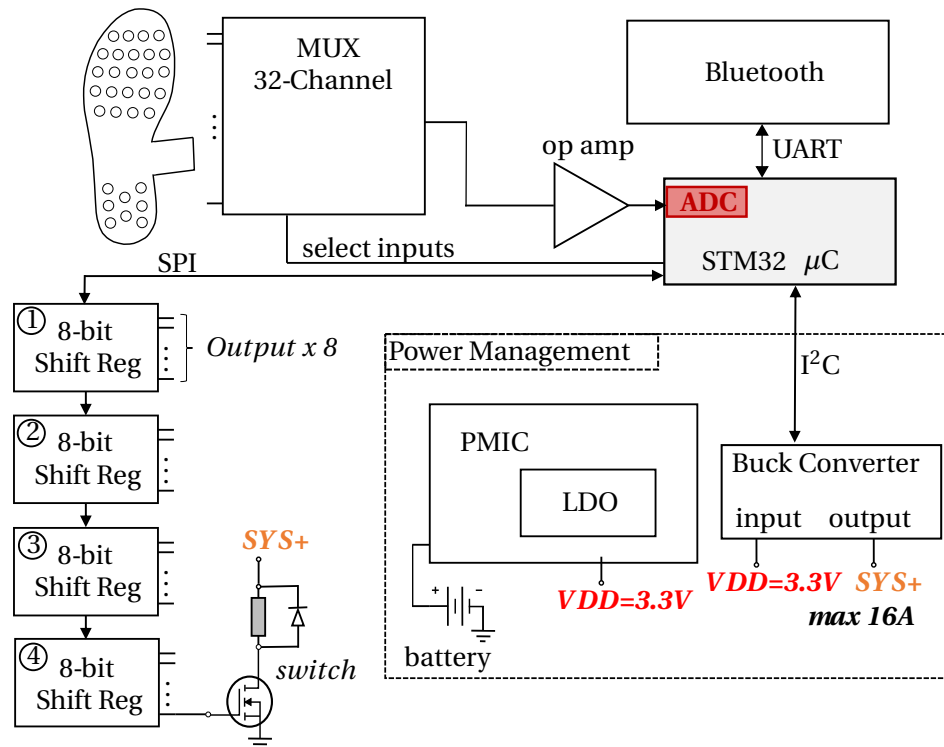


Figure 6.12: Block-diagram of control electronics. (Copyright: 978-1-6654-9302-4/22/\$31.00 © 2022 IEEE)

Chapter 6. Novel applications of miniaturized MR valve: Intelligent footwear for diabetic ulceration prevention

- A power management unit has been added that includes a fixed output LDO of 3.3 V to supply all the different components, as well as a buck converter that can provide up to 16 A and can power the MR modules.
- The prototype consists of a single PCB with components soldered on both sides and PCB's dimensions are 4x7.8 cm.

The block diagram of the final electronics for controlling the functionality of the intelligent footwear after the optimization process is shown in Fig. 6.12. The electronic system consists of a custom-made board that can now fit in the insole created by Giglio Orthopedics. A flexible connector connects the plantar pressure measurement insole to the PCB. The board includes a 32-Channel analog multiplexer to multiplex the different force sensor values. The multiplexer's output is connected to an operational amplifier. The analog output of the

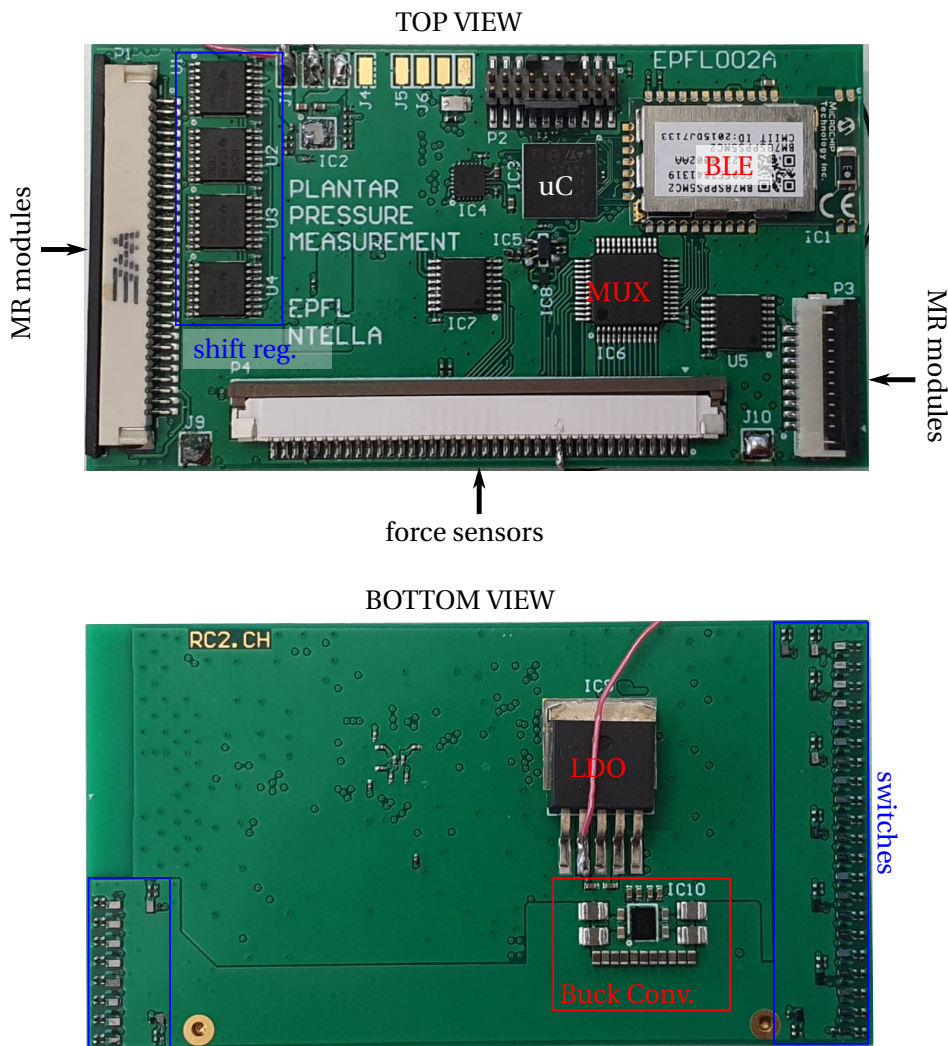


Figure 6.13: Fabricated PCB.

amplifier is connected to one analog channel of the low-power STM32 microcontroller where the force readings are collected.

The microcontroller's goal is to measure the force on the whole plantar surface, calculate the pressure, and turn the different MR modules ON or OFF according to the pressure readings. The current board is capable of controlling a maximum of 40 MR modules, with five 8-bit serial-in-parallel-out shift registers for simultaneous control of the MR modules. To select the valves' state simultaneously, each register's serial output is connected to the serial input of the next one. Like that, simultaneous output of a maximum of 40 channels is achieved. In every digital output, we connect a valve switch implemented with a minimal footprint N-MOSFET transistor, as in Fig. 6.12 and Fig. 6.13. The footprint minimization is imperative considering that in the existing architecture, each valve must be controlled independently, thus, one switch is needed for every valve. The buck converter is configured through I²C communication. This buck converter is a 16A-output high-performance regulator aimed at powering up multi-core CPUs and GPU Processors.

The top and bottom views of the final PCB are depicted in Fig. 6.13. Special flexible printed circuit connectors have been added on the left and right sides of the PCB. These connectors facilitate the connection of the MR modules in the front part and heel part of the foot. The plantar pressure measurement insole can be connected to the lateral flexible printed circuit connector. The buck converter is connected to the different MR module switches using a large polygon pour in the PCB layout to facilitate large current circulation (see Appendix).

6.4 MR module integration in insole

The functionality of one independent MR module has been validated in the two states, open and closed. The next step in the validation process toward the acquisition of a wearable device is the integration of multiple modules in an insole and the testing of the plantar pressure reduction functionality. In this case, 9 modules are inserted in the insole of Fig. 6.14. The insole has been fabricated by Giglio Orthopedics so that modules can be introduced in its front and rear part while in the middle there is space for battery and control electronics. The first preliminary test uses 9 modules in the front part, below the metatarsal area of the foot, where normally high pressure and ulcerations appear. The modules are simultaneously powered with a current of 0.77 A. The tests are performed statically, which means that while all the modules are ON, a person stands on top of the insole, and pressure measurements are performed. The pressure is measured and recorded using the Pedar-X system. The Pedar-X insoles consist of 99 different sensors. The rest of the spots where modules can be inserted are filled with fake modules, which are exact replicas of the MR modules and are 3D-printed, thus, always stiff. In Fig. 6.14 the fake modules are represented with white color, while on top of each of the 9 real modules, there is a force sensor. In this measurement, Pedar-X is preferred for pressure measurements instead of the force sensor to achieve maximum accuracy and robustness of plantar pressure measurements. The Pedar-X insole is placed on top of the modules. Each

Chapter 6. Novel applications of miniaturized MR valve: Intelligent footwear for diabetic ulceration prevention

module is numbered as in Fig. 6.14 to facilitate measurement plotting in the next steps.

The goal of this test is to validate the offloading capability of the modules inside the shoe in the static condition. To this purpose, a spheric object of 2.5 mm radius is placed consecutively on top of each of the nine modules, above the Pedar-X insoles. This object creates increased pressure spots above the MR module regions where pressure can be controlled by the MR modules. If an object is placed above a module, the module is turned off. This action is repeated after changing the position of the object for all nine modules consecutively. Each time the rest of the 8 modules are in the ON state. In the meantime, the plantar pressure is constantly measured with Pedar-X to compare the pressure distribution before and after turning off each module.

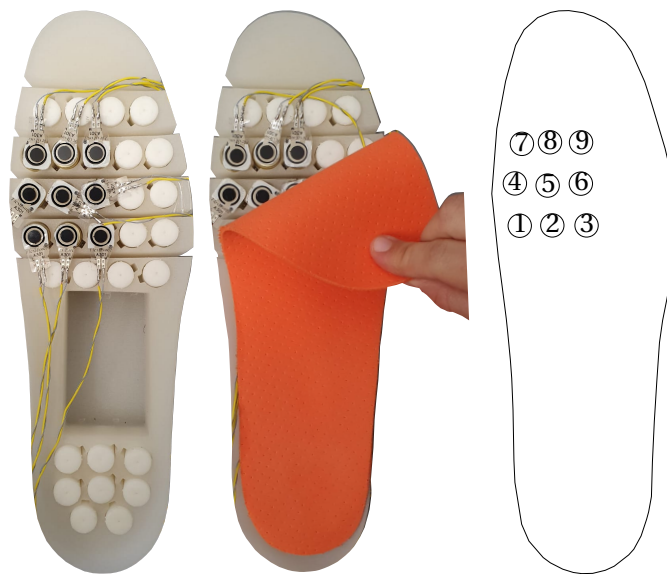


Figure 6.14: Picture of the insole prototype with 9 MR modules, and their numbering principle. The rest of the places in the insole are filled with fake modules.

Fig. 6.15 depicts the plantar pressure distribution on the right front foot in kPa measured by the Pedar-X insole. In each case, the distribution presented on the left side shows the case where all nine modules are turned on. On the right side of each case, the distribution corresponds to the one after opening the indicated MR module. The bottom part of the Pedar-X insole is not shown since it does not present any difference before and after opening the MR modules.

In all the different cases the placement of the external object leads to the creation of high-pressure spots. Turning off module M8 did not lead to any plantar distribution offloading and, thus, has not been shown in Fig. 6.15. The following observations are made for each case:

- (A) The initial pressure above module M1 is 168 kPa and drops to 130 kPa. However, there is a displacement of the high-pressure spot to the top of the insole, without noticing any increase in the maximum pressure.

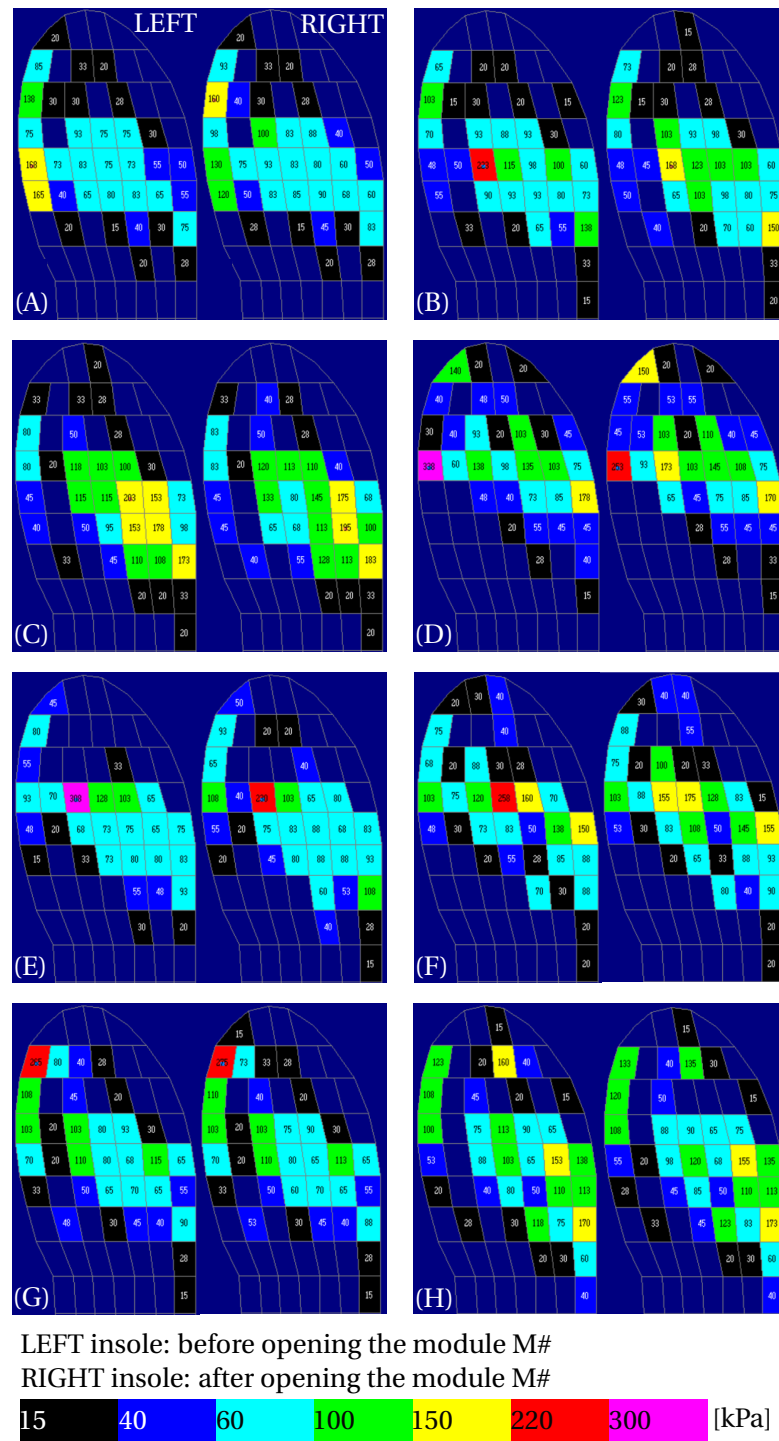


Figure 6.15: Measurements from Pedar-X right insole (only front part) before and after opening the MR modules (A) M1 (B) M1, M2 (C) M3 (D) M4 (E) M5, M6, M7, M9 (F) M6 (G) M7 (H) M9, M8, M6, M5. The bottom part is not shown because the plantar pressure distribution does not change after turning off the MR modules.

Chapter 6. Novel applications of miniaturized MR valve: Intelligent footwear for diabetic ulceration prevention

- (B) The initial pressure above M2 is 223 kPa and drops to 168 kPa, while there is pressure redistribution and an increase in the neighboring regions.
- (C) The initial high-pressure spot above M3 drops from 203 kPa to 145 kPa, however, a new spot of 195 kPa is created.
- (D) The same behavior appears above module M4 with a regional decrease of pressure and a slight increase of pressure in neighboring areas.
- (E) In the case where the object is placed above module M5, the opening of M5 does not lead to any change of pressure. M6, M7, and M9 open consecutively and only the opening of M9 leads to a decrease of pressure in the M5 region.
- (F) M6 region is offloaded with the opening of module M6.
- (G) The same happens for M7 region.
- (H) Finally, when the object is placed above module M9, the opening of M9 does not lead to a decrease in pressure. This happens after opening module M5, while modules M8 and M6 had already been opened.

The above results confirm the working principle and functionality of the MR modules to offload the high applied pressures. At the same time, the status of other modules, apart from the one where the peak pressure appears and is turned off, affects the total plantar pressure distribution. A special algorithm can potentially choose effectively, which modules to turn off and which to turn on. In this way, a plantar pressure distribution without high-pressure spots will be achieved and DFUs in diabetic patients will be prevented.

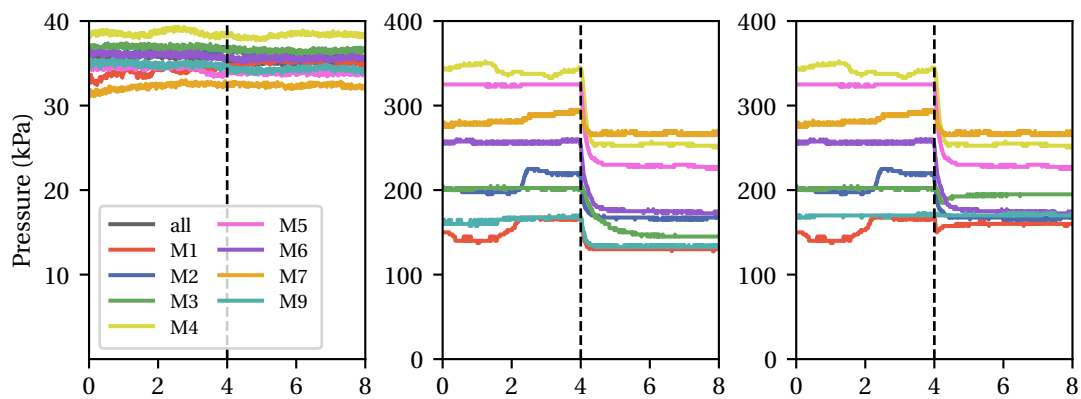


Figure 6.16: Average pressure on the whole plantar surface of the right foot before and after turning off different modules at $t = 4$ s (left), pressure over time on pressure sensor where peak pressures have been created with the addition of the object (middle), peak pressure on the total insole surface (all 99 sensors) over time (right).

Besides the representation of the plantar pressure distribution as a map on the insole (Fig. 6.15), the plantar pressure measurements acquired with Pedar-X are depicted in Fig. 6.16. More specifically, the figure consists of three parts. The plot on the left shows the mean pressure on the whole plantar surface of the right Pedar-X insole over time for the following different cases: either no external object is placed and all the modules are turned off ("all"), or the object is placed consecutively above the modules M1, M2, M3, M4, M5, M6, M7, and M9, and the modules explained in Fig. 6.14 are turned off in each case. For the cases where multiple MR modules must be turned off to achieve offloading (object above module M5 and M9), the opening is considered the moment the module that achieves offloading is turned off.

The plot in the middle depicts the pressure value over time for the sensor below the object and above the corresponding module shown in the legend each time. At $t = 4$ s, there happens the opening of the module that leads to a decrease in plantar pressure, as described previously. It is evident that there is a pressure decrease ranging between 35 kPa and 112 kPa.

The plot on the right depicts the peak pressure value on the whole plantar surface of the right foot. In fact, the overall peak pressure is very similar to the pressure of the sensor, above which the object is placed. This means that the addition of the object leads to the creation of peak pressures. In all the different cases, a decrease in the total peak pressure takes place. The exception is the case when the object is placed above module M9. Even in this case, though, there is no increase in the total peak pressure, but it remains constant.

This series of measurements proves the plantar pressure offloading capabilities of the MR modules in the static condition when inserted in a custom insole. As shown in the previous Fig. 6.15 and Fig. 6.16, the maximum pressure spots can be offloaded if the module in direct contact with them is turned off, with reduction of at least 35 kPa. At the same time, the pressure is displaced in other regions of the foot, but without an increase of the maximum pressure on the whole plantar surface. Further experimental trials can be exploited for the creation of a smart algorithm that will choose to turn off the specific MR modules that will lead to a healthy plantar pressure distribution without ulceration risks.

Full prototype of the intelligent shoe

Finally, Fig. 6.17 presents the full prototype of the shoe. It consists of the 3D-printed insole by Giglio Orthopedics, with MR modules inserted at the front part of the shoe. At the heel, there exist fake modules with the same design as the real ones. All the modules are connected on a flexible PCB at the bottom of the insole (Fig. 6.17(b)), which acts as a connector between the modules and the control electronics. The PCB and the batteries are placed in the middle of the insole, under the arch of the foot, where not much contact of the foot with the ground exists (Fig. 6.17(d)). Above the modules and the PCB, the flexible force measurement insole is placed (Fig. 6.17(c)). It is located above the modules in a way that each module corresponds to one sensor on the insole. On top of this insole, another green insole is placed (Fig. 6.17(a)) that makes the shoe more comfortable for the patient without limiting the offloading capabilities of the modules.

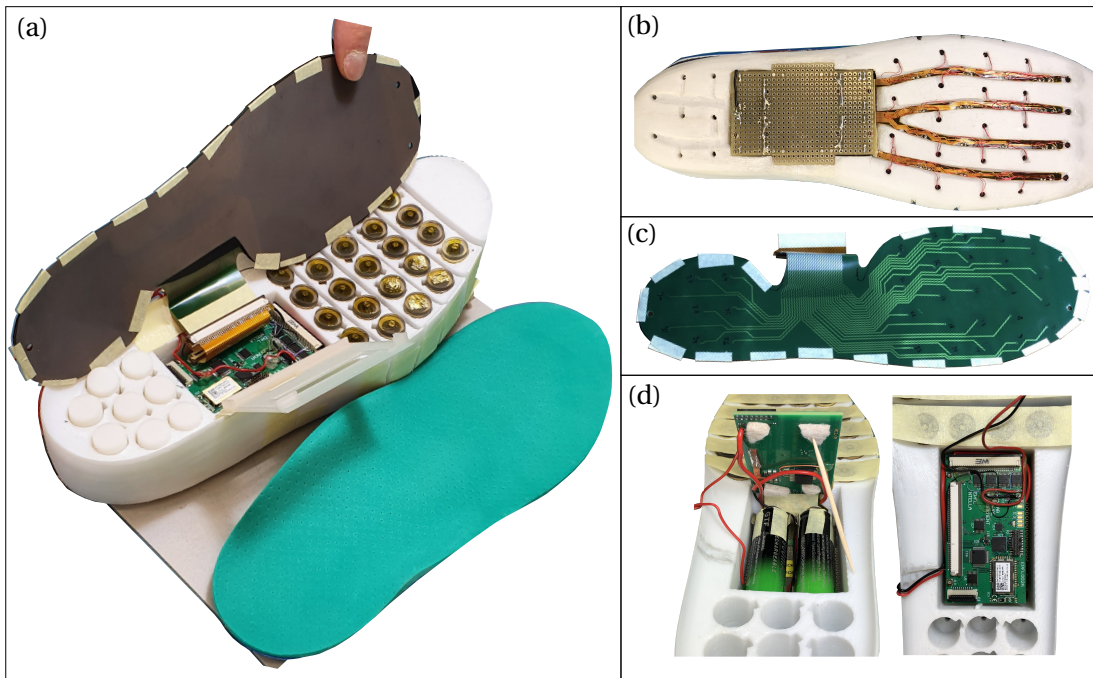


Figure 6.17: (a) Prototype of the full shoe, with MR modules in the front part and faked modules at the heel. The control electronics are placed in the middle of the insole and on top of all of these, the plantar force measurement insole is placed. The green insole is a soft insole placed on top of our system to increase comfortability for the patients. (b) The bottom view of the insole, with flexible PCB connectors that link the modules with the control electronics. (c) Flexible force measurement insole. (d) Control electronics and battery integration.

6.5 Conclusions and main contributions

MR valves have been studied extensively in the last two decades and have been employed in different kinds of applications, such as automotive systems of medical devices. In this chapter, a wearable device in the form of an insole for plantar pressure redistribution and diabetic foot ulcer prevention is presented. Current state-of-the-art prevention methods are bulky, passive mechanical systems. The proposed system aims at replacing these solutions with an active redistribution method that will offload dynamically high plantar pressure regions and prevent DFUs, without further deteriorating the patients' quality of life. The main contributions of this chapter are:

- The system architecture of the wearable device for DFU prevention. The following parts of the device are presented: (a) The MR module that is enabled by a MR valve and can operate in two modes, closed and open, to sustain or offload plantar pressure accordingly. The proposed module has been validated independently of other modules with a custom-made testbench; (b) The plantar pressure measurement techniques; (c) The custom electronics that can enable plantar pressure measurements and control of multiple MR modules in the insole simultaneously.

- The integration of the MR module in the shoe after independent tests and the validation of plantar pressure reduction. Nine modules have been inserted in a specially designed and fabricated insole by Giglio Orthopedics to test the offloading capabilities of multiple MR modules inserted in an insole in static conditions. Plantar pressure reduction is measured and evaluated.
- And finally, the integration of 23 MR modules in the front part of the insole together with the PCB, the battery, the flexible connectors, and the flexible pressure measurement insole.

The research output of this chapter, together with the findings of chapter 4 where the MR valve energy consumption is minimized, is paving the way for a complete wearable device for DFU and amputation prevention. The proposed hardware, accompanied by a smart algorithm that can be based on machine learning and can control the functionality of the MR modules in the direction of healthy plantar pressure distributions can lead to a fully working wearable device. The latter will overcome the disadvantages of the existing prevention methods that are cumbersome and uncomfortable, playing a key role in diabetic care and improving patients' life.

Publications related to this chapter:

- S. L. Ntella, K. Jeanmonod, Y. Civet, C. Koechli, & Y Perriard, "Pressure Offloading Device for Diabetic Footwear Based on Magnetorheological Fluids," in 2022 25th International Conference on Electrical Machines and Systems (ICEMS), pp. 1-5, IEEE, 2022. Copyright: 978-1-6654-9302-4/22/\$31.00 © 2022 IEEE
- B. Tiwari, C. Koechli, K. Jeanmonod, P. Germano, S.L. Ntella, Y. Civet, Y. Perriard, "A miniaturized passive valve for pressure sustention and release", patent submitted in March 2023, EP Patent Application Nr 23159412.8.
- S. L. Hemler, S. L. Ntella, et al., "Intelligent plantar pressure offloading for the prevention of diabetic foot ulcers and amputations", in *Frontiers in Endocrinology*, vol. 14, 2023.
- S. L. Hemler, S. L. Ntella, et al., "Evaluation of plantar pressure redistribution in novel footwear for people with diabetes", in *International Society of Biomechanics*, 2023.

7 Conclusions

MR valves have been extensively studied in recent decades due to their benefits, including fast time response and low power consumption. These benefits are due to the nature of the smart material that allows for viscosity change with the application of an external magnetic field. Specifically, the presence of ferromagnetic particles in the fluid allows for viscosity control through the application of the magnetic field, causing the particles to align parallel to the field lines. This change occurs in less than one millisecond with the use of simple electromagnets with currents in the range of a few amps. MR valves have been used in a wide range of applications, such as dampers for vehicles or seismic damping, as well as dampers for biomedical devices, such as prostheses and orthoses. Despite the significant developments in this field, there is still room for improvement, especially in applications where miniaturization and low power consumption are critical, such as in the biomedical or robotic industries. This thesis aimed to model, fabricate, and analyze magnetorheological valves with miniaturized size and low power consumption, capable of sustaining high fluidic pressures.

The **main contributions** of this thesis are:

- The design optimization of a conventional, miniaturized MR valve powered by an electromagnet. The optimization is accomplished with the use of Design of Experiments and Response Surface Methodology. The optimization objectives are the maximization of pressure drop and flow rate with parallel minimization of volume and power consumption. The magnetostatic numerical modeling of the valve is used to introduce a new model of the MR pressure drop. Finally, the MR valve functionality and the model are validated experimentally, including determining the maximum sustained pressure and the flow rate of the valve.
- The working principle, modeling, and experimental validation of a miniaturized MR valve that incorporates an electropermanent magnet in the core of the conventional MR valve structure. The magnet is made of a soft magnetic material that enables easy magnetization and demagnetization with sub-millisecond current pulses on the coil. The MR valve model estimates the magnetization and demagnetization current

limits, as well as the maximum sustained pressure of the valve in the closed state. The experimental validation in a fluidic flow environment confirms the modeling of the valve. This new MR valve prepares the groundwork for facilitating the use of MR fluids in a wide range of applications, where low volume, high pressure, and low power consumption are significant parameters.

- A preliminary study on pressure self-sensing MR valves. The study includes the correlation of applied pressure with the induced voltage on a miniaturized MR valve with two coils. The working principle of this valve is based on the addition of two coils in the MR valve, one for the excitation of magnetic field with DC current, and one for the induced voltage sensing. The variation of the magnetic path in the valve due to the applied pressure is responsible for the induced voltage. Additionally, a microfluidic device is presented to study microscopically the magnetic and rheological properties of the MR fluid and their link with induction phenomena that facilitate the self-sensing. Electron microscopy is used to obtain images of the MR fluid in the microfluidic device, while at the same time, the induced voltage on the sensing coil is measured. This work is accompanied by an alternative feasibility study where impedance variation is measured to create pressure self-sensing MR valves without a second coil but with the use of an AC current.
- The incorporation of the miniaturized MR valve into a wearable device for diabetic foot ulceration prevention. The device is in the form of an insole and consists of multiple modules on the plantar surface that can either sustain or offload the foot load. In this thesis, the device architecture and the first shoe prototype are presented, including the MR module, the control electronics, and the plantar pressure measurement methods. The use of multiple modules in the insole with the parallel static plantar pressure measurement confirms the ability of the insole to offload pressure. These results are paving the way for a complete wearable device that will actively prevent ulcerations and consequently amputations in diabetic patients, improving the quality of life of millions of people worldwide.

Future perspectives

Considering the accomplishments of this thesis, a possible direction of future research can be the full development and clinical test of the wearable device for diabetic patients. From a hardware perspective, multiple shoes of different sizes must be manufactured, with different numbers of modules depending on the shoe size. The shoes must be tested with multiple healthy subjects in different conditions, such as walking, running, climbing stairs, or standing. The test must be first conducted in laboratory conditions and then the subjects must repeat the same activities in their everyday life. These steps will validate the usability of the wearable device, proving at the same time that it does not provoke further problems for its users. In parallel, the pressure measurements will provide invaluable data for further processing and development of a redistribution technique.

Chapter 7. Conclusions

From a software perspective, a smart algorithm must be developed to automatically control MR modules without any user intervention. The goal is that the patient will wear the shoe and the offloading will be performed automatically by the algorithm, preventing effectively ulceration creation. Machine learning can be a possible methodology for ulceration prevention. It may also help in identifying features other than peak pressure to anticipate further ulceration. For this purpose, a dataset from multiple diabetic patients must be created that will include as input in-shoe plantar pressure measurements from different activities and as output the plantar pressure measurements after opening specific MR modules. This dataset can be used to train and validate a machine-learning model that will be further inserted into the shoe microcontroller and perform the active offloading. The proposed hardware together with the smart software will lead to a fully working wearable device for ulceration prevention in diabetic patients that will potentially revolutionize diabetes care.

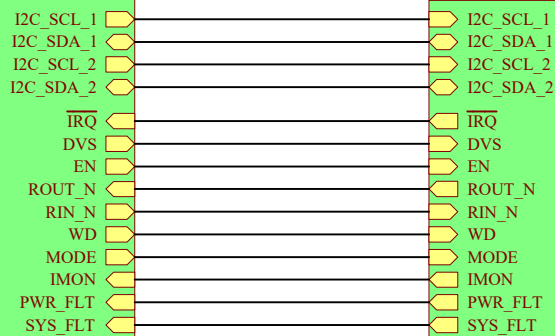
Besides the addition of valves in smart shoes for diabetic ulcer prevention, another potential use could include the emerging field of soft robotics. In this field, actuation is frequently accomplished with fluidic actuators that make use of bulky control systems comprising valves and pumps. Our miniaturized, low-power valve could contribute to the space minimization of the control systems of such actuators. In this case, the actuator will be activated hydraulically using MR fluid as working fluid, harvesting at the same time the advantages of high force and stroke generation appearing in hydraulic actuators. This type of soft actuator can be employed in a wide range of applications, such as gripping delicate products with soft grippers, space exploration of unknown territories, and wearable technologies that provide assistance, support, or augmentation for human users.

A PCB schematics & layout

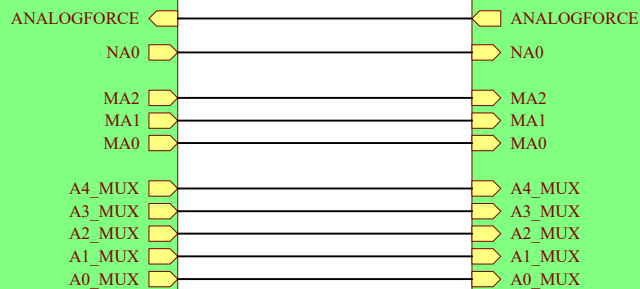
The schematics and layout of the PCB that is integrated into the smart insole can be found in the following pages. The PCB consists of 6 layers. It was developed by S.L. Ntella and designed by the company RC2 Electronique SA.

uCONTROLLER
uCONTROLLER.SchDoc

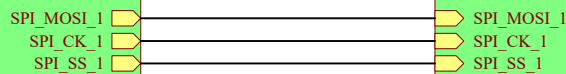
POWER MANAGEMENT
POWER MANAGEMENT.SchDoc



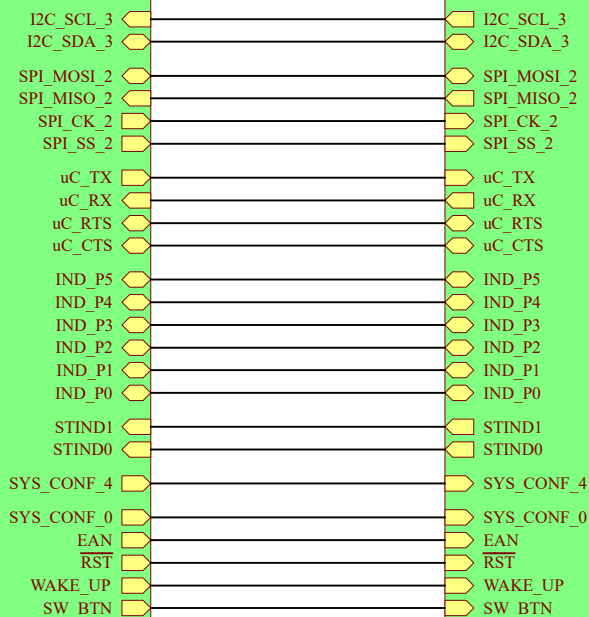
MUX ADC
MUX ADC.SchDoc



SHIFT REGISTER AND MEASUREMENT OUTPUT
SHIFT REGISTER, MEASUREMENT OUTPUT.SchDoc



PERIPHERAL DEVICES
PERIPHERAL DEVICES.SchDoc



Fixations & divers
FIXATIONS.SchDoc

EPFL

CH - 1015
LAUSANNE

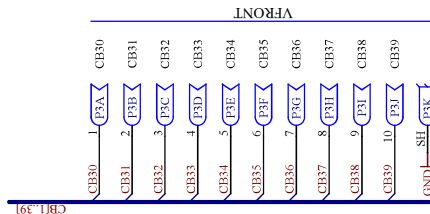
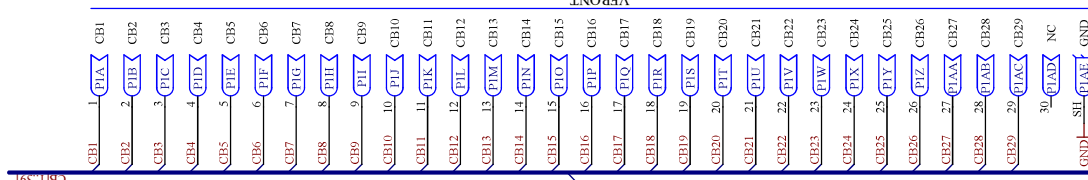
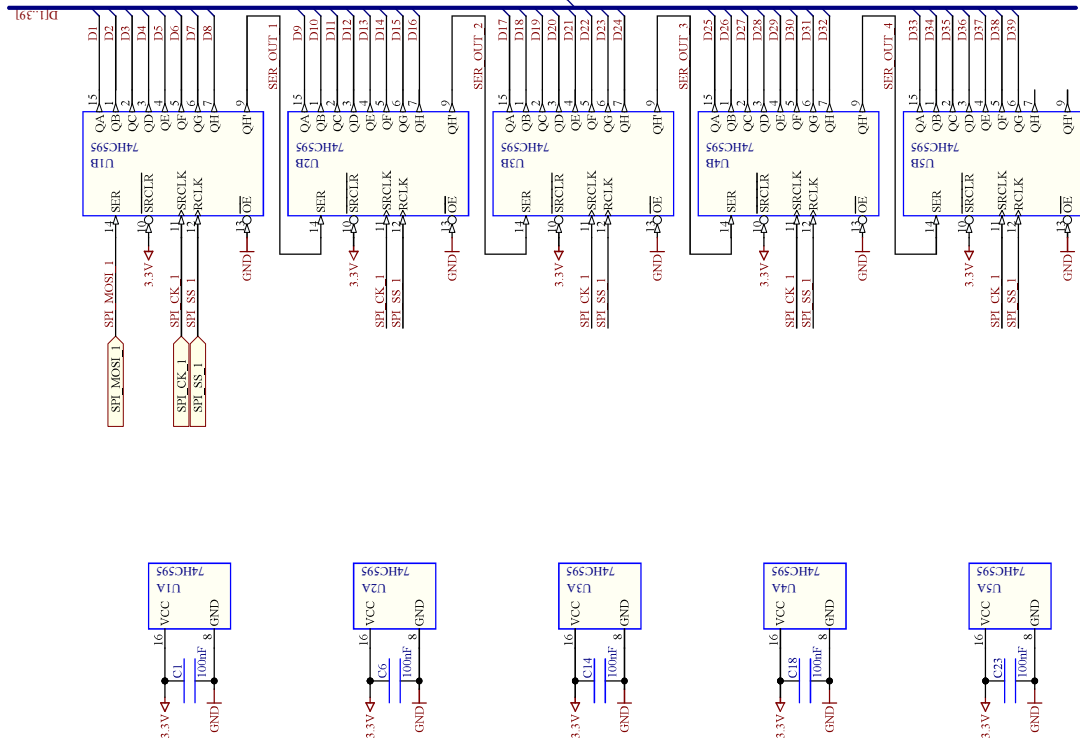
PLANTAR PRESSURE MEASUREMENT

TOP LEVEL
Variante : STD ASSY

Dessiné par : RC2-Pilloud	Préverengs le : 13.09.2022
Contr. par : - '	Modifié le : -
Apprv. par : - '	Modifié le : -
Format de la feuille : A4	Modifié le : -
Feuille 1 de 8	Modifié le : -

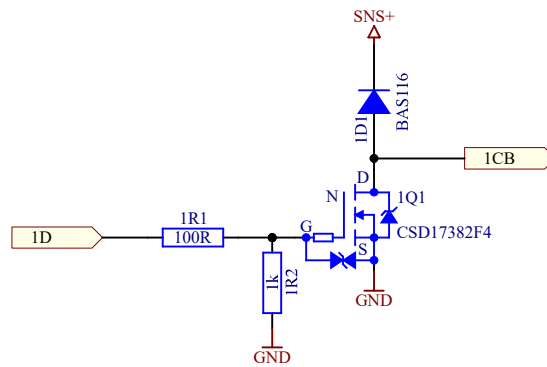
EPFL002A

<div>EPFL</div> <div>CH-1015 LAUSANNE</div>	PLANTAR PRESSURE MEASUREMENT			Dessiné par : RC24-PHILAUD	Prévu(e) le : 13/09/2022
	POWER MANAGEMENT			Contr. par : -	Modifié le : -
	Variante : STD ASSY			Appr. par : -	Modifié le : -
				Format de la feuille : A3	Modifié le : -
				Feuille : 2 de 8	Modifié le : -
EPFL NTELLA			EPFL002A		
TRAVAUX EXECUTES PAR : RC2 ELECTRONIQUE SA, CH-1028 PREVIERENNES, TEL : +41 (0)21 863 74.40, EMAIL : rc2@epc2.ch					
Fisher n° : POWER MANAGEMENT S&B&S					



<div>EPFL</div> <div>CH - 1015 LAUSANNE</div>	PLANTAR PRESSURE MEASUREMENT		Dessiné par : RC2-Phload		Prévalidé le : 13.09.2022	
			Contr. par : -		Modifié le : -	
			Appr. par : -		Modifié le : -	
			Format de la feuille : A3		Modifié le : -	
			Feuille : 4 de 8		Modifié le : -	
EPFL NTELLA		EPFL002A				
TRAVAUX EXÉCUTÉS PAR : RC2 ELECTRONIQUE SA, CH-1028 PREVERENGES, TEL. : +41 (0)21 865 74 40, EMAIL : rc2@rc2.ch						
Ficheur n° : SHIFT REGISTER, MEASUREMENT OUTPUT, SchDoe						

THIS SCHEMATIC IS REPEATED 39 x



CH - 1015
LAUSANNE

PLANTAR PRESSURE MEASUREMENT

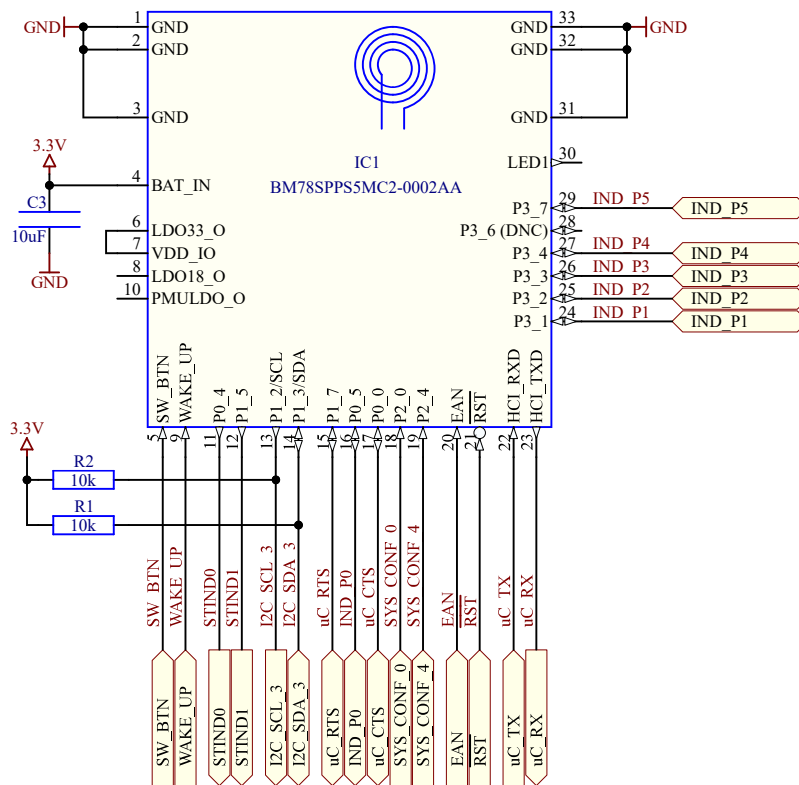
CURRENT REGULATOR
Variante : STD ASSY

EPFL NTELLA

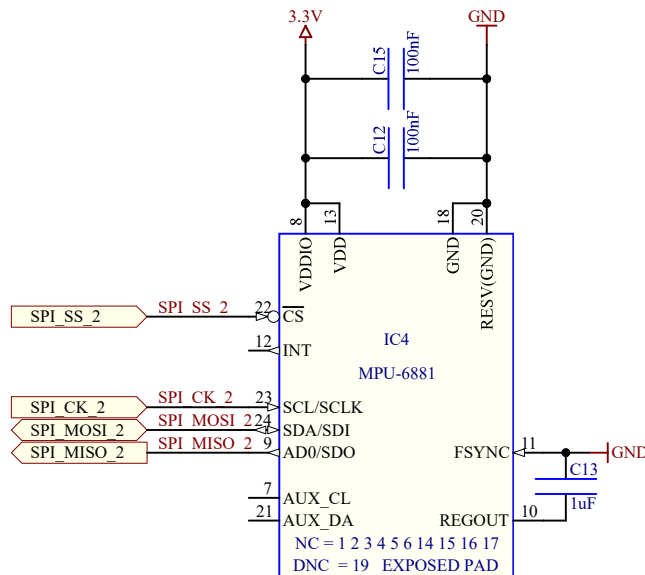
Dessiné par : RC2-Pilloud	Préverenges le : 13.09.2022
Contr. par : - '	Modifié le : -
Apprv. par : - '	Modifié le : -
Format de la feuille : A4	Modifié le : -
Feuille 5 de 8	Modifié le : -

EPFL002A

BLUETOOTH



GYROSCOPE

**EPFL**CH - 1015
LAUSANNE

PLANTAR PRESSURE MEASUREMENT

PERIPHERAL DEVICES
Variante : STD ASSY

EPFL NTELLA

Dessiné par : RC2-Pilloud	Préverengs le : 13.09.2022
Contr. par : -	Modifié le : -
Apprv. par : -	Modifié le : -
Format de la feuille : A4	Modifié le : -
Feuille 7 de 8	Modifié le : -

EPFL002A

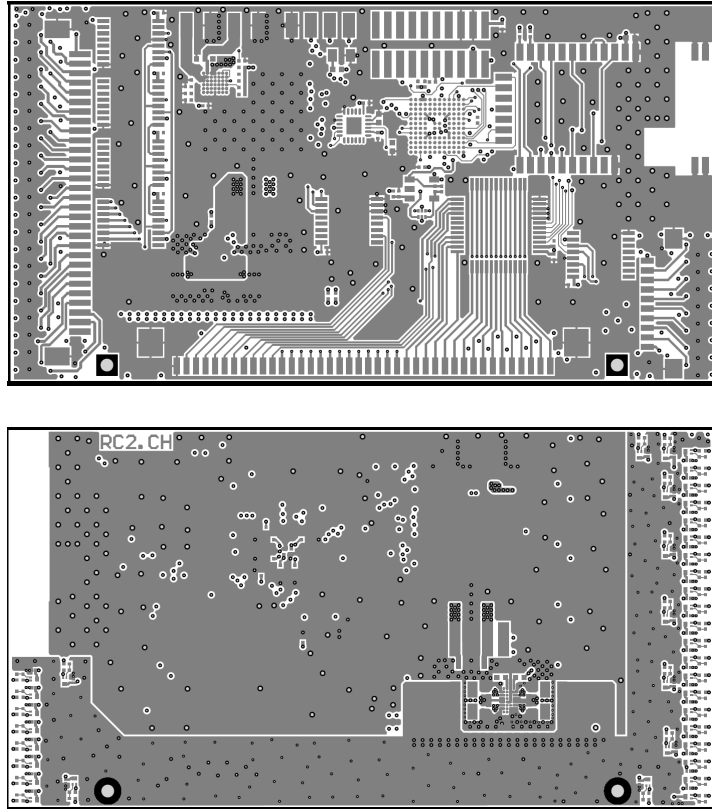


Figure A.1: Top and bottom layers

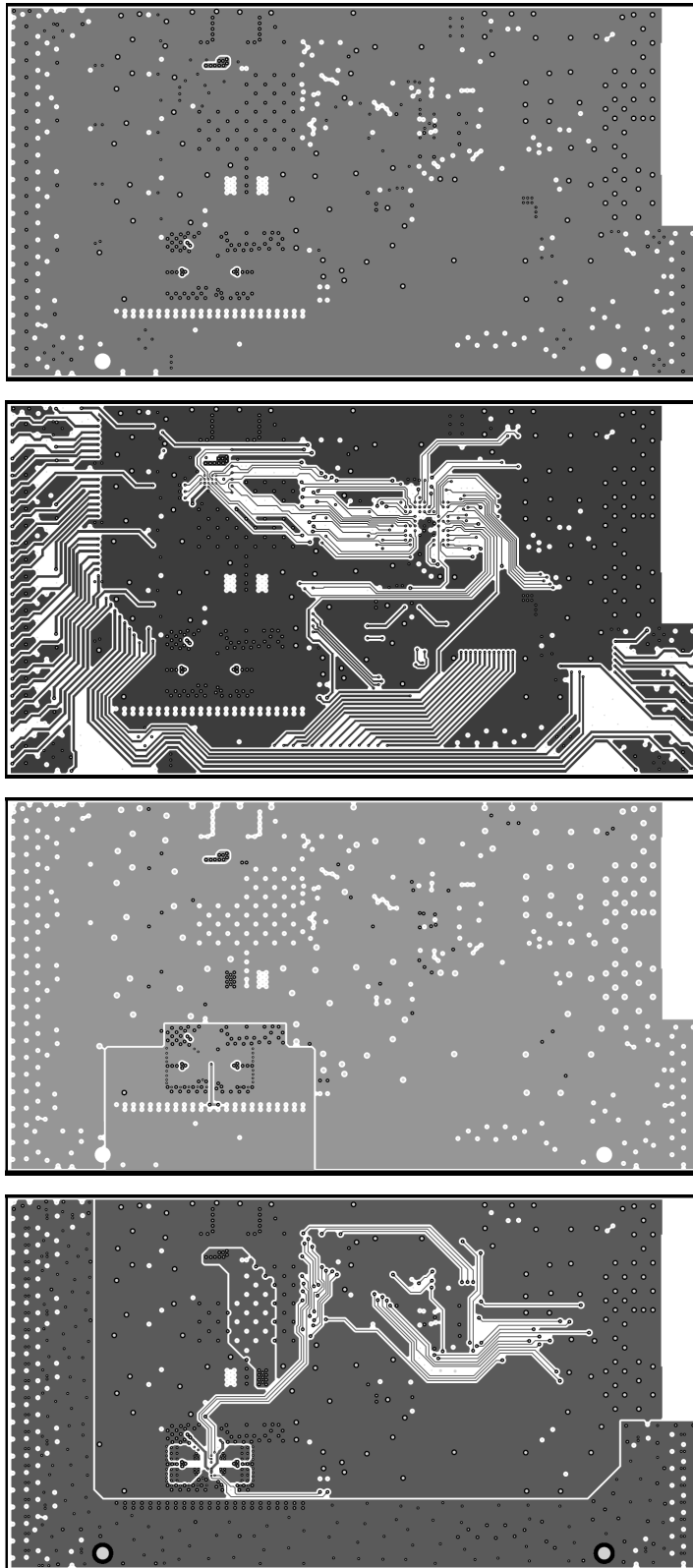


Figure A.2: Middle layers

B Materials

B.1 MR fluid

The MR fluid MRF-132DG by Lord Corporation is used as the working fluid in every experiment presented in this thesis. This fluid is chosen due to its magnetic properties (B-H and τ -H curves), as well as due to its consistency. Sedimentation does not appear so easily as in other types of fluids, too.

B.2 MR module

Regarding the MR module fabrication:

- The elastic membrane at the bottom of the module is fabricated using a latex sheet with 0.2 mm thickness.
- The metallic bellow is fabricated by Mera Bellows company.
- The module is filled through holes that are sealed with screws after the end of the sealing process.

The total height of the device is 30 mm and the total volume is 4618 mm³.

B.3 Bill of electronic components

Item	Value	Description	Manufacturer	QTE
1	BAS116LP3-7	Diode	Diodes Inc.	39
2	CSD17382F4T	MOSFET N-Channel	Texas Instruments	39
3	RC0201FR-07100RL	Resistor	Yageo	40
4	ERJ-1GNF1001	Resistor	Panasonic	39
5	CL03A104KO3NUNC	Capacitor Ceramic	Samsung	27
6	GRJ155R60J106ME11D	Capacitor Ceramic	Murata	1
7	CL05A475KP5NRNC	Capacitor Ceramic	Samsung	3
8	CL05X105KQ5NUNC	Capacitor Ceramic	Samsung	7
9	C0603X7S1A473K030BC	Capacitor Ceramic	TDK	1
10	CL05A106MQ5NUNC	Capacitor Ceramic	Samsung	4
11	AMK105EBJ226MV-F	Capacitor Ceramic	Taiyo Yuden	11
12	HSMG-C170	LED Green	Broadcom	1
13	BM78SPPS5MC2-0002AA	Bluetooth Module	Microchip Tech.	1
14	DA9070-08V36	Power Management IC	Dialog Sem.	1
15	STM32U585QII3	Microcontroller	STMicroelectronics	1
16	MPU-6881	Accel./Gyroscope 3D	TDK	1
17	MCP6001T-I/OT	Ampli Op	Microchip Tech.	1
18	ADG732BSUZ	Multiplexer	Analog Devices	1
19	CLV4051ATPWRG4Q1	Multiplexer	Texas Instruments	1
20	DG4157EDN-T1-GE4	Analog Switch SPDT	Vishay	1
21	TPS75933KTTR	Voltage Regulator	Texas Instruments	1
22	MAX77874	Quad Phase Buck Reg.	Maxim Integrated	1
23	68613014422	Connector FPC	Wurth Electronics	1
24	FTSH-110-01	Connector Header DIL	Samtec	1
25	686110148922	Connector FFC	Wurth Electronics	1
26	FFC3B07-40-T	Connector FFC	GCT	1
28	RC0201FR-0710KL	Resistor	Yageo	11
29	CRCW0402100RFK	Resistor	Vishay	1
30	RC0201FR-0722KL	Resistor	Yageo	1
31	RC0201JR-071K6L	Resistor	Yageo	1
32	CR0201-FW-1003GLF	Resistor	Bourns	1
33	CR0201AFW-1001GLF	Resistor	Bourns	1
34	CR0201-FW-1800GLF	Resistor	Bourns	1
35	RC0201FR-07100KL	Resistor	Yageo	1
38	DFE201610E-R24M=P2	Inductor	Murata	4
39	SN74HC595	Shift Register	Texas Instruments	5

Table B.1: Bill of materials for the PCB

Bibliography

- [1] J. Rabinow, "The magnetic fluid clutch," *Electrical Engineering* **67**(12), pp. 1167–1167, 1948.
- [2] A.-G. Olabi and A. Grunwald, "Design and application of magneto-rheological fluid," *Materials & design* **28**(10), pp. 2658–2664, 2007.
- [3] R. Ahamed, S.-B. Choi, and M. M. Ferdous, "A state of art on magneto-rheological materials and their potential applications," *Journal of Intelligent Material Systems and Structures* **29**(10), pp. 2051–2095, 2018.
- [4] F. Gordaninejad and S. P. Kelso, "Magneto-rheological fluid shock absorbers for hmwv," in *Smart Structures and Materials 2000: Damping and Isolation*, **3989**, pp. 266–273, SPIE, 2000.
- [5] B. M. Kavlicoglu, F. Gordaninejad, C. A. Evrensel, N. Cobanoglu, Y. Liu, A. Fuchs, and G. Korol, "High-torque magnetorheological fluid clutch," in *Smart Structures and Materials 2002: Damping and Isolation*, **4697**, pp. 393–400, SPIE, 2002.
- [6] S. Sassi, K. Cherif, L. Mezghani, M. Thomas, and A. Kotrane, "An innovative magnetorheological damper for automotive suspension: from design to experimental characterization," *Smart Materials and Structures* **14**(4), p. 811, 2005.
- [7] T. Oba, H. Kadone, M. Hassan, and K. Suzuki, "Robotic ankle-foot orthosis with a variable viscosity link using mr fluid," *IEEE/ASME Transactions on Mechatronics* **24**(2), pp. 495–504, 2019.
- [8] K. J. McDonald, L. Kinnicutt, A. M. Moran, and T. Ranzani, "Modulation of magnetorheological fluid flow in soft robots using electropermanent magnets," *IEEE Robotics and Automation Letters* **7**(2), pp. 3914–3921, 2022.
- [9] R. Balak and Y. C. Mazumdar, "Bistable valves for mr fluid-based soft robotic actuation systems," *IEEE Robotics and Automation Letters* **6**(4), pp. 8285–8292, 2021.
- [10] T.-H. Yang, H. Son, S. Byeon, H. Gil, I. Hwang, G. Jo, S. Choi, S.-Y. Kim, and J. R. Kim, "Magnetorheological fluid haptic shoes for walking in vr," *IEEE Transactions on Haptics* **14**(1), pp. 83–94, 2020.

Bibliography

- [11] R. W. Phillips, *Engineering applications of fluids with a variable yield stress*, University of California, Berkeley, 1969.
- [12] W. Li and H. Du, "Design and experimental evaluation of a magnetorheological brake," *The international journal of advanced manufacturing technology* **21**, pp. 508–515, 2003.
- [13] A. Sidpara, M. Das, and V. Jain, "Rheological characterization of magnetorheological finishing fluid," *Materials and Manufacturing Processes* **24**(12), pp. 1467–1478, 2009.
- [14] I. Frigaard and C. Nouar, "On the usage of viscosity regularisation methods for viscoplastic fluid flow computation," *Journal of non-newtonian fluid mechanics* **127**(1), pp. 1–26, 2005.
- [15] E. Williams, S. Rigby, J. Sproston, and R. Stanway, "Electrorheological fluids applied to an automotive engine mount," *Journal of Non-Newtonian Fluid Mechanics* **47**, pp. 221–238, 1993.
- [16] J. Goldasz and B. Sapinski, "Nondimensional characterization of flow-mode magnetorheological/electrorheological fluid dampers," *Journal of Intelligent Material Systems and Structures* **23**(14), pp. 1545–1562, 2012.
- [17] J. De Vicente, D. J. Klingenberg, and R. Hidalgo-Alvarez, "Magnetorheological fluids: a review," *Soft matter* **7**(8), pp. 3701–3710, 2011.
- [18] E. Lemaire, A. Meunier, G. Bossis, J. Liu, D. Felt, P. Bashtovoi, and N. Matoussevitch, "Influence of the particle size on the rheology of magnetorheological fluids," *Journal of Rheology* **39**(5), pp. 1011–1020, 1995.
- [19] B. De Gans, N. Duin, D. Van den Ende, and J. Mellema, "The influence of particle size on the magnetorheological properties of an inverse ferrofluid," *The Journal of Chemical Physics* **113**(5), pp. 2032–2042, 2000.
- [20] J. M. Ginder, L. Davis, and L. Elie, "Rheology of magnetorheological fluids: models and measurements," *International journal of modern physics b* **10**(23n24), pp. 3293–3303, 1996.
- [21] G. Bossis, O. Volkova, S. Lacis, and A. Meunier, "Magnetorheology: fluids, structures and rheology," *LECTURE NOTES IN PHYSICS-NEW YORK THEN BERLIN-*, pp. 202–232, 2002.
- [22] B. D. Chin, J. H. Park, M. H. Kwon, and O. O. Park, "Rheological properties and dispersion stability of magnetorheological (mr) suspensions," *Rheologica Acta* **40**, pp. 211–219, 2001.
- [23] Y. Rabbani, M. Ashtiani, and S. H. Hashemabadi, "An experimental study on the effects of temperature and magnetic field strength on the magnetorheological fluid stability and mr effect," *Soft matter* **11**(22), pp. 4453–4460, 2015.

-
- [24] S. Hong, G. Wang, W. Hu, and N. Wereley, "Liquid spring shock absorber with controllable magnetorheological damping," *Proceedings of the Institution of Mechanical Engineers, Part D: Journal of Automobile Engineering* **220**(8), pp. 1019–1029, 2006.
- [25] E. Kostamo, J. Kostamo, J. Kajaste, and M. Pietola, "Magnetorheological valve in servo applications," *Journal of Intelligent Material Systems and Structures* **23**(9), pp. 1001–1010, 2012.
- [26] M. Mao, W. Hu, Y.-T. Choi, and N. M. Wereley, "A magnetorheological damper with bifold valves for shock and vibration mitigation," *Journal of Intelligent Material Systems and Structures* **18**(12), pp. 1227–1232, 2007.
- [27] D. Grivon, Y. Civet, Z. Pataky, and Y. Perriard, "Design and characterization of a soft magneto-rheological miniature shock absorber for a controllable variable stiffness sole," *Archives of Electrical Engineering* **64**(4), pp. 547–558, 2015.
- [28] M. K. Thakur and C. Sarkar, "Investigation of different groove profile effects on torque transmission in shear mode magnetorheological clutch: numerical simulation and experimental study," *Journal of Tribology* **143**(9), 2021.
- [29] H. Wang and C. Bi, "Study of a magnetorheological brake under compression-shear mode," *Smart Materials and Structures* **29**(1), p. 017001, 2019.
- [30] G. Song and M. Zeng, "A thin-film magnetorheological fluid damper/lock," *Smart materials and structures* **14**(2), p. 369, 2005.
- [31] M. Jolly and J. Carlson, "Actuator 96," in *Proceedings of the 5 th International Conference on New Actuators. Bremen, Germany: Axon Technologie Consult GmbH*, 1996.
- [32] N. M. Wereley and L. Pang, "Nondimensional analysis of semi-active electrorheological and magnetorheological dampers using approximate parallel plate models," *Smart materials and structures* **7**(5), p. 732, 1998.
- [33] A. Grunwald and A.-G. Olabi, "Design of magneto-rheological (MR) valve," *Sensors and Actuators A: Physical* **148**(1), pp. 211–223, 2008.
- [34] M. R. Jolly, J. W. Bender, and J. D. Carlson, "Properties and applications of commercial magnetorheological fluids," *Journal of intelligent material systems and structures* **10**(1), pp. 5–13, 1999.
- [35] H.-Y. Yang and M. Pan, "Engineering research in fluid power: a review," *Journal of Zhejiang University-Science A* **16**(6), pp. 427–442, 2015.
- [36] M. G. El-Din and M. Rabi, *Fluid power engineering*, McGraw-Hill Education, 2009.
- [37] K.-E. Rydberg, "Energy efficient hydraulic hybrid drives," in *11th Scandinavian International Conference on Fluid Power, SICFP'09, June 2-4, Linköping, Sweden*, 2009.

- [38] T. Lin, Q. Wang, B. Hu, and W. Gong, "Development of hybrid powered hydraulic construction machinery," *Automation in construction* **19**(1), pp. 11–19, 2010.
- [39] O. Vorozhtsov, I. Plaksin, and A. Trifanov, "Application of gear hydraulic machines in the composition of hydrostatic transmissions," in *IOP Conference Series: Earth and Environmental Science*, **979**(1), p. 012023, IOP Publishing, 2022.
- [40] S. Sevagin and V. Mnatsakanyan, "Ensuring the required manufacturing quality of hydraulic-cylinder rods in mining machines," in *IOP Conference Series: Materials Science and Engineering*, **709**(4), p. 044095, IOP Publishing, 2020.
- [41] S.-H. Hyon, Y. Taniai, K. Hiranuma, K. Yasunaga, and H. Mizui, "Overpressure compensation for hydraulic hybrid servo booster applied to hydraulic manipulator," *IEEE Robotics and Automation Letters* **4**(2), pp. 942–949, 2019.
- [42] S.-R. Yang, Z.-M. Wang, Y. Yu, and Y.-F. Lu, "Design and research of underwater hydraulic driven diamond chain saw cutting machine," in *IOP Conference Series: Earth and Environmental Science*, **707**(1), p. 012006, IOP Publishing, 2021.
- [43] S. C. Lee, H. G. Moon, S. H. Hwang, D. B. Shin, I. H. Baek, D. I. Sun, J.-K. Ryu, and C. S. Han, "Development of an assembled gripper for a hydraulic cutting machine with a novel design for the stable holding of various shaped objects," *International Journal of Precision Engineering and Manufacturing* **22**(8), pp. 1413–1424, 2021.
- [44] E. Soriano, H. Rubio, C. Castejón, and J. García-Prada, "Design of a low-cost manipulator arm for industrial fields," in *New Trends in Mechanism and Machine Science: From Fundamentals to Industrial Applications*, pp. 839–847, Springer, 2015.
- [45] Y. Sun, S. Song, X. Liang, and H. Ren, "A miniature soft robotic manipulator based on novel fabrication methods," *IEEE Robotics and Automation Letters* **1**(2), pp. 617–623, 2016.
- [46] H. K. Yap, P. M. Khin, T. H. Koh, Y. Sun, X. Liang, J. H. Lim, and C.-H. Yeow, "A fully fabric-based bidirectional soft robotic glove for assistance and rehabilitation of hand impaired patients," *IEEE Robotics and Automation Letters* **2**(3), pp. 1383–1390, 2017.
- [47] Y. Jiang, J. Ma, D. Chen, Z. Liu, Y. Li, and J. Paik, "Compact pneumatic clutch with integrated stiffness variation and position feedback," *IEEE Robotics and Automation Letters* **6**(3), pp. 5697–5704, 2021.
- [48] W. Sun, H. Pan, and H. Gao, "Filter-based adaptive vibration control for active vehicle suspensions with electrohydraulic actuators," *IEEE Transactions on Vehicular Technology* **65**(6), pp. 4619–4626, 2015.
- [49] A. Ainla, M. S. Verma, D. Yang, and G. M. Whitesides, "Soft, rotating pneumatic actuator," *Soft robotics* **4**(3), pp. 297–304, 2017.

-
- [50] J. W. Booth, J. C. Case, E. L. White, D. S. Shah, and R. Kramer-Bottiglio, "An addressable pneumatic regulator for distributed control of soft robots," in *2018 IEEE International Conference on Soft Robotics (RoboSoft)*, pp. 25–30, IEEE, 2018.
- [51] G. Gerboni, T. Ranzani, A. Diodato, G. Ciuti, M. Cianchetti, and A. Menciassi, "Modular soft mechatronic manipulator for minimally invasive surgery (MIS): overall architecture and development of a fully integrated soft module," *Meccanica* **50**(11), pp. 2865–2878, 2015.
- [52] C. Chen, W. Tang, Y. Hu, Y. Lin, and J. Zou, "Fiber-reinforced soft bending actuator control utilizing on/off valves," *IEEE Robotics and Automation Letters* **5**(4), pp. 6732–6739, 2020.
- [53] K. Ahn and S. Yokota, "Intelligent switching control of pneumatic actuator using on/off solenoid valves," *Mechatronics* **15**(6), pp. 683–702, 2005.
- [54] S. Nam, W. Lee, S. Yoo, K. Kim, and W. K. Chung, "Development of backdrivable servovalve with feedback spring for enhanced electro-hydraulic torque actuator," *IEEE Robotics and Automation Letters* **5**(2), pp. 3145–3152, 2020.
- [55] J. Poccarr-Saudart, S. Xu, C. B. Teeple, N.-S. P. Hyun, K. P. Becker, and R. J. Wood, "Controlling soft fluidic actuators using soft DEA-based valves," *IEEE Robotics and Automation Letters* **7**(4), pp. 8837–8844, 2022.
- [56] S. Yoo, W. Lee, and W. K. Chung, "Intrinsically backdrivable hydraulic servovalve for interactive robot control," in *2017 IEEE International Conference on Robotics and Automation (ICRA)*, pp. 51–57, IEEE, 2017.
- [57] H. Shi, Z. Liu, H. Wang, and X. Mei, "Design and performance analysis of hydraulic switching valve driven by magnetic shape memory alloy," *Advances in Mechanical Engineering* **13**(5), p. 16878140211016985, 2021.
- [58] M. C. Carrozza, A. Arena, D. Accoto, A. Menciassi, and P. Dario, "A SMA-actuated miniature pressure regulator for a miniature robot for colonoscopy," *Sensors and Actuators A: Physical* **105**(2), pp. 119–131, 2003.
- [59] B. Mosadegh, C.-H. Kuo, Y.-C. Tung, Y.-s. Torisawa, T. Bersano-Begey, H. Tavana, and S. Takayama, "Integrated elastomeric components for autonomous regulation of sequential and oscillatory flow switching in microfluidic devices," *Nature physics* **6**(6), pp. 433–437, 2010.
- [60] P. Rothmund, A. Ainla, L. Belding, D. J. Preston, S. Kurihara, Z. Suo, and G. M. Whitesides, "A soft, bistable valve for autonomous control of soft actuators," *Science Robotics* **3**(16), p. eaar7986, 2018.
- [61] A. Zatopa, S. Walker, and Y. Menguc, "Fully soft 3D-printed electroactive fluidic valve for soft hydraulic robots," *Soft robotics* **5**(3), pp. 258–271, 2018.

- [62] F. Imaduddin, S. A. Mazlan, M. A. A. Rahman, H. Zamzuri, B. Ichwan, *et al.*, “A high performance magnetorheological valve with a meandering flow path,” *Smart Materials and Structures* **23**(6), p. 065017, 2014.
- [63] A. Tonazzini, A. Sadeghi, and B. Mazzolai, “Electrorheological valves for flexible fluidic actuators,” *Soft Robotics* **3**(1), pp. 34–41, 2016.
- [64] J.-W. Kim, K. Yoshida, K. Kouda, and S. Yokota, “A flexible electro-rheological microvalve (ferv) based on su-8 cantilever structures and its application to microactuators,” *Sensors and Actuators A: Physical* **156**(2), pp. 366–372, 2009.
- [65] K. Yoshida, K. Kamiyama, J.-w. Kim, and S. Yokota, “An intelligent microactuator robust against disturbance using electro-rheological fluid,” *Sensors and Actuators A: Physical* **175**, pp. 101–107, 2012.
- [66] K. Yoshida, M. Kikuchi, J.-H. Park, and S. Yokota, “Fabrication of micro electro-rheological valves (er valves) by micromachining and experiments,” *Sensors and Actuators A: Physical* **95**(2-3), pp. 227–233, 2002.
- [67] R. Balak and Y. C. Mazumdar, “Bistable valves for MR fluid-based soft robotic actuation systems,” *IEEE Robotics and Automation Letters* **6**(4), pp. 8285–8292, 2021.
- [68] T.-H. Lee, C. Han, and S.-B. Choi, “Design and damping force characterization of a new magnetorheological damper activated by permanent magnet flux dispersion,” *Smart Materials and Structures* **27**(1), p. 015013, 2017.
- [69] S. L. Ntella, M.-T. Duong, Y. Civet, Z. Pataky, and Y. Perriard, “Design optimization of miniature magnetorheological valves with self-sensing capabilities used for a wearable medical application,” in *2020 IEEE/ASME International Conference on Advanced Intelligent Mechatronics (AIM)*, pp. 409–414, IEEE, 2020.
- [70] H. Shi, Z. Liu, H. Wang, and X. Mei, “Design and performance analysis of hydraulic switching valve driven by magnetic shape memory alloy,” *Advances in Mechanical Engineering* **13**(5), p. 16878140211016985, 2021.
- [71] A. D. Marchese, C. D. Onal, and D. Rus, “Soft robot actuators using energy-efficient valves controlled by electropermanent magnets,” in *2011 IEEE/RSJ International Conference on Intelligent Robots and Systems*, pp. 756–761, IEEE, 2011.
- [72] Y. Miyaki and H. Tsukagoshi, “Self-excited vibration valve that induces traveling waves in pneumatic soft mobile robots,” *IEEE Robotics and Automation Letters* **5**(3), pp. 4133–4139, 2020.
- [73] K. Gilpin, A. Knaian, and D. Rus, “Robot pebbles: One centimeter modules for programmable matter through self-disassembly,” in *2010 IEEE International Conference on Robotics and Automation*, pp. 2485–2492, IEEE, 2010.

-
- [74] B. Haghighat, E. Droz, and A. Martinoli, "Lily: A miniature floating robotic platform for programmable stochastic self-assembly," in *2015 IEEE International Conference on Robotics and Automation (ICRA)*, pp. 1941–1948, May 2015.
- [75] T. Leps, P. Glick, D. Ruffatto III, A. Parness, M. Tolley, and C. Hartzell, "A low-power, jamming, magnetorheological valve using electropermanent magnets suitable for distributed control in soft robots," *Smart Materials and Structures* **29**(10), p. 105025, 2020.
- [76] K. J. McDonald, L. Kinnicutt, A. M. Moran, and T. Ranzani, "Modulation of magnetorheological fluid flow in soft robots using electropermanent magnets," *IEEE Robotics and Automation Letters* **7**(2), pp. 3914–3921, 2022.
- [77] J.-H. Yoo and N. M. Wereley, "Design of a high-efficiency magnetorheological valve," *Journal of Intelligent Material Systems and Structures* **13**(10), pp. 679–685, 2002.
- [78] N. Guo, H. Du, and W. Li, "Finite element analysis and simulation evaluation of a magnetorheological valve," *The international journal of advanced manufacturing technology* **21**, pp. 438–445, 2003.
- [79] N. C. Rosenfeld and N. M. Wereley, "Volume-constrained optimization of magnetorheological and electrorheological valves and dampers," *Smart Materials and Structures* **13**(6), p. 1303, 2004.
- [80] U. Dogruer, F. Gordaninejad, and C. A. Evrensel, "A new magnetorheological fluid damper for high-mobility multipurpose wheeled vehicle (hmmwv)," in *Smart Structures and Materials 2003: Damping and Isolation*, **5052**, pp. 198–206, SPIE, 2003.
- [81] A. Grunwald and A.-G. Olabi, "Design of magneto-rheological (mr) valve," *Sensors and Actuators A: Physical* **148**(1), pp. 211–223, 2008.
- [82] L. Yang, F. Duan, and A. Eriksson, "Analysis of the optimal design strategy of a magnetorheological smart structure," *Smart Materials and Structures* **17**(1), p. 015047, 2008.
- [83] M. M. Naserimojarad, M. Moallem, and S. Arzanpour, "A comprehensive approach for optimal design of magnetorheological dampers," *Journal of Intelligent Material Systems and Structures* **29**(18), pp. 3648–3655, 2018.
- [84] Q.-H. Nguyen, Y.-M. Han, S.-B. Choi, and N. M. Wereley, "Geometry optimization of mr valves constrained in a specific volume using the finite element method," *Smart Materials and Structures* **16**(6), p. 2242, 2007.
- [85] Q.-H. Nguyen, S.-B. Choi, and N. M. Wereley, "Optimal design of magnetorheological valves via a finite element method considering control energy and a time constant," *Smart Materials and Structures* **17**(2), p. 025024, 2008.
- [86] Q.-H. Nguyen and S.-B. Choi, "Optimal design of a vehicle magnetorheological damper considering the damping force and dynamic range," *Smart materials and Structures* **18**(1), p. 015013, 2008.

Bibliography

- [87] Q.-H. Nguyen and S.-B. Choi, "Optimal design of mr shock absorber and application to vehicle suspension," *Smart materials and Structures* **18**(3), p. 035012, 2009.
- [88] F. Gao, Y.-N. Liu, and W.-H. Liao, "Optimal design of a magnetorheological damper used in smart prosthetic knees," *Smart Materials and Structures* **26**(3), p. 035034, 2017.
- [89] Q. Zhao, Y. Wang, and F. Gao, "Multiobjective evolutionary optimization design of vehicle magnetorheological fluid damper," in *International Conference on Smart Materials and Nanotechnology in Engineering*, **6423**, pp. 793–800, SPIE, 2007.
- [90] K.-G. Sung, Y.-M. Han, and S.-B. Choi, "Geometric optimization of controllable magnetorheological shock absorber for commercial passenger vehicle," in *Active and Passive Smart Structures and Integrated Systems 2008*, **6928**, pp. 187–197, SPIE, 2008.
- [91] S. Ha, S. Choi, E. Rhee, and P. Kang, "Optimal design of a magnetorheological fluid suspension for tracked vehicle," in *Journal of Physics: Conference Series*, **149**(1), p. 012053, IOP Publishing, 2009.
- [92] Q. Nguyen, S. B. Choi, Y. Lee, and M. Han, "Optimal design of high damping force engine mount featuring mr valve structure with both annular and radial flow paths," *Smart Materials and Structures* **22**(11), p. 115024, 2013.
- [93] G. Hu, F. Zhou, and L. Yu, "Optimal design and performance analysis of radial mr valve with single excitation coil," in *Actuators*, **10**(2), p. 34, MDPI, 2021.
- [94] A. Hadadian, R. Sedaghati, and E. Esmailzadeh, "Optimal design of magnetorheological damper using response surface method," in *53rd AIAA/ASME/ASCE/AHS/ASC Structures, Structural Dynamics and Materials Conference 20th AIAA/ASME/AHS Adaptive Structures Conference 14th AIAA*, p. 1835, 2012.
- [95] Z. Parlak, T. Engin, and İ. Şahin, "Optimal magnetorheological damper configuration using the taguchi experimental design method," *Journal of Mechanical Design* **135**(8), 2013.
- [96] A. Hadadian, R. Sedaghati, and E. Esmailzadeh, "Design optimization of magnetorheological fluid valves using response surface method," *Journal of Intelligent Material Systems and Structures* **25**(11), pp. 1352–1371, 2014.
- [97] S. Mangal and A. Kumar, "Geometric parameter optimization of magneto-rheological damper using design of experiment technique," *International Journal of Mechanical and Materials Engineering* **10**, pp. 1–9, 2015.
- [98] H. Krishna, H. Kumar, and K. Gangadharan, "Optimization of magneto-rheological damper for maximizing magnetic flux density in the fluid flow gap through fea and ga approaches," *Journal of The Institution of Engineers (India): Series C* **98**, pp. 533–539, 2017.

-
- [99] A. Nanthakumar and J. Jancirani, "Design optimization of magnetorheological damper geometry using response surface method for achieving maximum yield stress," *Journal of Mechanical Science and Technology* **33**, pp. 4319–4329, 2019.
- [100] M. Keshav, A. Bhagyarajan, and S. Chandramohan, "Regression models for magnetic flux density using doe techniques and geometric optimization of mr valve," *Smart Materials and Structures* **28**(7), p. 075008, 2019.
- [101] M. Olivier and J. W. Sohn, "Design and geometric parameter optimization of hybrid magnetorheological fluid damper," *Journal of Mechanical Science and Technology* **34**, pp. 2953–2960, 2020.
- [102] J. Ren, F. Zhou, N. Wang, and G. Hu, "Multi-objective optimization design and dynamic performance analysis of an enhanced radial magnetorheological valve with both annular and radial flow paths," in *Actuators*, **11**(5), p. 120, MDPI, 2022.
- [103] G. Hu, F. Zhou, W. Zhu, L. Yu, and G. Li, "Geometric optimization and performance analysis of radial mr valve using taguchi orthogonal experiment method," *Journal of Mechanical Science and Technology* **36**(9), pp. 4593–4614, 2022.
- [104] G. Hu, L. Wu, Y. Deng, L. Yu, and G. Li, "Optimal design and performance analysis of magnetorheological damper based on multiphysics coupling model," *Journal of Magnetism and Magnetic Materials* **558**, p. 169527, 2022.
- [105] N. Nikhil Asok, S. Joshy, R. Suraj, A. Viswanath, and A. Rakesh, "Optimization of geometrical parameters in magnetorheological dampers using finite element modeling," in *Applications of Computation in Mechanical Engineering: Select Proceedings of 3rd International Conference on Computing in Mechanical Engineering (ICCME 2021)*, pp. 239–251, Springer, 2022.
- [106] K. Manjeet and C. M. Sujatha, "Modeling and optimization of non-linear herschel-bulkley fluid model based magnetorheological valve geometry," in *2018 IEEE/ASME International Conference on Advanced Intelligent Mechatronics (AIM)*, pp. 413–420, IEEE, 2018.
- [107] K. Manjeet and C. Sujatha, "Magnetorheological valves based on herschel–bulkley fluid model: modelling, magnetostatic analysis and geometric optimization," *Smart Materials and Structures* **28**(11), p. 115008, 2019.
- [108] M. Keshav and S. Chandramohan, "Geometric optimisation of magnetorheological valve using feedforward neural networks for distribution of magnetic flux density inside the valve," *Smart Materials and Structures* **28**(10), p. 105018, 2019.
- [109] P. Kuzhir, G. Bossis, and V. Bashtovoi, "Optimization of magnetorheological fluid valves," *International Journal of Modern Physics B* **19**(07n09), pp. 1229–1235, 2005.

Bibliography

- [110] Q. Nguyen, S. Choi, Y. Lee, and M. Han, "An analytical method for optimal design of mr valve structures," *Smart Materials and Structures* **18**(9), p. 095032, 2009.
- [111] X. Zhu, X. Jing, and L. Cheng, "Optimal design of control valves in magnetorheological fluid dampers using a nondimensional analytical method," *Journal of intelligent material systems and structures* **24**(1), pp. 108–129, 2013.
- [112] M. Jiang, X. Rui, F. Yang, W. Zhu, and Y. Zhang, "Multi-objective optimization design for a magnetorheological damper," *Journal of Intelligent Material Systems and Structures* **33**(1), pp. 33–45, 2022.
- [113] M. Abdalaziz, R. Sedaghati, and H. Vatandoost, "Design optimization and experimental evaluation of a large capacity magnetorheological damper with annular and radial fluid gaps," *Journal of Intelligent Material Systems and Structures* , p. 1045389X221151075, 2023.
- [114] A. Gholizadeh and M. Javanmard, "Magnetically actuated microfluidic transistors: Miniaturized micro-valves using magnetorheological fluids integrated with elastomeric membranes," *Journal of Microelectromechanical Systems* **25**(5), pp. 922–928, 2016.
- [115] T.-H. Yang, H.-J. Kwon, S. S. Lee, J. An, J.-H. Koo, S.-Y. Kim, and D.-S. Kwon, "Development of a miniature tunable stiffness display using mr fluids for haptic application," *Sensors and Actuators A: Physical* **163**(1), pp. 180–190, 2010.
- [116] H. Ai, D. Wang, and W. Liao, "Design and modeling of a magnetorheological valve with both annular and radial flow paths," *Journal of intelligent material systems and structures* **17**(4), pp. 327–334, 2006.
- [117] F. Imaduddin, S. A. Mazlan, H. Zamzuri, and I. I. M. Yazid, "Design and performance analysis of a compact magnetorheological valve with multiple annular and radial gaps," *Journal of Intelligent Material Systems and Structures* **26**(9), pp. 1038–1049, 2015.
- [118] G. Hu, M. Liao, and W. Li, "Analysis of a compact annular-radial-orifice flow magnetorheological valve and evaluation of its performance," *Journal of Intelligent Material Systems and Structures* **28**(10), pp. 1322–1333, 2017.
- [119] M. Abdalaziz, H. Vatandoost, R. Sedaghati, and S. Rakheja, "Development and experimental characterization of a large-capacity magnetorheological damper with annular-radial gap," *Smart Materials and Structures* **31**(11), p. 115021, 2022.
- [120] J. Li, W. Wang, Y. Xia, H. He, and W. Zhu, "The soft-landing features of a micro-magnetorheological fluid damper," *Applied Physics Letters* **106**(1), p. 014104, 2015.
- [121] S. Liu, L. Feng, D. Zhao, H. Huang, X. Shi, L. Chen, and J. Jiang, "The development of an outer multi-pole magneto-rheological damper with high dynamic range of damping force," *Smart Materials and Structures* **27**(11), p. 115025, 2018.

-
- [122] D. Grivon, "Design, modelling and sensing possibilities of magneto-rheological based devices," tech. rep., EPFL, 2017.
- [123] C. Bolzmacher, G. Changeon, V. Plaud, S. Roselier, J. Lozada, and M. Hafez, "Tactile refreshable screen based on magneto-rheological fluids for map exploration and navigation tasks," in *Smart Sensors, Actuators, and MEMS V*, **8066**, pp. 560–569, SPIE, 2011.
- [124] J. Huang, S. Li, Y. Zhou, T. Xu, Y. Li, H. Wang, and S. Wang, "A heavy-duty magnetorheological fluid mount with flow and squeeze model," *Smart Materials and Structures* **30**(8), p. 085012, 2021.
- [125] Y. Liu, Y. Zhang, B. Tang, M. Gao, and J. Dai, "Introducing the thermal field into multiphysics coupling for the modeling of mr fluid-based micro-brake," *International Journal of Heat and Mass Transfer* **180**, p. 121785, 2021.
- [126] R. Sukhnandan, K. Dai, and V. Webster-Wood, "A magnetorheological fluid-based damper towards increased biomimeticism in soft robotic actuators," in *2022 International Conference on Robotics and Automation (ICRA)*, pp. 11445–11451, IEEE, 2022.
- [127] D. Lai and D. Wang, "Principle, modeling, and validation of a relative displacement self-sensing magnetorheological damper," in *Smart Structures and Materials 2005: Smart Structures and Integrated Systems*, **5764**, pp. 130–141, SPIE, 2005.
- [128] D. Wang and T. Wang, "Principle, design and modeling of an integrated relative displacement self-sensing magnetorheological damper based on electromagnetic induction," *Smart Materials and Structures* **18**(9), p. 095025, 2009.
- [129] D. Wang, X. Bai, and W. Liao, "An integrated relative displacement self-sensing magnetorheological damper: prototyping and testing," *Smart Materials and Structures* **19**(10), p. 105008, 2010.
- [130] C. Chen and W.-H. Liao, "A self-powered, self-sensing magnetorheological damper," in *2010 IEEE International Conference on Mechatronics and Automation*, pp. 1364–1369, IEEE, 2010.
- [131] C. Chen and W.-H. Liao, "A self-sensing magnetorheological damper with power generation," *Smart Materials and Structures* **21**(2), p. 025014, 2012.
- [132] D.-H. Wang and X.-X. Bai, "Pareto optimization-based tradeoff between the damping force and the sensed relative displacement of a self-sensing magnetorheological damper," *Journal of Intelligent Material Systems and Structures* **22**(13), pp. 1451–1467, 2011.
- [133] D.-H. Wang and X.-X. Bai, "A magnetorheological damper with an integrated self-powered displacement sensor," *Smart Materials and Structures* **22**(7), p. 075001, 2013.

- [134] G. Hu, Y. Ru, and W. Li, "Design and development of a novel displacement differential self-induced magnetorheological damper," *Journal of Intelligent Material Systems and Structures* **26**(5), pp. 527–540, 2015.
- [135] M. M. Ferdaus, M. Rashid, M. Bhuiyan, and A. Muthalif, "Design and performance evaluation of a self-controlled magneto-rheological damper," *International Journal of Robotics and Mechatronics* **1**(2), pp. 74–80, 2014.
- [136] G. Hu, W. Zhou, and W. Li, "A new magnetorheological damper with improved displacement differential self-induced ability," *Smart Materials and Structures* **24**(8), p. 087001, 2015.
- [137] G. Hu, W. Zhou, M. Liao, and W. Li, "Static and dynamic experiment evaluations of a displacement differential self-induced magnetorheological damper," *Shock and Vibration* **2015**, 2015.
- [138] G. Hu, Y. Lu, S. Sun, and W. Li, "Development of a self-sensing magnetorheological damper with magnets in-line coil mechanism," *Sensors and Actuators A: Physical* **255**, pp. 71–78, 2017.
- [139] G. Hu, L. Li, H. Liu, and F. Liu, "Effects of winding cylinder materials on dynamic performances of a new mr damper," *IEEE Access* **8**, pp. 87829–87841, 2020.
- [140] G. Hu, F. Yi, H. Liu, and L. Zeng, "Performance analysis of a novel magnetorheological damper with displacement self-sensing and energy harvesting capability," *Journal of Vibration Engineering & Technologies* **9**, pp. 85–103, 2021.
- [141] D. Grivon, Y. Civet, Z. Pataky, and Y. Perriard, "Detection of pressure or flow rate variations in mr valves through magnetic flux analysis," in *2016 19th International Conference on Electrical Machines and Systems (ICEMS)*, pp. 1–5, IEEE, 2016.
- [142] Z. Chen, K. H. Lam, and Y. Ni, "Enhanced damping for bridge cables using a self-sensing mr damper," *Smart Materials and Structures* **25**(8), p. 085019, 2016.
- [143] X. Guan, Y. Ru, and Y. Huang, "A novel velocity self-sensing magnetorheological damper: Design, fabricate, and experimental analysis," *Journal of Intelligent Material Systems and Structures* **30**(4), pp. 497–505, 2019.
- [144] H. Deng, Y. Gao, R. Hu, S. Zhao, G. Han, X. Lian, M. Ma, and X. Zhong, "Self-sensing automotive magnetorheological dampers for low frequency vibration," *Smart Materials and Structures* **30**(11), p. 115015, 2021.
- [145] J. S. Kumar, P. S. Paul, G. Raghunathan, and D. G. Alex, "A review of challenges and solutions in the preparation and use of magnetorheological fluids," *International journal of mechanical and materials engineering* **14**, pp. 1–18, 2019.

-
- [146] W. Jiang, Y. Zhang, S. Xuan, C. Guo, and X. Gong, "Dimorphic magnetorheological fluid with improved rheological properties," *Journal of Magnetism and Magnetic Materials* **323**(24), pp. 3246–3250, 2011.
- [147] M. A. Portillo and G. Iglesias, "Magnetic nanoparticles as a redispersing additive in magnetorheological fluid," *Journal of Nanomaterials* **2017**, 2017.
- [148] Y. D. Liu, H. J. Choi, and S.-B. Choi, "Controllable fabrication of silica encapsulated soft magnetic microspheres with enhanced oxidation-resistance and their rheology under magnetic field," *Colloids and Surfaces A: Physicochemical and Engineering Aspects* **403**, pp. 133–138, 2012.
- [149] X. Zhang, Y. Yang, K. Guo, S. Sun, G. He, and Z. Li, "Methodology on a novel magnetorheological valve controlled damper synthesis design," *Smart Materials and Structures* **29**(4), p. 045006, 2020.
- [150] X.-X. Bai, W. Hu, and N. M. Wereley, "Magnetorheological damper utilizing an inner bypass for ground vehicle suspensions," *IEEE Transactions on Magnetics* **49**(7), pp. 3422–3425, 2013.
- [151] A. P. Marathe, S. Khot, and J. Nagler, "Development of low-cost optimal magnetorheological damper for automotive application," *Journal of Vibration Engineering & Technologies* **10**(5), pp. 1831–1850, 2022.
- [152] J. Gołdasz and S. Dzierżek, "Parametric study on the performance of automotive mr shock absorbers," in *IOP Conference Series: Materials Science and Engineering*, **148**(1), p. 012004, IOP Publishing, 2016.
- [153] L. Yang, S. Z. Chen, B. Zhang, and Z. Z. Feng, "A rotary magnetorheological damper for a tracked vehicle," in *Advanced Materials Research*, **328**, pp. 1135–1138, Trans Tech Publ, 2011.
- [154] S. P. Kelso, *Development and investigation of magneto-rheological fluid (MRF) dampers for off-highway, high-payload vehicles*, University of Nevada, Reno, 1998.
- [155] R. Madhavrao Desai, S. Acharya, M.-e.-H. Jamadar, H. Kumar, S. Joladarashi, and S. R. Sekaran, "Synthesis of magnetorheological fluid and its application in a twin-tube valve mode automotive damper," *Proceedings of the Institution of Mechanical Engineers, Part L: Journal of Materials: Design and Applications* **234**(7), pp. 1001–1016, 2020.
- [156] M. Makowski and L. Knap, "Investigation of an off-road vehicle equipped with magnetorheological dampers," *Advances in Mechanical Engineering* **10**(5), p. 1687814018778222, 2018.
- [157] A. M. Okamura, "Haptic feedback in robot-assisted minimally invasive surgery," *Current opinion in urology* **19**(1), p. 102, 2009.

- [158] S. Guo, Y. Song, X. Yin, L. Zhang, T. Tamiya, H. Hirata, and H. Ishihara, "A novel robot-assisted endovascular catheterization system with haptic force feedback," *IEEE Transactions on Robotics* **35**(3), pp. 685–696, 2019.
- [159] J. Guo, S. Guo, and Y. Yu, "Design and characteristics evaluation of a novel teleoperated robotic catheterization system with force feedback for vascular interventional surgery," *Biomedical microdevices* **18**, pp. 1–16, 2016.
- [160] F. Ahmadkhanlou, *Design, modeling and control of magnetorheological fluid-based force feedback dampers for telerobotic systems*. PhD thesis, The Ohio State University, 2008.
- [161] D. Wang, Y. Wang, B. Zi, Z. Cao, and H. Ding, "Development of an active and passive finger rehabilitation robot using pneumatic muscle and magnetorheological damper," *Mechanism and Machine Theory* **147**, p. 103762, 2020.
- [162] M. Hassan, M. Kennard, K. Yagi, H. Kadone, H. Mochiyama, and K. Suzuki, "Mrift: A semi-active lower back support exoskeleton based on mr fluid and force retention technology," in *2019 IEEE/RSJ International Conference on Intelligent Robots and Systems (IROS)*, pp. 7349–7354, IEEE, 2019.
- [163] A. Yi, A. Zahedi, Y. Wang, U.-X. Tan, and D. Zhang, "A novel exoskeleton system based on magnetorheological fluid for tremor suppression of wrist joints," in *2019 IEEE 16th International Conference on Rehabilitation Robotics (ICORR)*, pp. 1115–1120, IEEE, 2019.
- [164] D. Alvarado-Rivera, P. A. Niño-Suárez, and L. G. Corona-Ramírez, "Semiactive knee orthotic using a mr damper and a smart insole to control the damping force sensing the plantar pressure," *Frontiers in Neurorobotics* **16**, p. 64, 2022.
- [165] J. Zheng, Z. Li, Y. Lyu, J. Zhou, and R. Song, "Design and simulation of a rotating magnetorheological fluid damper for the ankle rehabilitation robot," in *2020 5th International Conference on Advanced Robotics and Mechatronics (ICARM)*, pp. 153–156, IEEE, 2020.
- [166] N. D. Nordin, A. G. Muthalif, M. K. M. Razali, A. Ali, and A. M. Salem, "Development and implementation of energy-efficient magnetorheological fluid bypass damper for prosthetics limbs using a fuzzy-logic controller," *IEEE Access* **10**, pp. 18978–18987, 2022.
- [167] G. Liu, F. Gao, and W.-H. Liao, "Magnetorheological damper with multi-grooves on piston for damping force enhancement," *Smart Materials and Structures* **30**(2), p. 025007, 2020.
- [168] C. Ochoa-Díaz, T. S. Rocha, L. de Levy Oliveira, M. G. Paredes, R. Lima, A. P. L. Bó, and G. A. Borges, "An above-knee prosthesis with magnetorheological variable-damping," in *5th IEEE RAS/EMBS International Conference on Biomedical Robotics and Biomechanics*, pp. 108–113, IEEE, 2014.
- [169] J.-H. Kim and J.-H. Oh, "Development of an above knee prosthesis using mr damper and leg simulator," in *Proceedings 2001 ICRA. IEEE International Conference on Robotics and Automation (Cat. No. 01CH37164)*, **4**, pp. 3686–3691, IEEE, 2001.

-
- [170] F. Li, H. Xie, W. Yuan, and Y. Liu, "The application research of mr damper in intelligent bionic leg," in *2009 Chinese Control and Decision Conference*, pp. 1327–1331, IEEE, 2009.
- [171] E. Asadi, A. Hoyle, and S. Arzanpour, "Design of a magnetorheological damper-based haptic interface for rehabilitation applications," *Journal of intelligent material systems and structures* **22**(11), pp. 1269–1277, 2011.
- [172] S. Dong, K.-Q. Lu, J. Sun, and K. Rudolph, "Rehabilitation device with variable resistance and intelligent control," *Medical engineering & physics* **27**(3), pp. 249–255, 2005.
- [173] S. Dong, K.-Q. Lu, J. Q. Sun, and K. Rudolph, "Adaptive force regulation of muscle strengthening rehabilitation device with magnetorheological fluids," *IEEE Transactions on neural systems and rehabilitation engineering* **14**(1), pp. 55–63, 2006.
- [174] D. Grivon, Y. Civet, Z. Pataky, and Y. Perriard, "Design and comparison of different magneto-rheological valves configurations," in *2015 IEEE International Conference on Advanced Intelligent Mechatronics (AIM)*, pp. 818–823, IEEE, 2015.
- [175] A. Koivikko, D.-M. Drotlef, M. Sitti, and V. Sariola, "Magnetically switchable soft suction grippers," *Extreme Mechanics Letters* **44**, p. 101263, 2021.
- [176] D. Hua, X. Liu, S. Sun, M. A. Sotelo, Z. Li, and W. Li, "A magnetorheological fluid-filled soft crawling robot with magnetic actuation," *IEEE/ASME Transactions on Mechatronics* **25**(6), pp. 2700–2710, 2020.
- [177] C. M. Hartzell, Y. T. Choi, N. M. Wereley, and T. J. Leps, "Performance of a magnetorheological fluid-based robotic end effector," *Smart Materials and Structures* **28**(3), p. 035030, 2019.
- [178] K. McDonald, A. Rendos, S. Woodman, K. A. Brown, and T. Ranzani, "Magnetorheological fluid-based flow control for soft robots," *Advanced Intelligent Systems* **2**(11), p. 2000139, 2020.
- [179] A. Pettersson, S. Davis, J. O. Gray, T. J. Dodd, and T. Ohlsson, "Design of a magnetorheological robot gripper for handling of delicate food products with varying shapes," *Journal of Food Engineering* **98**(3), pp. 332–338, 2010.
- [180] J. G. Williamson, C. Schell, M. Keller, and J. Schultz, "Extending the reach of single-chamber inflatable soft robots using magnetorheological fluids," in *2021 IEEE 4th International Conference on Soft Robotics (RoboSoft)*, pp. 119–125, IEEE, 2021.
- [181] Y. Tsugami, T. Barbié, K. Tadakuma, and T. Nishida, "Development of universal parallel gripper using reformed magnetorheological fluid," in *2017 11th Asian control conference (ASCC)*, pp. 778–783, IEEE, 2017.
- [182] S. Gorodkin, A. Lukianovich, and W. Kordonski, "Magnetorheological throttle valve in passive damping systems," *Journal of intelligent material systems and structures* **9**(8), pp. 637–641, 1998.

Bibliography

- [183] B. F. Spencer Jr, G. Yang, J. D. Carlson, and M. K. Sain, "Smart dampers for seismic protection of structures: a full-scale study," in *Proceedings of the second world conference on structural control*, **1**, pp. 417–426, Kyoto, 1998.
- [184] W.-M. Chen, T. Lee, P. V.-S. Lee, J. W. Lee, and S.-J. Lee, "Effects of internal stress concentrations in plantar soft-tissue—a preliminary three-dimensional finite element analysis," *Medical engineering & physics* **32**(4), pp. 324–331, 2010.
- [185] N. Hayafune, Y. Hayafune, and H. Jacob, "Pressure and force distribution characteristics under the normal foot during the push-off phase in gait," *The foot* **9**(2), pp. 88–92, 1999.
- [186] N. T. Abdel-Ghani, G. A. El-Chaghaby, M. H. ElGammal, and E.-S. A. Rawash, "Optimizing the preparation conditions of activated carbons from olive cake using koh activation," *New Carbon Materials* **31**(5), pp. 492–500, 2016.
- [187] A. Dean, D. Voss, D. Draguljić, A. Dean, D. Voss, and D. Draguljić, "Response surface methodology," *Design and analysis of experiments*, pp. 565–614, 2017.
- [188] T. Duong, S. L. Ntella, K. Jeanmonod, X. Ren, Y. Civet, Z. Pataky, and Y. Perriard, "Optimal design of magnetorheological valve integrated in an intelligent footwear for diabetic patients with foot insensitivity," in *2021 24th International Conference on Electrical Machines and Systems (ICEMS)*, pp. 111–115, IEEE, 2021.
- [189] B. Haghighat, E. Droz, and A. Martinoli, "Lily: A miniature floating robotic platform for programmable stochastic self-assembly," in *2015 IEEE international conference on robotics and automation (ICRA)*, pp. 1941–1948, IEEE, 2015.
- [190] A. N. Knaian, *Electropermanent magnetic connectors and actuators: devices and their application in programmable matter*. PhD thesis, Massachusetts Institute of Technology, 2010.
- [191] T. Tosun, J. Davey, C. Liu, and M. Yim, "Design and characterization of the ep-face connector," in *2016 IEEE/RSJ International Conference on Intelligent Robots and Systems (IROS)*, pp. 45–51, IEEE, 2016.
- [192] P. Ward and D. Liu, "Design of a high capacity electro permanent magnetic adhesion for climbing robots," in *2012 IEEE International Conference on Robotics and Biomimetics (ROBIO)*, pp. 217–222, IEEE, 2012.
- [193] S. Hauser, M. Mutlu, and A. J. Ijspeert, "Kubits: Solid-state self-reconfiguration with programmable magnets," *IEEE Robotics and Automation Letters* **5**(4), pp. 6443–6450, 2020.
- [194] G. Bertotti, *Hysteresis in magnetism: for physicists, materials scientists, and engineers*, Gulf Professional Publishing, 1998.
- [195] F. Thiel, A. Schnabel, S. Knappe-Gruneberg, D. Stollfuss, and M. Burghoff, "Proposal of a demagnetization function," *IEEE transactions on magnetics* **43**(6), pp. 2959–2961, 2007.

-
- [196] H. Wang, Z. Chen, J. Huang, L. Quan, and B. Zhao, "Development of high-speed on-off valves and their applications," *Chinese Journal of Mechanical Engineering* **35**(1), p. 67, 2022.
- [197] M. Pan and A. Plummer, "Digital switched hydraulics," *Frontiers of Mechanical Engineering* **13**, pp. 225–231, 2018.
- [198] S. Genç and P. P. Phulé, "Rheological properties of magnetorheological fluids," *Smart Materials and Structures* **11**(1), p. 140, 2002.
- [199] M. Ocalan and G. H. McKinley, "Rheology and microstructural evolution in pressure-driven flow of a magnetorheological fluid with strong particle-wall interactions," *Journal of Intelligent Material Systems and Structures* **23**(9), pp. 969–978, 2012.
- [200] S. S. Deshmukh, *Development, characterization and applications of magnetorheological fluid based "smart" materials on the macro-to-micro scale*. PhD thesis, Massachusetts Institute of technology, 2006.
- [201] P. Domínguez-García, S. Melle, J. Pastor, and M. Rubio, "Scaling in the aggregation dynamics of a magnetorheological fluid," *Physical review E* **76**(5), p. 051403, 2007.
- [202] Nikon, "Darkfield illumination." <https://www.microscopyu.com/techniques/stereomicroscopy/darkfield-illumination>, 2022. Accessed: 2023-03-17.
- [203] A. I. Abdel-Fattah, M. S. El-Genk, and P. W. Reimus, "On visualization of sub-micron particles with dark-field light microscopy," *Journal of colloid and interface science* **246**(2), pp. 410–412, 2002.
- [204] A. H. Sihvola, *Electromagnetic mixing formulas and applications*, no. 47, Iet, 1999.
- [205] C. M. Lin, Y. S. Lai, H. P. Liu, C. Y. Chen, and A. M. Wo, "Trapping of bioparticles via microvortices in a microfluidic device for bioassay applications," *Analytical chemistry* **80**(23), pp. 8937–8945, 2008.
- [206] J. B. Cole and J. C. Florez, "Genetics of diabetes mellitus and diabetes complications," *Nature reviews nephrology* **16**(7), pp. 377–390, 2020.
- [207] J. L. Harding, M. E. Pavkov, D. J. Magliano, J. E. Shaw, and E. W. Gregg, "Global trends in diabetes complications: a review of current evidence," *Diabetologia* **62**(1), pp. 3–16, 2019.
- [208] C. W. Hicks and E. Selvin, "Epidemiology of peripheral neuropathy and lower extremity disease in diabetes," *Current diabetes reports* **19**(10), pp. 1–8, 2019.
- [209] H. Abri, M. Aalaa, M. Sanjari, M. R. Amini, M. R. Mohajeri-Tehrani, and B. Larijani, "Plantar pressure distribution in diverse stages of diabetic neuropathy," *Journal of Diabetes & Metabolic Disorders* **18**(1), pp. 33–39, 2019.

Bibliography

- [210] D. J. Margolis and W. Jeffcoate, "Epidemiology of foot ulceration and amputation: can global variation be explained?," *Medical Clinics* **97**(5), pp. 791–805, 2013.
- [211] D. Atlas *et al.*, "Idf diabetes atlas," *International Diabetes Federation (9th editio)*. Retrieved from <http://www.idf.org/about-diabetes/facts-figures>, 2019.
- [212] Z. T. Bloomgarden, "American diabetes association 60th scientific sessions, 2000: the diabetic foot," *Diabetes Care* **24**(5), pp. 946–951, 2001.
- [213] R. E. Pecoraro, G. E. Reiber, and E. M. Burgess, "Pathways to diabetic limb amputation: basis for prevention," *Diabetes care* **13**(5), pp. 513–521, 1990.
- [214] B. J. Beuker, R. W. van Deursen, P. Price, E. A. Manning, J. G. Van Baal, and K. G. Harding, "Plantar pressure in off-loading devices used in diabetic ulcer treatment," *Wound repair and regeneration* **13**(6), pp. 537–542, 2005.
- [215] D. R. Sinacore, M. J. Mueller, J. E. Diamond, V. P. Blair III, D. Drury, and S. J. Rose, "Diabetic plantar ulcers treated by total contact casting: a clinical report," *Physical Therapy* **67**(10), pp. 1543–1549, 1987.
- [216] W. J. Jeffcoate, S. Y. Chipchase, P. Ince, and F. L. Game, "Assessing the outcome of the management of diabetic foot ulcers using ulcer-related and person-related measures," *Diabetes care* **29**(8), pp. 1784–1787, 2006.
- [217] P. R. Cavanagh and S. A. Bus, "Off-loading the diabetic foot for ulcer prevention and healing," *Journal of the American Podiatric Medical Association* **100**(5), pp. 360–368, 2010.
- [218] S. C. Wu, J. L. Jensen, A. K. Weber, D. E. Robinson, and D. G. Armstrong, "Use of pressure offloading devices in diabetic foot ulcers: do we practice what we preach?," *Diabetes care* **31**(11), pp. 2118–2119, 2008.
- [219] D. G. Armstrong, L. A. Lavery, H. R. Kimbriel, B. P. Nixon, and A. J. Boulton, "Activity patterns of patients with diabetic foot ulceration: patients with active ulceration may not adhere to a standard pressure off-loading regimen," *Diabetes care* **26**(9), pp. 2595–2597, 2003.
- [220] D. J. Gutekunst, M. K. Hastings, K. L. Bohnert, M. J. Strube, and D. R. Sinacore, "Removable cast walker boots yield greater forefoot off-loading than total contact casts," *Clinical Biomechanics* **26**(6), pp. 649–654, 2011.
- [221] E. Faglia, C. Caravaggi, G. Clerici, A. Sganzeroli, V. Curci, W. Vailati, D. Simonetti, and F. Sommalvico, "Effectiveness of removable walker cast versus nonremovable fiberglass off-bearing cast in the healing of diabetic plantar foot ulcer: a randomized controlled trial," *Diabetes care* **33**(7), pp. 1419–1423, 2010.

-
- [222] H. Q. Ontario *et al.*, “Fibreglass total contact casting, removable cast walkers, and irremovable cast walkers to treat diabetic neuropathic foot ulcers: a health technology assessment,” *Ontario health technology assessment series* **17**(12), p. 1, 2017.
 - [223] D. Brown, J. J. Wertsch, G. F. Harris, J. Klein, and D. Janisse, “Effect of rocker soles on plantar pressures,” *Archives of physical medicine and rehabilitation* **85**(1), pp. 81–86, 2004.
 - [224] S. J. Kavros, M. G. Van Straaten, K. A. C. Wood, and K. R. Kaufman, “Forefoot plantar pressure reduction of off-the-shelf rocker bottom provisional footwear,” *Clinical Biomechanics* **26**(7), pp. 778–782, 2011.
 - [225] L. Allet, S. Armand, R. A. de Bie, Z. Pataky, K. Aminian, F. R. Herrmann, and E. D. de Bruin, “Gait alterations of diabetic patients while walking on different surfaces,” *Gait & posture* **29**(3), pp. 488–493, 2009.
 - [226] K. Myers, J. Long, J. Klein, J. Wertsch, D. Janisse, and G. Harris, “Biomechanical implications of the negative heel rocker sole shoe: gait kinematics and kinetics,” *Gait & Posture* **24**(3), pp. 323–330, 2006.
 - [227] B. C. Albright and W. M. Woodhull-Smith, “Rocker bottom soles alter the postural response to backward translation during stance,” *Gait & posture* **30**(1), pp. 45–49, 2009.
 - [228] S. A. Bus, J. S. Ulbrecht, and P. R. Cavanagh, “Pressure relief and load redistribution by custom-made insoles in diabetic patients with neuropathy and foot deformity,” *Clinical biomechanics* **19**(6), pp. 629–638, 2004.
 - [229] “Sensoria artificial intelligence sportswear.” <https://www.sensoriafitness.com/>, 2023. Accessed: 2023-02-21.
 - [230] “Transforming footcare for people with diabetes.” <https://www.orpyx.com/>, 2023. Accessed: 2023-02-21.
 - [231] “Thorsis technologies.” <https://www.thorsis.com/en/>, 2023. Accessed: 2023-02-21.
 - [232] “Feetme - digital solutions to assess mobility, predict injury and improve life quality.” <https://feetmehealth.com/>, 2023. Accessed: 2023-02-21.
 - [233] C. Gerlach, D. Krumm, M. Illing, J. Lange, O. Kanoun, S. Odenwald, and A. Hübler, “Printed mwcnt-pdms-composite pressure sensor system for plantar pressure monitoring in ulcer prevention,” *IEEE Sensors Journal* **15**(7), pp. 3647–3656, 2015.
 - [234] C. Majewski, A. Perkins, D. Faltz, F. Zhang, H. Zhao, and W. Xiao, “Design of a 3d printed insole with embedded plantar pressure sensor arrays,” in *Proceedings of the 2017 ACM International Joint Conference on Pervasive and Ubiquitous Computing and Proceedings of the 2017 ACM International Symposium on Wearable Computers*, pp. 261–264, 2017.

- [235] P. Aqueveque, R. Osorio, F. Pastene, F. Saavedra, and E. Pino, "Capacitive sensors array for plantar pressure measurement insole fabricated with flexible pcb," in *2018 40th Annual International Conference of the IEEE Engineering in Medicine and Biology Society (EMBC)*, pp. 4393–4396, IEEE, 2018.
- [236] L. Motha, J. Kim, and W. S. Kim, "Instrumented rubber insole for plantar pressure sensing," *Organic Electronics* **23**, pp. 82–86, 2015.
- [237] D. Chen, Y. Cai, and M.-C. Huang, "Customizable pressure sensor array: Design and evaluation," *IEEE Sensors Journal* **18**(15), pp. 6337–6344, 2018.
- [238] C. Deng, W. Tang, L. Liu, B. Chen, M. Li, and Z. L. Wang, "Self-powered insole plantar pressure mapping system," *Advanced Functional Materials* **28**(29), p. 1801606, 2018.
- [239] J. Chen, Y. Dai, and S. Gao, "A piezoelectric flexible insole system for gait monitoring for the internet of health things," 2020.
- [240] Y. Dai, Y. Xie, J. Chen, S. Kang, L. Xu, and S. Gao, "A lamination-based piezoelectric insole gait analysis system for massive production for internet-of-health things," *International Journal of Distributed Sensor Networks* **16**(3), p. 1550147720905431, 2020.
- [241] S. Rajala, R. Mattila, I. Kaartinen, and J. Lekkala, "Designing, manufacturing and testing of a piezoelectric polymer film in-sole sensor for plantar pressure distribution measurements," *IEEE Sensors Journal* **17**(20), pp. 6798–6805, 2017.
- [242] W. Lee, S.-H. Hong, and H.-W. Oh, "Characterization of elastic polymer-based smart insole and a simple foot plantar pressure visualization method using 16 electrodes," *Sensors* **19**(1), p. 44, 2019.
- [243] X. Lin and B.-C. Seet, "Battery-free smart sock for abnormal relative plantar pressure monitoring," *IEEE transactions on biomedical circuits and systems* **11**(2), pp. 464–473, 2016.
- [244] C. Guignier, B. Camillieri, M. Schmid, R. M. Rossi, and M.-A. Bueno, "E-knitted textile with polymer optical fibers for friction and pressure monitoring in socks," *Sensors* **19**(13), p. 3011, 2019.
- [245] A. G. Leal-Junior, C. R. Díaz, C. Marques, M. J. Pontes, and A. Frizera, "3d-printed pof insole: Development and applications of a low-cost, highly customizable device for plantar pressure and ground reaction forces monitoring," *Optics & Laser Technology* **116**, pp. 256–264, 2019.
- [246] D. Vilarinho, A. Theodosiou, C. Leitão, A. G. Leal-Junior, M. D. F. Domingues, K. Kalli, P. André, P. Antunes, and C. Marques, "Pofbg-embedded cork insole for plantar pressure monitoring," *Sensors* **17**(12), p. 2924, 2017.
- [247] S. Crea, M. Donati, S. M. M. De Rossi, C. M. Oddo, and N. Vitiello, "A wireless flexible sensorized insole for gait analysis," *Sensors* **14**(1), pp. 1073–1093, 2014.

- [248] X. Hu, F. Shen, D. Peng, C. Luo, S. Mo, and X. Qu, "A portable insole for foot plantar pressure measurement based on a pressure sensitive etextile and voltage feedback method," in *2018 IEEE 23rd International Conference on Digital Signal Processing (DSP)*, pp. 1–5, IEEE, 2018.
- [249] L. Shu, T. Hua, Y. Wang, Q. Li, D. D. Feng, and X. Tao, "In-shoe plantar pressure measurement and analysis system based on fabric pressure sensing array," *IEEE Transactions on information technology in biomedicine* **14**(3), pp. 767–775, 2010.
- [250] A. Caselli, H. Pham, J. M. Giurini, D. G. Armstrong, and A. Veves, "The forefoot-to-rearfoot plantar pressure ratio is increased in severe diabetic neuropathy and can predict foot ulceration," *Diabetes care* **25**(6), pp. 1066–1071, 2002.

Sofia Lydia Ntella

Curriculum Vitae

Personal Details

Nationality **Greek**, *EU citizenship*.
Date of Birth **06.02.1994**.

Education

- 2019–present **PhD Assistant**, *EPFL, Integrated Actuators Laboratory, Neuchatel, Switzerland*.
I have been working on the design and fabrication of miniaturized valves based on magnetorheological fluids for fluidic actuation control, under the supervision of Prof. Perriard. A case study of the valves is their integration into modules, enabling their controllable stiffness. The goal of the project is to use multiple modules in order to create a controllable-stiffness insole that will prevent diabetic ulcerations. Part of my time is also dedicated to the development and testing of the insole control electronics, considering minimum power consumption and minimum dimensions of the PCB.
- 2012–2017 **Joint BSc & MSc degree in Electrical and Computer Engineering**, *Aristotle University of Thessaloniki, Greece*.
Specialization in Electronics and Computers

Work Experience

- 2023–present **Postdoctoral Researcher**, *Integrated Actuators Laboratory, EPFL, Lausanne*.
- 2019–2023 **Teaching Assistant**, *EPFL, Lausanne*.
Courses: Electromechanical actuators I & II and Electrotechnics I & II
- 2019–present **Master & Semester project supervision**, *EPFL, Lausanne*.
During 4 years of PhD I supervised 4 master project students and 5 semester project students.
- 2018–2019 **ASML**, *Eindhoven, Netherlands*.
Job description: Calibration tests design and implementation for lithography machines. Design and implementation of new functionalities of the wafer positioning system of the machine. Code maintenance. Programming languages used: Python, C and C++.

Projects

- 2017 **Master project**, *Electronic System Design for Temperature and pH Measurements in Biomedical Applications*.
An electronic system was developed for pH and temperature measurements in parallel with anesthesia monitoring of patients in operation rooms. The project included design, fabrication and testing of the electronic system, a GUI development, as well as testing with chemical samples (propofol diluted in buffer solution).

Patents

- B. Tiwari, C. Koechli, K. Jeanmonod, P. Germano, S.L. Ntella, Y. Civet, Y. Perriard, "A miniaturized passive valve for pressure sustention and release", submitted in March 2023, EP Patent Application Nr 23159412.8.
- S.L. Ntella, A. Thabuis, B. Tiwari, C. Koechli, K. Jeanmonod, Y. Perriard, "Miniaturized magnetorheological valve using electropermanent magnets", submitted in December 2022, EP Patent Application Nr 22212573.4.

Publications

- **S.L. Ntella**, et al., "Highly efficient miniaturized magnetorheological valves based on electropermanent magnet," *IEEE Robotics & Automation Letters*, Januray 2023.
- **S.L. Ntella**, Xinyu Jia, et al., "Design and Development of a Novel Magnetorheological Fluid Based Soft Actuator", *Sensors and Actuators A: Physical*, *Under Review*.
- S. Hemler, **S.L. Ntella**, et al., "Intelligent plantar pressure offloading for the prevention of diabetic foot ulcers and amputations", *Frontiers in Endocrinology*, June 2023.
- **S.L. Ntella**, et al., "Pressure Offloading Device for Diabetic Footwear Based on Magnetorheological Fluids," *2022 25th International Conference on Electrical Machines and Systems (ICEMS)*.
- T. Loayza*, **S.L. Ntella***, et al., "Microfluidic device for analysis of MRF properties", *2022 IEEE/ASME International Conference on Advanced Intelligent Mechatronics (AIM)*.
- **S.L. Ntella**, et al., "Preliminary Study of Pressure Self-Sensing Miniature Magnetorheological Valves", *2021 IEEE/ASME International Conference on Advanced Intelligent Mechatronics (AIM)*.
- **S.L. Ntella**, et al., "Design optimization of miniature magnetorheological valves with self-sensing capabilities used for a wearable medical application", *2020 IEEE/ASME International Conference on Advanced Intelligent Mechatronics (AIM)*.
- **S.L. Ntella**, et al., "Optimization of Radial Magnetorheological Valves with Constraints of Volume, Pressure Drop and Power Consumption," *2020 23th International Conference on Electrical Machines and Systems (ICEMS)*.
- **S.L. Ntella*** and F. Stradolini*, et al., "Architectures and Procedures for pH and Temperature Monitoring in Medical Applications", *IEEE Sensors Conference 2017*.
- S. Hemler, **S.L. Ntella**, et al., "Evaluation of plantar pressure redistribution in novel footwear for people with diabetes", *IBS 2023*.
- M.T. Duong, **S.L. Ntella**, et al., "Optimal design of magnetorheological valve integrated in an intelligent footwear for diabetic patients with foot insensitivity," *2021 24th International Conference on Electrical Machines and Systems (ICEMS)*.
- F. Stradolini, A. Tuoheti, T. Kilic, **S.L. Ntella**, et al., "An IoT Solution for On-line Monitoring of Anesthetics in Human Serum Based on an Integrated Fluidic Bio-Electronic System", in *IEEE Transaction on Biomedical Circuits and Systems*.

Teams Participation

2018–2019 **Falcons**: Member of the robotics team sponsored by ASML participating in the Middle Sized League of Robocup.

Languages

Greek (*Native*), English (*Full working proficiency*), French (*Full working proficiency*), German (*Limited working proficiency*)

Interests & Hobbies

- 12-year Piano Studies, Theoretical Music Studies in Harmony, Solfege, Dictee and Music History
- Yoga

Voluntary Work

2020–2022 Ambassador for E3 Excellence in Engineering Program at EPFL.

2015–2016 Thessaloniki Piano Festival, Greece, *production assistant*.